DOCTORAL THESIS

Aix-Marseille University

Doctoral School: *Sciences pour l'ingénieur : Mécanique, Physique, Micro et Nanoélectronique*

Speciality : **Mécanique et Physique des Fluides**

Dynamics of driven and spontaneous transport barriers in the edge plasma of tokamaks

---

Presented by:

Nicolas Nace

Board of examiners for public Ph.D. defense on March, 9th 2018

Pr. Jens Juul RASMUSSEN	Referee – Professor at Technical University of Denmark
Pr. Alain GHIZZO	Referee – Professor at University of Lorraine
Pr. Peter BEYER	Examiner – Professor at Aix-Marseille University
Dr. Fluvio MILITELLO	Examiner – Researcher at Culham Center for Fusion Energy
Dr. Laure VERMARE	Examiner – Researcher at Ecole Polytechnique, CNRS
Dr. Eric SERRE	Examiner – Research director at M2P2 laboratory, CNRS
Dr. Patrick TAMAIN	CEA supervisor – Researcher at IRFM, CEA
Dr. Guido CIRAOLO	PhD director – Researcher at IRFM, CEA
Dr. Michael KOMM	Invited – Researcher at IPP, Czech Academy of Sciences

Laboratory :

Institut de **R**echerche sur la **F**usion par confinement **M**agnétique

CEA – Cadarache

13108 Saint-Paul-lez-Durance, France

Nov 2014 – Mar 2018

Contents

Introduction

The sustain of the high temperature of the plasmas of magnetically confined devices is a requirement for the development of thermonuclear fusion reactors. For that, the confinement of plasma density and energy has to be optimized. An improved confinement regime, so-called the H-mode is obtained experimentally in most of the toroidal magnetic devices when a threshold on the input power is exceeded. This operational regime is characterized by the increase of pressure in the core plasma due to the formation of a transport barrier in closed fields line region in the vicinity of the transition with open field lines in the so-called pedestal region. Within the transport barrier, the gradients of pressure and density strongly increase and a suppression of the turbulent transport is observed associated with a well of the radial electric field. Radial derivatives of the electric field - the $\mathbf{E}\times\mathbf{B}$ shear and the $\mathbf{E}\times\mathbf{B}$ curvature - are believed to be important players on the development of these edge transport barriers. Simple predator-prey models demonstrate the complex interplay between the mean equilibrium $\mathbf{E}\times\mathbf{B}$ shear flow, $\mathbf{E}\times\mathbf{B}$ oscillating flow (zonal flow) and turbulence. If the main mechanisms involve in the transition from low (L) to high (H) confinement regimes have now been analysed in experiments and simple 0D and 1D models, the complex interplay between these mechanisms during the L-H transition is still not fully understood. A consistent modelling tool reproducing most of the experimental features of the L-H transition is required to validate our understanding of the phenomenology of the H-mode physics.

Consequently, the development of advanced first-principle numerical codes is a major topic for the tokamak edge plasma community. The analysis of realistic numerical simulations of edge plasma - usually using the fluid approach - aims at a better understanding of the interplay between turbulence and $\mathbf{E}\times\mathbf{B}$ flows which can lead to the formation of an edge transport barrier. In the last decade, major progress has been realized on the modelling of the L-H transition. Some features of this transition have recently been recovered with simple 2D slab codes. Spontaneous transport barriers are obtained in the confined plasma with the edge fluid code Tokam2D when the closed field lines are included in the isothermal model pointing out the key role of the transition between open and closed field lines. Meanwhile, simulations with the 2D edge fluid code Hesel exhibit an improved confinement regime when a threshold on the input power is reached, underlying the key role of the ion energy channel. Finally, more complex 3D codes such as Emedge3D recover the behavior of an L-H transition in closed field lines when a neoclassical friction force is added in the model. Nevertheless, no simulations have reproduced a consistent L-H transition including all the key physical ingredients (geometry, both closed and open field lines, consistent and advanced model, ...)

This thesis aims at pursuing the efforts on the modelling of the L-H transition using fluid turbulence codes. For that, the existence and the dynamics of driven and spontaneous edge transport barriers are investigated by using numerical tools of increasing complexity. We focus in particular on the influence of the magnetic geometry, on the impact of the parallel dynamic, on the importance of the coupling between stabilizing and unstabilizing regions for the turbulence development and on the impact of the twisting of magnetic field lines. The relevancy of the results from simple to complex simulations for the L-H transition is discussed, pointing out the strengths and weaknesses of these models.

The first Chapter is an introduction dedicated on generalities on the physics of nuclear fusion. The conditions required to achieve fusion reactions between hydrogen isotopes are detailed as well as the magnetic configuration and geometry of tokamaks. A focus is particularly made on the radial transport and on turbulence in the edge plasma. We finally present the main characteristics of the H-mode and of the L-H transition existing in the literature from experimental point of view, from simple predator-prey models and from realistic first-principle numerical simulations.
The derivation of fluid equations is investigated in Chapter 2. Fluid equations of continuity, momentum and energy are derived from the particle and kinetic descriptions and the Braginskii's closures - predominant in the modelling of edge plasma - are especially detailed. An ordering procedure is thus suggested to improve current models and to retain only the dominant terms involved in the edge plasma. From that, the drift velocities are recovered. The 2D and 3D numerical tools used in this thesis - respectively the new thermal version of Tokam2D and the isothermal version of Tokam3X - are detailed in terms of equations and geometry while the main assumptions are underlined for both codes.
In Chapter 3, two mechanisms expected to generate transport barriers are driven in the Scrape-Off Layer region in dedicated Tokam2D isothermal simulations. These mechanisms - the $\mathbf{E}\times\mathbf{B}$ shear and the $\mathbf{E}\times\mathbf{B}$ curvature - correspond respectively to first and second radial derivatives of the radial electric field and are believed to be involved on the L-H transition. A criterion - the barrier efficiency - is set up to analyse the dynamics of transport barriers and to evaluate the ability of a flux-surface to stop the radial propagation by turbulence. The main discrepancies between the two mechanisms are revealed and the relevancy of driven transport barriers with respect to the H-mode physics is discussed.
Chapter 4 focuses on the existence of spontaneous edge transport barriers in slab geometry. In Tokam2D, the study of spontaneous transport barriers obtained with the bi-periodic isothermal model is extended to the new thermal version. The role of the ion heat channel is investigated as well as the interplay between turbulence and $\mathbf{E}\times\mathbf{B}$ shear. The inherent limits of simple 2D slab model are discussed, in particular through a comparison with 3D slab simulations.
Then, Chapter 5 is dedicated to the effects of a circular limiter geometry in our simulations. The existence of spontaneous transport barriers in realistic geometry is investigated by an increase of the ion energy channel contribution through the so-called generalized vorticity. The discrepancies with slab simulations are studied by using vorticity balances. Finally, the impact of the magnetic configuration on turbulence and on transport properties is investigated by modifying the safety factor profile in our simulations. A special focus is done on the magnetic shear by mimicking the safety factor profile of a divertor X-point geometry. The relevancy for the L-H transition of these results with numerical tools of increasing complexity is analysed as a conclusion.

Chapter 1

Introduction: confinement, turbulence and edge transport barriers

Problems are often stated in vague terms ... because it is quite uncertain what the problems really are.

John von Neumann

1.1 Current and forecast worldwide energy supply

The energy supply is a critical topic for most countries in the world from economical, geopolitical and ecological points of view. In this section, we briefly introduce the main issues raised by the worlwide energy supply.

1.1.1 Expected global increase of world energy supply

The energy supply in the world keeps increasing since the beginning of the industrial era during the 19th century. Recently, the energy consumption is stabilizing in developed countries and one can even expect a decrease in the near future mainly due to improvements of energy efficiency. Conversely, the energy supply keeps increasing in developing countries due to an improvement of standard living. Indeed, a net correlation has been established between energy consumption and quality of life [Lambert 14], [Brown 11] in modern societies even if government policies can strongly mitigate this correlation [Pasten 12]. In addition to the increase of quality of life, the world energy supply is also expected to grow because of the increase of the world population which should rise from 7.5 to almost 10 billion by 2050 according to a recent United Nations report [United Nations report 17].

1.1.2 A current worldwide energy supply massively provided by fossil fuels

A focus is now made on the current situation of energy supply in the world. According to a 2017 IEA report [International Energy Agency report 17], the total amount of world primary energy supply in 2015 was 158714 TWh. The repartition of this supply by fuel sources is presented on the left panel of Figure 1.1. A large majority (81.4%) of the world total primary energy supply is provided by fossil fuels: oil (31.7%), coal (28.1%) and natural gas (21.6%). Others sources of primary energy are nuclear fission (4.9%) and renewable energies: hydro (2.5%), biofuels and waste (9.7%) and others (1.5% in particular solar, wind, geothermal and heat).

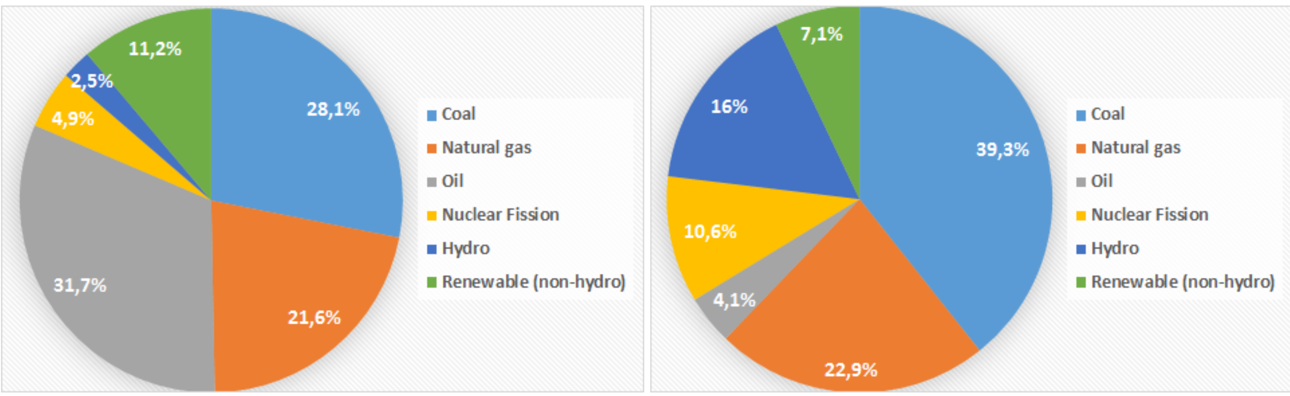

Figure 1.1: Pie charts of world supply in 2015 in terms of fuel sources for:
Left panel: total primary energy (total: 158714 TWh)
Right panel: electricity generation (total: 24255 TWh)

This total primary energy is mainly used for transports, heat, industries and electricity production. The latter consists in 2015 of 15.28% of world total primary energy consumption. The world electricity generation by fuel sources is presented on the right panel of Figure 1.1. Almost two third of world electricity generation is produced by fossil fuels mainly coal and natural gas.

1.1.3 Threats induced by fossil fuels on future human development

The analysis of world energy supply demonstrates how much humanity is nowadays dependant of fossil fuels. The first issue raised is the question of availability and depletion of fossil resources. Indeed, fossil fuels are non-renewable resources (at an human-time frame) and their reserves are estimated at 85 years at current production levels [BP 17]: around 50 years for oil and natural gas and 150 years for coal. But reserve rarefactions are not the main issue of fossil fuel exploitation. Indeed, an Earth's climate change (also called global warming) has been measured since the 1950s characterized by a global elevation of atmosphere and ocean mean temperatures, a rise of sea level, an ocean acidification and a diminution of snow and ice. Since pre-industrial times, atmospheric concentrations of greenhouse gases and especially of carbon dioxide CO_2 have increased by 40%. The development of climate model demonstrates the correlation between this increase of CO_2 atmospheric concentration and the unprecedented known climate changes detailed previously [Stocker 14]. This report concludes on a clear Human influence due to large emission of anthropogenic greenhouse gases. The main sources of man-made greenhouse emissions are agricultural activities (24%) especially livestock, industry (21%), transport (14%) and electricity (and heat) production (25%) [IPCC 14]. The 2015 United Nations Climate Change Conference (COP21) - signed by 175 countries - fixed as an objective to limit the global warming to 1.5 to $2°C$ compared to pre-industrial levels. To achieve this objective, an energy transition is required in order to substitute fossil fuels supply by carbon-free energy. On the following section, a focus is made on current and prospective alternatives to fossil fuels for electricity generation. Note that it could also strongly reduced the greenhouse gas emissions from transport activities as carbon-free electricity can be used to reload batteries of electric motors as a substitution of standard heat engines.

1.1.4 Alternatives to fossil fuels

Renewable energies: solar, wind, hydro, . . .

Renewable energies are usually believed to be the best solution to achieve the energy transition. Their main advantage is to not require any consumable fuels as the electricity is obtained by exploiting infinite (on a human timescale) resources: sunlight, wind and hydrological cycle. If electricity generation by renewable energies produces generally lower greenhouse gas emissions compared to fossil fuel exploitation, a large discrepancy of emissions is found when the full life cycle of renewable technologies are included [Amponsah 14]. The absence of waste during electricity production is also a strength of renewable energy exploitation. However, a world fully provided by renewable energy seems currently unreachable due to several issues. The main drawback of renewable energies is the intermittency of sources (sunlight, wind) which are not available continuously to be converted into electricity. Associated with the lack of efficient solutions for grid energy storage, it consists of a major impediment of development of fully renewable energy supply. Another issue is related to the strong land use induced by renewable technologies. For example, a simple calculation shows that around 40km^2 of photovoltaic panels are required in France to produce as much in average in a year as one nuclear fission reactor. Such large land use can be an issue to supply in electricity megalopolis and large industrial sites for which the urbanisation is already maximal. A solution could be a total reorganization of urbanized areas to include renewable energy electricity produces locally. In summary, even with an efficient renewable energy mix, a world fully provided by renewable energies appears to be currently unreachable. Nevertheless, a breakthrough in electricity storage efficiency may overcome the main issue of intermittent renewable electricity production.

Nuclear fission: Nuclear fission consists of the split of an atom nucleus into smaller parts: lighter nucleus, neutrons and gamma photons. An exothermic nuclear reaction can be obtained from nucleus heavier than iron (element with the highest binding energy per nucleon and thus the most stable). This energy excess results of mass defect according to famous Einstein's equation $E = mc^2$. In nuclear fission reactors, this process is used to generate electricity. A chain reaction is obtained when a heavy nucleus (typically uranium-235) absorbs a neutron and fissions into two smaller nucleus with a release of several neutrons which can sustain new fission reactions. A large amount of heat is generated and used to produce electricity by boiling water. Nuclear fission reactors have low carbon emissions and can continuously provide electricity with a relatively low land use. The use of nuclear fission reactors as a substitution of fossil fuels is however controversy. First, these reactors present a risk of nuclear disaster with significant health and environmental consequences as the Chernobyl disaster in 1986 and the Fukushima Daiichi nuclear disaster in 2011. The question of the management of radioactive waste is also a matter of debate and these waste - with half-life which can exceed millions of years - are currently planned to be buried in deep geological repositories. Due to the availability of fuel resources (especially uranium), both from geopolitical considerations and the risk of fuel depletion, a substitution of fossil fuel electricity generators by current nuclear fission reactors is unrealisable at the world scale. Indeed, identified uranium resources are sufficient for around 100 years of supply based on current requirements according to IAEA. The new generation IV of fission reactors is still developing and can tackle some of the issues of the generation III: using current nuclear waste as fuel to reduce the half life of nuclear waste, producing electricity directly from depleted uranium, replacement of uranium by thorium (three times more abundant than uranium on earth) and improvement of nuclear safety. To conclude, nuclear fission energy - which provides continuous electricity - can be used as a complement of intermittent renewable energies in a low carbon energy mix to achieve energy transition. New generation of fission reactors can overcome some of the issues of this technology but public opinion on nuclear fission, risk of nuclear proliferation and the threat of a new nuclear disaster are bottlenecks to a massive world development of the new generation of nuclear fission reactors.

Nuclear fusion: The principle of nuclear fusion is the opposite of nuclear fission: when two nucleus come close enough a fusion occurs and leads to the formation of an heavier element and other products (lighter elements, neutron, photons). It can results in an exothermic reaction for elements lighter than iron, the excess energy being determined by mass defect. Fusion reactions are the motor of the stars, it is up to now the high concentrated way to extract energy from matter with a released energy per reaction up to 3 to 4 times larger than fission reactions. Compared to nuclear fission, fusion reactors do not relied on a chain reaction so that a core meltdown cannot occurred. Nuclear fusion reactors produce no high activity, long-lived nuclear waste and the only waste should be the activated walls with a half-life of a few decades. The question of the availability of fusion fuels depends on the fusion reaction considered and will be discussed in section 1.2.2. Fusion reactors will thus be more energetic than fission ones without a risk of major nuclear disaster or the issue of very long lived nuclear waste management. The problem of fusion is the feasibility of reactors. The following section aims at understanding why conditions to sustain fusion reactions in a reactor are so difficult to achieve both from theoretical and engineering point of view. Nuclear fusion is one of the most promising solution of energy transition in a intermediate to long term as first fusion reactors would not be set up before the second half of the current century.

1.2 Fusion energy

1.2.1 Required conditions

In order to achieve a fusion reaction, protons must overcome the Coulomb repulsive barrier and be sufficiently close to fuse by quantum tunnelling effect. This happens only in extreme temperature conditions of the order of 10 to 100 million of degree Celsius. At such high temperature, the matter is a plasma in which electrons are stripped from atoms and evolve freely. Achieving and sustaining such extreme temperature conditions is one of the issue of fusion reactor physics.

1.2.2 Fusion reactions and fuel resources

Many fusion reactions involving lighter nucleus are exothermic. The selected reaction must fulfil some characteristics: the excess energy and the reaction cross-section has to be as large as possible and temperature conditions have to be achievable. The best reaction involves two hydrogen isotopes - Deuterium and Tritium:

$$ {}^2_1\mathrm{D} \;+\; {}^3_1\mathrm{T} \;\rightarrow\; {}^4_2\mathrm{He}\ (3.5\mathrm{MeV}) \;+\; {}^1_0\mathrm{n}\ (14.1\mathrm{MeV}) \tag{1.1} $$

This reaction cross-section is maximal for a temperature around 60keV. Note that from now on, temperatures are expressed in energy units by including Boltzmann constant and the electronvolt (eV) is used as the reference unit ($1\mathrm{eV} = 1.602 \times 10^{-19}\mathrm{J} \approx 10^4 K$). The Deuterium-Tritium (DT) reaction produces an alpha particle (Helium-4) and a high energy neutron (14.1MeV). Another key point is the availability of these reactants on Earth. Deuterium represents 0.016% of total hydrogen in the oceans and can be extracted from salt water at reasonable cost. Tritium is not a stable isotope, this radioactive isotope has an half-life of 12.32 years. But it can be produced in situ in a reactor by neutron-activation of Lithium-6 through the exothermic reaction:

$$ {}^6_3\mathrm{Li} \;+\; {}^1_0\mathrm{n} \;\rightarrow\; {}^4_2\mathrm{He}\ (2.05\mathrm{MeV}) \;+\; {}^3_1\mathrm{T}\ (2.75\mathrm{MeV}) \tag{1.2} $$

Lithium is the 25th most abundant element on earth crust and Lithium-6 isotope represents 7.6% of this total. Consequently, fuel resources are not a major issue for fusion power supply both from availability and economical points of view.

As seen previously, DT reaction produces an high energy neutron which can activate machine walls. The neutron carries most of the output energy and a thermal cycle is thus required to extract neutron energy by boiling water. Such procedure leads to a reduction of the global efficiency of a future power plant. From this point of view, an aneutronic reaction would be preferable but such reaction is not reachable nowadays either due to a lack of reactants for $^3_2$He reactions (the Helium-3 isotope is extremely rare on Earth) or due to too high temperature requirements (128keV for proton-boron reaction). In the following, we focus on DT reaction which is the most promising and studied fusion reaction.

1.2.3 Fusion energy gain factor

The fusion energy gain factor is a measure of the efficiency of a nuclear fusion device. It corresponds to the ratio of fusion power produced in the reactor to the input power needed to sustain fusion plasma in a steady-state. The breakeven - for which the fusion power equals the input power - is thus reached for $Q = 1$. In fact, a factor of $Q = 4$ or $Q = 5$ is required to maintain the fusion reactions as a significant part of fusion power is not reabsorbed by the plasma. Above this value, the ignition is reached and a value of at least $Q > 40$ has been estimated for a fusion reactor in order to be economically viable. An energy balance of a fusion plasma between sources and sinks permits to obtain a relation between the fusion energy gain factor and plasma conditions - so called the Lawson criterion. In order to achieve ignition and $Q > 40$, this relation writes:

$$nT_i\tau_E > 2.7 \times 10^{21}\mathrm{m}^{-3}.\mathrm{keV.s} \tag{1.3}$$

where n is the plasma density, T_i is the ion plasma temperature and τ_E the energy confinement time. The latter measures the decay rate of plasma energy in the absence of external heating.

1.2.4 Inertial and magnetic confinement fusion

The Lawson criterion characterizes the performance of a fusion device with three players. The DT cross-section optimum imposes a condition on plasma temperature: $T_i \approx 30$keV so that only two physical quantities, the plasma density and the energy confinement time determine the mean efficiency of fusion reactors. Two different approaches are investigated to achieve fusion reactors.

Inertial confinement fusion: Fusion reactions are obtained by compressing and heating a DT target by the use of high energy beams. In such configuration, the density is very high $n \approx 10^{31}m^{-3}$ and a very low confinement time has to be ensured $\tau_e \approx 10^{-11}s$. Two large scale experimental devices, the National Ignition Facility (NIF) in the US and more recently the Laser Mégajoule in France investigate the feasibility of inertial confinement fusion. In 2014 at the NIF, the energy released by a DT target has exceeded for the first time the energy amount applied to this target [Hurricane 14].

Magnetic confinement fusion: with this approach, an high energy confinement time $\tau_e \approx 1s$ is expected in a low density plasma of $n \approx 10^{20}m^{-3}$. Any material walls facing directly plasma at such temperature and pressure conditions will instantaneously melt. The idea is to confine the hot plasma from the reactor walls by use of a magnetic field. In the following section, the magnetic field used to obtain such confinement is detailed.

1.3 The issue of magnetic confinement in fusion devices

1.3.1 Magnetic confinement devices

In a plasma, charged particles follow helical motion around magnetic field lines. This gyration motion is characterized by an angular frequency so-called cyclotron frequency $\omega_{c_s} = |q_s|B/m_s$ (where q_s and m_s are respectively the electric charge and the mass of the particle of the specie "s" and B is the magnetic field magnitude) and a radius of gyration so-called Larmor radius $\rho_{L_s} = v_\perp/\omega_{c_s}$ where $v_\perp$ is the velocity in the direction perpendicular to the magnetic field. For magnetic field magnitude of a few Tesla, an hydrogen isotope of several keV has a Larmor radius typically of the order of millimeters. That is to say that charged particles are strongly confined in directions perpendicular (transverse) to the magnetic field direction (call the parallel direction). In order to also obtain a particle confinement in the parallel direction - and thus increasing the particle confinement time - the magnetic field lines are closed on themselves so that particles experienced a free toroidal movement. Such toroidal magnetic field is realized using external coils distributed along the toroidal direction with respect to a symmetry axis as picture on the left scheme of Figure 1.2.

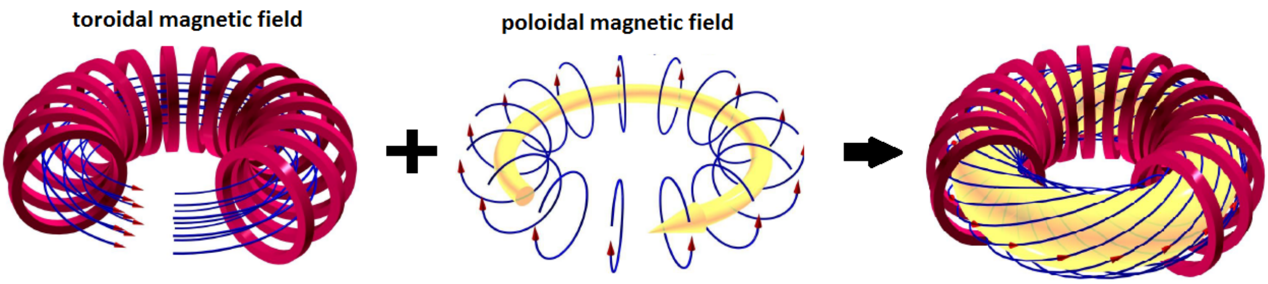

Figure 1.2: Scheme of magnetic field configuration on a tokamak. A toroidal magnetic field created by external coils (in red) is combined with a poloidal magnetic field induced by the plasma current (in yellow). It results that magnetic field lines have an helical shape rolled around the torus (in blue).

The resulting magnetic field has a curvature which is responsible of a vertical drift of particles which limits strongly the confinement time to a few milliseconds. The solution is to twist magnetic field lines around the torus in helical shape so that the vertical drift of a particle is compensated in average on a turn. For that, two main devices are considered. The first one - so-called stellerator - consists of a direct generation of this helical magnetic field using complex 3D external coils distributed toroidally. An experimental stellerator, the Wendelstein 7-X (W7-X) reactor, has been recently built in Germany to demonstrate the capability of such device to obtain long continuous plasma discharges and first hydrogen plasmas were obtained in 2016. One of the main advantages of stellerators is the absence of disruptions (abrupt loss of plasma confinement which can strongly damaged fusion devices). If stellerators are promising for fusion reactors, the most advanced and studied magnetic confinement device is the tokamak. The poloidal magnetic field, required to obtain an helical magnetic field, is produced directly by the plasma current flowing in the plasma I_p which results of transformer effect thanks to a central solenoid. Both poloidal and total magnetic fields of tokamaks are presented re-

spectively on the central and right schemes of Figure 1.2. Note that the plasma current is also used in tokamaks to heat the plasma through Joule effect. Such heating can drive the plasma up to 1keV and additional external heating systems are used to reach the optimal temperature of fusion reactions.
The International Thermonuclear Experimental Reactor, so-called ITER, under construction at Cadarache in the south of France, will be the largest tokamak in the world. It aims at demonstrating the feasibility for a tokamak to produce net energy with an objective in terms of fusion energy gain factor of $Q \geq 10$.

1.3.2 Tokamak configuration

A tokamak is a toroidal chamber. We first define two directions: the toroidal direction φ and the poloidal direction θ as presented in the scheme of a tokamak poloidal cut on Figure 1.3. Another main torus parameter is described in this scheme: the major radius R_0 - the distance between the torus axis of revolution and the center of a poloidal section. Any position of the plasma in a poloidal section can be described using cylindrical coordinates: r (distance from the plasma center) and θ or using Cartesian coordinates (R, Z) where $R = R_0 + r\cos\theta$ and $Z = r\sin\theta$.

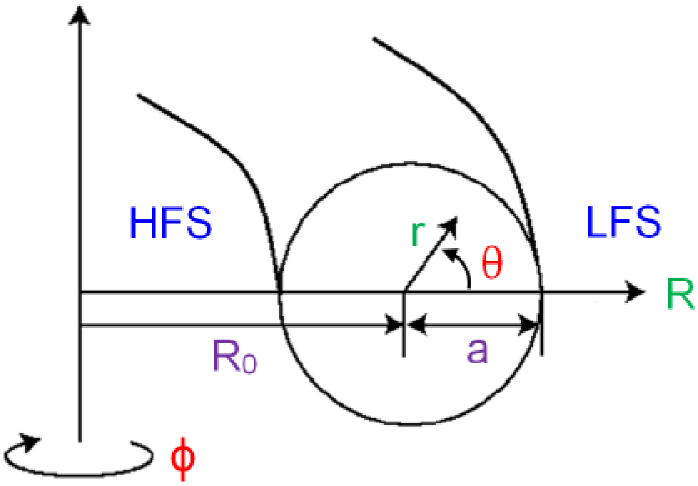

Figure 1.3: Schematic representation of the geometrical parameters of a circular tokamak.

Such description is valid only for circular plasmas. For non-circular ones, the radial direction is labelled using ψ, the flux surface index. A flux surface is the toroidally nested surface which contains a magnetic field line. The winding of the magnetic field lines is characterized by the safety factor q (see Equation (1.4)). The whole flux surface is covered by a magnetic field line for non rational safety factor values as the magnetic field line never closes on itself.

$$q(r) = \frac{\mathbf{B} \cdot \boldsymbol{\nabla}\phi}{\mathbf{B} \cdot \nabla\theta} \tag{1.4}$$

The radial variation of the safety factor is characterized by the global magnetic shear s defined as:

$$s = \frac{r}{q}\frac{dq}{dr} \tag{1.5}$$

Note that the magnetic equilibrium is obtained when pressure and Lorentz forces are compensating each other: $\mathbf{j}\times\mathbf{B} = 0$. It follows that at equilibrium, the magnetic flux surfaces are isobars: $\mathbf{B}\cdot\boldsymbol{\nabla}p = 0$. Due to the disposition of external coils in the toroidal direction, the toroidal magnetic field decreases with the major radius: $B_{\mathrm{tor}} \propto 1/R$. That is to say that a gradient of magnetic field ∇B is always directed toward the axis of revolution. Consequently, in a tokamak, the Low Field Side (LFS) corresponds to the outer part of the torus and the High Field Side (HFS) to its inner part.
External coils, which generate the toroidal magnetic field, have to be protected from the plasma so that the latter cannot have an infinite radial extension. A solid wall is ultimately used to intercept magnetic field surfaces at a certain radius so-called minor radius a and this magnetic field line determines the Last Closed Flux Surface (LCFS, or separatrix). The region of confined plasma is called the Closed Field Line region (CFL) while the plasma region extended after the LCFS is the Scrape Off Layer (SOL) also called Open Field Line region (OFL). In the SOL, the plasma ends up at the material walls (the Plasma Facing Components - PFCs). If the confined plasma is directly in contact with a material wall at the LCFS, this PFC is called a limiter. A more complex configuration - called divertor configuration - is created with a magnetic X-point (i.e a zero poloidal magnetic field) which isolates material walls from the confined plasma. It reduces the heat fluxes at material walls and prevents the contamination of confined plasma by impurities resulting from the erosion of the PFCs.

1.4 Radial transport in tokamaks

Tokamak plasma experienced a strong temperature variation of several order of magnitudes between the core plasma of several keV - in order to obtain fusion reactions - to a few eV in the edge plasma close to the first wall - to not damage the PFCs. Such discrepancy in a few meters leads to the existence of strong gradients of temperature (and of density and pressure) in tokamak plasmas. In fact, the plasma can be seen as a system out of equilibrium in which an energy source is applied on the center (through heating and fusion reactions). Such system aims at dissipating its energy by minimizing these gradients: a radial transport drives a part of the particles and the energy from the core plasma to the target walls - a sink - in the open field line region.

1.4.1 Role and nature of radial transport in core and edge plasma

For the confined plasma, the radial transport deteriorates tokamak performance by increasing particle and energy losses. Conversely, the radial transport is found to increase the lifetime of the PFCs in the edge plasma. Indeed, the radial transport beyond the LCFS determines the SOL width which corresponds to the characteristic length of deposition of the exhaust energy on the PCFs. That is to say that a large radial transport in open field line region increases the spreading of the heat fluxes at the solid targets. For ITER, the limit of divertor materials has been estimated in steady-state at 10MW.m^{-2}. The scaling law usually used to predict the SOL width in standard ITER conditions [Eich 13] strongly exceeds this design limit. The estimation of SOL width and consequently of radial transport level is thus a major concern of future tokamak devices. Several processes lead to the existence of a radial transport in tokamak plasmas.

Classical transport: Coulomb collisions between particles of adjacent magnetic field lines can lead to a deconfinement of the particle towards an external magnetic field line. In average, it leads to a diffusive transport for which the characteristic frequency depends on plasma density and temperature $\nu_c \propto nT^{-3/2}$ and of characteristic length equal to the Larmor radius ρ_L. This classical transport can thus be expressed with a classical perpendicular diffusive coefficient:

$$D_\perp^{\text{classical}} \sim \nu_c \rho_L \tag{1.6}$$

In the whole plasma of tokamaks, this coefficient is of the order of $10^{-2}\text{m}^2.\text{s}^{-1}$.

Neoclassical transport: The toroidal geometry and the associated magnetic field curvature generate another radial transport calls neoclassical transport. Indeed, due to the difference of magnetic field magnitude in a poloidal plane, some of the particles are trapped in the Low Field Side. These particles creates several regimes of transport depending on the value of the plasma collisionality [ITER Physics 99]. As for classical transport, the neoclassical transport can be described by a diffusive transport. The neoclassical diffusive coefficient $D_\perp^{\text{neoclassical}}$ is found to be larger than the classical one but still of the same order of magnitude:

$$D_\perp^{\text{neoclassical}} \gtrsim D_\perp^{\text{classical}} \tag{1.7}$$

The detail of classical and neoclassical transports can be found in [Hinton 76].

Turbulent transport: Classical and neoclassical transport are not sufficient to explain the level of radial transport measures experimentally in tokamaks [Wagner 93]. This missing contribution of radial transport is found both theoretically and experimentally to be the turbulence [Liewer 85], [Connor 95], [Conway 08]. Turbulence corresponds to a self-organized flow in which unsteady vortices of multi-scales are interacting with each other and resulting in a chaotic complex convective transport. Turbulence appears in system in which dissipative processes (for example viscosity and classical diffusion) cannot overcome the increase of kinetic energy of a fluid flow so that the system self-reorganizes to increase dissipation by multi-scale interactions.

1.4.2 Origin of the turbulent transport in tokamaks

In tokamaks, the radial transport due to turbulence is induced by the development of micro-instabilities. The latter are due to the interaction between fluctuations of the plasma parameters with the magnetic field through the perpendicular drifts. In the following, we focus on electrostatic turbulence and the two main micro-instabilities believed to develop in the edge plasma - the drift-wave and the interchange mechanisms [Scott 05]- are detailed.

Drift-wave mechanism: Drift-waves result of the interaction between a homogeneous magnetic field and a density gradient so that this instability can occur in slab geometry (rectangular cuboid geometry with simplify magnetic configuration). Drift-waves can be schematically explained by assuming periodical poloidal (vertical) perturbations of electric potential and electron density as presented on Figure 1.4. Positive and negative potential volumes induce a poloidal (vertical) electric field. This electric field leads to a radial (horizontal) transport of particle directed inward or outward by interacting with the magnetic field: this is the $\mathbf{E} \times \mathbf{B}$ drift defined as:

$$\mathbf{v}_{\perp}^{E\times B} = \frac{\mathbf{E} \times \mathbf{B}}{B^2} \tag{1.8}$$

If electron density and electric potential fluctuations are perfectly in phase, the horizontal transport is compensated by super and sub density region such that it results only in a poloidal (vertical) phase velocity without modifying the magnitude of the perturbations. This is no longer true if the electron density and electric potential perturbations are out of phase. In this case, the compensation between sub and super density region is not ensured and the perturbation wave grows in magnitude: this is the drift-wave instability.

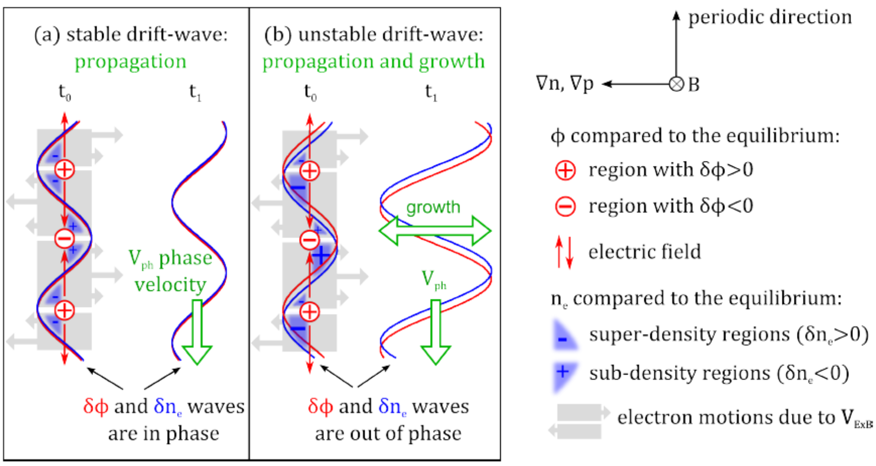

Figure 1.4: Schematic view of the drift-waves instability

Interchange mechanism: The second main instability developing in the edge plasma is the interchange instability. The development of this instability requires the existence of a magnetic field gradient such as in a toroidal geometry. Schematically, this instability can be explained by assuming a succession of positive and negative equipotential convection cells in the poloidal direction of a flux surface as presented on Figure 1.5. An upward or downward poloidal electric field appears between each positive and negative cells. It results in a radial $\mathbf{E}\times\mathbf{B}$ drift whose direction depends on the orientation of the poloidal electric field. The amount of particles carried by this radial $\mathbf{E} \times \mathbf{B}$ drift depends on the density gradient across the flux surface. These particles experienced a vertical (poloidal) transport due to the curvature of the magnetic field and especially the grad-B (or ∇B) particle drift:

$$\mathbf{v}_{\perp}^{\nabla B} = \frac{\mu_s \mathbf{B} \times \boldsymbol{\nabla} B}{q_s B^2} \tag{1.9}$$

where μ_s is the magnetic moment and q_s the electric charge of the particle s. In a fluid approach (see Chapter 2), this grad-B drift is included in the diamagnetic drift which results from collective effects of the interaction between the pressure gradient and the magnetic field:

$$\mathbf{u}^{\star}_{\perp_s} = \frac{\mathbf{B} \times \boldsymbol{\nabla}_{\perp} p_s}{n_s q_s B^2} \tag{1.10}$$

The direction of the grad-B drift determines if the convection cells grow or decay. Consequently, it is found that the interchange mechanism is stable on the HFS and unstable on the LFS such that the interchange instability is ballooned on the Low Field Side. The growth of convection cells generates finally an outward radial transport through the $\mathbf{E} \times \mathbf{B}$ drift.

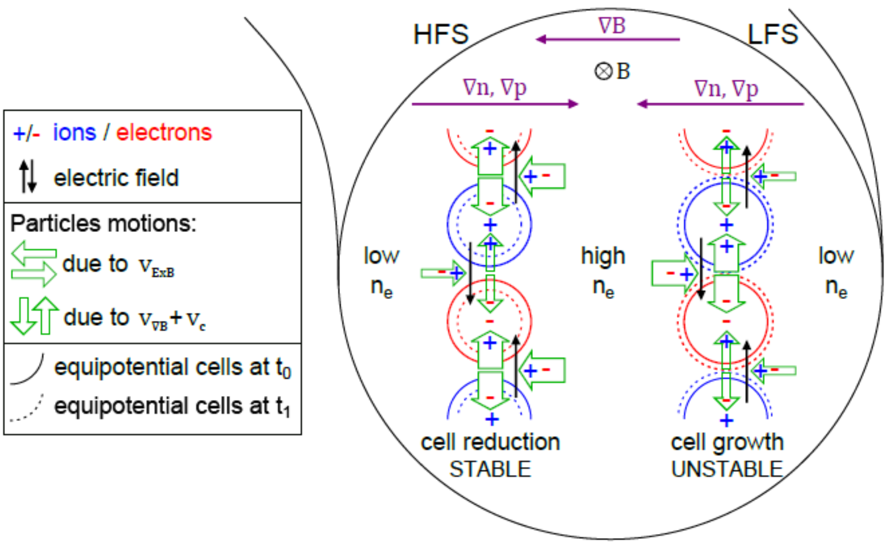

Figure 1.5: Schematic view of the interchange instability

Note finally that interchange modes can develop only if particles remains long enough on the LFS region so that the parallel transport has a stabilizing effect on interchange instability while trapped particles are especially subjected to experience interchange modes.

1.5 Improved confinement regime: the H-mode

The previous section exhibits the key role of the radial transport in the plasmas of tokamaks and especially in terms of particle and energy confinement. In 1982, an improved confinement regime - the H-mode - has been obtained in the ASDEX divertor tokamak [Wagner 82]. It is characterized by the formation of a pedestal region - i.e a region with a large pressure gradient - just before the separatrix [Wagner 84] as presented on Figure 1.6. Such increase of the pressure gradient compared to a standard confinement - so-called L-mode - is due to the suppression of the turbulence: an edge transport barrier develops. The energy confinement time is typically twice larger in H-mode compared to L-mode.

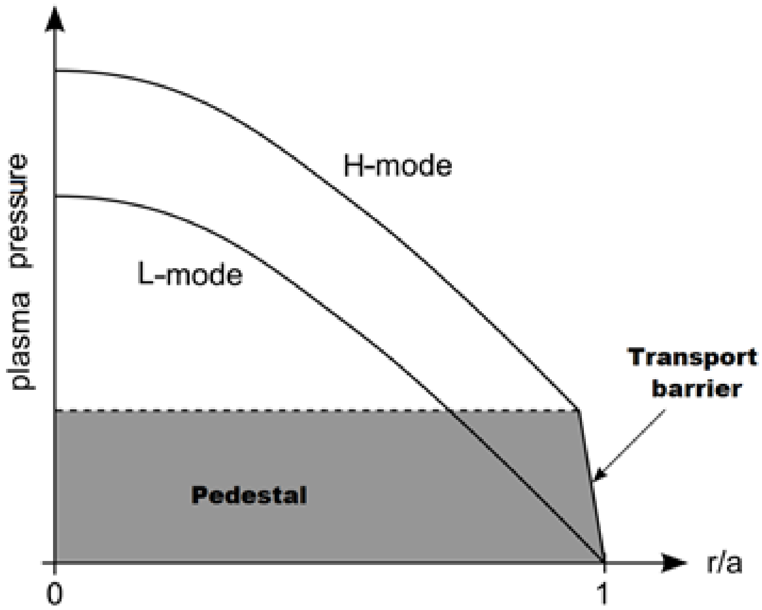

Figure 1.6: Typical pressure profiles in L-mode and H-mode.

A H-mode can be obtained only when a certain threshold on the input power is exceeded, and the region between L and H-mode cannot be reached: it consists thus on a bifurcation mechanism. In the following, the main observations on the transition from L- to H-mode are detailed from the experimental point of view. We describe then simple predator-prey like models to explain the main mechanisms involved in the L-H transition and briefly detail the main results on transport barriers from numerical modelling point of view.

1.5.1 H-mode experiments

The study of H-mode has been one of the major concern of fusion community since its discovery in the 1980s. Consequently, a complete review of experimental observations cannot be detailed on this manuscript and only the main characteristics of concern are presented. We focus in particular on qualitative observations of the mechanisms involved in the L-H transition.

The H-mode is found to be a general feature of toroidal magnetic devices. Indeed, H-mode has been obtained with most of stellerator and tokamak devices, in divertor and limiter configurations and from various heating power systems (see [Wagner 07] for a complete review). That is to say that the L-H transition must be the consequence of a universal mechanism. The main paradigm in the L-H transition is the key role of radial electric field which is found to become more negative in the pedestal region in experiments (for example on DIII-D [Groebner 90] and on JFT-2M [Ida 90]). This radial electric field well is associated with a reduction of edge density fluctuations [Doyle 91]. The suppression of turbulence is explained by the speeding-up of non-linear decorrelation of turbulence by $\mathbf{E} \times \mathbf{B}$ velocity shear (first derivative of E_r) as rigorously presented in the reviews [Burrell 97] and [Terry 00].

The origin of the radial electric well remains an opening debate as well as the origin of the threshold on the input power. In the closed field line region, the electric field is determined by the radial force balance and can be impacted by many mechanisms: neoclassical considerations [Viezzer 14] including

the ion heat channel [Ryter 14], [Ryter 16], impurities [Dunne 17], toroidal plasma rotation [Gohil 08], ... In the open field line region, the electric field is mainly determined by the boundary conditions at the target plates. The change in the parallel dynamics between the closed and the open field lines is believed to have a significant role during the L-H transition. Indeed, the pedestal is always localized in the vicinity of this transition between confined and unconfined domains.
Recent experiments [Kamiya 18] on the JT-60U tokamak point out the role of $\mathbf{E} \times \mathbf{B}$ curvature (second derivative of E_r) on the edge transport barrier structure in addition to the well-known $\mathbf{E} \times \mathbf{B}$ shear. Another player, the magnetic shear, can also impact on both turbulence and $\mathbf{E} \times \mathbf{B}$ shear [Burrell 97]. Both mean and oscillating (zonal flows) sheared flows impact on transport barrier dynamics [Hidalgo 11]. A complex interplay between $\mathbf{E} \times \mathbf{B}$ mean equilibrium flow, zonal flows and turbulence occurs in experiments [Conway 11], [Fujisawa 06], [Stroth 11], [Schmitz 12] and turbulence is believed to be one of the main source of the $\mathbf{E} \times \mathbf{B}$ shear flow [Tynan 13].

1.5.2 Simple predator-prey like model

In parallel with experimental investigations of the L-H transition, simple models have been developed since the H-mode discovery to explain the transition. At the beginning, simple 0D models underline the key role of radial electric field [Itoh 88] and the existence of bifurcations [Shaing 89]. Later, dynamical bifurcation models have been derived - similarly to predator-prey models - pointing out the interplay between $\mathbf{E} \times \mathbf{B}$ shear, fluctuations level and pressure gradient as well as the role of the Reynolds stress [Diamond 94], [Carreras 94]. The complexity of predator-prey like models has been increased by the inclusion of the dynamics and the impacts of zonal flows in [Diamond 01], [Kim 03] and [Itoh 14]. More recently, similar models have been extended to include the effect of the $\mathbf{E} \times \mathbf{B}$ curvature on the turbulence suppression in [Itoh 15] and [Itoh 16]. Complex 1D predator-prey models are now able to recover many features of the L-H transition, including the dynamics of the intermediate I-phase which can occur experimentally in certain conditions [Miki 12].

1.5.3 Transport barrier modelling

Predator-prey models are useful tools to improve our understanding on the L-H transition and to study the bifurcation branches but remain restricted due to their inherent simplicity. The development of advanced numerical tools is thus necessary to reproduce the dynamics and the complexity of edge plasmas of tokamaks and especially of the L-H transition. In the last decade, such first-principle numerical codes have been intensively developed. In the edge plasmas, the fluid approach appears to be the best compromise between the reliability of the results and the numerical cost induced by such simulations. In the L-H transition framework, fluid simulations have been used first to investigate the impact of driven transport barriers on turbulence properties both in 2D slab simulations for the Scrape-Off Layer with Tokam-2D [Ghendrih 03], [Floriani 13] and in 3D simulations for closed field lines with Emedge3D [Beyer 00], [Benkadda 01], [Beyer 07]. In all cases, the driven flows are found to lead to the suppression of turbulence and to the development of driven edge transport barriers. More recently, spontaneous transport barriers have been obtained in 2D slab geometry when closed field lines are added in Tokam2D isothermal model [Norscini 15]. Simultaneously, the 2D Hesel code reproduced several features of the L-H transition including the existence of a threshold on ion input power and comparisons with EAST measurements in [Nielsen 15], [Rasmussen 16] and especially by taking into account the diamagnetic contribution in the ion polarization drift. Some progresses have also been obtained with three-dimensional non-linear simulations. Features of the L-H transition are obtained in closed field lines when a neoclassical friction force is implemented in Emedge3D [Chôné 15]. A similar result is found in [Park 15]. Other leading edge plasma 3D codes, such as Tokam3X, BOUT++, or GBS, dedicate large efforts to recover a complete L-H transition involving all the mechanisms detailed previously.

Chapter 2

Derivation of fluid models applied in the Tokam2D/3X edge plasma turbulence codes

Now it would be very remarkable if any system existing in the real world could be exactly represented by any simple model. However, cunningly chosen parsimonious models often do provide remarkably useful approximations. (...) For such a model there is no need to ask the question "Is the model true?". If "truth" is to be the "whole truth" the answer must be "No". The only question of interest is "Is the model illuminating and useful?".

George E. P. Box

This chapter aims at detailing a complete derivation of the fluid equations used in the models studied in this thesis and based on the Braginskii's closure which relies on strongly magnetized plasma hypothesis. A focus is particularly given on all the assumptions made at each step of the derivation procedure to obtain the three first statistical moments. The momentum equations are then projected into parallel and perpendicular components. A new ordering is set up to obtain first and second order velocity drifts. Then, the final assumptions applied to obtain Tokam2D and Tokam3X equations are detailed and these two numerical codes are finally presented.

2.1 Derivation of kinetic description

2.1.1 Particle description

The most detailed way to describe the dynamic of a plasma is to treat each particle individually by solving the fundamental equation of dynamics (2.1). We consider a particle j of mass m_j and charge q_j within a plasma of N_0 particles of one or several species. In the $(1+6)\,D$ phase space, the particle coordinates are noted $(t, \mathbf{X}_j, \mathbf{V}_j)$ where $\mathbf{X}_j$ and $\mathbf{V}_j$ correspond respectively to the position and velocity of the particle j in the Lagrangian specification. Thereby, the exact classical motion of the particle can be determined[1]:

$$m_j d_t \mathbf{V}_j = \mathbf{F}_j \tag{2.1}$$

where $\mathbf{F}_j$ corresponds to the resulting force applied on particle j. In fusion magnetized plasma, this net force is due to the Lorentz force since gravitation can be neglected. Indeed, the ratio between gravitational and Lorentz forces writes $\frac{|m_s \mathbf{g}|}{|q_s(\mathbf{E}^l+\mathbf{V}\times\mathbf{B}^l)|} \approx \frac{m_s g}{eB_0 v_\perp} \approx \frac{g}{\omega_{c_s} v_{th_s}} \approx 10^{-12} - 10^{-14}$ for thermal protons under typical tokamak plasma conditions ($B_0 = 1 - 10T; T_0 = 10\text{eV} - 10\text{keV}$).

$$m_j d_t \mathbf{V}_j = q_j \left(\mathbf{E}^l + \mathbf{V}_j \times \mathbf{B}^l\right) \tag{2.2}$$

where $\mathbf{E}^l$ and $\mathbf{B}^l$ stand respectively for the local electric and local magnetic fields. These local fields are generated both by external fields and by the impact of all the other plasma particles according to Maxwell's equations:

$$\begin{cases} \boldsymbol{\nabla}\cdot\mathbf{E}^l = \dfrac{\rho^l}{\varepsilon_0} \\ \boldsymbol{\nabla}\cdot\mathbf{B}^l = 0 \\ \boldsymbol{\nabla}\times\mathbf{E}^l = -\partial_t \mathbf{B}^l \\ \boldsymbol{\nabla}\times\mathbf{B}^l = \mu_0\left(\mathbf{j}^l + \varepsilon_0 \partial_t \mathbf{E}^l\right) \end{cases} \tag{2.3}$$

where ρ^l and $\mathbf{j}^l$ are respectively the local charge and the local current densities.
For the particle j, these two quantities write:

$$\begin{cases} \rho^l(t,\mathbf{x}) = \displaystyle\sum_{k=1}^{N_0} q_k \delta(\mathbf{x}-\mathbf{X}_k) \\ \mathbf{j}^l(t,\mathbf{x}) = \displaystyle\sum_{k=1}^{N_0} q_k \delta(\mathbf{x}-\mathbf{X}_k)\,\mathbf{V}_k \end{cases} \tag{2.4}$$

[1] Note that for relativistic particles, an equivalent relation can be obtained according to special relativity theory.

Note that $\mathbf{x}$ and $\mathbf{v}$ correspond respectively to position and velocity coordinates in the Eulerian specification.
In modern tokamaks, the plasma volume is of the order of hundreds of cubic meters (100m^3 for JET and 840m^3 for ITER) and the average plasma density is of the order of 10^{19}m^{-3}. The total number of particles in fusion devices is thus of the order of 10^{21}. Using such particle description would thus required to solve 10^{21} equations simultaneously with Maxwell's equations.

2.1.2 Klimontovich equation

Instead of considering each particle individually, one can describe a plasma using a microscopic distribution function $\mathcal{N}_s$ for each species s in the six-dimensional phase space $(\mathbf{x}, \mathbf{v})$:

$$\mathcal{N}_s(t, \mathbf{x}, \mathbf{v}) = \sum_{k=1}^{N_{0_s}} \delta(\mathbf{x} - \mathbf{X}_k(t))\,\delta(\mathbf{v} - \mathbf{V}_k(t)) \tag{2.5}$$

with N_{0_s} the number of particles for the species "s" which verifies $\sum_s N_{0_s} = N_0$.
The Klimontovich distribution is a discrete function of the phase space. For the particle j, equations of motion write:

$$\begin{cases} \dot{\mathbf{X}}_j(t) = \mathbf{V}_j(t) \\ \dot{\mathbf{V}}_j(t) = \dfrac{q_j}{m_j}\left(\mathbf{E}^l + \mathbf{V}_j \times \mathbf{B}^l\right) \end{cases} \tag{2.6}$$

The time evolution equation of phase space density $\mathcal{N}_s(t, \mathbf{x}, \mathbf{v})$ can be obtained by writing the conservation law of particles in the phase space $d_t\mathcal{N}_s = 0$ using equations (2.5) and (2.6):

$$\boxed{\partial_t\mathcal{N}_s + \mathbf{v}\cdot\boldsymbol{\nabla}\mathcal{N}_s + \frac{q_s}{m_s}\left(\mathbf{E}^l + \mathbf{v}\times\mathbf{B}^l\right)\cdot\boldsymbol{\nabla}_v\mathcal{N}_s = 0} \tag{2.7}$$

This equation can also be written in a conservative form (2.8) by introducing a generalized velocity $\widehat{\mathbf{V}} \equiv (\dot{\mathbf{x}}, \dot{\mathbf{v}})$ and a generalized divergence operator $\widehat{\boldsymbol{\nabla}}\cdot \equiv (\boldsymbol{\nabla}_x, \boldsymbol{\nabla}_v)\cdot \_$:

$$\boxed{\partial_t\mathcal{N}_s + \widehat{\boldsymbol{\nabla}}\cdot\left(\mathcal{N}_s\widehat{\mathbf{V}}\right) = 0} \tag{2.8}$$

This result can be obtained because the Lorentz force is $\mathbf{v}$-divergence free:

$$\boldsymbol{\nabla}_\mathbf{v}\cdot\left(\mathbf{E}^l(t,\mathbf{x}) + \mathbf{v}\times\mathbf{B}^l(t,\mathbf{x})\right) = \underbrace{\boldsymbol{\nabla}_\mathbf{v}\cdot\mathbf{E}^l(t,\mathbf{x})}_{=0} + \mathbf{B}^l(t,\mathbf{x})\cdot\underbrace{(\boldsymbol{\nabla}_\mathbf{v}\times\mathbf{v})}_{=0} - \mathbf{v}\cdot\underbrace{\left(\boldsymbol{\nabla}_\mathbf{v}\times\mathbf{B}^l(t,\mathbf{x})\right)}_{=0} = 0 \tag{2.9}$$

One can notice that the Klimontovich equation is solved for each species involved in the plasma. The interactions between different species are taken into account through the local charge and current densities.
The particle description is unreachable from numerical point of view whether in terms of present computing power or storage capacity. Moreover, such approach would generate an unnecessary large amount of data since the expected output of simulation are usually macroscopic and statistical quantities such as average properties (density, heat fluxes, ...) or transport level for example.

2.1.3 Boltzmann and Vlasov equations

As said previously, the particle description provides a full discrete description of particle coordinates and trajectories while a statistical continuous description of plasma is fully sufficient to describe the plasma at a macroscopic scale. For that, the probability to find a particle in a given volume of phase space is analysed. Averaging over a large amount of events permits to switch from a discontinuous quantity - $\mathcal{N}_s$ - to a continuous one, noted f_s for a species "s", and called distribution function:

$$f_s\left(t,\mathbf{x},\mathbf{v}\right) = \langle \mathcal{N}_s\left(t,\mathbf{x},\mathbf{v}\right)\rangle \tag{2.10}$$

This distribution function corresponds to the probability to find a particle of species "s" in a infinitesimal volume $\Delta\mathbf{x}\Delta\mathbf{v}$ centred in $(\mathbf{x},\mathbf{v})$ and normalized by this volume in order to obtain a large and thus statistical physical quantity. The volume $\Delta\mathbf{x}\Delta\mathbf{v}$ must fulfil the following properties:

$$n_0^{-1/3} \ll l_x \equiv ||\Delta\mathbf{x}|| \ll \lambda_D = \left(\frac{\varepsilon_0 T_e}{n_0 e^2}\right)^{1/2} \tag{2.11}$$

$$l_v \equiv ||\Delta\mathbf{v}|| \ll v_{th_s} = \left(\frac{T_s}{m_s}\right)^{1/2} \tag{2.12}$$

The inequations (2.11) and (2.12) ensure that the selected volume is both homogeneous ($l_x \ll \lambda_D$ such as the electric charges are shielded and $l_v \ll v_{th_s}$, the thermal velocity) and sufficiently statistical ($l_x \gg n_0^{-1/3}$, the average distance between particles). All the microscopic quantities used in the particle description can be split using this average:

$$\begin{cases} \mathcal{N}_s\left(t,\mathbf{x},\mathbf{v}\right) = f_s\left(t,\mathbf{x},\mathbf{v}\right) + \delta\mathcal{N}_s\left(t,\mathbf{x},\mathbf{v}\right) \\ \mathbf{E}^l\left(t,\mathbf{x}\right) = \mathbf{E}\left(t,\mathbf{x}\right) + \delta\mathbf{E}\left(t,\mathbf{x}\right) \\ \mathbf{B}^l\left(t,\mathbf{x}\right) = \mathbf{B}\left(t,\mathbf{x}\right) + \delta\mathbf{B}\left(t,\mathbf{x}\right) \end{cases} \tag{2.13}$$

where $\delta\mathcal{N}_s$,$\delta\mathbf{E}$ et $\delta\mathbf{B}$ have a zero mean.
Global electric and magnetic fields, $\mathbf{E} =< \mathbf{E}^l >$ and $\mathbf{B} =< \mathbf{B}^l >$ satisfy the following "macroscopic" Maxwell equations :

$$\begin{cases} \boldsymbol{\nabla}\cdot\mathbf{E} = \dfrac{\rho}{\varepsilon_0} \\ \boldsymbol{\nabla}\cdot\mathbf{B} = 0 \\ \boldsymbol{\nabla}\times\mathbf{E} = -\partial_t\mathbf{B} \\ \boldsymbol{\nabla}\times\mathbf{B} = \mu_0\left(\mathbf{j} + \varepsilon_0\partial_t\mathbf{E}\right) \end{cases} \tag{2.14}$$

where ρ and $\mathbf{j}$ are respectively the charge and current densities:

$$\begin{cases} \rho\left(t,\mathbf{x}\right) =< \rho^l >= \sum_s q_s \displaystyle\int f_s d^3\mathbf{v} \\ \mathbf{j}\left(t,\mathbf{x}\right) =< \mathbf{j}^l >= \sum_s q_s \displaystyle\int \mathbf{v} f_s d^3\mathbf{v} \end{cases} \tag{2.15}$$

By using this averaging procedure, the Klimontovich equation (2.7) leads to the so-called Boltzmann (or collisional Vlasov) equation:

$$\boxed{\partial_t f_s\left(t,\mathbf{x},\mathbf{v}\right)+\mathbf{v}.\boldsymbol{\nabla} f_s+\frac{q_s}{m_s}\left(\mathbf{E}+\mathbf{v}\times\mathbf{B}\right)\cdot\boldsymbol{\nabla}_v f_s=C_s} \tag{2.16}$$

The left hand side of equation (2.16) contains terms resulting from collective effects and thus insensitive to the discrete nature of particles in the plasma. Conversely, the right hand side corresponds to the result of collisional processes between discrete particles. C_s is thus called *collisional operator* and takes into account the discontinuity of phase space at small scales:

$$C_s=-\frac{q_s}{m_s}\langle\left(\delta\mathbf{E}+\mathbf{v}\times\delta\mathbf{B}\right)\cdot\boldsymbol{\nabla}_v\delta\mathcal{N}_s\rangle \tag{2.17}$$

The collisional operator is a small correction of the left hand side of equation (2.16). This Boltzmann equation corresponds to the exact form of the plasma kinetic equation. This collisional operator is however often neglected and leads to the so-called Vlasov equation (also called collisionless Boltzmann equation):

$$\boxed{\partial_t f_s\left(t,\mathbf{x},\mathbf{v}\right)+\mathbf{v}.\boldsymbol{\nabla} f_s+\frac{q_s}{m_s}\left(\mathbf{E}+\mathbf{v}\times\mathbf{B}\right)\cdot\boldsymbol{\nabla}_v f_s=0} \tag{2.18}$$

As for the Klimontovich equation, both Boltzmann and Vlasov equations can be written in conservative form using (2.9). This leads to:

$$\boxed{\partial_t f_s\left(t,\mathbf{x},\mathbf{v}\right)+\boldsymbol{\nabla}_{\mathbf{x}}\cdot\left(f_s\mathbf{v}\right)+\boldsymbol{\nabla}_{\mathbf{v}}\cdot\left(\frac{q_s}{m_s}\left(\mathbf{E}+\mathbf{v}\times\mathbf{B}\right)f_s\right)=\begin{cases}0 & \textbf{Vlasov}\\ C_s & \textbf{Boltzmann}\end{cases}} \tag{2.19}$$

One can notice that the number of particles N_{0_s} and the entropy $S_s=-\iint_\Omega f_s\ln\left(f_s\right)d^3\mathbf{x}d^3\mathbf{v}$ are conserved over time for a species "s" by the Vlasov equation (2.18). This is not longer true with the collisional Vlasov equation (2.16) which only conserves the total number of particle N_0 of the phase space. Note that the total entropy $S=-\sum_s\iint_\Omega f_s\ln\left(f_s\right)d^3\mathbf{x}d^3\mathbf{v}$ is not conserved due to collisions.

2.2 From kinetic to fluid description

2.2.1 Methodology

Fluid equations can be obtained by taking momenta of the kinetic equation. The n^{th} momentum is obtained by multiplying the collisional Vlasov equation (2.19) by the n^{th} tensor powers of the velocity vector and then by integrating over all the 3D velocity space: $\forall n\in\mathbb{N}$,

$$\int_{\mathbf{v}}\mathbf{v}^{\otimes n}\partial_t f_s d^3\mathbf{v}+\int_{\mathbf{v}}\mathbf{v}^{\otimes n}\boldsymbol{\nabla}_{\mathbf{x}}\cdot\left(\mathbf{v}f_s\right)d^3\mathbf{v}+\int_{\mathbf{v}}\mathbf{v}^{\otimes n}\boldsymbol{\nabla}_{\mathbf{v}}\cdot\left(\frac{q_s}{m_s}\left(\mathbf{E}+\mathbf{v}\times\mathbf{B}\right)f_s\right)d^3\mathbf{v}=\int_{\mathbf{v}}\mathbf{v}^{\otimes n}C_s d^3\mathbf{v} \tag{2.20}$$

with $\mathbf{v}^{\otimes n} \equiv \underbrace{\mathbf{v} \otimes \cdots \otimes \mathbf{v}}_{\text{n times}}$. and $\mathbf{v}^{\otimes 0} \equiv 1$.

Equation (2.20) can be redrafted by considering commutative properties and leads to: $\forall n \in \mathbb{N}$,

$$\boxed{\partial_t \int_{\mathbf{v}} \mathbf{v}^{\otimes n} f_s d^3\mathbf{v} + \boldsymbol{\nabla}_{\mathbf{x}} \cdot \int_{\mathbf{v}} \mathbf{v}^{\otimes n+1} f_s d^3\mathbf{v} + \int_{\mathbf{v}} \mathbf{v}^{\otimes n} \boldsymbol{\nabla}_{\mathbf{v}} \cdot \left(\frac{q_s}{m_s} \left(\mathbf{E} + \mathbf{v} \times \mathbf{B}\right) f_s \right) d^3\mathbf{v} = \int_{\mathbf{v}} \mathbf{v}^{\otimes n} C_s d^3\mathbf{v}} \tag{2.21}$$

The infinite set of fluid momentum equations is strictly equivalent to the collisional Vlasov equation. However, the fluid description is always restricted to few momentum equations: for example, an isothermal fluid model has only two equations and most of thermal fluid models are constituted of three equations per species because it provides all the information for a Maxwellian distribution. One can observe in equation (2.21) that the n^{th} momentum of the kinetic equation involves both the n^{th} and the $(n+1)^{th}$ momenta such as a fluid closure is required on the $(n+1)^{th}$ momentum in order to close the fluid approach at the order n. This closure relies generally the $(n+1)^{th}$ momentum with low order momenta (n^{th},$(n-1)^{th}$,...). This complex issue of fluid closure is discussed in Section 2.3 as well as closure on collisional terms.

In the following, the distribution function f_s is assumed to be at least exponentially vanishing at infinity in the velocity space:

$$\forall n \in \mathbb{N}, \lim_{|\mathbf{v}| \to +\infty} \mathbf{v}^{\otimes n} f_s = 0 \tag{2.22}$$

2.2.2 Zero moment: continuity equation

For $n = 0$, the equation (2.21) writes:

$$\partial_t \left(\int_{\mathbf{v}} f_s d^3\mathbf{v} \right) + \boldsymbol{\nabla}_{\mathbf{x}} \cdot \left(\int_{\mathbf{v}} \mathbf{v} f_s d^3\mathbf{v} \right) + \int_{\mathbf{v}} \boldsymbol{\nabla}_{\mathbf{v}} \cdot \left(\frac{\mathbf{F}_s}{m_s} f_s \right) d^3\mathbf{v} = \int_{\mathbf{v}} C_s d^3\mathbf{v} \tag{2.23}$$

Some fluid quantities have to be introduced:

- particle density n_s: $n_s \equiv \int_{\mathbf{v}} f_s d^3\mathbf{v}$;
- fluid velocity $\mathbf{u}_s$: $n_s \mathbf{u}_s \equiv \int_{\mathbf{v}} \mathbf{v} f_s d^3\mathbf{v}$;
- collisional particle source S_s: $S_s \equiv \int_{\mathbf{v}} C_s d^3\mathbf{v}$;

Lets compute the third LHS term of the equation (2.23) using the hypothesis (2.22):

$$\int_{\mathbf{v}} \boldsymbol{\nabla}_{\mathbf{v}} \cdot \left(\frac{\mathbf{F}_s}{m_s} f_s \right) d^3\mathbf{v} = \lim_{\mathbf{v} \to +\infty} \left[\frac{\mathbf{F}_s}{m_s} f_s \right]_{-\mathbf{v}}^{+\mathbf{v}} = 0 \tag{2.24}$$

Finally, the particle balance equation is:

$$\boxed{\partial_t n_s + \boldsymbol{\nabla} \cdot (n_s \mathbf{u}_s) = S_s} \tag{2.25}$$

2.2.3 First moment: momentum balance equation

For $n = 1$, the equation (2.21) writes:

$$\partial_t \left(\int_{\mathbf{v}} \mathbf{v} f_s d^3\mathbf{v} \right) + \boldsymbol{\nabla}_{\mathbf{x}} \cdot \left(\int_{\mathbf{v}} \mathbf{v} \otimes \mathbf{v} f_s d^3\mathbf{v} \right) + \int_{\mathbf{v}} \mathbf{v} \boldsymbol{\nabla}_{\mathbf{v}} \cdot \left(\frac{\mathbf{F}_s}{m_s} f_s \right) d^3\mathbf{v} = \int_{\mathbf{v}} \mathbf{v} C_s d^3\mathbf{v} \tag{2.26}$$

The following definitions are used to introduce other fluid quantities:

- velocity of particles in the moving frame of the fluid $\mathbf{w}_s$: $\mathbf{w}_s \equiv \mathbf{v} - \mathbf{u}_s$.
  By definition: $\int_{\mathbf{v}} \mathbf{w}_s f_s d^3\mathbf{v} = 0$;
- total pressure tensor $\bar{\bar{\Pi}}_s^{tot}$: $\bar{\bar{\Pi}}_s^{tot} \equiv m_s \int_{\mathbf{v}} \mathbf{w}_s \otimes \mathbf{w}_s f_s d^3\mathbf{v}$;
- collisional momentum source $\mathbf{R}_s$: $\mathbf{R}_s \equiv m_s \int_{\mathbf{v}} \mathbf{w}_s C_s d^3\mathbf{v}$;

Equation (2.26) becomes:

$$\partial_t (n_s \mathbf{u}_s) + \underbrace{\boldsymbol{\nabla}_{\mathbf{x}} \cdot \left(\int_{\mathbf{v}} (\mathbf{u}_s + \mathbf{w}_s) \otimes (\mathbf{u}_s + \mathbf{w}_s) f_s d^3\mathbf{v} \right)}_{\boxed{(2.27)\mathrm{i}}} + \underbrace{\int_{\mathbf{v}} \mathbf{v} \boldsymbol{\nabla}_{\mathbf{v}} \cdot \left(\frac{\mathbf{F}_s}{m_s} f_s \right) d^3\mathbf{v}}_{\boxed{(2.27)\mathrm{ii}}} = \frac{1}{m_s} \mathbf{R}_s + \mathbf{u}_s S_s \tag{2.27}$$

The calculation of the two underlined terms can be found in Appendix A.1 and the momentum balance finally writes:

$$\boxed{\partial_t (m_s n_s \mathbf{u}_s) + \boldsymbol{\nabla} \cdot \left(m_s n_s \mathbf{u}_s \otimes \mathbf{u}_s + \bar{\bar{\Pi}}_s^{tot} \right) = q_s n_s (\mathbf{E} + \mathbf{u}_s \times \mathbf{B}) + \mathbf{R}_s + m_s \mathbf{u}_s S_s} \tag{2.28}$$

Note that the divergence of the fluid velocity tensor product can be written in a non-conservative form:

$$\boldsymbol{\nabla} \cdot (m_s n_s \mathbf{u}_s \otimes \mathbf{u}_s) = (\boldsymbol{\nabla} \cdot (m_s n_s \mathbf{u}_s)) \mathbf{u}_s + m_s n_s (\mathbf{u}_s \cdot \boldsymbol{\nabla}) \mathbf{u}_s \tag{2.29}$$

With such formulation and by combining with the particle balance equation (2.25), the momentum equation can be simplified and recast in a non conservative form:

$$\boxed{m_s n_s \partial_t \mathbf{u}_s + m_s n_s (\mathbf{u}_s \cdot \boldsymbol{\nabla}) \mathbf{u}_s + \boldsymbol{\nabla} \cdot \bar{\bar{\Pi}}_s^{tot} = q_s n_s (\mathbf{E} + \mathbf{u}_s \times \mathbf{B}) + \mathbf{R}_s} \tag{2.30}$$

2.2.4 Second moment: energy equation

For $n = 2$, the equation (2.21) writes:

$$\underbrace{\partial_t \left(\int_{\mathbf{v}} \mathbf{v} \otimes \mathbf{v} f_s d^3\mathbf{v} \right)}_{\boxed{(2.31)\mathrm{i}}} + \underbrace{\boldsymbol{\nabla}_{\mathbf{x}} \cdot \left(\int_{\mathbf{v}} \mathbf{v} \otimes \mathbf{v} \otimes \mathbf{v} f_s d^3\mathbf{v} \right)}_{\boxed{(2.31)\mathrm{ii}}} + \underbrace{\int_{\mathbf{v}} \mathbf{v} \otimes \mathbf{v} \boldsymbol{\nabla}_{\mathbf{v}} \cdot \left(\frac{\mathbf{F}_s}{m_s} f_s \right) d^3\mathbf{v}}_{\boxed{(2.31)\mathrm{iii}}} = \int_{\mathbf{v}} \mathbf{v} \otimes \mathbf{v} C_s d^3\mathbf{v} \tag{2.31}$$

Here again, we introduce some other fluid quantities:

- pressure flux tensor $\bar{\bar{\bar{Q}}}_s$: $\bar{\bar{\bar{Q}}}_s \equiv \frac{1}{2} m_s \int_{\mathbf{v}} \mathbf{w}_s \otimes \mathbf{w}_s \otimes \mathbf{w}_s f_s d^3\mathbf{v}$;

- collisional pressure source tensor $\bar{\bar{H}}_s$: $\bar{\bar{H}}_s \equiv \frac{1}{2} m_s \int_{\mathbf{v}} C_s \mathbf{w}_s \otimes \mathbf{w}_s d^3\mathbf{v}$;
- work tensor of the Lorentz force $\bar{\bar{W}}_s^{\mathbf{v}\times\mathbf{B}}$: $\bar{\bar{W}}_s^{\mathbf{v}\times\mathbf{B}} \equiv \frac{1}{2} q_s \int_{\mathbf{v}} \left((\mathbf{v}\times\mathbf{B}) \otimes \mathbf{v} + \mathbf{v} \otimes (\mathbf{v}\times\mathbf{B}) \right) f_s d^3\mathbf{v}$;

The three underlined terms of equation (2.31) are calculated separately in Appendix A.2 and lead to:

$$\partial_t \left(n_s \mathbf{u}_s \otimes \mathbf{u}_s + \frac{1}{m_s} \bar{\bar{\Pi}}_s^{tot} \right) + \boldsymbol{\nabla} \cdot \left[n_s \mathbf{u}_s \otimes \mathbf{u}_s \otimes \mathbf{u}_s + \frac{1}{m_s} \left(\bar{\bar{\Pi}}_s^{tot} \otimes \mathbf{u}_s + \mathbf{u}_s \otimes \bar{\bar{\Pi}}_s^{tot} \right) + \int_{\mathbf{v}} \mathbf{w}_s \otimes \mathbf{u}_s \otimes \mathbf{w}_s f_s d^3\mathbf{v} \right]$$
$$= -\frac{2}{m_s} \boldsymbol{\nabla} \cdot \bar{\bar{\bar{Q}}}_s + \frac{q_s}{m_s} n_s \left(\mathbf{E} \otimes \mathbf{u}_s + \mathbf{u}_s \otimes \mathbf{E} \right) + \frac{2}{m_s} \bar{\bar{W}}_s^{\mathbf{v}\times\mathbf{B}} + \frac{2}{m_s} \bar{\bar{H}}_s + \frac{1}{m_s} \left(\mathbf{R}_s \otimes \mathbf{u}_s + \mathbf{u}_s \otimes \mathbf{R}_s \right) + \mathbf{u}_s \otimes \mathbf{u}_s S_s \tag{2.32}$$

We introduce the energy tensor $\bar{\bar{\varepsilon}}_s$:

$$n_s \bar{\bar{\varepsilon}}_s \equiv \frac{1}{2} m_s n_s \mathbf{u}_s \otimes \mathbf{u}_s + \frac{1}{2} \bar{\bar{\Pi}}_s^{tot} \tag{2.33}$$

By multiplying equation (2.32) by $\frac{1}{2} m_s$, we obtain:

$$\boxed{\begin{aligned} &\partial_t \left(n_s \bar{\bar{\varepsilon}}_s \right) + \boldsymbol{\nabla} \cdot \left(\frac{1}{2} n_s \left(\bar{\bar{\varepsilon}}_s \otimes \mathbf{u}_s + \mathbf{u}_s \otimes \bar{\bar{\varepsilon}}_s \right) + \frac{1}{2} \int_{\mathbf{v}} m_s \mathbf{w}_s \otimes \mathbf{u}_s \otimes \mathbf{w}_s f_s d^3\mathbf{v} + \bar{\bar{\bar{Q}}}_s \right) \\ &\quad = \frac{1}{2} q_s n_s \left(\mathbf{E} \otimes \mathbf{u}_s + \mathbf{u}_s \otimes \mathbf{E} \right) + \bar{\bar{W}}_s^{\mathbf{v}\times\mathbf{B}} + \bar{\bar{H}}_s + \frac{1}{2} \left(\mathbf{R}_s \otimes \mathbf{u}_s + \mathbf{u}_s \otimes \mathbf{R}_s \right) + \frac{1}{2} m_s \mathbf{u}_s \otimes \mathbf{u}_s S_s \end{aligned}} \tag{2.34}$$

One can notice that the total pressure tensor $\bar{\bar{\Pi}}_s^{tot} \equiv m_s \int_{\mathbf{v}} \mathbf{w}_s \otimes \mathbf{w}_s f_s d^3\mathbf{v}$ is a symmetric tensor. The energy tensor $\bar{\bar{\varepsilon}}_s$ is thus also symmetric. Equation (2.34) is a tensor equation which details transfers of energy between the different directions of the coordinates system. Such precision on the directions which carry the energy is usually unnecessary and unused in standard plasma fluid codes due to the numerical cost such tensor equation implies. The information on the total energy carried and transported in the system is generally sufficient to describe turbulence in tokamak edge plasmas. An equipartition of energy due to collisions is usually asserted to justify such simplification. For that, the trace of the tensor equation (2.34) is calculated and leads to a scalar equation on the total energy of the species "s":

$$\boxed{\partial_t E_s^{\mathrm{tot}} + \boldsymbol{\nabla} \cdot \left(E_s^{\mathrm{tot}} \mathbf{u}_s + \mathbf{u}_s \cdot \bar{\bar{\Pi}}_s^{\mathrm{tot}} + \mathbf{q}_s \right) = n_s q_s \mathbf{E} \cdot \mathbf{u}_s + S_{C_s} + \mathbf{R}_s \cdot \mathbf{u}_s + \frac{1}{2} m_s |\mathbf{u}_s|^2 S_s} \tag{2.35}$$

where :

- $p_s = \frac{1}{3} \mathrm{Tr} \left(\bar{\bar{\Pi}}_s^{\mathrm{tot}} \right)$ is the scalar pressure ;
- $E_s^{\mathrm{tot}} = \frac{1}{2} m_s n_s |\mathbf{u}_s|^2 + \frac{3}{2} p_s$ is the total energy carried by the species s ;
- $S_{C_s} = \frac{1}{2} m_s \int_{\mathbf{v}} |\mathbf{w}_s|^2 C_s d^3\mathbf{v}$ is the collisional energy source;
- $\mathbf{q}_s = \frac{1}{2} m_s \int_{\mathbf{v}} |\mathbf{w}_s|^2 \mathbf{w}_s f_s d^3\mathbf{v}$ is the heat flux

The energy equation (2.35) can also be simplified using particle and momentum conservation equations and leads to:

$$\boxed{\partial_t\left(\frac{3}{2}p_s\right)+\boldsymbol{\nabla}\cdot\left(\frac{3}{2}p_s\mathbf{u}_s\right)+\left(\bar{\bar{\Pi}}_s^{tot}\cdot\boldsymbol{\nabla}\right)\cdot\mathbf{u}_s+\boldsymbol{\nabla}\cdot\mathbf{q}_s=S_{C_s}} \tag{2.36}$$

2.3 Braginskii's closure

In this section, we detail the closure on plasma fluid equations develop by Braginskii [Braginskii 65]. The first part focus on closures linked to the collisional operator and the second part aims at understanding closure on velocity fluctuation terms: the heat fluxes and terms linked to the total pressure tensor.

2.3.1 Closure on collisional terms

The collisional operator can be divided into two parts, intra-species and inter-species collisions:

$$C_s=C_{ss}+\sum_{s'\neq s}C_{ss'}\left(f_s,f_{s'}\right) \tag{2.37}$$

In this work, we only consider elastic collisions (Coulomb collisions) and not inelastic ones. Under this hypothesis, the collisional terms have to fulfil the following properties of momentum and energy conservations.
For intra-species collisions:

$$\begin{cases}\displaystyle\int_{\mathbf{v}}m_s\mathbf{v}C_{ss}d^3\mathbf{v}=0\\ \displaystyle\int_{\mathbf{v}}\frac{1}{2}m_s|\mathbf{v}|^2C_{ss}d^3\mathbf{v}=0\end{cases} \tag{2.38}$$

For inter-species collisions:

$$\forall s';\begin{cases}\displaystyle\int_{\mathbf{v}}m_s\mathbf{v}C_{ss'}d^3\mathbf{v}+\int_{\mathbf{v}}m_{s'}\mathbf{v}C_{s's}d^3\mathbf{v}=0\\ \displaystyle\int_{\mathbf{v}}\frac{1}{2}m_s|\mathbf{v}|^2C_{ss'}d^3\mathbf{v}+\int_{\mathbf{v}}\frac{1}{2}m_{s'}|\mathbf{v}|^2C_{s's}d^3\mathbf{v}=0\end{cases} \tag{2.39}$$

Closure on collisional particle source S_s: The collisional particle source is induced by the creation or extinction of particles of the species s and thus only appearing if processes such ionizations, dissociations, fusion reactions which can modify the number of particles are taken into account. In the following these processes are neglected such as:

$$\forall s';\int_{\mathbf{v}}C_{ss'}d^3\mathbf{v}=0 \tag{2.40}$$

This leads to:

$$\boxed{S_s=\int_{\mathbf{v}}C_sd^3\mathbf{v}=\sum_{s'}\int_{\mathbf{v}}C_{ss'}d^3\mathbf{v}=0} \tag{2.41}$$

Note that in our models a constant source term will be added in order to obtain a flux-driven approach. This constant particle source can be seen either as the result of not self-consistently calculated ionization processes or as the result of particles coming from the core plasma.

In the following, we consider a plasma of two species: electrons ($q_e = -e$) and one ion species of hydrogen isotope ($q_i = e$, *i.e.* charge number $Z = 1$). The limit case of strongly magnetized plasma ($\omega_{c_e}\tau_e \gg 1$ and $\omega_{c_i}\tau_i \gg 1$) is considered in Braginskii's closure [Braginskii 65] where $\tau_e \propto m_e^{1/2}T_e^{3/2}/n_i$ and $\tau_i \propto m_i^{1/2}T_i^{3/2}/n_i$ are respectively the electron and ion collision times [Wesson 11].

Closure on collisional momentum source $\mathbf{R}_s$:

$$\mathbf{R}_s = \int_{\mathbf{v}} m_s \mathbf{w}_s C_s d^3\mathbf{v} = \mathbf{R}_s^u + \mathbf{R}_s^T \tag{2.42}$$

For electrons, this collisional momentum source is made of two contributions:

- A friction force $\mathbf{R}_e^u$ coming from the existence of a relative velocity between ions and electrons:

$$\mathbf{R}_e^u = -\frac{m_e n_e}{\tau_e}\left(0.51\left(u_{e_\parallel} - u_{i_\parallel}\right)\mathbf{b} + \mathbf{u}_{e_\perp} - \mathbf{u}_{i_\perp}\right) = e n_e\left(\eta_\parallel j_\parallel \mathbf{b} + \eta_\perp \mathbf{j}_\perp\right) \tag{2.43}$$

  where $\mathbf{j} = j_\parallel \mathbf{b} + \mathbf{j}_\perp = -e n_e(\mathbf{u}_e - \mathbf{u}_i)$ is the current density and where $\eta_\parallel$ and $\eta_\perp$ are the parallel and perpendicular Spitzer resistivities:

$$\eta_\perp = \frac{m_e}{e^2 n_e \tau_e} = \frac{1}{0.51}\eta_\parallel \propto T_e^{-3/2} \tag{2.44}$$

- A thermal force $\mathbf{R}_e^T$ resulting of the existence of an electron temperature gradient:

$$\mathbf{R}_e^T = -0.71 n_e \boldsymbol{\nabla}_\parallel T_e - \frac{3}{2}\frac{n_e}{\omega_{c_e}\tau_e}\mathbf{b}\times\boldsymbol{\nabla}_\perp T_e \tag{2.45}$$

From equation (2.39), we have:

$$\mathbf{R}_i = -\mathbf{R}_e \tag{2.46}$$

Closure on the total collisional energy source S_{c_s}:

$$S_{c_s} = \int_{\mathbf{v}} \frac{1}{2} m_s |\mathbf{w}_s|^2 C_s d^3\mathbf{v} \tag{2.47}$$

For ions:

$$S_{c_i} = 3\frac{m_e}{m_i}\frac{p_e - p_i}{\tau_e} \tag{2.48}$$

For electrons, the energy conservation for collisions (2.39) leads to:

$$S_{c_e} = -\mathbf{R}_e\cdot(\mathbf{u}_e - \mathbf{u}_i) - S_{c_i} = \eta_\parallel j_\parallel^2 + \eta_\perp j_\perp^2 + \frac{1}{e n_e}\mathbf{j}\cdot\mathbf{R}_e^T - 3\frac{m_e}{m_i}\frac{p_e - p_i}{\tau_e} \tag{2.49}$$

2.3.2 Closure on fluctuating velocity terms

2.3.2.1 Closure on heat fluxes $\mathbf{q}_s$

$$\mathbf{q}_s = \int_{\mathbf{v}} \frac{1}{2} m_s |\mathbf{w}_s|^2 \mathbf{w}_s f_s d^3\mathbf{v} = \mathbf{q}_s^u + \mathbf{q}_s^T \tag{2.50}$$

Electron friction heat flux:

$$\mathbf{q}_e^u = 0.71 p_e \left(u_{e_\parallel} - u_{i_\parallel} \right) \mathbf{b} + \frac{3}{2} \frac{p_e}{\omega_{c_e} \tau_e} \mathbf{b} \times (\mathbf{u}_{e_\perp} - \mathbf{u}_{i_\perp}) \tag{2.51}$$

Electron and ion thermal heat fluxes:

$$\mathbf{q}_e^T = -\chi_{e_\parallel} \boldsymbol{\nabla}_\parallel T_e - \chi_{e_\perp} \boldsymbol{\nabla}_\perp T_e - \frac{5}{2} \frac{p_e}{m_e \omega_{c_e}} \mathbf{b} \times \boldsymbol{\nabla}_\perp T_e \tag{2.52}$$

$$\mathbf{q}_i^T = -\chi_{i_\parallel} \boldsymbol{\nabla}_\parallel T_i - \chi_{i_\perp} \boldsymbol{\nabla}_\perp T_i + \frac{5}{2} \frac{p_i}{m_e \omega_{c_e}} \mathbf{b} \times \boldsymbol{\nabla}_\perp T_i \tag{2.53}$$

where ion and electron thermal conductivities are defined as:

$$\chi_{e_\parallel} = 3.16 \frac{p_e \tau_e}{m_e} \quad ; \quad \chi_{i_\parallel} = 3.9 \frac{p_i \tau_i}{m_i} \tag{2.54}$$

$$\chi_{e_\perp} = 4.66 \frac{p_e}{m_e \tau_e \omega_{c_e}^2} \quad ; \quad \chi_{i_\perp} = 2 \frac{p_i}{m_i \tau_i \omega_{c_i}^2} \tag{2.55}$$

2.3.2.2 Total pressure tensor

The total pressure tensor $\bar{\bar{\Pi}}_s^{tot}$ is decomposed into a scalar pressure p_s and a residual stress tensor that we call Braginskii's stress tensor $\bar{\bar{\Pi}}_s^{\text{Brag}}$ in the following:

$$\bar{\bar{\Pi}}_s^{\text{tot}} = p_s \mathbb{1} + \bar{\bar{\Pi}}_s^{\text{Brag}} \tag{2.56}$$

For a standard basis $(\mathbf{e}_x, \mathbf{e}_y, \mathbf{e}_z)$ in which $\mathbf{b} = \mathbf{e}_z$, this Braginskii's stress tensor $\bar{\bar{\Pi}}_s^{\text{Brag}}$ writes :

$$\bar{\bar{\Pi}}_s^{\text{Brag}} = - \begin{pmatrix} \frac{\eta_0^s}{2}(W_{xx}+W_{yy}) + \frac{\eta_1^s}{2}(W_{xx}-W_{yy}) + \eta_3^s W_{xy} & \eta_1^s W_{xy} - \frac{\eta_3^s}{2}(W_{xx}-W_{yy}) & 4\eta_1^s W_{xz} + 2\eta_3^s W_{yz} \\ \eta_1^s W_{xy} - \frac{\eta_3^s}{2}(W_{xx}-W_{yy}) & \frac{\eta_0^s}{2}(W_{xx}+W_{yy}) + \frac{\eta_1^s}{2}(W_{yy}-W_{xx}) - \eta_3^s W_{xy} & 4\eta_1^s W_{yz} - 2\eta_3^s W_{xz} \\ 4\eta_1^s W_{xz} + 2\eta_3^s W_{yz} & 4\eta_1^s W_{yz} - 2\eta_3^s W_{xz} & \eta_0^s W_{zz} \end{pmatrix} \tag{2.57}$$

In this formulation, the rate-of-strain tensor $\bar{\bar{W}}$ is a measure of the deformation of plasma volume elements and is defined as:

$$W_{jk} = \frac{\partial u_j}{\partial x_k} + \frac{\partial u_k}{\partial x_j} - \frac{2}{3} \delta_{jk} \boldsymbol{\nabla} \cdot \mathbf{u} \tag{2.58}$$

The Braginskii's stress tensor formulation (2.57) involves three different viscosity coefficients which differ slightly for ions and electrons:

$$\begin{aligned} \eta_0^i = &\ 0.96 p_i \tau_i \quad ; \quad \eta_0^e = \ 0.73 p_e \tau_e \\ \eta_1^i = &\ 0.3 \tfrac{p_i}{\omega_{c_i}^2 \tau_i} \quad ; \quad \eta_1^e = \ 0.51 \tfrac{p_e}{\omega_{c_e}^2 \tau_e} \\ \eta_3^i = &\ 0.5 \tfrac{p_i}{\omega_{c_i}} \quad ; \quad \eta_3^e = \ -0.5 \tfrac{p_e}{\omega_{c_e}} \end{aligned} \tag{2.59}$$

One can notice that the ratios between these three viscosity coefficients are proportional to powers of $\omega_{c_s}\tau_s$:

$$\frac{\eta_0^s}{\eta_3^s} \propto \omega_{c_s}\tau_s \gg 1 \quad ; \quad \frac{\eta_0^s}{\eta_1^s} \propto (\omega_{c_s}\tau_s)^2 \gg 1 \quad ; \quad \frac{\eta_3^s}{\eta_1^s} \propto \omega_{c_s}\tau_s \gg 1 \tag{2.60}$$

which leads - under the assumption of strongly magnetized plasma - to:

$$\eta_0^s \gg \eta_3^s \gg \eta_1^s \tag{2.61}$$

It is thus convenient to separate the Braginskii's stress tensor into three tensors according to the dependency of these different viscosity coefficients:

$$\bar{\bar{\Pi}}_s^{\mathrm{Brag}} = \bar{\bar{\Pi}}_s^{\mathrm{vis}} + \bar{\bar{\Pi}}_s^{\mathrm{FLR}} + \bar{\bar{\Pi}}_s^{\mathrm{res}} \tag{2.62}$$

Viscous tensor: Terms proportional to η_0^s correspond to the viscous part of Braginskii's stress tensor:

$$\bar{\bar{\Pi}}_s^{\mathrm{vis}} = \begin{pmatrix} -\frac{\eta_0^s}{2}(W_{xx} + W_{yy}) & 0 & 0 \\ 0 & -\frac{\eta_0^s}{2}(W_{xx} + W_{yy}) & 0 \\ 0 & 0 & -\eta_0^s W_{zz} \end{pmatrix} \tag{2.63}$$

If we neglect curvature effects, the divergence of this viscous tensor writes:

$$\boldsymbol{\nabla} \cdot \bar{\bar{\Pi}}_s^{\mathrm{vis}} = \boldsymbol{\nabla}_\parallel G_s - \frac{1}{3}\boldsymbol{\nabla} G_s \tag{2.64}$$

where we used the following definition for G_s:

$$G_s = \alpha_s p_s \tau_s \left(\boldsymbol{\nabla} \cdot \mathbf{u}_s - 3\nabla_\parallel u_{s_\parallel} \right) \tag{2.65}$$

with $\alpha_i = 0.96$ and $\alpha_e = 0.73$. The inclusion of curvature effects leads to an additional term which has been neglected in this derivation but probably not justified for any edge plasma conditions.

Gyro-viscous or Finite Larmor Radius tensor:

$$\bar{\bar{\Pi}}_s^{\mathrm{FLR}} = \begin{pmatrix} -\eta_3^s W_{xy} & \frac{\eta_3^s}{2}(W_{xx} - W_{yy}) & -2\eta_3^s W_{yz} \\ \frac{\eta_3^s}{2}(W_{xx} - W_{yy}) & \eta_3^s W_{xy} & 2\eta_3^s W_{xz} \\ -2\eta_3^s W_{yz} & 2\eta_3^s W_{xz} & 0 \end{pmatrix} \tag{2.66}$$

We realize a new calculation of the divergence of Finite Larmor Radius (FLR) part of Braginskii's tensor for a standard basis and by neglecting corrections due to field line curvature it writes exactly (for $Z = 1$):

$$\begin{aligned} \boldsymbol{\nabla} \cdot \bar{\bar{\Pi}}_s^{\mathrm{FLR}} = & - m_s n_s \left(\mathbf{u}_s^\star \cdot \boldsymbol{\nabla}\right) \mathbf{u}_s \\ & + m_s \frac{q_s}{|q_s|^2} \left[\boldsymbol{\nabla}_\perp \left(\frac{p_s}{2B} \boldsymbol{\nabla} \cdot (\mathbf{b} \times \mathbf{u}_s) \right) + \mathbf{b} \times \boldsymbol{\nabla}_\perp \left(\frac{p_s}{2B} \left(\boldsymbol{\nabla} \cdot \mathbf{u}_{s_\perp}\right) \right) + p_s \left(\left(\boldsymbol{\nabla}_\perp \times \frac{\mathbf{b}}{B} \right) \cdot \boldsymbol{\nabla} \right) \mathbf{u}_s \right. \\ & \left. - \boldsymbol{\nabla}_\perp \times \left(\frac{p_s}{B} \nabla_\parallel \mathbf{u}_{s_\perp} \right) - \nabla_\parallel \left(\frac{p_s}{B} \boldsymbol{\nabla}_\perp \times \left(u_{s_\parallel} \mathbf{b} \right) \right) + \mathbf{b} \times \nabla_\parallel \left(\frac{p_s}{B} \nabla_\parallel \mathbf{u}_s \right) \right] \end{aligned} \tag{2.67}$$

where $u_s^\star$ is the diamagnetic fluid velocity introduced in Chapter 1:

$$\mathbf{u}_s^\star = \frac{\mathbf{b} \times \boldsymbol{\nabla}_\perp p_s}{n_s q_s B} \tag{2.68}$$

Note that the FLR part of the Braginskii's tensor does not depend on collision frequencies.

Residual viscous tensor:

$$\bar{\bar{\Pi}}_s^{\mathrm{res}} = \begin{pmatrix} -\frac{\eta_1^s}{2}(W_{xx} - W_{yy}) & -\eta_1^s W_{xy} & -4\eta_1^s W_{xz} \\ -\eta_1^s W_{xy} & -\frac{\eta_1^s}{2}(W_{yy} - W_{xx}) & -4\eta_1^s W_{yz} \\ -4\eta_1^s W_{xz} & -4\eta_1^s W_{yz} & 0 \end{pmatrix} \tag{2.69}$$

The remaining terms of the Braginskii's tensor constitute the residual viscous tensor. These terms are proportional to $\eta_1^s \propto \eta_0^s \left(\omega_{c_s} \tau_s\right)^{-2}$ and are thus negligible in the limit of strongly magnetized plasmas with respect to viscous and FLR parts of the Braginskii's tensor. In fact, this tensor is expected to play a role only in plasma conditions out of the validity domain of Braginskii's closure. For that and for simplicity reasons, this tensor is neglected in the following formulas.

2.3.2.3 Heat generated as a result of viscosity via Braginskii's tensor

It can be shown [Hinton 71] that the heat generated by Braginskii's viscous tensor writes for the species s:

$$\boldsymbol{\nabla} \cdot \left(\mathbf{u}_s \cdot \bar{\bar{\Pi}}_s^{\mathrm{vis}} \right) = \nabla_\parallel \left(G_s u_{s_\parallel} \right) - \frac{1}{3} \boldsymbol{\nabla} \cdot \left(G_s \mathbf{u}_s \right) \tag{2.70}$$

2.3.3 Focus on momentum equations

In tokamaks, the dynamic of plasma in the direction parallel to the magnetic field strongly differs of the dynamics in the perpendicular direction in terms of characteristic velocity, length and time. It is therefore logical to treat these two components separately. We first recall the electron and ion momentum equations obtained using Braginskii's closure:
Electron momentum conservation:

$$\begin{aligned}\partial_t\left(m_e n_e \mathbf{u}_e\right)+\boldsymbol{\nabla}\cdot\left(m_e n_e \mathbf{u}_e\otimes\mathbf{u}_e\right)=&-\boldsymbol{\nabla}p_e-en_e\left(\mathbf{E}+\mathbf{u}_e\times\mathbf{B}\right)\\&-\frac{m_e n_e}{\tau_e}\left(0.51\left(u_{e_\parallel}-u_{i_\parallel}\right)\mathbf{b}+\mathbf{u}_{e_\perp}-\mathbf{u}_{i_\perp}\right)-0.71n_e\boldsymbol{\nabla}_\parallel T_e-\frac{3}{2}\frac{n_e}{\omega_{c_e}\tau_e}\mathbf{b}\times\boldsymbol{\nabla}_\perp T_e\\&-\boldsymbol{\nabla}\cdot\bar{\bar{\Pi}}_e^{\text{vis}}-\boldsymbol{\nabla}\cdot\bar{\bar{\Pi}}_e^{\text{FLR}}\end{aligned}\tag{2.71}$$

Ion momentum conservation:

$$\begin{aligned}\partial_t\left(m_i n_i \mathbf{u}_i\right)+\boldsymbol{\nabla}\cdot\left(m_i n_i \mathbf{u}_i\otimes\mathbf{u}_i\right)=&-\boldsymbol{\nabla}p_i+en_i\left(\mathbf{E}+\mathbf{u}_i\times\mathbf{B}\right)\\&+\frac{m_e n_e}{\tau_e}\left(0.51\left(u_{e_\parallel}-u_{i_\parallel}\right)\mathbf{b}+\mathbf{u}_{e_\perp}-\mathbf{u}_{i_\perp}\right)+0.71n_e\boldsymbol{\nabla}_\parallel T_e+\frac{3}{2}\frac{n_e}{\omega_{c_e}\tau_e}\mathbf{b}\times\boldsymbol{\nabla}_\perp T_e\\&-\boldsymbol{\nabla}\cdot\bar{\bar{\Pi}}_i^{\text{vis}}-\boldsymbol{\nabla}\cdot\bar{\bar{\Pi}}_i^{\text{FLR}}\end{aligned}\tag{2.72}$$

2.3.3.1 Parallel projection of momentum equation

The parallel electron momentum equation is obtained by calculating the dot product of Eq. (2.71) with $\mathbf{b}$:

$$\begin{aligned}\partial_t\left(m_e n_e u_{e_\parallel}\right)-\overbrace{\cancel{m_e n_e \mathbf{u}_{e_\perp}\cdot\partial_t\mathbf{b}}}^{\text{electrostatic}}+\boldsymbol{\nabla}\cdot\left(m_e n_e u_{e_\parallel}\mathbf{u}_e\right)-m_e n_e\mathbf{u}_{e_\perp}\cdot\left(\left(\mathbf{u}_e\cdot\boldsymbol{\nabla}\right)\mathbf{b}\right)-m_e n_e u_{e_\parallel}\overbrace{\cancel{\mathbf{b}\cdot\left(\left(\mathbf{u}_e\cdot\boldsymbol{\nabla}\right)\mathbf{b}\right)}}^{=0}\\=-\nabla_\parallel p_e-en_eE_\parallel-\frac{m_e n_e}{\tau_e}0.51\left(u_{e_\parallel}-u_{i_\parallel}\right)-0.71n_e\nabla_\parallel T_e\\-\frac{2}{3}\nabla_\parallel\left(0.73p_e\tau_e\left(\boldsymbol{\nabla}\cdot\mathbf{u}_e-3\nabla_\parallel u_{e_\parallel}\right)\right)\\+m_e n_e\left(\mathbf{u}_e^\star\cdot\boldsymbol{\nabla}\right)u_{e_\parallel}+\frac{m_e}{e}p_e\left(\left(\boldsymbol{\nabla}_\perp\times\frac{\mathbf{b}}{B}\right)\cdot\boldsymbol{\nabla}\right)u_{e_\parallel}-\frac{m_e}{e}\mathbf{b}\cdot\left(\boldsymbol{\nabla}_\perp\times\left(\frac{p_e}{B}\nabla_\parallel\mathbf{u}_{e_\perp}\right)\right)\end{aligned}\tag{2.73}$$

We used here the fact that a unit vector is orthogonal to its temporal derivative, *i.e.* $\mathbf{b}\cdot\partial_t\mathbf{b}=0$. Similarly, the parallel projection is made on the ion momentum equation $\mathbf{b}\cdot$(2.72) :

$$\begin{aligned}\partial_t\left(m_i n_i u_{i_\parallel}\right)+\boldsymbol{\nabla}\cdot\left(m_i n_i u_{i_\parallel}\mathbf{u}_i\right)-m_i n_i\mathbf{u}_{i_\perp}\cdot\left(\left(\mathbf{u}_i\cdot\boldsymbol{\nabla}\right)\mathbf{b}\right)\\=-\nabla_\parallel p_i+en_iE_\parallel+\frac{m_e n_e}{\tau_e}0.51\left(u_{e_\parallel}-u_{i_\parallel}\right)+0.71n_e\nabla_\parallel T_e\\-\frac{2}{3}\nabla_\parallel\left(0.96p_i\tau_i\left(\boldsymbol{\nabla}\cdot\mathbf{u}_i-3\nabla_\parallel u_{i_\parallel}\right)\right)\\+m_i n_i\left(\mathbf{u}_i^\star\cdot\boldsymbol{\nabla}\right)u_{i_\parallel}-\frac{m_i}{e}p_i\left(\left(\boldsymbol{\nabla}_\perp\times\frac{\mathbf{b}}{B}\right)\cdot\boldsymbol{\nabla}\right)u_{i_\parallel}+\frac{m_i}{e}\mathbf{b}\cdot\left(\boldsymbol{\nabla}_\perp\times\left(\frac{p_i}{B}\nabla_\parallel\mathbf{u}_{i_\perp}\right)\right)\end{aligned}\tag{2.74}$$

2.3.3.2 Perpendicular projection of momentum equation

The perpendicular electron momentum equation is obtained by calculating the cross product of equation (2.71) with $\mathbf{b}$:

$$\begin{aligned}
&\partial_t\left(m_e n_e \mathbf{u}_{e_\perp}\times\mathbf{b}\right) - \overbrace{\cancel{m_e n_e u_{e_\parallel}\mathbf{b}\times\partial_t\mathbf{b}}}^{\text{electrostatic}} + m_e\left[\left(\mathbf{u}_e\cdot\boldsymbol{\nabla}\right)\left(n_e\mathbf{u}_e\right)\right]\times\mathbf{b} + m_e n_e\left(\boldsymbol{\nabla}\cdot\mathbf{u}_e\right)\mathbf{u}_{e_\perp}\times\mathbf{b}\\
&= \mathbf{b}\times\boldsymbol{\nabla}_\perp p_e - e n_e\mathbf{E}\times\mathbf{b} + e n_e B\mathbf{u}_{e_\perp} - \frac{m_e n_e}{\tau_e}\left(\mathbf{u}_{e_\perp}-\mathbf{u}_{i_\perp}\right)\times\mathbf{b} - \frac{3}{2}\frac{n_e}{\omega_{c_e}\tau_e}\boldsymbol{\nabla}_\perp T_e\\
&\quad - \frac{0.73}{3}\mathbf{b}\times\boldsymbol{\nabla}_\perp\left(p_e\tau_e\left(\boldsymbol{\nabla}\cdot\mathbf{u}_e - 3\nabla_\parallel u_{e_\parallel}\right)\right)\\
&\quad + m_e n_e\left(\mathbf{u}_e^\star\cdot\boldsymbol{\nabla}\right)\left(\mathbf{u}_{e_\perp}\times\mathbf{b}\right) - \frac{m_e}{e}\mathbf{b}\times\boldsymbol{\nabla}_\perp\left(\frac{p_e}{2B}\boldsymbol{\nabla}\cdot\left(\mathbf{b}\times\mathbf{u}_{e_\perp}\right)\right) + \frac{m_e}{e}\boldsymbol{\nabla}_\perp\left(\frac{p_e}{2B}\boldsymbol{\nabla}\cdot\mathbf{u}_{e_\perp}\right)\\
&\quad + \frac{m_e}{e}p_e\left(\left(\boldsymbol{\nabla}_\perp\times\frac{\mathbf{b}}{B}\right)\cdot\boldsymbol{\nabla}\right)\left(\mathbf{u}_{e_\perp}\times\mathbf{b}\right) + \frac{m_e}{e}\nabla_\parallel\left(\frac{p_e}{B}\boldsymbol{\nabla}_\perp u_{e_\parallel}\right) + \frac{m_e}{e}\nabla_\parallel\left(\frac{p_e}{B}\nabla_\parallel\mathbf{u}_{e_\perp}\right)
\end{aligned}\tag{2.75}$$

Similarly, the perpendicular projection is made on the ion momentum equation: (2.72) $\times\,\mathbf{b}$

$$\begin{aligned}
&\partial_t\left(m_i n_i \mathbf{u}_{i_\perp}\times\mathbf{b}\right) + m_i\left[\left(\mathbf{u}_i\cdot\boldsymbol{\nabla}\right)\left(n_i\mathbf{u}_i\right)\right]\times\mathbf{b} + m_i n_i\left(\boldsymbol{\nabla}\cdot\mathbf{u}_i\right)\mathbf{u}_{i_\perp}\times\mathbf{b}\\
&= \mathbf{b}\times\boldsymbol{\nabla}_\perp p_i + e n_i\mathbf{E}\times\mathbf{b} - e n_i B\mathbf{u}_{i_\perp} + \frac{m_e n_e}{\tau_e}\left(\mathbf{u}_{e_\perp}-\mathbf{u}_{i_\perp}\right)\times\mathbf{b} + \frac{3}{2}\frac{n_e}{\omega_{c_e}\tau_e}\boldsymbol{\nabla}_\perp T_e\\
&\quad - \frac{0.96}{3}\mathbf{b}\times\boldsymbol{\nabla}_\perp\left(p_i\tau_i\left(\boldsymbol{\nabla}\cdot\mathbf{u}_i - 3\nabla_\parallel u_{i_\parallel}\right)\right)\\
&\quad + m_i n_i\left(\mathbf{u}_i^\star\cdot\boldsymbol{\nabla}\right)\left(\mathbf{u}_{i_\perp}\times\mathbf{b}\right) + \frac{m_i}{e}\mathbf{b}\times\boldsymbol{\nabla}_\perp\left(\frac{p_i}{2B}\boldsymbol{\nabla}\cdot\left(\mathbf{b}\times\mathbf{u}_{i_\perp}\right)\right) - \frac{m_i}{e}\boldsymbol{\nabla}_\perp\left(\frac{p_i}{2B}\boldsymbol{\nabla}\cdot\mathbf{u}_{i_\perp}\right)\\
&\quad - \frac{m_i}{e}p_i\left(\left(\boldsymbol{\nabla}_\perp\times\frac{\mathbf{b}}{B}\right)\cdot\boldsymbol{\nabla}\right)\left(\mathbf{u}_{i_\perp}\times\mathbf{b}\right) - \frac{m_i}{e}\nabla_\parallel\left(\frac{p_i}{B}\boldsymbol{\nabla}_\perp u_{i_\parallel}\right) - \frac{m_i}{e}\nabla_\parallel\left(\frac{p_i}{B}\nabla_\parallel\mathbf{u}_{i_\perp}\right)
\end{aligned}\tag{2.76}$$

2.4 Drift-ordering of fluid equations

Fluid equations combined with Braginskii's closure involve a large number of terms which cover magnitudes of several decades. One can find useful to keep only dominant terms in these equations in order to understand key ingredients involved in the studied phenomenon and to make the numerical implementation of the model simpler. This section aims at detailing the ordering of fluids equations to obtain the so-called drift velocities. It is important to notice that the ordering used is an arbitrary choice. In particular, in the edge plasma, most of the fields such as density or temperature exhibit variations of several decades of magnitudes for example between last closed field lines and the far Scrape-Off Layer or between the pedestal and a fully turbulent region. It means that the ordering can sometimes reach its validity limits in some regions of the simulated plasma.

2.4.1 Ordering procedure

2.4.1.1 Normalisation

Each variable F appearing in fluid equations is normalized with respect to a reference quantity, noted F_0, in order to generate a dimensionless variable $\widehat{F}$ such as: $F = F_0\widehat{F}$ and $|\widehat{F}| \sim 1$. Scalar fields and their normalisations involved in the system of fluid equations are presented in the Table 2.1 as well as the typical value at the LCFS for Tore Supra when it is relevant.

Field	$n_s[\mathrm{m}^{-3}]$	$T_s[\mathrm{eV}]$	$p_s[\mathrm{Pa}]$	ϕ	$B[\mathrm{T}]$
Normalized by	n_0	T_0	$n_0 T_0$	T_0/e	B_0
Dimensionless field	$\widehat{n}_s$	$\widehat{T}_s$	$\widehat{p}_s = \widehat{n}_s \widehat{T}_s$	$\widehat{\phi}$	$\widehat{B}$
Tore Supra at LCFS	5×10^{18}	30	25		3.1

Table 2.1: Fields with associated normalizations

Similarly, reference time, velocity and length scales are also normalized and detailed respectively in Table 2.2, 2.3 and 2.4. The characteristic time scales of interest for edge plasma modelling is that of perpendicular transport and is represented by the frequency ω. The fluid approach does not take into account gyrations of individual particles and we focus thus only on time scales larger than the gyro-frequency. It leads to $\omega \ll \omega_{c_{i_0}}$ and we note $\varepsilon_\omega = \frac{\omega}{\omega_{c_{i_0}}} \ll 1$ the ratio between these two frequencies.

Variable	∂_t	$\omega_{c_i} = \frac{eB}{m_i}[\mathrm{s}^{-1}]$	$\omega_{c_e} = \frac{eB}{m_e}[\mathrm{s}^{-1}]$	$\tau_e[\mathrm{s}]$	$\tau_i[\mathrm{s}]$
Normalized by	ω	$\omega_{c_{i_0}} = \frac{eB_0}{m_i}$	$\omega_{c_{e_0}} = \frac{m_i}{m_e}\omega_{c_{i_0}}$	$\tau_{e_0} = \frac{3(2\pi)^{3/2}\varepsilon_0^2\sqrt{m_e}T_0^{3/2}}{n_0 e^4 \ln\Lambda_0}$	$\tau_{i_0} = \sqrt{2\frac{m_i}{m_e}}\tau_{e_0}$
Dimensionless variable	$\partial_{\widehat{t}}$	$\widehat{B}$	$\widehat{B}$	$\widehat{T}_e^{3/2}/\widehat{n}$	$\widehat{T}_i^{3/2}/\widehat{n}$
Tore Supra at LCFS		3×10^8	5×10^{11}	10^{-6}	5×10^{-5}

Table 2.2: Characteristic times with associated normalizations

Note that in the normalizations of collision times τ_i and τ_e, we have assumed for simplicity that the Coulomb logarithm is a constant: $\ln\Lambda = \ln\Lambda_0 = \ln\left(12\pi\varepsilon_0^{3/2}T_0^{3/2}e^{-3}n_0^{-1/2}\right)$. This can be justify as in the whole range of tokamak plasma conditions (n_0 from 10^{18} to $10^{20}m^{-3}$ and T_0 from 10eV to 10keV) this Coulomb logarithm varies only by a factor 2 (from 10 to 20).

In a plasma, the dynamic of the direction parallel to the magnetic field is similar to that of a compressible gas. Acoustic waves are propagating in such media and we choose thus to normalized the parallel velocity to the thermal (or acoustic) velocity: $u_{\|_0} = c_{s_0} = \sqrt{T_0/m_i}$. Another argument to justify this choice is to notice that in the Scrape-Off Layer, Bohm boundary conditions impose outgoing fluxes at the sheath entrance (i.e near the wall) close to the acoustic velocity [Stangeby 00]. In the perpendicular direction, the typical velocity is smaller than the acoustic velocity: $u_{\perp_0} \ll c_{s_0}$. We note $\varepsilon_u = \frac{u_{\perp_0}}{c_{s_0}} \ll 1$ the ratio between perpendicular and parallel characteristic velocities.

Variable	$c_s = \sqrt{\frac{T_e+T_i}{m_i}}$[m.s^{-1}]	$u_{s_\parallel}$	$u_{s_\perp}$	$j_\parallel$[kA.m^{-2}]	$j_\perp$
Normalized by	$c_{s0} = \sqrt{\frac{T_0}{m_i}}$	$u_{\parallel 0} = c_{s0}$	$u_{\perp 0} = \varepsilon_u c_{s0}$	$en_0 c_{s0}$	$en_0 \varepsilon_u c_{s0}$
Dimensionless variable	$\sqrt{\widehat{T}_e + \widehat{T}_i}$	$\widehat{u}_{s_\parallel}$	$\widehat{u}_{s_\perp}$	$\widehat{j}_\parallel = \widehat{n}(\widehat{u}_{i_\parallel} - \widehat{u}_{e_\parallel})$	$\widehat{j}_\perp$
Tore Supra at LCFS	5×10^4			40	

Table 2.3: Characteristic velocities and currents density with associated normalizations

In order to normalize the gradients, we introduce reference parallel and perpendicular lengths, noted $l_\parallel$ and $l_\perp$. The perpendicular length $l_\perp$ corresponds to the typical length of transport in the perpendicular direction and can varies from the turbulent scale (few Larmor radius $\rho_{L_{i_0}}$) to the machine scale (small radius a). We introduce thus $\varepsilon_l = \frac{\rho_{L_{i0}}}{l_\perp} \ll 1$ the ratio between ion Larmor radius and the reference perpendicular length. The parallel length $l_\parallel$ is generally much larger as fields are homogenizing faster in the parallel direction than in the perpendicular one. This parallel length can reach up to the length of magnetic field lines ($\sim qR_0 \gg a$). We note $\varepsilon_\nabla = \frac{l_\perp}{l_\parallel} \leq 1$ the ratio between perpendicular and parallel reference lengths. One can notice in Table 2.4 that the normalizations of the gradients applied on the magnetic field differ from the gradient normalizations of others fields F. Instead of being normalized by $l_\perp$ and $l_\parallel$, perpendicular and parallel gradients of magnetic field are respectively normalized to the lengths $l_{B_\perp}$ and $l_{B_\parallel}$. This can be explained as, in our electrostatic limit, a scale separation is made between the equilibrium magnetic field and its fluctuations, the latter being neglected in this work (low-β plasmas). The equilibrium magnetic field characteristic lengths are typically of the order of the machine scale such as $l_{B_\perp} = R_0 = \mathcal{A}a$ and $l_{B_\parallel} = qR_0 = q\mathcal{A}a$ where $\mathcal{A} = R_0/a > 1$ is the tokamak aspect ratio.

Variable	$\rho_{L_i} = \frac{c_s}{\omega_{c_i}}$[m]	$\rho_{L_e} = \frac{c_s}{\omega_{ce}}$[m]	$\nabla_\perp F$	$\nabla_\parallel F$	$\nabla_\perp B$	$\nabla_\parallel B$
Normalized by	$\rho_{L_{i_0}} = \frac{c_{s0}}{\omega_{c_{i_0}}}$	$\rho_{L_{e0}} = \frac{m_e}{m_i}\rho_{L_{i0}}$	$\frac{F_0}{l_\perp}$	$\frac{F_0}{l_\parallel}$	$\frac{B_0}{l_{B_\perp}} = \frac{B_0}{\mathcal{A}a}$	$\frac{B_0}{l_{B_\parallel}} = \frac{B_0}{q\mathcal{A}a}$
Dimensionless variable	$\frac{\sqrt{\widehat{T}_e+\widehat{T}_i}}{\widehat{B}}$	$\frac{\sqrt{\widehat{T}_e+\widehat{T}_i}}{\widehat{B}}$	$\widehat{\nabla}_\perp \widehat{F}$	$\widehat{\nabla}_\parallel \widehat{F}$	$\widehat{\nabla}_\perp \widehat{B}$	$\widehat{\nabla}_\parallel \widehat{B}$
Tore Supra at LCFS	2×10^{-4}	10^{-7}				

Table 2.4: Characteristic lengths with associated normalizations

Finally, we introduce two dimensionless parameters, commonly used in plasma physics, which take into account tokamak geometry: $\rho_\star = \frac{\rho_{L_{i0}}}{a}$ and the collisionality $\nu_\star = \frac{a}{c_{s0}\tau_{e0}}$. One can notice that the product of these two dimensionless parameters are linked to the gyro-frequency and electron-ion collision time: $\rho_\star \nu_\star = \left(\omega_{c_{i_0}} \tau_{e0}\right)^{-1}$.

The value of this dimensionless product $\rho_\star\nu_\star$ is presented in Figure 2.1 in a whole range of edge plasma conditions: density n_0 from 10^{-18} to 5×10^{-19}m^{-3}, temperature T_0 from 1eV to 1keV and a magnetic field of 3.1T which corresponds to the typical value of the magnetic field at the LCFS of Tore Supra.

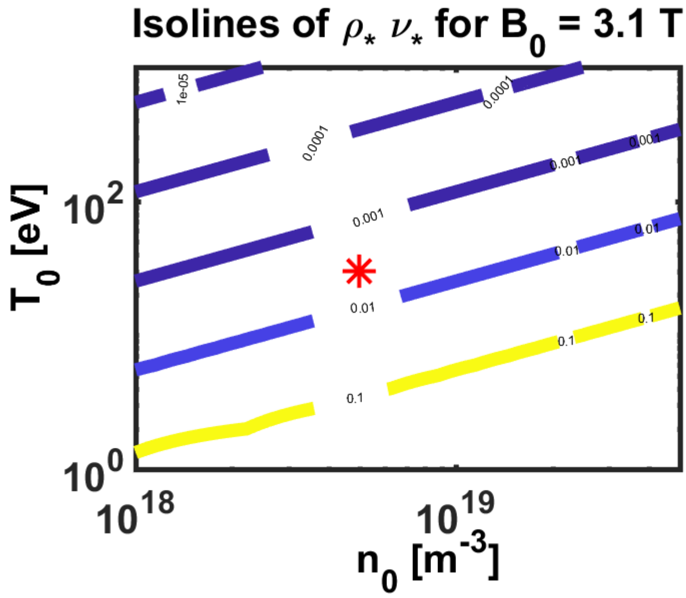

Figure 2.1: Isolines of $\rho_\star\nu_\star$ as a function of reference density n_0 and temperature T_0 and for a magnetic field of 3.1T in a log-log scale. The red asterix corresponds to the typical value of Tore Supra plasma at the LCFS ($n_0 = 5\times10^{18}$m^{-3},$T_0 = 30$eV).

The value of $\rho_\star\nu_\star$ is found to be small compared to unity in the whole range of edge plasma conditions with a maximal value obtained for a very cold plasma temperature of several eV. For typical Tore Supra plasma, the value of $\rho_\star\nu_\star$ is slightly smaller than 10^{-2}. In the following, we assume thus:

$$\rho_\star\nu_\star \ll 1 \tag{2.77}$$

In summary, 9 dimensionless parameters should be used to realize the full ordering of the system of fluid equations with Braginskii's closure: $\varepsilon_\omega, \varepsilon_u, \varepsilon_l, \varepsilon_\nabla$, $\nu_\star$, the ratio of mass m_e/m_i and three geometrical parameters: $\mathcal{A}$, q and $\rho_\star$.

2.4.1.2 Reduction of the number of dimensionless parameters

Such complex ordering analysis is beyond the scope of this thesis. In the following, some assumptions are made to reduce the number of dimensionless parameters:

- the Scrape-Off-Layer width is obtained, at quasi steady-state, when the characteristic times of perpendicular and parallel transport - $\tau_\perp = l_\perp/u_{\perp_0}$ and $\tau_\parallel = l_\parallel/c_{s_0}$ - become equal. Indeed, a structure can propagate outward radially until being totally damped at target losses due to parallel transport. It follows:

$$\varepsilon_v = \varepsilon_l \tag{2.78}$$

  The validity of such assumption in closed field line region is more questionable.

- the radial transport in the SOL is mainly generated by turbulence. We can thus assume that characteristic time of turbulence ω^{-1} is similar to the characteristic time of perpendicular transport in the SOL $\tau_\perp$. Such hypothesis leads to:

$$\varepsilon_v \varepsilon_l = \varepsilon_\omega \tag{2.79}$$

  Here again, the validity of such hypothesis is more challenging especially inside a transport barrier in which turbulence disappears and strong gradients are developing.

- the final assumption - probably the most questionable - is to assume that the characteristic length of perpendicular transport is at an intermediate range between the finest scale of the model - the ion Larmor radius - and the characteristic length of parallel transport $l_\parallel \sim qR_0$. This writes:

$$\varepsilon_\nabla = \varepsilon_v \tag{2.80}$$

  At LCFS of Tore Supra, the ion Larmor radius is about 2×10^{-4}m and the parallel length is of order of magnitude from 10 to 100 meters. If we take for simplicity $l_\parallel = 20$m, the characteristic perpendicular length must be of the order of 6 cm which is in good agreement with experimental measurements of density decay length in Tore Supra [Kočan 10] .

By combining the 3 hypothesis (2.78), (2.79) and (2.80), the 4 ε_i dimensionless coefficients can be regrouped under one coefficient ε:

$$\boxed{\varepsilon = \varepsilon_l = \varepsilon_v = \varepsilon_\nabla = \sqrt{\varepsilon_\omega}} \tag{2.81}$$

Such assumptions also imply $l_\perp < a < l_\parallel$ and lead to the following inequality:

$$\rho_\star \varepsilon < \varepsilon^2 < \rho_\star < \varepsilon < \frac{\rho_\star}{\varepsilon} < 1 \tag{2.82}$$

Finally, the effect of two geometrical parameters - the aspect ratio $\mathcal{A}$ and the safety factor q - will be neglected in the ordering. Indeed, these two parameters are expected to have a maximal magnitude of 10^1 and are thus assumed to be negligible with respect to ε^{-1} and $\rho_\star^{-1}$. Such hypothesis may lead to an overestimation of curvature terms in the ordering procedure.

2.4.2 Ordering of Braginskii's fluid equations

2.4.2.1 Ordering on continuity equation

The normalizations detailed previously are applied on continuity equation (2.25) and by dividing by ε^2 we obtain for the species s:

$$\boxed{\partial_{\hat{t}} \hat{n} + \widehat{\boldsymbol{\nabla}} \cdot (\hat{n}\hat{\mathbf{u}}_s) = 0} \tag{2.83}$$

2.4.2.2 Ordering on parallel momentum equations

Electron parallel momentum:

The ordering procedure is done on electron parallel momentum equation (2.73):

$$\begin{aligned}
-\widehat{\nabla}_{\parallel}\widehat{p}_e + \widehat{n}\widehat{\nabla}_{\parallel}\widehat{\phi} - 0.71\widehat{n}\widehat{\nabla}_{\parallel}\widehat{T}_e = &\frac{m_e}{m_i}\Bigg\{\partial_{\widehat{t}}\left(\widehat{n}\widehat{u}_{e_\parallel}\right) + \widehat{\boldsymbol{\nabla}}\cdot\left(\widehat{n}\widehat{u}_{e_\parallel}\widehat{\mathbf{u}}_e\right) + \widehat{n}\left(\widehat{\mathbf{u}}_e^{\star}\cdot\widehat{\boldsymbol{\nabla}}_{\perp}\right)\widehat{u}_{e_\parallel} - \frac{\rho_\star\nu_\star}{\varepsilon^2}0.51\frac{\widehat{j}_\parallel\widehat{n}}{\widehat{T}_e^{3/2}} \\
&- \frac{\rho_\star}{\varepsilon}\left[\widehat{n}\widehat{\mathbf{u}}_{e_\perp}\cdot\left(\left(\widehat{u}_{e_\parallel}\widehat{\nabla}_\parallel\right)\mathbf{b}\right) + \widehat{p}_e\left(\left(\widehat{\boldsymbol{\nabla}}_\perp\times\frac{\mathbf{b}}{\widehat{B}}\right)\cdot\widehat{\boldsymbol{\nabla}}_\perp\right)\widehat{u}_{e_\parallel}\right] \\
&- \rho_\star\widehat{n}\widehat{\mathbf{u}}_{e_\perp}\cdot\left(\left(\widehat{\mathbf{u}}_{e_\perp}\cdot\widehat{\boldsymbol{\nabla}}_\perp\right)\mathbf{b}\right) + \varepsilon^2\mathbf{b}\cdot\left(\widehat{\boldsymbol{\nabla}}_\perp\times\left(\frac{\widehat{p}_e}{\widehat{B}}\widehat{\nabla}_\parallel\widehat{\mathbf{u}}_{e_\perp}\right)\right)\Bigg\} \\
&+ \frac{\varepsilon^2}{\rho_\star\nu_\star}1.46\widehat{\nabla}_\parallel\left(\widehat{T}_e^{5/2}\left(\frac{1}{3}\widehat{\boldsymbol{\nabla}}\cdot\widehat{\mathbf{u}}_e - \widehat{\nabla}_\parallel\widehat{u}_{e_\parallel}\right)\right)
\end{aligned} \tag{2.84}$$

where the normalized diamagnetic velocity $\widehat{\mathbf{u}}_s^{\star} = \frac{\mathbf{b}\times\widehat{\boldsymbol{\nabla}}_\perp\widehat{p}_s}{\widehat{n}_s\widehat{B}}$ has the same sign for electron and ions. In the edge plasma, the electron-ion collision time is usually smaller than turbulent characteristic time ω. The Braginskii's closure relies on this assumption of high collisionality. It follows that:

$$\frac{\rho_\star\nu_\star}{\varepsilon^2} = \left(\omega\tau_{e0}\right)^{-1} \gg 1 \tag{2.85}$$

In particular, we will assume:

$$\frac{m_e}{m_i}\frac{\rho_\star\nu_\star}{\varepsilon^2} \sim 1 \quad ; \quad \sqrt{\frac{m_i}{m_e}}\frac{\varepsilon^2}{\rho_\star\nu_\star} = o\left(1\right) \tag{2.86}$$

If only dominant terms - of order unity - are retained, we obtained the electron parallel momentum equation which corresponds to the parallel Ohm's law:

$$\boxed{\widehat{\nabla}_\parallel\widehat{p}_e - \widehat{n}\widehat{\nabla}_\parallel\widehat{\phi} + 0.71\widehat{n}\widehat{\nabla}_\parallel\widehat{T}_e = \frac{m_e}{m_i}\frac{\rho_\star\nu_\star}{\varepsilon^2}0.51\frac{\widehat{j}_\parallel\widehat{n}}{\widehat{T}_e^{3/2}} + o\left(1\right)} \tag{2.87}$$

Ion parallel momentum:

The ordering procedure is now done on the ion parallel momentum equation (2.74):

$$\begin{aligned}
&-\widehat{\nabla}_\parallel\widehat{p}_i - \widehat{n}\widehat{\nabla}_\parallel\widehat{\phi} + 0.71\widehat{n}\widehat{\nabla}_\parallel\widehat{T}_e \\
=&\partial_{\widehat{t}}\left(\widehat{n}\widehat{u}_{i_\parallel}\right) + \widehat{\boldsymbol{\nabla}}\cdot\left(\widehat{n}\widehat{u}_{i_\parallel}\widehat{\mathbf{u}}_i\right) - \widehat{n}\left(\widehat{\mathbf{u}}_i^{\star}\cdot\widehat{\boldsymbol{\nabla}}_\perp\right)\widehat{u}_{i_\parallel} + \frac{m_e}{m_i}\frac{\rho_\star\nu_\star}{\varepsilon^2}0.51\frac{\widehat{j}_\parallel\widehat{n}}{\widehat{T}_e^{3/2}} \\
&+ \frac{\rho_\star}{\varepsilon}\left[\widehat{p}_i\left(\left(\widehat{\boldsymbol{\nabla}}_\perp\times\frac{\mathbf{b}}{\widehat{B}}\right)\cdot\widehat{\boldsymbol{\nabla}}_\perp\right)\widehat{u}_{i_\parallel} - \widehat{n}\widehat{\mathbf{u}}_{i_\perp}\cdot\left(\left(\widehat{u}_{i_\parallel}\widehat{\nabla}_\parallel\right)\mathbf{b}\right)\right] - \rho_\star\widehat{n}\widehat{\mathbf{u}}_{i_\perp}\cdot\left(\left(\widehat{\mathbf{u}}_{i_\perp}\cdot\widehat{\boldsymbol{\nabla}}_\perp\right)\mathbf{b}\right) \\
&- \varepsilon^2\mathbf{b}\cdot\left(\widehat{\boldsymbol{\nabla}}_\perp\times\left(\frac{\widehat{p}_i}{\widehat{B}}\widehat{\nabla}_\parallel\widehat{\mathbf{u}}_{i_\perp}\right)\right) + \sqrt{\frac{m_i}{m_e}}\frac{\varepsilon^2}{\rho_\star\nu_\star}1.92\sqrt{2}\widehat{\nabla}_\parallel\left(\widehat{T}_i^{5/2}\left(\frac{1}{3}\widehat{\boldsymbol{\nabla}}\cdot\widehat{\mathbf{u}}_i - \widehat{\nabla}_\parallel\widehat{u}_{i_\parallel}\right)\right)
\end{aligned} \tag{2.88}$$

Here again, only dominant terms are kept to obtain the ion parallel momentum equation:

$$\partial_{\widehat{t}}\left(\widehat{n}\widehat{u}_{i_\parallel}\right)+\widehat{\boldsymbol{\nabla}}\cdot\left(\widehat{n}\widehat{u}_{i_\parallel}\widehat{\mathbf{u}}_i\right)-\widehat{n}\left(\widehat{\mathbf{u}}_i^\star\cdot\widehat{\boldsymbol{\nabla}}_\perp\right)\widehat{u}_{i_\parallel}+\widehat{\nabla}_\parallel\widehat{p}_i+\widehat{n}\widehat{\nabla}_\parallel\widehat{\phi}-0.71\widehat{n}\widehat{\nabla}_\parallel\widehat{T}_e+\frac{m_e}{m_i}\frac{\rho_\star\nu_\star}{\varepsilon^2}0.51\frac{\widehat{j}_\parallel\widehat{n}}{\widehat{T}_e^{3/2}}=o\left(1\right) \quad (2.89)$$

One can notice that this equation can easily be combined with the Ohm's law (2.87) to obtain:

$$\boxed{\partial_{\widehat{t}}\left(\widehat{n}\widehat{u}_{i_\parallel}\right)+\widehat{\boldsymbol{\nabla}}\cdot\left(\widehat{n}\widehat{u}_{i_\parallel}\widehat{\mathbf{u}}_i\right)-\widehat{n}\left(\widehat{\mathbf{u}}_i^\star\cdot\widehat{\boldsymbol{\nabla}}_\perp\right)\widehat{u}_{i_\parallel}+\widehat{\nabla}_\parallel\left(\widehat{p}_i+\widehat{p}_e\right)=0} \quad (2.90)$$

2.4.2.3 Ordering on perpendicular momenta

Ordering on electron perpendicular momentum equation (2.75) :

$$\begin{aligned}
&\widehat{n}\widehat{B}\widehat{\mathbf{u}}_{e_\perp}+\left(\mathbf{b}\times\widehat{\boldsymbol{\nabla}}_\perp\widehat{p}_e-\widehat{n}\mathbf{b}\times\widehat{\boldsymbol{\nabla}}_\perp\widehat{\phi}\right)\\
=&\frac{m_e}{m_i}\left\{\varepsilon^2\left[\partial_{\widehat{t}}\left(\widehat{n}\widehat{\mathbf{u}}_{e_\perp}\times\mathbf{b}\right)+\left(\left(\widehat{\mathbf{u}}_e\cdot\widehat{\boldsymbol{\nabla}}\right)\widehat{n}\widehat{\mathbf{u}}_{e_\perp}\right)\times\mathbf{b}+\widehat{n}\left(\widehat{\boldsymbol{\nabla}}\cdot\widehat{\mathbf{u}}_e\right)\widehat{\mathbf{u}}_{e_\perp}\times\mathbf{b}-\widehat{n}\left(\widehat{\mathbf{u}}^\star\cdot\widehat{\boldsymbol{\nabla}}_\perp\right)\left(\mathbf{b}\times\widehat{\mathbf{u}}_{e_\perp}\right)\right.\right.\\
&\left.+\mathbf{b}\times\widehat{\boldsymbol{\nabla}}_\perp\left(\frac{\widehat{p}_e}{2\widehat{B}}\widehat{\boldsymbol{\nabla}}_\perp\cdot\left(\mathbf{b}\times\widehat{\mathbf{u}}_{e_\perp}\right)\right)-\widehat{\boldsymbol{\nabla}}_\perp\left(\frac{\widehat{p}_e}{2\widehat{B}}\widehat{\boldsymbol{\nabla}}_\perp\cdot\widehat{\mathbf{u}}_{e_\perp}\right)-\widehat{\nabla}_\parallel\left(\frac{\widehat{p}_e}{\widehat{B}}\widehat{\boldsymbol{\nabla}}_\perp\widehat{u}_{e_\parallel}\right)\right] \quad (2.91)\\
&+\frac{\rho_\star}{\varepsilon}\left(\left(\widehat{\mathbf{u}}_e\cdot\widehat{\boldsymbol{\nabla}}\right)\widehat{n}\widehat{u}_{e_\parallel}\mathbf{b}\right)-\rho_\star\varepsilon\widehat{p}_e\left(\left(\widehat{\boldsymbol{\nabla}}_\perp\times\frac{\mathbf{b}}{\widehat{B}}\right)\cdot\widehat{\boldsymbol{\nabla}}_\perp\right)\left(\widehat{\mathbf{u}}_{e_\perp}\times\mathbf{b}\right)\\
&\left.-\varepsilon^4\widehat{\nabla}_\parallel\left(\frac{\widehat{p}_e}{\widehat{B}}\widehat{\nabla}_\parallel\widehat{\mathbf{u}}_{e_\perp}\right)+\rho_\star\nu_\star\left(\frac{\widehat{n}^2}{\widehat{T}_e^{3/2}}\left(\widehat{\mathbf{u}}_{e_\perp}-\widehat{\mathbf{u}}_{i_\perp}\right)\times\mathbf{b}+\frac{3}{2}\frac{\widehat{n}^2}{\widehat{B}\widehat{T}_e^{3/2}}\widehat{\boldsymbol{\nabla}}_\perp\widehat{T}_e\right)\right\}\\
&+\frac{\varepsilon^2}{\rho_\star\nu_\star}0.73\ \mathbf{b}\times\widehat{\boldsymbol{\nabla}}_\perp\left(\widehat{T}_e^{5/2}\left(\frac{1}{3}\widehat{\boldsymbol{\nabla}}\cdot\widehat{\mathbf{u}}_e-\widehat{\nabla}_\parallel\widehat{u}_{e_\parallel}\right)\right)
\end{aligned}$$

Ordering on ion perpendicular momentum equation (2.76):

$$\begin{aligned}
&\widehat{n}\widehat{B}\widehat{\mathbf{u}}_{i_\perp}-\left(\mathbf{b}\times\widehat{\boldsymbol{\nabla}}_\perp\widehat{p}_i+\widehat{n}\mathbf{b}\times\widehat{\boldsymbol{\nabla}}_\perp\widehat{\phi}\right)\\
=&\varepsilon^2\left[-\partial_{\widehat{t}}\left(\widehat{n}\widehat{\mathbf{u}}_{i_\perp}\times\mathbf{b}\right)-\left(\left(\widehat{\mathbf{u}}_i\cdot\widehat{\boldsymbol{\nabla}}\right)\widehat{n}\widehat{\mathbf{u}}_{i_\perp}\right)\times\mathbf{b}-\widehat{n}\left(\widehat{\boldsymbol{\nabla}}\cdot\widehat{\mathbf{u}}_i\right)\widehat{\mathbf{u}}_{i_\perp}\times\mathbf{b}-\widehat{n}\left(\widehat{\mathbf{u}}^\star\cdot\widehat{\boldsymbol{\nabla}}_\perp\right)\left(\mathbf{b}\times\widehat{\mathbf{u}}_{i_\perp}\right)\right.\\
&\left.+\mathbf{b}\times\widehat{\boldsymbol{\nabla}}_\perp\left(\frac{\widehat{p}_i}{2\widehat{B}}\widehat{\boldsymbol{\nabla}}_\perp\cdot\left(\mathbf{b}\times\widehat{\mathbf{u}}_{i_\perp}\right)\right)-\widehat{\boldsymbol{\nabla}}_\perp\left(\frac{\widehat{p}_i}{2\widehat{B}}\widehat{\boldsymbol{\nabla}}_\perp\cdot\widehat{\mathbf{u}}_{i_\perp}\right)-\widehat{\nabla}_\parallel\left(\frac{\widehat{p}_i}{\widehat{B}}\widehat{\boldsymbol{\nabla}}_\perp\widehat{u}_{i_\parallel}\right)\right] \quad (2.92)\\
&+\frac{\rho_\star}{\varepsilon}\left(\left(\widehat{\mathbf{u}}_i\cdot\widehat{\boldsymbol{\nabla}}\right)\widehat{n}\widehat{u}_{i_\parallel}\mathbf{b}\right)-\rho_\star\varepsilon\widehat{p}_i\left(\left(\widehat{\boldsymbol{\nabla}}_\perp\times\frac{\mathbf{b}}{\widehat{B}}\right)\cdot\widehat{\boldsymbol{\nabla}}_\perp\right)\widehat{\mathbf{u}}_{i_\perp}\\
&-\varepsilon^4\widehat{\nabla}_\parallel\left(\frac{\widehat{p}_i}{\widehat{B}}\widehat{\nabla}_\parallel\widehat{\mathbf{u}}_{i_\perp}\right)+\frac{m_e}{m_i}\rho_\star\nu_\star\left(\frac{\widehat{n}^2}{\widehat{T}_e^{3/2}}\left(\widehat{\mathbf{u}}_{e_\perp}-\widehat{\mathbf{u}}_{i_\perp}\right)\times\mathbf{b}+\frac{3}{2}\frac{\widehat{n}^2}{\widehat{B}\widehat{T}_e^{3/2}}\widehat{\boldsymbol{\nabla}}_\perp\widehat{T}_e\right)\\
&-\sqrt{\frac{m_i}{m_e}}\frac{\varepsilon^2}{\rho_\star\nu_\star}0.96\sqrt{2}\ \mathbf{b}\times\widehat{\boldsymbol{\nabla}}_\perp\left(\widehat{T}_i^{5/2}\left(\frac{1}{3}\widehat{\boldsymbol{\nabla}}\cdot\widehat{\mathbf{u}}_i-\widehat{\nabla}_\parallel\widehat{u}_{i_\parallel}\right)\right)
\end{aligned}$$

2.4.2.4 Drift velocities

The ordering procedure on perpendicular momentum equations makes appear that the perpendicular fluid velocities can, at largest order, be expressed directly as a function of pressure and potential gradient. For that, an asymptotic expansion by $\varepsilon_\omega = \varepsilon^2$ is made on the perpendicular velocity:

$$\widehat{\mathbf{u}}_{s_\perp} = \widehat{\mathbf{u}}_{s_\perp}^{(1)} + \varepsilon^2 \widehat{\mathbf{u}}_{s_\perp}^{(2)} + o\left(\varepsilon^2\right) \tag{2.93}$$

This expansion can be used in equations (2.91) and (2.92) to calculate by identification first and second velocity drifts $\widehat{\mathbf{u}}_{s_\perp}^{(1)}$ and $\widehat{\mathbf{u}}_{s_\perp}^{(2)}$.

First order drifts:

$$\boxed{\widehat{\mathbf{u}}_{i_\perp}^{(1)} = \widehat{\mathbf{u}}_{\perp}^{\mathrm{E\times B}} + \widehat{\mathbf{u}}_{i_\perp}^{\star} = \frac{\mathbf{b}\times\widehat{\boldsymbol{\nabla}}_\perp \widehat{\phi}}{\widehat{B}} + \frac{\mathbf{b}\times\widehat{\boldsymbol{\nabla}}_\perp \widehat{p}_i}{\widehat{n}\widehat{B}}} \tag{2.94}$$

$$\boxed{\widehat{\mathbf{u}}_{e_\perp}^{(1)} = \widehat{\mathbf{u}}_{\perp}^{\mathrm{E\times B}} + \widehat{\mathbf{u}}_{e_\perp}^{\star} = \frac{\mathbf{b}\times\widehat{\boldsymbol{\nabla}}_\perp \widehat{\phi}}{\widehat{B}} - \frac{\mathbf{b}\times\widehat{\boldsymbol{\nabla}}_\perp \widehat{p}_e}{\widehat{n}\widehat{B}}} \tag{2.95}$$

The standard $\mathbf{E}\times\mathbf{B}$ and diamagnetic drifts are obtained by denormalising these drifts:

$$\mathbf{u}_{s_\perp}^{(1)} = \mathbf{u}_{\perp}^{\mathrm{E\times B}} + \mathbf{u}_{s_\perp}^{\star} = \frac{\mathbf{b}\times\boldsymbol{\nabla}_\perp \phi}{B} + \frac{\mathbf{b}\times\boldsymbol{\nabla}_\perp p_s}{q_s n B} \tag{2.96}$$

These two drifts are appearing in fluid equations mainly through the divergence of their fluxes:

$$\widehat{\boldsymbol{\nabla}}\cdot\left(\widehat{n}\widehat{\mathbf{u}}_{\perp}^{E\times B}\right) = \frac{1}{\widehat{B}}\left[\widehat{\phi},\widehat{n}\right] + \frac{\rho_\star}{\varepsilon}\frac{2\widehat{n}}{\widehat{B}^2}\left[\widehat{B},\widehat{\phi}\right] \tag{2.97}$$

$$\widehat{\boldsymbol{\nabla}}\cdot\left(\widehat{n}\widehat{\mathbf{u}}_{s_\perp}^{\star}\right) = \frac{\rho_\star}{\varepsilon}\frac{q_s}{|q_s|}\frac{2}{\widehat{B}^2}\left[\widehat{B},\widehat{p}_s\right] \tag{2.98}$$

where $\left[f,g\right] = \mathbf{b}\cdot\left(\widehat{\boldsymbol{\nabla}}_\perp f\times\widehat{\boldsymbol{\nabla}}_\perp g\right)$ is a Poisson backet.
Finally, the divergence of particle flux associated with first order drifts writes:

$$\boxed{\widehat{\boldsymbol{\nabla}}\cdot\left(\widehat{n}\widehat{\mathbf{u}}_{s_\perp}^{(1)}\right) = \frac{1}{\widehat{B}}\left[\widehat{\phi},\widehat{n}\right] + \frac{\rho_\star}{\varepsilon}\left(\frac{2\widehat{n}}{\widehat{B}^2}\left[\widehat{B},\widehat{\phi}\right] + \frac{q_s}{|q_s|}\frac{2}{\widehat{B}^2}\left[\widehat{B},\widehat{p}_s\right]\right)} \tag{2.99}$$

Second order drifts:

$$\boxed{\widehat{\mathbf{u}}_{i_\perp}^{(2)} = \widehat{\mathbf{u}}_{i_\perp}^{\mathrm{centr}} + \widehat{\mathbf{u}}_{i_\perp}^{\mathrm{pol}} + \widehat{\mathbf{u}}_{i_\perp}^{\mathrm{R_i}} + \widehat{\mathbf{u}}_{i_\perp}^{\mathrm{vis}} + \widehat{\mathbf{u}}_{i_\perp}^{\mathrm{FLR}}} \tag{2.100}$$

where the second order drifts are:

- the centrifugal force drift:

$$\widehat{\mathbf{u}}_{i_\perp}^{\mathrm{centr}} = \frac{\rho_\star}{\varepsilon^3}\frac{1}{\widehat{n}\widehat{B}}\left(\left(\widehat{\mathbf{u}}_i\cdot\widehat{\boldsymbol{\nabla}}\right)\widehat{n}\widehat{u}_{i_\parallel}\mathbf{b}\right)\times\mathbf{b} \tag{2.101}$$

  The centrifugal force drift is the dominant term of second order drifts and can even be considered as a first order drift. This drift is usually neglected in most of 3D fluid code including Tokam3X. In fact, our ordering overestimates the weight of the centrifugal force because the parallel velocity is smaller than the acoustic velocity in the edge plasma except at the target plates so that the centrifugal force remains marginal.

- the polarization drift:

$$\widehat{\mathbf{u}}_{i\perp}^{\mathrm{pol}} = \frac{1}{\widehat{n}\widehat{B}}\left[\partial_{\widehat{t}}\left(\widehat{n}\,\mathbf{b}\times\widehat{\mathbf{u}}_{i\perp}^{(1)}\right) - \widehat{n}\left(\widehat{\boldsymbol{\nabla}}\cdot\widehat{\mathbf{u}}_i\right)\widehat{\mathbf{u}}_{i\perp}^{(1)}\times\mathbf{b} + \left(\left(\widehat{\mathbf{u}}_i\cdot\widehat{\boldsymbol{\nabla}}\right)\widehat{n}\widehat{\mathbf{u}}_{i\perp}^{(1)}\right)\times\mathbf{b}\right] \tag{2.102}$$

where $\widehat{\mathbf{u}}_i = \widehat{u}_{i_\parallel}\mathbf{b} + \widehat{\mathbf{u}}_{i\perp}^{(1)}$.

- the collisional momentum drift:

$$\widehat{\mathbf{u}}_{i\perp}^{\mathrm{R_i}} = \frac{m_e}{m_i}\frac{\rho_\star\nu_\star}{\varepsilon^2}\left(\frac{\widehat{n}}{\widehat{B}\widehat{T}_e^{3/2}}\left(\widehat{\mathbf{u}}_{e\perp}^{(1)} - \widehat{\mathbf{u}}_{i\perp}^{(1)}\right)\times\mathbf{b} + \frac{3}{2}\frac{\widehat{n}}{\widehat{B}^2\widehat{T}_e^{3/2}}\widehat{\boldsymbol{\nabla}}_\perp\widehat{T}_e\right) \tag{2.103}$$

- the viscous drift:

$$\widehat{\mathbf{u}}_{i\perp}^{\mathrm{vis}} = -\sqrt{\frac{m_i}{m_e}}\frac{1}{\rho_\star\nu_\star}0.96\sqrt{2}\frac{1}{\widehat{n}\widehat{B}}\mathbf{b}\times\widehat{\boldsymbol{\nabla}}_\perp\left(\widehat{T}_i^{5/2}\left(\frac{1}{3}\widehat{\boldsymbol{\nabla}}\cdot\widehat{\mathbf{u}}_i - \widehat{\nabla}_\parallel\widehat{u}_{i_\parallel}\right)\right) \tag{2.104}$$

- the FLR drift:

$$\begin{aligned}\widehat{\mathbf{u}}_{i\perp}^{\mathrm{FLR}} = \frac{1}{\widehat{n}\widehat{B}}\Big[&-\widehat{n}\left(\widehat{\mathbf{u}}^\star\cdot\widehat{\boldsymbol{\nabla}}_\perp\right)\left(\mathbf{b}\times\widehat{\mathbf{u}}_{i\perp}^{(1)}\right) + \mathbf{b}\times\widehat{\boldsymbol{\nabla}}_\perp\left(\frac{\widehat{p}_i}{2\widehat{B}}\widehat{\boldsymbol{\nabla}}_\perp\cdot\left(\mathbf{b}\times\widehat{\mathbf{u}}_{i\perp}^{(1)}\right)\right)\\ &-\widehat{\boldsymbol{\nabla}}_\perp\left(\frac{\widehat{p}_i}{2\widehat{B}}\widehat{\boldsymbol{\nabla}}_\perp\cdot\widehat{\mathbf{u}}_{i\perp}^{(1)}\right) - \widehat{\nabla}_\parallel\left(\frac{\widehat{p}_i}{\widehat{B}}\widehat{\boldsymbol{\nabla}}_\perp\widehat{u}_{i_\parallel}\right)\Big]\end{aligned} \tag{2.105}$$

For electrons, only the centrifugal force, the viscous and the collisional momentum drifts are second order terms:

$$\boxed{\widehat{\mathbf{u}}_{e\perp}^{(2)} = \widehat{\mathbf{u}}_{e\perp}^{\mathrm{centr}} + \widehat{\mathbf{u}}_{e\perp}^{\mathrm{vis}} + \widehat{\mathbf{u}}_{e\perp}^{\mathrm{R_e}}} \tag{2.106}$$

with:

$$\widehat{\mathbf{u}}_{e\perp}^{\mathrm{centr}} = \frac{m_e}{m_i}\frac{\rho_\star}{\varepsilon^3}\frac{1}{\widehat{n}\widehat{B}}\left(\left(\widehat{\mathbf{u}}_e\cdot\widehat{\boldsymbol{\nabla}}\right)\widehat{n}\widehat{u}_{e_\parallel}\mathbf{b}\right)\times\mathbf{b} \tag{2.107}$$

$$\widehat{\mathbf{u}}_{e\perp}^{\mathrm{vis}} = \frac{1}{\rho_\star\nu_\star}0.73\frac{1}{\widehat{n}\widehat{B}}\mathbf{b}\times\widehat{\boldsymbol{\nabla}}_\perp\left(\widehat{T}_e^{5/2}\left(\frac{1}{3}\widehat{\boldsymbol{\nabla}}\cdot\widehat{\mathbf{u}}_e - \widehat{\nabla}_\parallel\widehat{u}_{e_\parallel}\right)\right) \tag{2.108}$$

$$\widehat{\mathbf{u}}_{e\perp}^{\mathrm{R_e}} = \frac{m_e}{m_i}\frac{\rho_\star\nu_\star}{\varepsilon^2}\left(\frac{\widehat{n}^2}{\widehat{T}_e^{3/2}}\left(\widehat{\mathbf{u}}_{e\perp}^{(1)} - \widehat{\mathbf{u}}_{i\perp}^{(1)}\right)\times\mathbf{b} + \frac{3}{2}\frac{\widehat{n}^2}{\widehat{B}\widehat{T}_e^{3/2}}\widehat{\boldsymbol{\nabla}}_\perp\widehat{T}_e\right) \tag{2.109}$$

2.4.2.5 Charge conservation - Vorticity equation

Another property that our models must satisfy is the charge conservation:

$$\boldsymbol{\nabla}\cdot\mathbf{j} = 0 \tag{2.110}$$

This equation can easily be obtained by combining ion and electron continuity equation with quasi-neutrality. This current is then decomposed in parallel and perpendicular parts. The former is obtained from the Ohm's law (2.87) while the latter is determined by the velocity drifts. As the $\mathbf{E}\times\mathbf{B}$ drift does not depend on the charge of the species, this drift does not carry any current: $\mathbf{j}_\perp^{E\times B} = 0$.

$$\boldsymbol{\nabla}\cdot\mathbf{j} = \boldsymbol{\nabla}\cdot\left(j_\parallel\mathbf{b}\right) + \boldsymbol{\nabla}\cdot\left(en\left(\mathbf{u}_i^\star - \mathbf{u}_e^\star\right)\right) + \boldsymbol{\nabla}\cdot\left(en\mathbf{u}_{i\perp}^{(2)}\right) = 0 \tag{2.111}$$

2.4.2.6 Ordering on energy equations

As for continuity and momentum equations, the ordering procedure is realized on ion and electron energy equations.

Ion energy

$$\begin{aligned}
&\partial_{\widehat{t}}\left(\frac{1}{2}\widehat{n}|\widehat{\mathbf{u}}_i|^2+\frac{3}{2}\widehat{p}_i\right)+\widehat{\boldsymbol{\nabla}}\cdot\left(\frac{1}{2}\widehat{n}|\widehat{\mathbf{u}}_i|^2\widehat{\mathbf{u}}_i+\frac{5}{2}\widehat{p}_i\widehat{\mathbf{u}}_i\right)+\widehat{n}\widehat{\mathbf{u}}_i\cdot\widehat{\boldsymbol{\nabla}}\widehat{\phi}+\widehat{\boldsymbol{\nabla}}_\perp\cdot\left(\frac{5}{2}\frac{\widehat{p}_i}{\widehat{B}}\mathbf{b}\times\widehat{\boldsymbol{\nabla}}_\perp\widehat{T}_i\right)-0.71\widehat{n}\widehat{u}_{i_\parallel}\widehat{\nabla}_\parallel\widehat{T}_e\\
=&\frac{m_e}{m_i}\frac{\rho_\star\nu_\star}{\varepsilon^2}\frac{\widehat{n}^2}{\widehat{T}_e^{3/2}}\left(0.51\left(\widehat{u}_{e_\parallel}-\widehat{u}_{i_\parallel}\right)\widehat{u}_{i_\parallel}+3\left(\widehat{T}_e-\widehat{T}_i\right)\right)+\sqrt{\frac{m_e}{m_i}}\rho_\star\nu_\star\sqrt{2}\widehat{\boldsymbol{\nabla}}_\perp\cdot\left(\frac{\widehat{n}^2}{\widehat{B}^2\widehat{T}_i^{1/2}}\widehat{\boldsymbol{\nabla}}_\perp\widehat{T}_i\right)\\
&+\frac{m_e}{m_i}\rho_\star\nu_\star\left(\frac{\widehat{n}^2}{\widehat{T}_e^{3/2}}\left(\widehat{\mathbf{u}}_{e_\perp}-\widehat{\mathbf{u}}_{i_\perp}\right)\cdot\widehat{\mathbf{u}}_{i_\perp}+\frac{\widehat{n}^2}{\widehat{B}\widehat{T}_e^{3/2}}\widehat{\mathbf{u}}_{i_\perp}\cdot\left(\mathbf{b}\times\widehat{\boldsymbol{\nabla}}_\perp\widehat{T}_e\right)\right)\\
&+\sqrt{\frac{m_i}{m_e}}\frac{\varepsilon^2}{\rho_\star\nu_\star}\left[0.96\sqrt{2}\left(\widehat{\nabla}_\parallel\left(\widehat{T}_i^{5/2}\widehat{u}_{i_\parallel}\left(\widehat{\boldsymbol{\nabla}}\cdot\widehat{\mathbf{u}}_i-3\widehat{\nabla}_\parallel\widehat{u}_{i_\parallel}\right)\right)-\frac{1}{3}\widehat{\boldsymbol{\nabla}}\cdot\left(\widehat{T}_i^{5/2}\widehat{\mathbf{u}}_i\left(\widehat{\boldsymbol{\nabla}}\cdot\widehat{\mathbf{u}}_i-3\widehat{\nabla}_\parallel\widehat{u}_{i_\parallel}\right)\right)\right)\right.\\
&\qquad\left.+3.9\sqrt{2}\widehat{\boldsymbol{\nabla}}_\parallel\cdot\left(\widehat{T}_i^{5/2}\widehat{\boldsymbol{\nabla}}_\parallel\widehat{T}_i\right)\right]
\end{aligned}\tag{2.112}$$

By retaining only largest order terms, the ion energy equation writes:

$$\boxed{\begin{aligned}
&\partial_{\widehat{t}}\left(\widehat{E}_i^{\text{tot}}\right)+\widehat{\boldsymbol{\nabla}}\cdot\left(\widehat{E}_i^{\text{tot}}\widehat{\mathbf{u}}_i+\widehat{p}_i\widehat{\mathbf{u}}_i\right)+\widehat{n}\widehat{\mathbf{u}}_i\cdot\widehat{\boldsymbol{\nabla}}\widehat{\phi}+\widehat{\boldsymbol{\nabla}}_\perp\cdot\left(\frac{5}{2}\frac{\widehat{p}_i}{\widehat{B}}\mathbf{b}\times\widehat{\boldsymbol{\nabla}}_\perp\widehat{T}_i\right)-0.71\widehat{n}\widehat{u}_{i_\parallel}\widehat{\nabla}_\parallel\widehat{T}_e\\
=&\frac{m_e}{m_i}\frac{\rho_\star\nu_\star}{\varepsilon^2}\frac{\widehat{n}^2}{\widehat{T}_e^{3/2}}\left(0.51\left(\widehat{u}_{e_\parallel}-\widehat{u}_{i_\parallel}\right)\widehat{u}_{i_\parallel}+3\left(\widehat{T}_e-\widehat{T}_i\right)\right)
\end{aligned}}\tag{2.113}$$

where $\widehat{E}_i^{\text{tot}}=\frac{1}{2}\widehat{n}|\widehat{\mathbf{u}}_i|^2+\frac{3}{2}\widehat{p}_i$

Note that our ordering procedure makes disappear the ion diffusive heat flux while this term is usually included in most of edge plasma codes. In order to validate our ordering, the weight of this ion diffusive heat flux should be estimated in dedicated numerical simulations.

Electron energy

$$\begin{aligned}
&\partial_{\widehat{t}}\left(\frac{3}{2}\widehat{p}_e\right)+\widehat{\boldsymbol{\nabla}}\cdot\left(\frac{5}{2}\widehat{p}_e\widehat{\mathbf{u}}_e\right)-\widehat{n}\widehat{\mathbf{u}}_e\cdot\widehat{\boldsymbol{\nabla}}\widehat{\phi}-\widehat{\boldsymbol{\nabla}}_\perp\cdot\left(\frac{5}{2}\frac{\widehat{p}_e}{\widehat{B}}\mathbf{b}\times\widehat{\boldsymbol{\nabla}}_\perp\widehat{T}_e\right)+0.71\widehat{T}_e\widehat{\nabla}_\parallel\left(\widehat{n}\left(\widehat{u}_{e_\parallel}-\widehat{u}_{i_\parallel}\right)\right)\\
&=-0.71\widehat{\boldsymbol{\nabla}}\cdot\left(\widehat{p}_e\left(\widehat{\mathbf{u}}_{e_\parallel}-\widehat{\mathbf{u}}_{i_\parallel}\right)\mathbf{b}\right)+\frac{m_e}{m_i}\left\{\partial_{\widehat{t}}\left(\frac{1}{2}\widehat{n}|\widehat{\mathbf{u}}_e|^2\right)+\widehat{\boldsymbol{\nabla}}\cdot\left(\frac{1}{2}\widehat{n}|\widehat{\mathbf{u}}_e|^2\widehat{\mathbf{u}}_e\right)\right.\\
&\quad-\frac{\rho_\star\nu_\star}{\varepsilon^2}\frac{\widehat{n}^2}{\widehat{T}_e^{3/2}}\left(3\left(\widehat{T}_e-\widehat{T}_i\right)+0.51\widehat{u}_{i_\parallel}\left(\widehat{u}_{e_\parallel}-\widehat{u}_{i_\parallel}\right)\right)\\
&\quad+\rho_\star\nu_\star\left[\frac{\widehat{n}^2}{\widehat{T}_e^{3/2}}\left(\widehat{\mathbf{u}}_{e_\perp}-\widehat{\mathbf{u}}_{i_\perp}\right)^2+\frac{3}{2}\frac{\widehat{n}^2}{\widehat{B}\widehat{T}_e^{3/2}}\left(\widehat{\mathbf{u}}_{e_\perp}-\widehat{\mathbf{u}}_{i_\perp}\right)\cdot\left(\mathbf{b}\times\widehat{\boldsymbol{\nabla}}_\perp\widehat{T}_e\right)+4.66\widehat{\boldsymbol{\nabla}}_\perp\cdot\left(\frac{\widehat{n}}{\widehat{B}^2\widehat{T}_e^{1/2}}\widehat{\boldsymbol{\nabla}}_\perp\widehat{T}_e\right)\right.\\
&\quad\left.\left.-\widehat{\boldsymbol{\nabla}}_\perp\cdot\left(\frac{3}{2}\frac{\widehat{n}}{\widehat{B}\widehat{T}_e^{1/2}}\mathbf{b}\times\left(\widehat{\mathbf{u}}_{e_\perp}-\widehat{\mathbf{u}}_{i_\perp}\right)\right)\right]\right\}+\frac{m_i}{m_e}\frac{\varepsilon^2}{\rho_\star\nu_\star}3.16\widehat{\boldsymbol{\nabla}}_\parallel\cdot\left(\widehat{T}_e^{5/2}\widehat{\boldsymbol{\nabla}}_\parallel\widehat{T}_e\right)\\
&\quad+\frac{\varepsilon^2}{\rho_\star\nu_\star}0.73\left(\widehat{\nabla}_\parallel\left(\widehat{T}_e^{5/2}\widehat{u}_{e_\parallel}\left(\widehat{\boldsymbol{\nabla}}\cdot\widehat{\mathbf{u}}_e-3\widehat{\nabla}_\parallel\widehat{u}_{e_\parallel}\right)\right)-\frac{1}{3}\widehat{\boldsymbol{\nabla}}\cdot\left(\widehat{T}_e^{5/2}\widehat{\mathbf{u}}_e\left(\widehat{\boldsymbol{\nabla}}\cdot\widehat{\mathbf{u}}_e-3\widehat{\nabla}_\parallel\widehat{u}_{e_\parallel}\right)\right)\right)
\end{aligned}\tag{2.114}$$

By keeping large order terms:

$$\boxed{\begin{aligned}&\partial_{\widehat{t}}\left(\frac{3}{2}\widehat{p}_e\right)+\widehat{\boldsymbol{\nabla}}\cdot\left(\frac{5}{2}\widehat{p}_e\widehat{\mathbf{u}}_e\right)-\widehat{\boldsymbol{\nabla}}_\perp\cdot\left(\frac{5}{2}\frac{\widehat{p}_e}{\widehat{B}}\mathbf{b}\times\widehat{\boldsymbol{\nabla}}_\perp\widehat{T}_e\right)+0.71\widehat{T}_e\widehat{\nabla}_\parallel\left(\widehat{n}\left(\widehat{u}_{e_\parallel}-\widehat{u}_{i_\parallel}\right)\right)\\&=-0.71\widehat{\boldsymbol{\nabla}}\cdot\left(\widehat{p}_e\left(\widehat{\mathbf{u}}_{e_\parallel}-\widehat{\mathbf{u}}_{i_\parallel}\right)\mathbf{b}\right)+\widehat{n}\widehat{\mathbf{u}}_e\cdot\widehat{\boldsymbol{\nabla}}\widehat{\phi}\\&\quad-\frac{m_e}{m_i}\frac{\rho_\star\nu_\star}{\varepsilon^2}\frac{\widehat{n}^2}{\widehat{T}_e^{3/2}}\left(3\left(\widehat{T}_e-\widehat{T}_i\right)+0.51\widehat{u}_{i_\parallel}\left(\widehat{u}_{e_\parallel}-\widehat{u}_{i_\parallel}\right)\right)+\frac{m_i}{m_e}\frac{\varepsilon^2}{\rho_\star\nu_\star}3.16\widehat{\boldsymbol{\nabla}}_\parallel\cdot\left(\widehat{T}_e^{5/2}\widehat{\boldsymbol{\nabla}}_\parallel\widehat{T}_e\right)\end{aligned}} \tag{2.115}$$

2.4.3 Final set of normalized Braginskii's fluid equations

$$\boxed{\partial_{\widehat{t}}\widehat{n} + \widehat{\boldsymbol{\nabla}} \cdot (\widehat{n}\widehat{\mathbf{u}}_s) = 0} \tag{2.116}$$

$$\boxed{\widehat{\nabla}_\parallel \widehat{p}_e - \widehat{n}\widehat{\nabla}_\parallel \widehat{\phi} + 0.71\widehat{n}\widehat{\nabla}_\parallel \widehat{T}_e = \frac{m_e}{m_i}\frac{\rho_\star \nu_\star}{\varepsilon^2} 0.51 \frac{\widehat{j}_\parallel \widehat{n}}{\widehat{T}_e^{3/2}}} \tag{2.117}$$

$$\boxed{\partial_{\widehat{t}}\left(\widehat{n}\widehat{u}_{i_\parallel}\right) + \widehat{\boldsymbol{\nabla}} \cdot \left(\widehat{n}\widehat{u}_{i_\parallel}\widehat{\mathbf{u}}_i\right) - \widehat{n}\left(\widehat{\mathbf{u}}_i^\star \cdot \widehat{\boldsymbol{\nabla}}_\perp\right)\widehat{u}_{i_\parallel} + \widehat{\nabla}_\parallel\left(\widehat{p}_i + \widehat{p}_e\right) = 0} \tag{2.118}$$

$$\boxed{\widehat{\boldsymbol{\nabla}} \cdot \widehat{\mathbf{j}} = \widehat{\boldsymbol{\nabla}} \cdot \left(\widehat{j}_\parallel \mathbf{b}\right) + \widehat{\boldsymbol{\nabla}} \cdot \left(\widehat{n}\left(\widehat{\mathbf{u}}_{i_\perp}^\star - \widehat{\mathbf{u}}_{e_\perp}^\star\right)\right) + \widehat{\boldsymbol{\nabla}} \cdot \left(\widehat{n}\widehat{\mathbf{u}}_{i_\perp}^{(2)}\right) = 0} \tag{2.119}$$

$$\boxed{\begin{aligned} &\partial_{\widehat{t}}\left(\widehat{E}_i^{\rm tot}\right) + \widehat{\boldsymbol{\nabla}} \cdot \left(\widehat{E}_i^{\rm tot}\widehat{\mathbf{u}}_i + \widehat{p}_i\widehat{\mathbf{u}}_i\right) + \widehat{n}\widehat{\mathbf{u}}_i \cdot \widehat{\boldsymbol{\nabla}}\widehat{\phi} + \widehat{\boldsymbol{\nabla}}_\perp \cdot \left(\frac{5}{2}\frac{\widehat{p}_i}{\widehat{B}}\mathbf{b} \times \widehat{\boldsymbol{\nabla}}_\perp \widehat{T}_i\right) - 0.71\widehat{n}\widehat{u}_{i_\parallel}\widehat{\nabla}_\parallel \widehat{T}_e \\ &= \frac{m_e}{m_i}\frac{\rho_\star \nu_\star}{\varepsilon^2}\frac{\widehat{n}^2}{\widehat{T}_e^{3/2}}\left(0.51\left(\widehat{u}_{e_\parallel} - \widehat{u}_{i_\parallel}\right)\widehat{u}_{i_\parallel} + 3\left(\widehat{T}_e - \widehat{T}_i\right)\right) \end{aligned}} \tag{2.120}$$

$$\boxed{\begin{aligned} &\partial_{\widehat{t}}\left(\frac{3}{2}\widehat{p}_e\right) + \widehat{\boldsymbol{\nabla}} \cdot \left(\frac{5}{2}\widehat{p}_e\widehat{\mathbf{u}}_e\right) - \widehat{\boldsymbol{\nabla}}_\perp \cdot \left(\frac{5}{2}\frac{\widehat{p}_e}{\widehat{B}}\mathbf{b} \times \widehat{\boldsymbol{\nabla}}_\perp \widehat{T}_e\right) + 0.71\widehat{T}_e\widehat{\nabla}_\parallel\left(\widehat{n}\left(\widehat{u}_{e_\parallel} - \widehat{u}_{i_\parallel}\right)\right) \\ &= -0.71\widehat{\boldsymbol{\nabla}} \cdot \left(\widehat{p}_e\left(\widehat{\mathbf{u}}_{e_\parallel} - \widehat{\mathbf{u}}_{i_\parallel}\right)\mathbf{b}\right) + \widehat{n}\widehat{\mathbf{u}}_e \cdot \widehat{\boldsymbol{\nabla}}\widehat{\phi} \\ &\quad - \frac{m_e}{m_i}\frac{\rho_\star \nu_\star}{\varepsilon^2}\frac{\widehat{n}^2}{\widehat{T}_e^{3/2}}\left(3\left(\widehat{T}_e - \widehat{T}_i\right) + 0.51\widehat{u}_{i_\parallel}\left(\widehat{u}_{e_\parallel} - \widehat{u}_{i_\parallel}\right)\right) + \frac{m_i}{m_e}\frac{\varepsilon^2}{\rho_\star \nu_\star} 3.16\widehat{\boldsymbol{\nabla}}_\parallel \cdot \left(\widehat{T}_e^{5/2}\widehat{\boldsymbol{\nabla}}_\parallel \widehat{T}_e\right) \end{aligned}} \tag{2.121}$$

$$\boxed{\widehat{\mathbf{u}}_s = \widehat{u}_{s_\parallel}\mathbf{b} + \widehat{\mathbf{u}}_{s_\perp}^{(1)} + \widehat{\mathbf{u}}_{s_\perp}^{(2)}} \tag{2.122}$$

$$\boxed{\widehat{\mathbf{u}}_{s_\perp}^{(1)} = \widehat{\mathbf{u}}_\perp^{E\times B} + \widehat{\mathbf{u}}_{s_\perp}^\star} \tag{2.123}$$

$$\boxed{\widehat{\mathbf{u}}_{i_\perp}^{(2)} = \widehat{\mathbf{u}}_{i_\perp}^{\rm centr} + \widehat{\mathbf{u}}_{i_\perp}^{\rm pol} + \widehat{\mathbf{u}}_{i_\perp}^{\rm R_i} + \widehat{\mathbf{u}}_{i_\perp}^{\rm vis} + \widehat{\mathbf{u}}_{i_\perp}^{\rm FLR}} \tag{2.124}$$

$$\boxed{\widehat{\mathbf{u}}_{e_\perp}^{(2)} = \widehat{\mathbf{u}}_{e_\perp}^{\rm centr} + \widehat{\mathbf{u}}_{e_\perp}^{\rm vis} + \widehat{\mathbf{u}}_{e_\perp}^{\rm R_e}} \tag{2.125}$$

The consistency of this final set of drift-ordered equations requires further investigations. In particular, the conservation of physical quantities such as the total energy would have to be checked.

Further hypothesis: In the following and as in most of edge turbulence fluid codes, most of these second order drifts will be neglected in our models. In fact, only the polarization drift and the first term of the FLR drift - which leads to the so-called diamagnetic cancellation - are kept:

$$\widehat{\mathbf{u}}_{i_\perp}^{(2)} = \frac{1}{\widehat{n}\widehat{B}}\left[\partial_{\widehat{t}}\left(\widehat{n}\,\mathbf{b} \times \widehat{\mathbf{u}}_{i_\perp}^{(1)}\right) - \widehat{n}\left(\widehat{\boldsymbol{\nabla}} \cdot \widehat{\mathbf{u}}_i\right)\widehat{\mathbf{u}}_{i_\perp}^{(1)} \times \mathbf{b} - \left(\left(\widehat{\mathbf{u}}_i \cdot \widehat{\boldsymbol{\nabla}}\right)\widehat{n}\widehat{\mathbf{u}}_{i_\perp}^{(1)}\right) \times \mathbf{b} - \widehat{n}\left(\widehat{\mathbf{u}}^\star \cdot \widehat{\boldsymbol{\nabla}}_\perp\right)\left(\mathbf{b} \times \widehat{\mathbf{u}}_{i_\perp}^{(1)}\right)\right] \tag{2.126}$$

$$\widehat{\mathbf{u}}_{e_\perp}^{(2)} = 0 \tag{2.127}$$

Such reduction of second order drifts is a large approximation which is not fully justifiable within the ordering used. This derivation and this ordering of full Braginskii's fluid equations should be used as a starting point for future improvements of Tokam2D and Tokam3X equations.

2.5 3D turbulence model in realistic geometry: Tokam3X

2.5.1 Presentation of the model

Tokam3X is a first principle 3D turbulence fluid code for edge plasma. The main specificity of Tokam3X within the edge plasma modelling community is its ability to be run in flexible and realistic geometry. The code solves drift fluid equations based on Braginskii's closure detailed in the previous sections with some simplifications. First, although an anisothermal version of the code is now available [Baudoin 18], we focus in this work only on the isothermal version of Tokam3X in which ion and electron temperatures are assumed to be constant in space and time: $\widehat{T}_e = \widehat{T}_i = 1$. The balance equations solved by the code are: the ion density equation (2.128), the ion parallel momentum equation (2.129), the vorticity equation (2.130), the Ohm's law (2.131) as well as the generalized vorticity expression (2.132).

$$\partial_t \widehat{n} + \widehat{\boldsymbol{\nabla}} \cdot \left(\widehat{\Gamma}_{i_\parallel} \mathbf{b} + \widehat{n} \widehat{\mathbf{u}}_\perp^{E\times B} \right) = \widehat{\boldsymbol{\nabla}} \cdot \left(D_N \widehat{\boldsymbol{\nabla}}_\perp \widehat{n} \right) + S_N \tag{2.128}$$

$$\partial_t \widehat{\Gamma}_{i_\parallel} + \widehat{\boldsymbol{\nabla}} \cdot \left(\widehat{\Gamma}_{i_\parallel} \widehat{u}_{i_\parallel} \mathbf{b} + \widehat{\Gamma}_{i_\parallel} \widehat{\mathbf{u}}_\perp^{E\times B} \right) = -\widehat{\nabla}_\parallel \left(\widehat{p}_i + \widehat{p}_e \right) + \widehat{\boldsymbol{\nabla}} \cdot \left(D_{\Gamma_i} \widehat{\boldsymbol{\nabla}}_\perp \widehat{\Gamma}_{i_\parallel} \right) + S_{\Gamma_i} \tag{2.129}$$

$$\partial_t \widehat{W} + \widehat{\boldsymbol{\nabla}} \cdot \left(\widehat{W} \widehat{u}_{i_\parallel} \mathbf{b} + \widehat{W} \widehat{\mathbf{u}}_\perp^{E\times B} + \widehat{W} \widehat{\mathbf{u}}_{i_\perp}^{\nabla B} \right) = \widehat{\boldsymbol{\nabla}} \cdot \left(\widehat{n} \left(\widehat{\mathbf{u}}_{i_\perp}^{\nabla B} - \widehat{\mathbf{u}}_{e_\perp}^{\nabla B} \right) \right) + \widehat{\boldsymbol{\nabla}} \cdot \left(\widehat{j}_\parallel \mathbf{b} \right) + \widehat{\boldsymbol{\nabla}} \cdot \left(D_W \widehat{\boldsymbol{\nabla}}_\perp \widehat{W} \right) + S_W \tag{2.130}$$

$$\eta_\parallel \widehat{n} \widehat{j}_\parallel = \widehat{T}_e \widehat{\nabla}_\parallel \widehat{n} - \widehat{n} \widehat{\nabla}_\parallel \widehat{\phi} \tag{2.131}$$

$$\widehat{W} = \widehat{\boldsymbol{\nabla}} \cdot \left(\frac{1}{\widehat{B}^2} \widehat{\boldsymbol{\nabla}}_\perp \widehat{\phi} + \frac{1}{\widehat{n}\widehat{B}^2} \widehat{\boldsymbol{\nabla}}_\perp \widehat{p}_i \right) \tag{2.132}$$

where $\widehat{\Gamma}_{i_\parallel} = \widehat{n} \widehat{u}_{i_\parallel}$ is the ion parallel flux.

Some hypothesis have been made compared to the final set of fluid equations obtained in section 2.4.3:

- Sources have been added to ion density, ion parallel momentum and vorticity balances. It permits to simulate the edge plasma under a flux-driven approach in which no scale separation is assumed between equilibrium and fluctuations. These source terms are poloidally and toroidally symmetric volumetric sources located near the inner radial boundary with a Gaussian shape in the radial direction. We consider usually that these sources model the particle and momentum fluxes incoming from central plasma.

- Diffusive terms are also added to ion density, ion parallel momentum and vorticity balances. Such terms are necessary from the numerical point of view but also represent dissipations at scales smaller than mesh grid. Diffusive coefficients D_N, D_{Γ_i} and D_W are typically of the order $5 \times 10^{-3} \rho_{\mathrm{L_i}} c_{\mathrm{s0}}$ in our simulations which corresponds to $5 \times 10^{-2} \mathrm{m}^2.\mathrm{s}^{-1}$ at the LCFS of Tore Supra.

- The diamagnetic drift $\widehat{\mathbf{u}}_{s_\perp}^\star$ is substituted in Tokam3X by the curvature drift $\widehat{\mathbf{u}}_{s_\perp}^{\nabla B}$. It can be shown that the divergence of these two drifts is equal when the diamagnetic cancellation term coming from the FLR Braginskii's tensor is taken into account.

- Ion density and parallel momentum equations are stopped at largest order due to numerical considerations. In particular, one can see that the divergence of the flux associated to the ∇B-drift - a second order term - is not appearing in these two equations.

- A Boussinesq approximation is realized in the charge conservation equation in order to obtained the vorticity evolution equation and the vorticity formulation. It consists in substituting the normalized density by the reference density n_0 so that the effect of the density gradient is not taken into account in the vorticity expression.

- The parallel resistivity $\eta_\parallel = (m_e/m_i)\, 0.51 \rho_\star \nu_\star \widehat{T_e}^{-3/2}$ used in Ohm's law (2.131) is a constant in time and space and does not depend on density or electron temperature in our model. The expected value at LCFS for Tore Supra is about $10^{-6} B_0/(en_0)$ while we used usually $\eta_\parallel = 10^{-5} B_0/(en_0)$ to limit the numerical cost of our simulations. Indeed, small values of the parallel resistivity lead to a badly conditioned operator in the inversion of the vorticity.

Numerical aspects of Tokam3X code are not the main purpose of this thesis and are consequently not detailed. These informations can be found in [Tamain 16].

2.5.2 Magnetic configuration

Tokam3X is an electrostatic code such that the fluctuations of magnetic field are not taken into account. The magnetic field is thus fixed and is an input parameter of the code. This magnetic equilibrium is assumed to be toroidally symmetric and can be described using a 2D map corresponding to the poloidal plane. Two input parameters determined this magnetic equilibrium: a toroidal flux number $F = B_0 R_0$ and a poloidal flux function $\psi(R, Z) = r\psi_0/a$ where (R, Z, φ) is a fixed cylindrical coordinates system and φ the toroidal angle. The magnetic field is computed according to the following formula:

$$\mathbf{B} = B\mathbf{b} = F\nabla\varphi + \nabla\psi \times \nabla\varphi \tag{2.133}$$

According to equation (2.133), iso-ψ are tangent to the magnetic field and ψ labels each flux surface. The mesh used in Tokam3X is flux-surface aligned and the metric of the system is ensured by the use of covariant and contravariant basis associated to the curvilinear system of coordinates $\left(\psi, \widehat{\theta}, \varphi\right)$ where $\widehat{\theta}$ is a curvilinear abscissa along magnetic flux surface in the poloidal plan (R, Z). The covariant $\left(\mathbf{e}_\psi, \mathbf{e}_{\widehat{\theta}}, \mathbf{e}_\varphi\right)$ and contravariant $\left(\mathbf{e}^\psi, \mathbf{e}^{\widehat{\theta}}, \mathbf{e}^\varphi\right)$ basis are defined - for a position vector $\mathbf{r}$ with respect to an arbitrary origin point - by:

$$\mathbf{e}_\psi = \partial_\psi \mathbf{r}; \qquad \mathbf{e}_{\widehat{\theta}} = \partial_{\widehat{\theta}} \mathbf{r}; \qquad \mathbf{e}_\varphi = \partial_\varphi \mathbf{r}; \qquad [\mathbf{e}_i] = [\mathrm{m}] \tag{2.134}$$

$$\mathbf{e}^\psi = \nabla\psi; \qquad \mathbf{e}^{\widehat{\theta}} = \nabla\widehat{\theta}; \qquad \mathbf{e}^\varphi = \nabla\varphi; \qquad [\mathbf{e}^i] = [\mathrm{m}^{-1}] \tag{2.135}$$

In such covariant basis, the magnetic field (2.133) writes:

$$\mathbf{B} = B_{\mathrm{pol}} \frac{\mathbf{e}_{\widehat{\theta}}}{|\mathbf{e}_{\widehat{\theta}}|} + B_{\mathrm{tor}} \frac{\mathbf{e}_\varphi}{|\mathbf{e}_\varphi|} \tag{2.136}$$

where B_{pol} and B_{tor} are respectively the poloidal and toroidal components of the magnetic field and $B_{\mathrm{pol}} \ll B_{\mathrm{tor}}$ in tokamaks. The amplitudes of poloidal and toroidal magnetic field determine the magnetic equilibrium through the cylindrical safety factor q_{cyl}:

$$q_{\mathrm{cyl}}(\psi) = < \frac{rB_{\mathrm{tor}}}{RB_{\mathrm{pol}}} >_{\widehat{\theta}} = \frac{1}{2\pi}\oint \frac{rB_{\mathrm{tor}}}{RB_{\mathrm{pol}}} |\mathbf{e}_{\widehat{\theta}}| d\widehat{\theta} \tag{2.137}$$

2.5.3 Flexible geometry

Tokam3X models a toroidal ring of edge plasma between two radii r_{min} and r_{max}. In all this manuscript, these two radii are chosen symmetric with respect to the minor radius a and we use $r_{\mathrm{min}}/a = 0.8$ and $r_{\mathrm{max}}/a = 1.2$ such as both open and closed field lines are taken into account. The divertor configuration requires a more complex system of coordinates which is not detailed in this thesis as no divertor simulations are presented. As said previously, Tokam3X can be run in any axisymmetric magnetic equilibrium. We focus on three magnetic configurations: the slab configuration, circular concentric flux surfaces obtained with limiter configuration and complex and realistic shape including an X-point for divertor configurations. For a given magnetic configuration, three geometrical input parameters control the shape and size of the simulated plasma: the ratio between ion Larmor radius (smallest scale of the model) and the minor radius, $\rho_\star = \rho_{L_{i_0}}/a$ and the aspect ratio $\mathcal{A} = R_0/a$. The last control parameter is the angular length of the toroidal periodic direction L_φ: in order to reduce the numerical cost of our simulation only a fraction of the toroidal ring is simulated and the remaining part of the torus is assumed to be periodic.

Limiter configuration: This is the standard and most studied configuration of Tokam3X until recently. An infinitely thin vertical wall usually at the bottom of the poloidal plane constitutes the toroidal limiter. The position $\widehat{\theta} = 0$ corresponds to the outboard LFS midplane and increases in the electron diamagnetic direction. The limiter is thus located at $\widehat{\theta} = -90°$. Geometric parameters used in limiter configuration is $\rho_\star^{-1} = 256$ and an aspect ratio $\mathcal{A} = 3.75$. Simulations are made for a quarter of the torus in the toroidal direction. In the standard reference case, the cylindrical safety factor increases radially from 3 at the inner core region up to 6 in the outer SOL region. Concerning the grid, the resolution of the mesh used during this work is: $(N_\psi, N_\theta, N_\varphi) = (64, 512, 32)$.

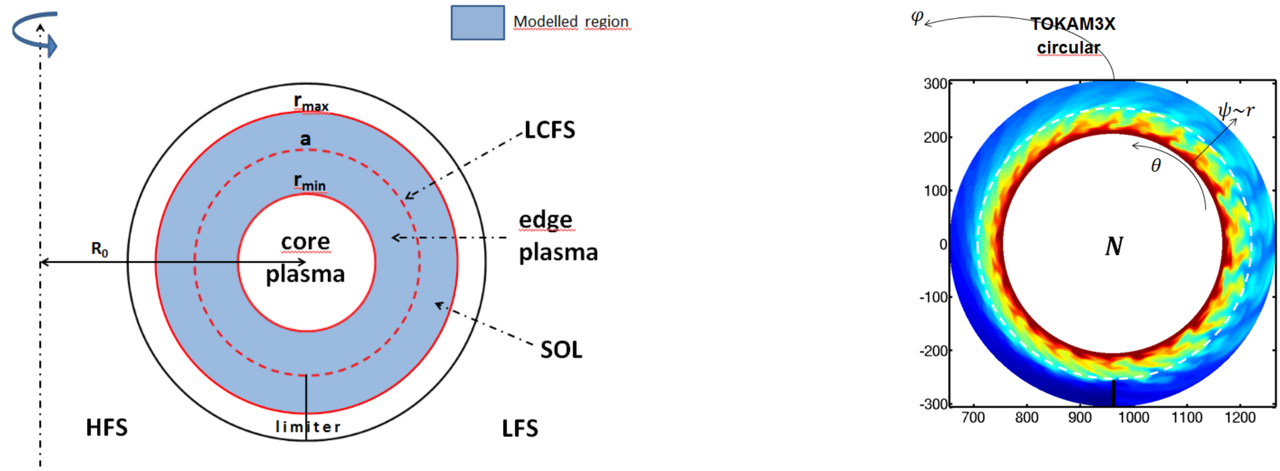

Figure 2.2:
Left panel: Scheme of the modelled region of the poloidal plane for circular configuration of Tokam3X.
Right panel: Example of a snapshot of the density field in circular configuration.

Slab configuration: This is the simplest configuration of Tokam3X. In order to obtain a slab configuration, the major radius R_0 is artificially multiplied by a large number, typically 10^6. The angular toroidal length L_φ has to be divided by the same large number in order to keep finite volumes of the mesh not too stretched which permits to avoid numerical issues. With such a large aspect ratio and such small toroidal length, magnetic field lines are purely toroidal and the poloidal magnetic field vanishes. The simulated box - see Figure 2.3 - is then an orthogonal rectangular cuboid, its square section corresponds to a fraction of the poloidal plane around LFS midplane and its width is the toroidal and magnetic field direction. Periodic boundary conditions are assumed in the vertical - poloidal - direction and the limiter is now a poloidal limiter at the extremities of the toroidal direction in open field lines. With such geometry, the radial variation of the toroidal magnetic field is negligible. Without the magnetic field curvature, the interchange driven turbulence cannot develop in the simulations. An effective magnetic field curvature g - constant in our model - is added in order to obtain interchange-driven turbulence. This same parameter is used in Tokam2D, and its definition is given in 2.6.1.1.

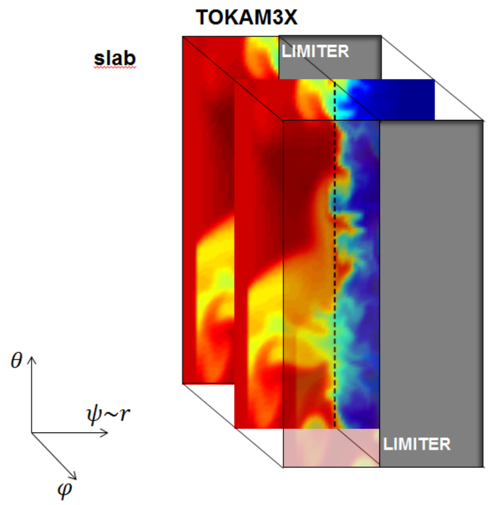

Figure 2.3: Scheme of the slab configuration with a snapshot of the density field resulting from Tokam3X slab simulation.

Divertor configuration: This is the most complex magnetic configuration used up to now in Tokam3X. This configuration was not directly part of the work of this thesis such as only a brief introduction to such configuration is presented. This configuration is mentioned because some general results obtained in such configuration are discussed on Chapter 5 and compared to simulations in circular limiter geometry. This complex configuration exhibits a X-point as it can be seen on Figure 2.4. Moreover, flux surfaces are no longer circular and and strongly poloidally varying flux expansion can be observed in such configuration.

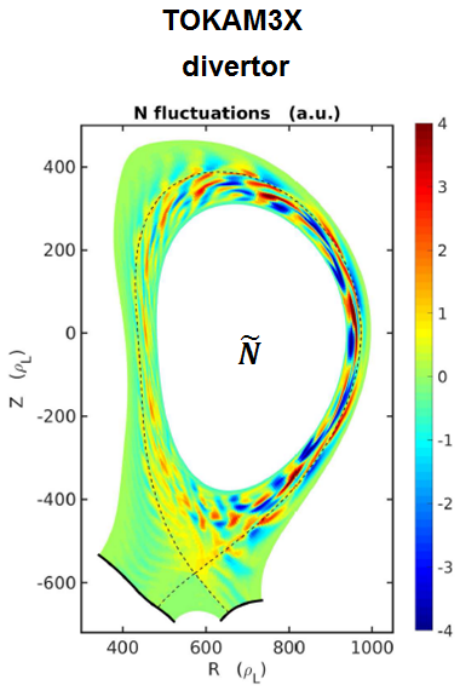

Figure 2.4: Example of density fluctuations resulting from divertor X-point configuration in a COMPASS-like configuration.

2.5.4 Boundary conditions

Finally, we briefly detailed the conditions used at the boundaries of the simulated plasma:

Toroidal periodicity: Only a quarter of the torus is modelled in circular configuration in order to reduce the numerical cost of our simulations. Such approximation modifies the modes described in our simulations which can impact on the simulations as shown in Chapter 5.

Inner and outer radial boundaries: homogeneous Neumann boundary conditions are used on all fields at the inner and outer radial boundaries. Combined with a buffer zone which enhances strongly the poloidal diffusion, it avoids the existence of inward or outward spurious radial fluxes at these boundaries.

Walls-Targets: In a linearised version, the Bohm-Chodura boundary conditions [Stangeby 95] lead to:

$$\widehat{j}_{\|} = \pm \widehat{n} \left(\Lambda - \widehat{\phi} \right) \tag{2.138}$$

By combining with the Ohm's law, we obtained:

$$\widehat{\nabla}_{\|} \widehat{\phi} = \widehat{T}_e \frac{\widehat{\nabla}_{\|} \widehat{n}}{\widehat{n}} \pm \eta_{\|} \widehat{n} \left(\Lambda - \widehat{\phi} \right) \tag{2.139}$$

The code also imposes sonic conditions: $|\widehat{\Gamma_{i_\parallel}}| \geq \widehat{n}$, a free boundary on the density: $\partial^2_{\widehat{\theta}}\widehat{n} = 0$ and $\partial_{\widehat{\theta}}\widehat{W} = 0$.

2.6 Reduced 2D turbulence model in slab geometry: Tokam2D

Tokam2D models turbulence generated by the interchange instability in edge plasmas. The simulated domain is representative of the edge region around Low-Field Side midplane. The geometric configuration is slab, meaning that the simulated box has a rectangular shape where $x = (r-a)/\rho_L$ and $y = a\theta/\rho_L$ are respectively the radial and poloidal directions. The flute hypothesis ($k_\parallel = 0$) is used to reduce the model from 3D to 2D. Under this assumption, parallel transport is described only by integrating all fields along magnetic field lines (FL). For any field F it writes: $< F >_{FL} = \frac{1}{2L_\parallel}\int_{-L_\parallel}^{L_\parallel} F dz$ where z corresponds to the curvilinear abscissa along magnetic field lines. All fields are thus assumed to be homogeneous in the parallel direction (for example $< N >_{FL} = N$) and only terms linked to the parallel transport lead to additional loss terms in open field lines resulting from Bohm sheath boundary conditions. The pitch angle of the magnetic field is neglected such that the toroidal direction corresponds to the parallel one. However a curvature term - motor of the interchange instability - is required and added in order to develop interchange turbulence. Tokam-2D model is thus very simple and can be seen as the minimal model to obtain interchange turbulence. Finally, as in Tokam3X, the flux-driven approach is ensured by a poloidally uniform Gaussian particle source close to the inner radial boundary.

2.6.1 Previous versions

Here, we detailed briefly the two previous versions of Tokam2D.

2.6.1.1 Isothermal version

Historically, the first - and most used - version of Tokam2D is an isothermal model with cold ions ($T_e = 1$,$T_i = 0$). This version was created analytically in 1991 [Garbet 91] and developed numerically in 1998 [Sarazin 98]. The goal was originally to explain the existence of turbulence in the SOL and this version focuses thus only in the open field line region. The equations solved by the code are the electron density conservation and the charge balance:

$$\partial_t N + [\phi, N] - D_N \nabla^2_\perp N = S_N - \sigma N \exp\{(\Lambda - \phi)\} \tag{2.140}$$

$$\partial_t W + [\phi, W] - \nu \nabla^2_\perp W = -\frac{g}{N}\partial_y N + \sigma\left(1 - \exp\{(\Lambda - \phi)\}\right) \tag{2.141}$$

where:

- $W = \nabla^2_\perp \phi$ is the vorticity
- $[\phi, \cdot] = \partial_x\phi\partial_y \cdot - \partial_y\phi\partial_x \cdot$ corresponds to the Poisson bracket representing advection by $E \times B$ drift velocity.
- In each equation, the last term corresponds to parallel losses resulting from the flute hypothesis. $\Lambda = \frac{1}{2}\ln\frac{m_i}{2\pi m_e}$ is the normalized sheath potential drop while the level of parallel losses is deter-

mined by the control parameter $\sigma = \rho_L/L_\parallel$ corresponding to the sheath conductivity. The term $\exp\{(\Lambda - \phi)\}$ corresponds to the screening effect of slow electrons by the sheath.

- D_N and ν are transverse dissipative coefficients representing respectively diffusion and viscosity.
- S_N is the Gaussian particle source ensuring the flux-driven approach.
- The g coefficient represents the magnetic field curvature and is rigorously defined as: $g = [(1+s)\sin\Delta\theta - s\Delta\theta\cos\Delta\theta]\, 2q\rho_L/L_\parallel$ where $\Delta\theta$ corresponds to the angle between the two limiter at the extremities of the parallel direction, and s is the magnetic shear defined in Chapter 1. Note that the interchange instability is analogous to the Rayleigh-Bénard instability in which the g coefficient is equivalent to the gravity.

Another specificity of this historical version is that both radial and poloidal directions are periodic. If the poloidal periodicity is straightforward to justify, the radial periodicity can be puzzling at first sight. In fact, the left hand side of the Gaussian source is stable for the interchange instability such that the turbulent events crossing the outer radial periodic boundary are damped before impacting the center of the particle source. Such hypothesis on radial periodicity leads to a constraint on profiles especially for the electrostatic potential. However, in the isothermal model, the mean electrostatic potential is expected to be constant and equal to the sheath potential drop Λ so that this constrain does not impact significantly the simulation. The bi-periodicity is set up in order to simplify and optimise the numerical part of the code. Indeed, bi-periodic boundaries permit the use of a pseudo-spectral scheme based on Fast Fourier Transforms (FFT) which are far more accurate than traditional finite differences on low resolution grids used at that time.

2.6.1.2 First anisothermal cold ions version

A first anisothermal version of Tokam2D was developed in 2014 and presented in [Moulton 14] as an extension of the isothermal model. The main goal of this code modification was to study the correlations between electron temperature and density fluctuations in the SOL. The model included thus the electron heat balance while ions are still assumed to be cold ($T_i = 0$). The code was strongly modified in order to overcome the hypothesis on radial and poloidal periodicities. The code becomes fully explicit and a MUSCL scheme is used for advective terms. This scheme is expected to be fully efficient to deal with discontinuities, shocks and large gradients [van Leer 79]. The three equations solved by this version are:

$$\partial_t N + [\phi, N] - D_N \nabla_\perp^2 N = S_N - \sigma N \sqrt{T_e} \exp\Big\{(\Lambda - \frac{\phi}{T_e})\Big\} \tag{2.142}$$

$$\partial_t W + [\phi, W] - \nu \nabla_\perp^2 W = -\frac{g}{N}\partial_y P_e + \sigma\sqrt{T_e}(1 - \exp\Big\{(\Lambda - \frac{\phi}{T_e})\Big\}) \tag{2.143}$$

$$\partial_t \frac{3}{2} P_e + \frac{3}{2}[\phi, P_e] - \frac{3}{2}\chi_e \nabla_\perp^2 P_e = T_e^{\mathrm{inj}} S_N - \gamma_e \sigma P_e \sqrt{T_e} \exp\Big\{(\Lambda - \frac{\phi}{T_e})\Big\} \tag{2.144}$$

One can observe that the electron density and charge balance equations are quite similar to the isothermal model. The only differences are that the effect of electron temperature is taken into account in parallel losses both in $c_s = \sqrt{T_e}$ and in the exponential term such as the mean electrostatic potential is now expected to be equal to ΛT_e. The additional equation is the electron intern energy balance and is really similar to the electron density balance. The electron heat source is located at the same position that the particle one and the source amplitude is controlled by the electron injection temperature parameter T_e^{inj}. The parameter γ_e corresponds to the electron sheath heat transmission coefficient.

2.6.2 New full anisothermal version

At the beginning of this thesis, several recent results pointed out the role of the ion heat channel on L-H transition and more generally on transport barrier formation and dynamics both experimentally [Ryter 14] and from 2D modelling with the HESEL code [Nielsen 15]. The idea was thus to include the ion energy channel to Tokam2D model. Starting from the anisothermal cold ions version, the addition of the ion internal energy evolution equation (2.148) is straightforward as identical to the electron one (2.147). However, the ion energy channel has also an impact on the vorticity formulation and leads to the generalized vorticity: $W = \nabla_\perp^2 \phi + \boldsymbol{\nabla} \cdot (\frac{1}{N} \boldsymbol{\nabla}_\perp P_i)$. This formulation creates an additional coupling between density, electrostatic potential through the ion channel such that the computation of the electrostatic potential from other fields is more complex from numerical point of view. It turns out that the MUSCL scheme was not adapted to solve the new system of fluid equations due to a compensation between transverse components of drift velocities which leads to a checkerboard numerical instability as presented in Figure 2.5.

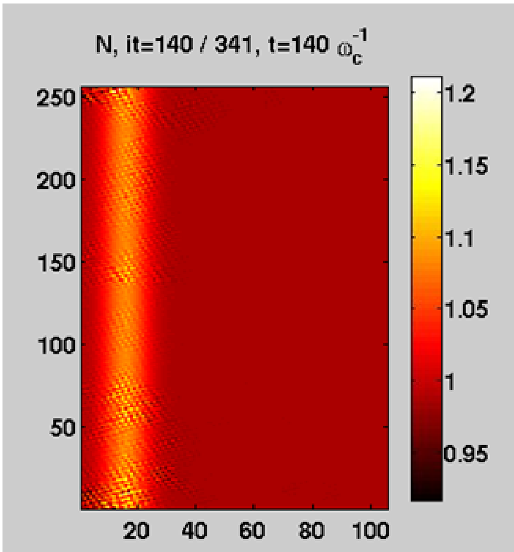

Figure 2.5: Example of the checkerboard instability appearing in the first anisothermal version when the generalized vorticity was included and leading to the crash of the simulation.

The anisothermal cold ions version also presented several drawbacks: the code was not written clearly for the users and the computation time was not optimised. As a consequence, I choose to develop a new version from scratch, including the evolution of both electron and ion energies in order to study the impact of the ion energy channel on edge transport. The full anisothermal model solved by this new version is:

$$\partial_t N + [\phi, N] - D_N \nabla_\perp^2 N = S_N + \mathcal{L}_N \tag{2.145}$$

$$\partial_t W + [\phi, W] - \nu \nabla_\perp^2 W = -\frac{g}{N}\partial_y (P_e + P_i) + \mathcal{L}_W \tag{2.146}$$

$$\partial_t \frac{3}{2} P_e + \frac{3}{2}[\phi, P_e] - \frac{3}{2}\chi_e \nabla_\perp^2 P_e = T_e^{\text{inj}} S_N + \mathcal{L}_e \tag{2.147}$$

$$\partial_t \frac{3}{2} P_i + \frac{3}{2}[\phi, P_i] - \frac{3}{2}\chi_i \nabla_\perp^2 P_i = T_i^{\text{inj}} S_N + \mathcal{L}_i \tag{2.148}$$

$$W = \nabla_\perp^2 \phi + \boldsymbol{\nabla} \cdot \left(\frac{1}{N} \boldsymbol{\nabla}_\perp P_i\right) \tag{2.149}$$

where χ_e and χ_i are transverse dissipative coefficients representing electron and ion heat conductions and γ_i is the ion sheath heat transfer coefficients. Note that the ion and electron sheath heat transfer coefficients can be either taken constant (as in most of fluid codes) or calculated self-consistently from local plasma parameters using an analytical derivation detailed in Appendix B. The terms $\mathcal{L}$ corresponds to the losses in the parallel direction which differ for open and closed field lines:

$$\mathcal{L}_N = \begin{cases} -\sigma N \sqrt{T_e + T_i} \exp\left\{\left(\Lambda - \dfrac{\phi}{T_e}\right)\right\} & \text{in open field lines (OFL)} \\ 0 \quad \text{in closed field lines (CFL)} \end{cases} \tag{2.150}$$

$$\mathcal{L}_W = \begin{cases} +\sigma \sqrt{T_e + T_i} \left(1 - \exp\left\{\left(\Lambda - \dfrac{\phi}{T_e}\right)\right\}\right) & \text{OFL} \\ \sigma \left(c_s \phi - < c_s \phi >_y\right) \quad \text{CFL} \end{cases} \tag{2.151}$$

$$\mathcal{L}_e = \begin{cases} -\gamma_e \sigma P_e \sqrt{T_e + T_i} \exp\left\{\left(\Lambda - \dfrac{\phi}{T_e}\right)\right\} & \text{OFL} \\ 0 \quad \text{CFL} \end{cases} \tag{2.152}$$

$$\mathcal{L}_i = \begin{cases} -\gamma_i \sigma P_i \sqrt{T_e + T_i} & \text{OFL} \\ 0 \quad \text{CFL} \end{cases} \tag{2.153}$$

In closed field lines, due to the periodicity in the parallel/toroidal direction, all these sinks terms are vanishing except for the vorticity equation in which a damping on non-mean flow ($k_y \neq 0$) is required to avoid the unphysical development of structures of the size of the whole simulated closed field lines region.

Concerning boundary conditions, all radial fluxes are forced to zero at boundaries with Neumann conditions. The only losses of charges are through the parallel direction and current circulating through limiter plates. In order to keep charge conservation and not polarized the plasma, this net current lost in the limiter are reinjected in all simulation by adjusting the mean electrostatic potential.

For advective terms, we choose to use a WENO scheme as it is done in Tokam3X. Such high resolution scheme can outperform MUSCL scheme especially around discontinuities and provides high order accuracy in smooth regions [Shu 09]. This new full thermal version of the code has been parallelized by OpenMP and leads to a strong improvement of a simulation duration as displayed in Figure 2.6. Indeed, even without OpenMP parallelization, the code is found with the full thermal model to be faster that the historical isothermal FFT version of the Tokam2D code. The increase of the OpenMP threads leads to a drop of computational time.

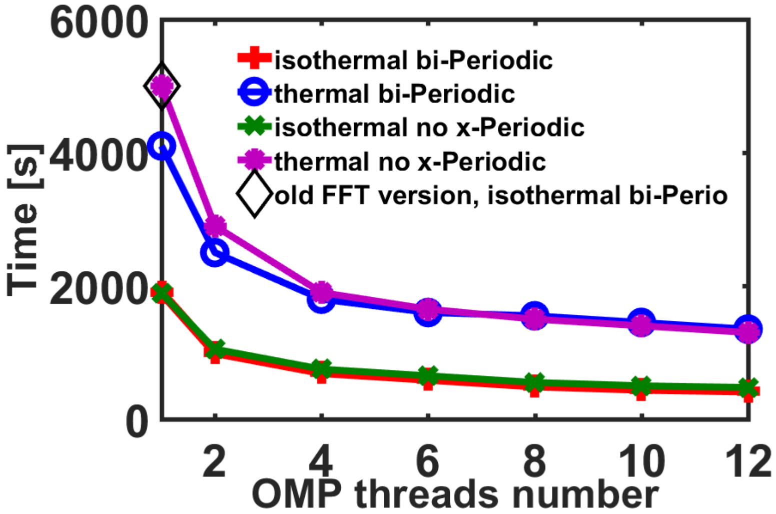

Figure 2.6: For mesh grid of $(N_x, N_y) = (256 \times 256)$, time required for a standard Tokam2D simulation of 50.000 iterations with the same time step as a function of the number of OpenMP threads for the bi-periodic FFT version (black triangle) and the new version with isothermal and full anisothermal model and with or without radial periodicity.

In conclusion, the drift ordered Braginskii fluid equations have been fully derived with a special attention on all the assumptions made during the procedure. A new exact formulation for the divergence of the Finite Larmor Radius part of the Braginskii tensor is found. The final hypothesis made to obtain Tokam2D and Tokam3X model equations have been highlighted as well as the specificity of the two codes in terms of geometry and magnetic configuration. In particular, a new thermal version including ion energy channel has been developed during this thesis. Such analytical work must be seen as a preliminary step for future improvement of both Tokam2D and Tokam3X models.

Chapter 3

Driven transport barriers in the Scrape-Off-Layer in 2D turbulence slab simulations

It is exceptional that one should be able to acquire the understanding of a process without having previously acquired a deep familiarity with running it, with using it, before one has assimilated it in an instinctive and empirical way.

John von Neumann

Any mechanism able to modify turbulence properties appears to be of great interest for the control of edge plasma transport and thus for tokamak operations. In this chapter, two mechanisms able to generate transport barriers - the $\mathbf{E}\times\mathbf{B}$ shear and its gradient, the $\mathbf{E}\times\mathbf{B}$ curvature - are compared, implemented in our 2D slab model and analysed. We focus exclusively on the isothermal cold ions version of Tokam2D in the open field lines region. We first analyse properties of 2D interchange driven turbulence in the Scrape-Off-Layer and compare them qualitatively - when it is possible - with edge plasma experimental measurements. Then, the two mechanisms are detailed from theoretical point of view as well as their numerical implementation in Tokam2D. Finally, transport barriers generated by these two mechanisms are characterized using a criterion so-called barrier efficiency which measures the capability of a flux surface to stop the radial propagation of turbulence.

3.1 Main characteristics of 2D interchange turbulence in Tokam2D

3.1.1 Linear analysis of the interchange instability

The linear growth rate of the interchange instability in Tokam2D can be analytically calculated as a function of radial and poloidal wave numbers. For that, we study the plasma response to a small perturbation of the equilibrium state. Within this small perturbations limit, the non-linear terms involved in the evolution equations are negligible which means that a scale separation can be assumed between equilibrium and fluctuations. Any field F is split between equilibrium and fluctuating parts: $F = F_{\mathrm{eq}} + \widetilde{F}$ with $F_{\mathrm{eq}} = \langle F\rangle_{t,y}$ and $\widetilde{F} \ll F_{\mathrm{eq}}$. The equilibrium state of Tokam2D is assumed to depend only of the radial direction:

$$\partial_y \phi_{\mathrm{eq}} = \partial_y n_{\mathrm{eq}} = \partial_t n_{\mathrm{eq}} = \partial_t \phi_{\mathrm{eq}} = 0 \tag{3.1}$$

In the following, the radial profile of equilibrium density is expected to be an exponential decay in the Scrape-Off-Layer such as $n_{\mathrm{eq}}(x) = n_0 \exp(-x/\lambda_n)$ where n_0 is a reference density and λ_n the density decay length. The equilibrium electrostatic potential is mainly determined by the parallel direction and especially governed by sheath boundary conditions. In the isothermal limit of Tokam2D, Bohm's boundary conditions lead to a flat potential profile in the SOL: $\phi_{\mathrm{eq}} = \Lambda$. In particular, we have:

$$\partial_x \phi_{\mathrm{eq}} = 0\ ,\ \ \partial_x n_{\mathrm{eq}} = -\frac{n_{\mathrm{eq}}}{\lambda_n} \quad \text{and} \quad \partial_x^2 n_{\mathrm{eq}} = \frac{n_{\mathrm{eq}}}{\lambda_n^2} \tag{3.2}$$

The consistency of density and potential equilibrium profiles shapes will be checked afterwards in this section.

In the Fourier-Laplace transform framework, a mode $k = (\Omega_k, k_x, k_y)$ - respectively frequency, radial and poloidal wave numbers of the mode - is selected. The mode becomes unstable when its linear growth rate becomes positive: $\gamma_k = \mathrm{Re}(\Omega_k) > 0$. The perturbation of the equilibrium writes:

$$\begin{pmatrix} \widetilde{n}_k \\ \\ \\ \widetilde{\phi}_k \end{pmatrix} = \begin{pmatrix} \widetilde{n}_{k_x,k_y} \\ \\ \\ \widetilde{\phi}_{k_x,k_y} \end{pmatrix} \exp\left(i\left(k_x x + k_y y\right)\right) \exp\left(\Omega_k t\right) + \text{complex conjugate} \tag{3.3}$$

The terms involved in the density (2.145) and vorticity (2.146) Tokam2D isothermal evolution equations can be split into equilibrium and fluctuating parts:

$$\begin{cases} \partial_t \left(n_{eq} + \widetilde{n}_k\right) + \left[\phi_{\text{eq}} + \widetilde{\phi}_k, n_{\text{eq}} + \widetilde{n}_k\right] - D_N \nabla_\perp^2 \left(n_{\text{eq}} + \widetilde{n}_k\right) & = -\sigma_N \left(n_{\text{eq}} + \widetilde{n}_k\right)\left(1 - \widetilde{\phi}_k\right) \\ \partial_t \left(\nabla_\perp^2 \phi_{\text{eq}} + \nabla_\perp^2 \widetilde{\phi}_k\right) + \left[\phi_{\text{eq}} + \widetilde{\phi}_k, \nabla_\perp^2 \phi_{\text{eq}} + \nabla_\perp^2 \widetilde{\phi}_k\right] - \nu \nabla_\perp^4 \phi_{\text{eq}} - \nu \nabla_\perp^4 \widetilde{\phi}_k & = -g \frac{\partial_y \left(n_{\text{eq}} + \widetilde{n}_k\right)}{n_{\text{eq}} + \widetilde{n}_k} + \sigma_W \widetilde{\phi}_k \end{cases} \tag{3.4}$$

Using (3.1) and neglecting second order terms - *i.e* products of two fluctuating quantities - the system (3.4) can be simplified into:

$$\begin{cases} \partial_t \widetilde{n}_k - D_N \nabla_\perp^2 \widetilde{n}_k + \sigma_N \widetilde{n}_k - \left(\partial_x n_{\text{eq}}\right) \partial_y \widetilde{\phi}_k + \left(\partial_x \phi_{\text{eq}}\right) \partial_y \widetilde{n}_k - \sigma_N n_{\text{eq}} \widetilde{\phi}_k & = D_N \partial_x^2 n_{\text{eq}} - \sigma_N n_{\text{eq}} \\ \partial_t \nabla_\perp^2 \widetilde{\phi}_k - \left(\partial_x^3 \phi_{\text{eq}}\right) \partial_y \widetilde{\phi}_k + \left(\partial_x \phi_{\text{eq}}\right) \partial_y \left(\nabla_\perp^2 \widetilde{\phi}_k\right) - \sigma_W \widetilde{\phi}_k - \nu \nabla_\perp^4 \widetilde{\phi}_k + g \frac{\partial_y \widetilde{n}_k}{n_{\text{eq}}} & = \nu \partial_x^4 \phi_{\text{eq}} \end{cases} \tag{3.5}$$

Equations on equilibrium fields can be obtained by time averaging equations (3.5). All left hand side terms vanish and it yields:

$$\partial_x^2 n_{\text{eq}} = \frac{\sigma_N}{D_N} n_{\text{eq}} \quad \text{and} \quad \partial_x^4 \phi_{\text{eq}} = 0 \tag{3.6}$$

One can check that the density and potential equilibrium profiles detailed previously are solutions of the ordinary differential equations (3.6) with:

$$\lambda_N = \sqrt{\frac{D_N}{\sigma_N}} \tag{3.7}$$

The remaining part of equations (3.5) is composed of all fluctuation terms. We combined them with perturbation formula (3.3) and hypothesis on equilibrium profiles (3.2) to obtain the following linear system of equations:

$$\begin{pmatrix} \Omega_k + \sigma_N + D_N k_\perp^2 & i \frac{k_y}{\lambda_N} - \sigma_N \\ \\ -ig \frac{k_y}{k_\perp^2} & \Omega_k + \frac{\sigma_W}{k_\perp^2} + \nu k_\perp^2 \end{pmatrix} \begin{pmatrix} \widetilde{n}_k / n_{\text{eq}} \\ \\ \widetilde{\phi}_k \end{pmatrix} = \begin{pmatrix} 0 \\ \\ 0 \end{pmatrix} \tag{3.8}$$

where $k_\perp^2 = k_x^2 + k_y^2$.
The dispersion relation is obtained when the determinant of this matrix vanishes. It yields a second order equation for Ω_k:

$$\Omega_k^2 + b_k \Omega_k + c_k = 0 \tag{3.9}$$

where $b_k = \frac{\sigma_W}{k_\perp^2} + \sigma_N + (D_N + \nu) k_\perp^2$ and $c_k = \left(\sigma_N + D_N k_\perp^2\right)\left(\frac{\sigma_W}{k_\perp^2} + \nu k_\perp^2\right) - \frac{g k_y^2}{\lambda_N k_\perp^2} - ig\sigma_N \frac{k_y}{k_\perp^2}$.
One can notice that b_k is a real strictly positive. The discriminant of this second order equation is $\Delta_k = b_k^2 - 4c_k$ and the analytical growth rate is the real part of the maximal solution of this second order equation:

$$\gamma_k = \text{Re}\left(\Omega_k\right) = \text{Re}\left(\frac{-b_k + \sqrt{\Delta_k}}{2}\right) = -\frac{1}{2} b_k + \frac{1}{2} \text{Re}\left(\sqrt{\Delta_k}\right) \tag{3.10}$$

One can already see that the terms involved in b_k have a stabilizing effect. Small scales are damped by diffusive terms (D_N,ν) while large scales are stabilized by current parallel losses (σ_W). Note also a homogeneous damping at all scales by particle parallel losses (σ_N). On the other hand, destabilization comes from the interplay between the curvature (g) and density gradient (λ_N). Indeed, if we neglect all stabilizing terms (*i.e.* $\sigma_N = \sigma_W = D_N = \nu = 0$), the linear growth rate writes simply $\gamma_k = \sqrt{g/\lambda_N} k_y/k_\perp$.
In the general case, the most unstable mode is found for $k_x = 0$ and a finite value of k_y. The linear growth rate (3.10) is presented on the left panel of Figure 3.1 as a function of the poloidal wave number k_y and for $k_x = 0$. Typical parameter values used for these plots - realistic of edge plasma of medium size tokamaks - are displayed in the Table on the right panel of Figure 3.1 and will constitute our reference case.

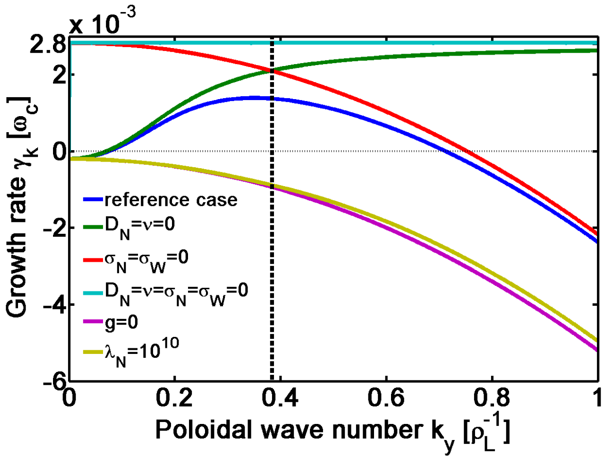

Parameter	g	λ_N	D_N, ν	σ_N, σ_W
Value	6×10^{-4}	75	5×10^{-3}	2×10^{-4}

Figure 3.1:
Left panel: Linear growth rate as a function of poloidal wave number k_y for $k_x = 0$. Parallel losses and diffusive terms stabilized the growth rate while the competition between curvature and density gradient generates the instability.
Right panel: Values of Tokam2D parameters for the reference case.

One can recover the main results mentioned previously:

- Small scales (large k_y) are stabilized by diffusion processes.
- Parallel losses lead to a damping of large scale structures (small k_y).
- All modes become unstable when all these stabilizing terms are suppressed. The growth rate is then constant: $\gamma_k = \sqrt{g/\lambda_N} = 2.8 \times 10^{-3}\omega_c$.
- Interchange is stable at every scale when the curvature **or** the density gradient are quenched.
- The most unstable mode is determined by a competition between small and large scale stabilizations. This mode coincides mostly with the intersection of the cases without diffusion or without parallel losses which corresponds to $k_y^{\max} = (\sigma_W/(D_N + \nu))^{1/4} = 0.38\rho_L^{-1}$.

3.1.2 Transport properties

3.1.2.1 Importance of fluctuations on the equilibrium

The main assumption of the linear analysis approach is the scale separation between equilibrium fields and fluctuations such as these latter do not impact the equilibrium. We confront this hypothesis with 2D slab turbulence simulations obtained with Tokam2D using the same conditions and parameters from Figure 3.1. The density profiles obtained with Tokam2D are presented on the left panel of Figure 3.2. The density profile of the reference case matches nearly perfectly with an exponential decay with $\lambda_N = 75\rho_L$. It validates here again the shape of the equilibrium density profile used in the linear analysis. However, one can notice that the density decay length differs strongly from the theoretical profile obtained in the small perturbation limit where $\lambda_N = \sqrt{D_N/\sigma_N} = 7\rho_L$. The equilibrium must thus have been strongly impacted by fluctuations - *i.e.* turbulence. When running without curvature term (case $g = 0$) and thus without turbulence from interchange instability, Tokam2D simulations recovered the decay length of the small perturbations limit which confirms the key role played by fluctuations on equilibrium state. The radial profile of the relative fluctuation level $\text{STD}_{t,y}(n)/\langle n\rangle_{t,y}$ in the Scrape-Off-Layer of Tokam2D reference simulation is presented on the right panel of Figure 3.2. The notation $\text{STD}_{t,y}(n)$ corresponds to the standard deviation where time and poloidal direction are assumed to play the same role on the statistics (ergodic hypothesis). The fluctuation level increases radially from 25% at the inner source to 55% at $x = 160\rho_L$. Such trend in fluctuations level is qualitatively coherent with edge plasma experimental measurements on ASDEX Upgrade [Horacek 10] and Tore Supra [Hornung 13] in which a fluctuation level around 50% is observed at the near SOL and above 100% at the far SOL. Note however that the fluctuation level starts slightly to decrease after $x = 160\rho_L$ in our simulations which may be due to the effect of the outer radial boundary condition.

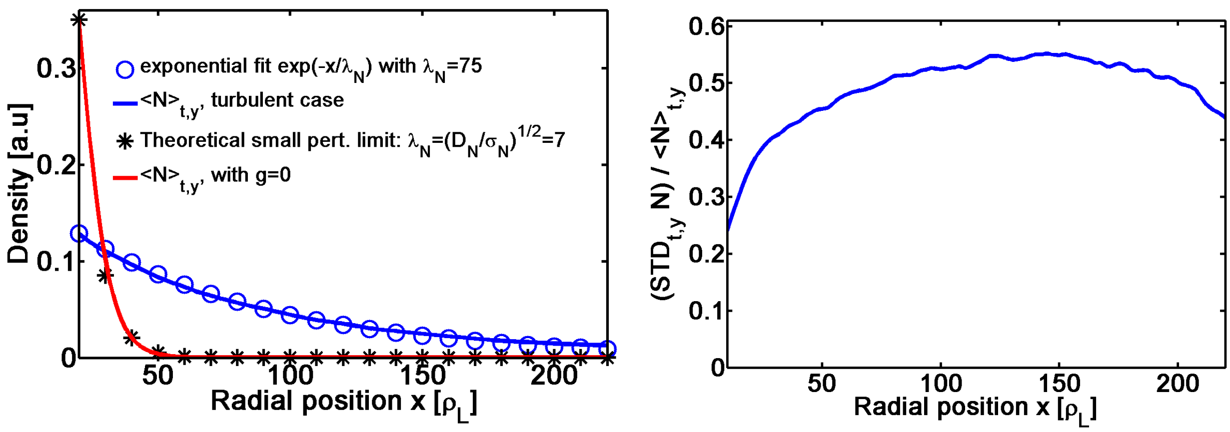

Figure 3.2: Radial profiles of:
Left panel: time and poloidally averaged density of standard Tokam2D simulation with turbulence (blue line) and associated exponential fit (blue circles), without turbulence ($g = 0$, red line) and theoretical profile in the small perturbations limit (black stars).
Right panel: normalized fluctuation level $\text{STD}_{t,y}(n)/\langle n\rangle_{t,y}$ where $\text{STD}_{t,y}(n) = \sqrt{\langle (n - \langle n\rangle_{t,y})^2\rangle_{t,y}}$

On the other hand, such large fluctuation levels are in total contradiction with the small perturbation limit of the linear analysis. Linear analysis cannot thus be used as a predictive tool to determine edge plasma transport even in terms of equilibrium profiles. It gives however asymptotic behaviour especially on the effect of the different phenomenons involved in plasma fluid equations: diffusive processes, damping by parallel transport, effect of coupling between magnetic field curvature and density gradient. Moreover, linear analysis permits to understand the growth of structures due to interchange instability before non-linear effects become the dominant player. The comparison between linear analysis, turbulence simulations and experimental observations of fluctuations level reinforces the choice of a flux-driven approach where any scale separation has been assumed instead of a gradient-driven approach where the shape of equilibrium profiles are prescribed.

3.1.2.2 Characterization of turbulent transport

In the following, the development of turbulent structures is detailed and the radial transport in Tokam2D simulations is characterized. When the density profile is too flat, interchange is linearly stable at all scales and finite poloidal structures cannot appear. If dissipative processes (diffusion, parallel losses) are not too large, the particle source then increases the density gradient until interchange becomes linearly unstable at one or several scales. These scales develop and lead to the formation of finite poloidal structures that are usually called blobs. The correlation between density and electrostatic potential fluctuations and especially their phase shift leads to non-linear transport generated by the $\mathbf{E} \times \mathbf{B}$ drift. It results on an outward radial transport of these structures which interact with each other and leads to turbulent transport. Typical $2D$-(x, y) snapshots of density and electrostatic potential can be found in Figure 3.3 at an arbitrary time. Turbulent density structures propagate radially in the form of filaments and avalanche-like events [Sarazin 03]. Contours of relative density fluctuations $(\widetilde{n} - \langle n \rangle_y) / \langle n \rangle_y$ have been added to the electrostatic potential snapshot in order to understand how turbulent structures propagate radially. If blob shapes can appear quite random at first sight, some clear characteristics can be noticed. First, blobs are more elongated radially than poloidally $(k_x < k_y)$. Then, density structures propagate into potential corridors, preferentially in the middle of potential dipoles. Density and potential structures are nearly in phase quadrature as expected from the linear analysis. Finally, some filaments appear to have lost radial coherence and to be split into several smaller blobs. Each density structure impacts on the electrostatic potential, interacts with many others blobs and leaves a footprint of its path which will perturb the trajectory of following blobs. The characteristic lifetime of a blob is then way smaller than its footprint lifetime. The result is thus an intermittent radial propagation of blobs of many sizes and shapes which leads to a net outward self-organized radial turbulent transport.

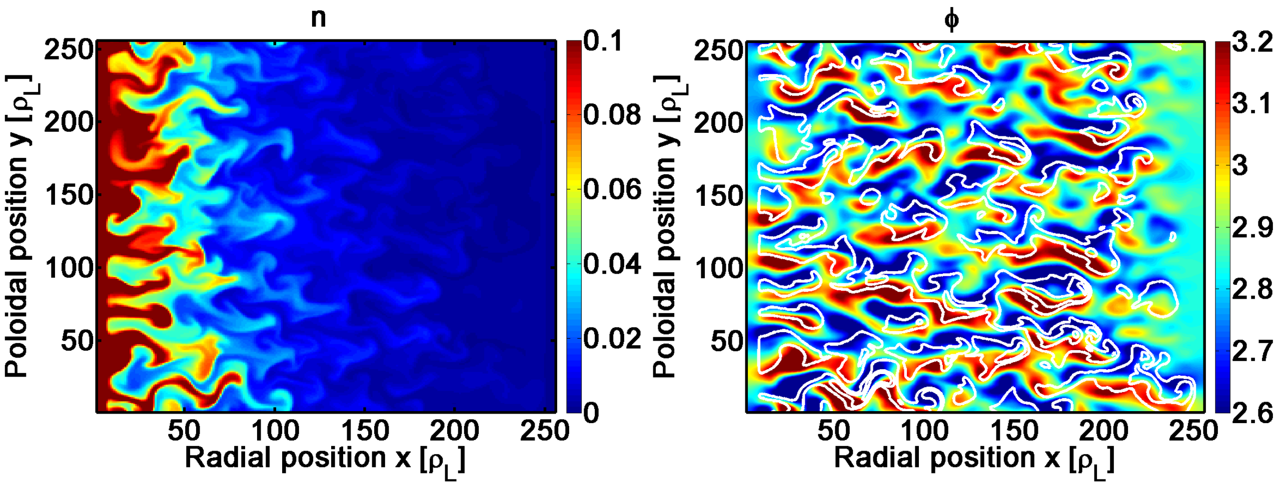

Figure 3.3: 2D - radial and poloidal - snapshots of:
Left panel: density n
Right panel: electrostatic potential ϕ with relative density fluctuations contours $(\tilde{n} - \langle n \rangle_y) / \langle n \rangle_y$ in white.

The ballistic nature of interchange driven turbulence transport is reported on the left panel of Figure 3.4 in which the poloidally averaged $\mathbf{E} \times \mathbf{B}$ radial flux $\langle \Gamma_x^{E\times B} \rangle_y = -\langle n \partial_y \phi \rangle_y$ is presented as a function of radial direction and time. This turbulent flux emerges at the location of the source and propagates outward radially in a quasi-ballistic motion. These avalanches from the center to the end of the SOL do not exhibit a clear characteristic frequency. Some of these events propagate until the end of the simulated box while others disappear prematurely. The characteristic velocity of this ballistic avalanche-like events is of the order of 0.05 c_s, which is the order of magnitude found in edge turbulence measurements of blobs velocity [Myra 06], even if these two quantities are not exactly equivalent.

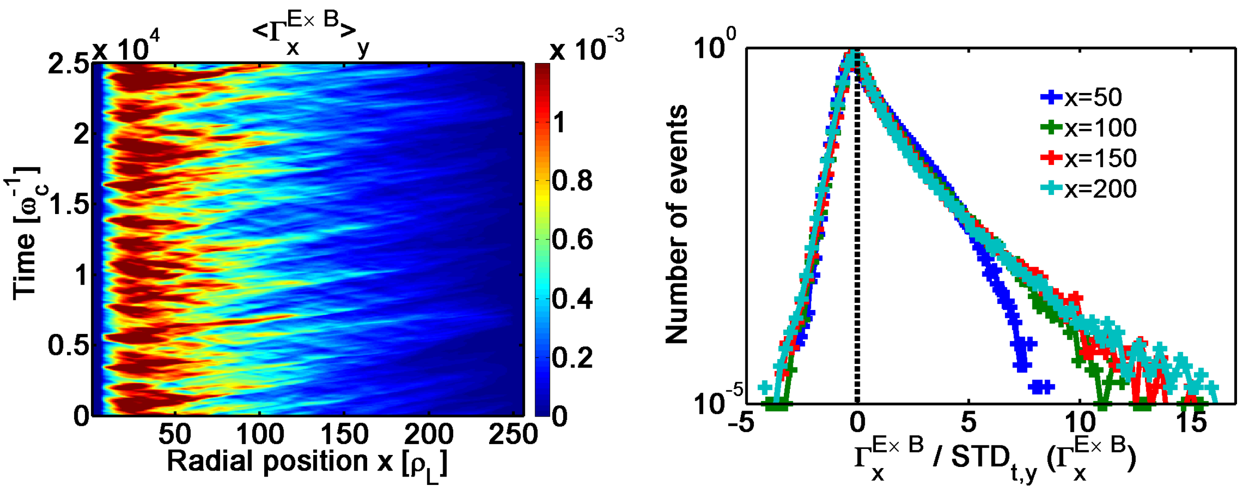

Figure 3.4:
Left panel: 2D-(x, t) map of $\mathbf{E} \times \mathbf{B}$ turbulent radial particle flux $\langle \Gamma_x^{E\times B} \rangle_y$
Right panel: PDF of normalized $\mathbf{E} \times \mathbf{B}$ turbulent radial particle flux $\Gamma_x^{E\times B} / \mathrm{STD}_{t,y} \langle \Gamma_x^{E\times B} \rangle_{t,y}$ for several radial locations

The probability distribution function (PDF) of the radial $\mathbf{E} \times \mathbf{B}$ flux is depicted on the right panel of Figure 3.4 for 4 different radial locations. This flux has been normalized to its standard deviation computed from both time and poloidal direction at each radial position. It is found that the PDF of the normalized turbulent flux does not depend strongly on the radial position. As reported previously [Sarazin 03], the most probable flux has a slightly negative value and is thus inward. Note also that the low amplitude part of the PDF matches with a Gaussian fit. Large events - consequences of avalanche-like transport - generate a strong positive tail of the PDFs that is to say a positive skewness and these blobs carried most of the radial transport. The amplitude of the tail slightly increases with the radial position and the strong discrepancy found between the PDF at $x = 50\rho_L$ and further radial positions can be explained as filaments are still linked to the source region at $x = 50\rho_L$ while ballistic motion of blobs start mostly from $x = 70\rho_L$ as it can be seen on the left panel of Figure 3.4.

3.2 Theoretical approach on the impact of two barrier generation mechanisms

In the following, we impose in our Tokam2D simulations two forcing mechanisms in the Scrape-Off Layer, the $\mathbf{E} \times \mathbf{B}$ shear and the radial gradient of this shear. Forcing such mechanisms in the Scrape-Off Layer can be seen as a modelling of edge plasma biasing experiments. Biased electrodes have been used experimentally to modify the electric field in the Scrape-Off Layer which impacts on SOL transport and profiles. Historically, polarization electrodes have been used for example in TEXTOR [Weynants 92] and in CCT (Continuous Current Tokamak) [Taylor 89] to generate an edge radial electric field in the SOL which increases the core confinement. Edge biasing improves confinement even for mirror machines [Sakai 93]. More recently, a review on edge plasma biasing experiments on TEXTOR, CASTOR, T-10, ISTTOK and RFX confirms the key role of $\mathbf{E} \times \mathbf{B}$ shear on transport barrier formation, turbulence stabilisation and improvement of plasma confinement [Oost 03]. In NSTX, biased electrodes are found to generate a strong radial $\mathbf{E} \times \mathbf{B}$ flow in the SOL [Zweben 09] which leads to the increase of the radial SOL width for an outward $\mathbf{E} \times \mathbf{B}$ drift.

3.2.1 Presentation of the two mechanisms

3.2.1.1 $\mathbf{E} \times \mathbf{B}$ shear

The first mechanism is the $\mathbf{E} \times \mathbf{B}$ shear which corresponds to the radial shear of the poloidal $\mathbf{E} \times \mathbf{B}$ drift: $\partial_r \bar{u}_\theta^{E\times B}$. This shear is suspected to be the key player of the transport barrier formation during the L-H transition probably by decorrelation of turbulence [Biglari 90],[Itoh 96]. It leads to a radially localized quench of turbulence which is stabilized non-linearly by this $\mathbf{E} \times \mathbf{B}$ shear. The interaction between turbulence and $\mathbf{E} \times \mathbf{B}$ shear can be very complex and cannot be totally analysed within a simple model. Here, we focus only on the effect of a stationary $\mathbf{E} \times \mathbf{B}$ shear flow on turbulence properties without taking into account feedback of turbulence on this mean flow.

3.2.1.2 $\mathbf{E}\times\mathbf{B}$ curvature

The $\mathbf{E}\times\mathbf{B}$ curvature corresponds to the radial gradient of the $\mathbf{E}\times\mathbf{B}$ shear: $\partial_r^2 \bar{u}_\theta^{E\times B}$. The effect of the electric field curvature on turbulence has been investigated for a long time from theoretical point of view [Staebler 91]. For an arbitrary electric field, most of the linear turbulence stabilisation comes from $\mathbf{E}\times\mathbf{B}$ curvature rather than $\mathbf{E}\times\mathbf{B}$ shear [Sidikman 94]. Unlike for the $\mathbf{E}\times\mathbf{B}$ shear mechanism, the sign of the curvature term is important and can lead to stabilisation or destabilisation of turbulence. More recently, the interaction between the radial electric field and its curvature was found to play a role on the suppression of turbulence both from theoretical approach [Itoh 15] and experimental measurements [Kamiya 16]. The latter shows that the peak of the gradient at the edge barrier appears at the peak of the $\mathbf{E}\times\mathbf{B}$ curvature and not at the peak of $\mathbf{E}\times\mathbf{B}$ shear.

3.2.2 Expected impact on turbulence

3.2.2.1 $\mathbf{E}\times\mathbf{B}$ curvature: a linear mechanism

The effect of the third derivative of the equilibrium electrostatic potential $\partial_x^3\phi_{\text{eq}}$ can be investigated using the linear analysis. Indeed, as mentioned in [Ghendrih 03] and as it can be seen from the system of equations (3.5), this term appears explicitly in the linear analysis of the vorticity equation (2.146) within the Poisson bracket $[\widetilde{\phi}, \partial_x^2\phi_{\text{eq}}]$. The contribution of $\partial_x^3\phi_{\text{eq}}$ is taken into account in the linear analysis by assuming an arbitrary potential equilibrium constant in time, uniform along the poloidal direction but varying in the radial one. The coefficients of the second order equation on Ω_k (3.9) are modified accordingly:

$$b_k = \frac{\sigma_W}{k_\perp^2} + \sigma_N + (D_N + \nu)\, k_\perp^2 + \frac{ik_y}{k_\perp^2}\partial_x^3\phi_{\text{eq}} + 2ik_y\partial_x\phi_{\text{eq}} \tag{3.11}$$

$$c_k = \left(\sigma_N + D_N k_\perp^2 + ik_y\partial_x\phi_{\text{eq}}\right)\left(\frac{\sigma_W}{k_\perp^2} + \nu k_\perp^2 + ik_y\partial_x\phi_{\text{eq}} + \frac{ik_y}{k_\perp^2}\partial_x^3\phi_{\text{eq}}\right) - \frac{gk_y^2}{\lambda_N k_\perp^2} - ig\sigma_N\frac{k_y}{k_\perp^2} \tag{3.12}$$

One can notice that by assuming a non flat profile of the equilibrium potential, the first radial derivative of this equilibrium potential also appears in the linear analysis in both density and charge balance equations through the Poisson brackets $[\phi_{\text{eq}}, \widetilde{n}]$ and $[\phi_{\text{eq}}, \partial_x^2\widetilde{\phi}]$. However, this mean poloidal electric drift velocity interacts the same way for density and potential fluctuations, inducing only a turbulence frequency shift similar to a Doppler effect. This effect has thus no consequence on the amplitude and behaviour of the linear growth rate γ_k and can thus be put aside in equations (3.11) and (3.12) by the introduction of a new angular frequency $\omega_k = \Omega_k + ik_y\partial_x\phi_{\text{eq}}$ and we have $\gamma_k = \text{Re}(\Omega_k) = \text{Re}(\omega_k)$. The inclusion of the third radial derivative of ϕ_{eq} does not impact the asymptotic behaviour of the linear growth rate γ_k as a function of the poloidal wave number k_y. Indeed, small scale structures are still damped by dissipative processes (D_N, ν) while large scale structures are stabilized by losses in the parallel direction (σ_W). The linear growth rate evolution with respect to radial and poloidal wave numbers for different values of $\partial_x^3\phi_{\text{eq}}$ is presented in Figure 3.5. The linear growth rate is reported as a function of the poloidal wave number k_y for $k_x = 0$ on the left panel and as a function of k_x for the most unstable mode $k_y\rho_L = 0.38$ on the right panel. Both plots confirm the stabilizing effect of $\partial_x^3\phi_{\text{eq}}$. Largest radial scales (small k_x) are stabilized first while intermediate poloidal scales ($k_y \in [0.1, 0.5]$) are damped for non-zero $\partial_x^3\phi_{\text{eq}}$. We observe also a shift of the position of the maximal amplitude of

γ_k to small poloidal scales when the imposed $\partial_x^3\phi_{\rm eq}$ amplitude increases.

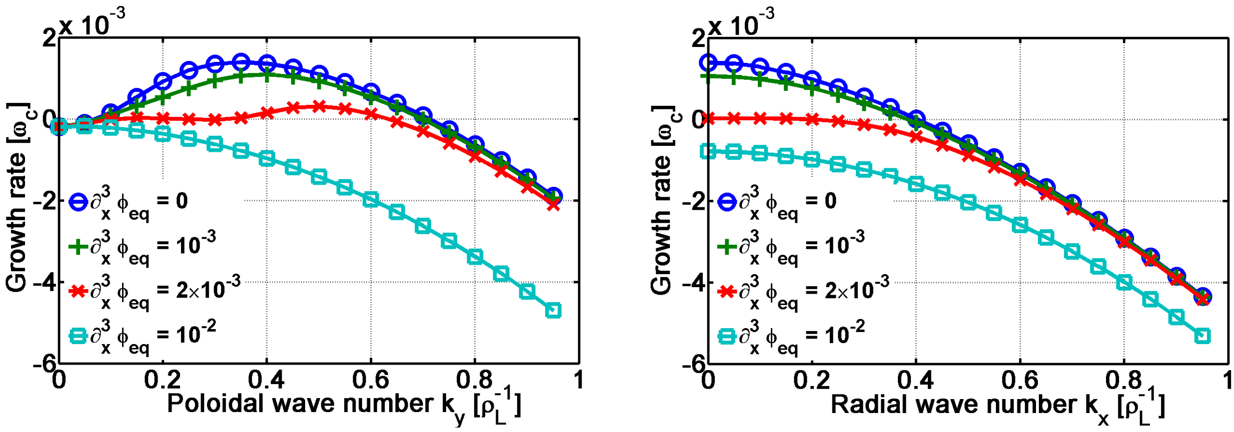

Figure 3.5: Impact of $\partial_x^3\phi_{\rm eq}$ on the linear growth rate:
Left panel: as a function of the poloidal wave number k_y for $k_x = 0$.
Right panel: as a function of the radial wave number k_x for the most unstable unstable poloidal wave number $k_y\rho_L = 0.38$.

Moreover, for $\partial_x^3\phi_{\rm eq} \geq 0.05$ the linear growth rate is negative for all radial and poloidal wave numbers meaning that the interchange instability is locally totally suppressed which might lead to the formation of a transport barrier, at least in the absence of turbulence spreading. Note that such impact of turbulence spreading into a linearly stable region in Tokam2D has been investigated in [Ghendrih 07].

3.2.2.2 Non-linear effect of $\mathbf{E}\times\mathbf{B}$ shear

In Tokam2D, the magnetic field is assumed to be a constant and the $\mathbf{E}\times\mathbf{B}$ shear writes thus simply:

$$\partial_r \bar{u}_\theta^{E\times B} = \partial_x \bar{u}_y^{E\times B} = \partial_x^2\phi_{\rm eq} \tag{3.13}$$

Unlike the $\mathbf{E}\times\mathbf{B}$ curvature mechanism, this shear does not appear explicitly in the linear analysis of Tokam2D model. However, the effect of this shear layer on turbulence can be foreseen by looking at a simpler problem. Indeed, the evolution of an initial pulse subjected to such stationary shear flow consists on a non-linear problem with analytical solution [Beyer 05].
A radial shear $\omega_{E\times B}$ applied on the poloidal flow is assumed uniform such as:

$$\partial_x \bar{u}_y^{E\times B} = \omega_{E\times B} \Leftrightarrow \bar{u}_y^{E\times B} = \bar{u}_y^0 + \omega_{E\times B}x \tag{3.14}$$

The evolution of an initial density perturbation is thus driven by:

$$\partial_t \widetilde{n}_{k_y} = \gamma_{\rm lin}\widetilde{n}_{k_y} + ik_y\,\omega_{E\times B}x\widetilde{n}_{k_y} + D_N\partial_x^2\widetilde{n}_{k_y} \tag{3.15}$$

In the equation (3.15), $\gamma_{\rm lin}$ corresponds to the linear growth rate without taking into account dissipative and mean velocity effects. Assuming an initial Dirac distribution localized at $x = 0$, the solution of equation (3.15) writes:

$$\widetilde{n}_{k_y}(t,x) = \frac{n_0}{\sqrt{4\pi D_N t}} \exp\left\{\left(-\frac{x^2}{4D_N t}\right)\right\} \exp\left\{\left(\frac{ik_y\omega_{E\times B}x}{2}t\right)\right\} \exp\left\{\left(\gamma_{\text{lin}}t - \frac{1}{3}\left(\frac{t}{\tau_D}\right)^3\right)\right\} \tag{3.16}$$

where $\tau_D = \left(D_N k_y^2 \omega_{E\times B}^2/4\right)^{-1/3}$ is the characteristic Dupree time [Beyer 05],[Ghendrih 09] combining shearing and diffusive effects. In the expression (3.16), the first exponential is a damping mechanism due to diffusive processes with Maxwellian width equal to $\Delta = \sqrt{2D_N t}$. The second exponential term corresponds to a filamentation process, as its real part can be written as $\cos(k_D x)$ with $k_D = k_y\omega_{E\times B}t/2$ the radial spatial frequency of filaments. Finally, the last exponential term of equation (3.16) reveals a competition between the linear growth rate, acting linearly in time, and the non-linear term, cubic in time, induced by the interplay between diffusive and shearing processes. The perturbation is first amplified by the linearly unstable growth rate for small times until shearing effects become the dominant mechanism and damp this perturbation. The transition in the drive by linear or by non-linear mechanisms occurs for Kubo number $\text{Ku} = \gamma_{\text{lin}}\left(D_N k_y^2 \omega_{E\times B}^2\right)^{-1/3}$ around unity. This dimensionless number is the ratio between linear and non-linear terms and characterizes the transport regime in turbulent systems [Zimbardo 00]. One can notice the fundamental role played by diffusion processes in the turbulence lifetime and penetration length inside the barrier generated by the radial shear of the poloidal flow. The evolution of the initial pulse without shearing effect ($\omega_{E\times B} = 0$) can be foreseen on the left panel of Figure 3.6 in which the radial profiles of fluctuating density are plotted for different times. Parameters used in this case are $n_0 = 1$, $D_N = 5\times 10^{-3}\rho_L^2\omega_c$ and $\gamma_{\text{lin}} = 2.5\times 10^{-3}\omega_c$. The fluctuations in such case write simply:

$$\widetilde{n}(t,x) = \frac{n_0}{\sqrt{4\pi D_N t}} \exp\left\{\left(-\frac{x^2}{4D_N t}\right)\right\} \exp\{(\gamma_{\text{lin}}t)\} \tag{3.17}$$

For $t \in [10^{-6}, 100]\omega_c^{-1}$ the density essentially experienced the effect of radial spreading by diffusive effect: the central peak at $x = 0$ diminishes with time and the width of the peak increases. At longer time, the fluctuations are destabilized by the unstable linear growth rate which increases the perturbation amplitude everywhere. The effect of the filamentation term can be understood by the analysis of the right panel of Figure 3.6. Only the filamentation part of formula (3.16) is presented: $\widetilde{n}_{k_y} = n_0 \exp\left(ik_y\omega_{E\times B}xt/2\right)$ for $\omega_{E\times B} = 5\times 10^{-3}\omega_c$. In the limit $t \to 0$, this function is equal to 1 uniformly at any radial position. When t increases the filamentation process starts and the spatial period of the function is decreasing: for $t = 50\omega_c^{-1}$ the spatial period is about $50\rho_L$ and drops to $5\rho_L$ for $t = 500\omega_c^{-1}$. This filamentation process leads to a succession of over- and sub- density fluctuations and thus to a spatial tilting and shearing of density structures.

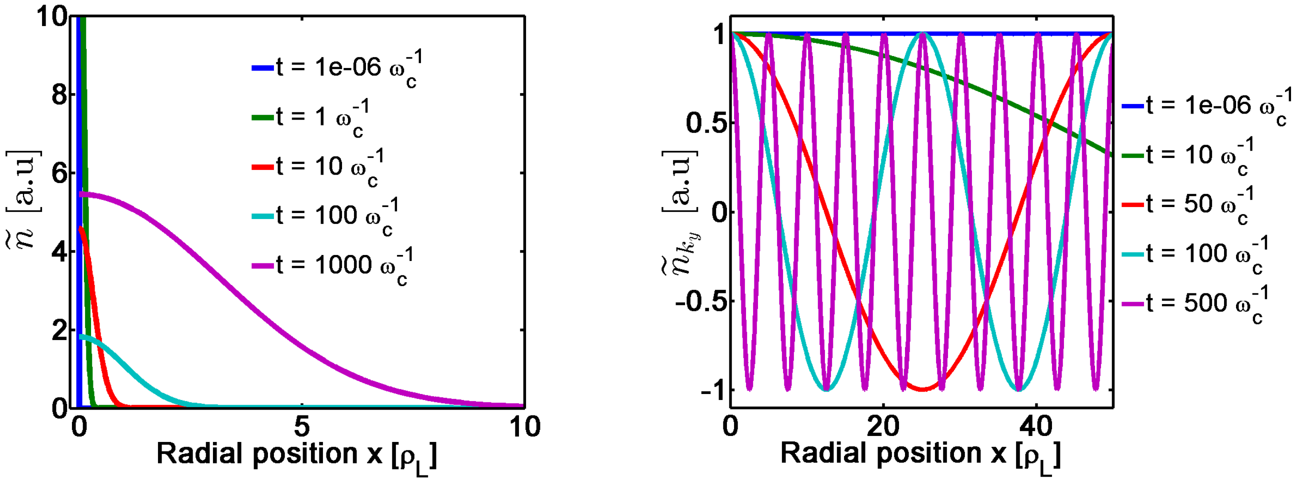

Figure 3.6: Radial profiles of:
Left panel: the evolution of an initial pulse without shearing effects and due only to diffusive effects ($D_N = 5 \times 10^{-3}\rho_L^2\omega_c$) and unstable linear growth rate ($\gamma_{\text{lin}} = 2.5 \times 10^{-3}\omega_c$).
Right panel: the evolution of the filamentation process due to shearing effect with $\omega_{E\times B} = 5\times 10^{-3}\omega_c$.

The theoretical effect of combined filamentation and shearing processes is more complex and strongly depends on the set of parameters used such as no representation of the equation (3.16) is provided here. The competition between these two effects is mainly determined by the value of the Kubo number.

3.2.3 Numerical implementation

Tokam2D equations are slightly modified in order to artificially drive one mechanism without generating a strong impact on the other one. The third radial derivative of the equilibrium electrostatic potential is quite simple to impose in the model. Indeed, as seen previously, it appears explicitly in the linear analysis through the Poisson bracket $[\widetilde{\phi}, \partial_x^2\phi_{\text{eq}}]$. The vorticity equation has thus been reworked to add such contribution:

$$\partial_t W + [\phi, W] - \boxed{\alpha(x)\partial_y\phi} - \nu\nabla_\perp^2 W = -g\frac{\partial_y n}{n} + \sigma_W\left((1 - \exp\{(\Lambda - \phi)\}\right) \tag{3.18}$$

with $\alpha(x) = \partial_x^3\phi_{\text{eq}}^0 \exp\left(-\frac{1}{2}\left(\frac{x-x_c}{\Delta}\right)^2\right)$ a time- and poloidally- constant Gaussian centred on $x_c = 120$, with an amplitude $\partial_x^3\phi_{\text{eq}}^0$ and a width Δ varying in the different simulations. The shape of the imposed $\mathbf{E}\times\mathbf{B}$ shear gradient can be seen on the left panel of Figure 3.7 for an amplitude $\partial_x^3\phi_{\text{eq}}^0 = 10^{-2}$ and a half-width $\Delta = 12\rho_L$. The two vertical dashed grey lines on both sides of the central black dashed line at $x = x_c$ symbolize the width of the barrier. These lines are localized at $x = x_c - \Delta$ and $x = x_c + \Delta$.

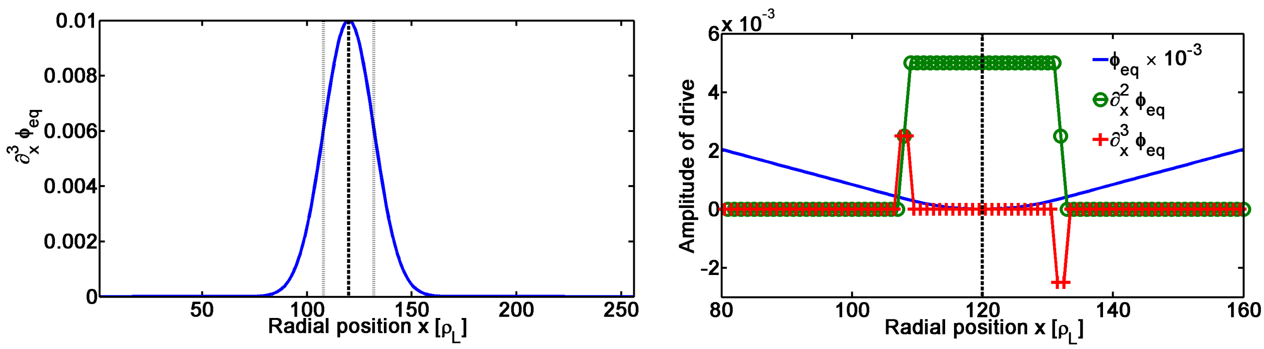

Figure 3.7: Radial profile of forced mechanisms:
Left panel: Shape of the $\alpha = \partial_x^3 \phi_{\text{eq}}$ function used in the Poisson brackets which corresponds to driven $\mathbf{E} \times \mathbf{B}$ curvature.
Right panel: Modified equilibrium electrostatic potential to generate $\mathbf{E} \times \mathbf{B}$ shear drive and corresponding second and third derivatives as seen by the code.

The other stabilizing mechanism, the radial shear of the E×B velocity, is more difficult to impose in the model as it requires to generate locally a second derivative without a third one. Nevertheless, a second radial derivative of the mean electrostatic potential close to a gate function can be obtained with an almost-zero third radial derivative. For that, an artificial time- and poloidally-constant electrostatic potential ϕ_{eq} (see eq.(3.19)) is added on the electrostatic potential which appears in the Poisson brackets of equations (2.145) and (2.146). These Poisson brackets become respectively $[\phi + \phi_{\text{eq}}, n]$ and $[\phi + \phi_{\text{eq}}, W]$.

$$\phi_{\text{eq}}(x) = \frac{1}{2}\partial_x^2 \phi_{\text{eq}}^0 * \begin{cases} -\Delta\left(2\left(x - x_c\right) + \Delta\right) & \text{if } x < x_c - \Delta \\ \left(x - x_c\right)^2 & \text{if } x_c - \Delta \leq x \leq x_c + \Delta \\ \Delta\left(2\left(x - x_c\right) - \Delta\right) & \text{if } x > x_c + \Delta \end{cases} \tag{3.19}$$

with x_c the center of the region where the mechanism is artificially forced and Δ the half-width of this region. One can easily check on the right panel of Figure 3.7 that the second radial derivative of the function ϕ_{eq} has actually a gate shape. The linear extensions on each side of the quadratic region of ϕ_{eq} ensure a minimal third derivative of this function which is reduced to two Dirac-like peaks on both sides of the gate. Note that the symbols displayed on the curves correspond to the resulting second and third derivatives of ϕ_{eq} as seen by the discretization scheme in the code Tokam2D. We actually checked that the effect of this third derivative in these simulations is negligible by observing that no transport barriers appear when this profile of third derivative is forced in a dedicated simulation.
The two forcing mechanisms are characterized by an amplitude $\partial_x^2 \phi_{\text{eq}}^0$ and $\partial_x^3 \phi_{\text{eq}}^0$ and by a width Δ. For the $\mathbf{E} \times \mathbf{B}$ shear drive, the width corresponds to the half-width of the Gate function such as the second derivative is equal to zero for $x \notin [x_c - \Delta, x_c + \Delta]$. Conversely, for the $\mathbf{E} \times \mathbf{B}$ curvature forcing, the width corresponds to the half-width of the Gaussian function and the third derivative is thus non-zero for at least $x \in [x_c - 3\Delta, x_c + 3\Delta]$. Such difference on the impact area of each mechanism can generate some discrepancies which are not due to the inherent nature of the mechanism.

3.3 Characterization of driven barriers

3.3.1 Modification of Scrape-Off Layer radial transport

The first question of interest is to know if the two driven mechanisms are able to modify Scrape-Off-Layer characteristics and especially radial transport. If so, one can expect to modify equilibrium properties at least in the area where the two mechanisms are artificially forced. The radial profiles of equilibrium density are plotted on Figure 3.8 for 2 different amplitudes of $\mathbf{E} \times \mathbf{B}$ shear drive and compared to a simulation with no forcing. The vertical black dashed line at $x = 120\rho_L$ represents the center x_c of the driven mechanism region. Note that a similar behaviour is obtained when a forcing by the $\mathbf{E} \times \mathbf{B}$ curvature is applied. The presence of a barrier strongly impacts the equilibrium density profile which is no longer an exponential decay. The density on the upstream region of the barrier is larger than without forcing which means that the particle confinement has been improved consistently with what we expect from the existence of a transport barrier. A large steepening of density profiles is observed in the region where mechanisms are forced around $x = 120\rho_L$. Consequently, the density in the downstream region of the barrier is reduced when a drive is set up.

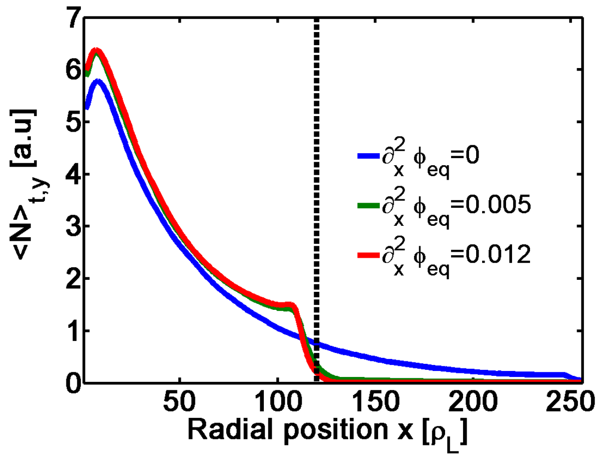

Figure 3.8: Radial profiles of density $\langle n \rangle_{t,y}$ for a simulation without forcing and two simulations with different amplitude of $\mathbf{E} \times \mathbf{B}$ shear drive with a width $\Delta = 12\rho_L$. The vertical black dashed line at $x = 120\rho_L$ represents the center x_c of the driven mechanism region.

The modification of density equilibrium profile when a drive is applied is associated with a change in radial transport. Figure 3.9 presents the radial profile of the mean total radial particle fluxes without forcing any mechanism and with the two driven mechanisms. The total radial flux is composed of the turbulent $\mathbf{E} \times \mathbf{B}$ flux and the diffusive one. For the $\mathbf{E} \times \mathbf{B}$ shear, the forcing is made with an amplitude of 1.2×10^{-2} while an amplitude of 2.4×10^{-2} is used for the $\mathbf{E} \times \mathbf{B}$ curvature. In both case, the forcing is made with a width $\Delta = 12\rho_L$. One can notice a strong discrepancy between the case without forcing and the two forcing ones. Without any forcing, the total radial flux decreases progressively in the radial direction from 1.08 at the outside of the source ($x = 25\rho_L$) to 0.21 at $x = 120\rho_L$ and tends to zero at the right limit of the simulated domain ($x = 250\rho_L$). When a forcing by any of the two mechanisms is applied, we observe a very strong reduction of the total radial flux which drops from about 1 at the outside of the source to almost zero (5×10^{-3}) at the center of the imposed region ($x = 120\rho_L$). The radial transport is then strongly reduced when any of the two mechanisms is set up which confirms the presence of a transport barrier. In fact, this reduction of total radial particle fluxes can be explained by the raise of the density in the upstream region of the barrier. Indeed, such increase leads to an enhancement of the particle losses at the target through the parallel transport. As the competition between parallel and perpendicular transport determines the width of the Scrape-Off Layer, an increase of parallel transport - and thus of parallel losses - is associated with a decrease of radial transport. Finally, a slight difference in the shape of the radial profiles can be observed between the two drives: the drive by electric field curvature displays a steeper slope than by the $\mathbf{E} \times \mathbf{B}$ shear just before the radial region where the forcing is applied (around $x = 100\rho_L$). In a next part, we will try to understand if this discrepancy can be explained by the difference of the forcing shape or if the difference is inherent of the nature of the drive.

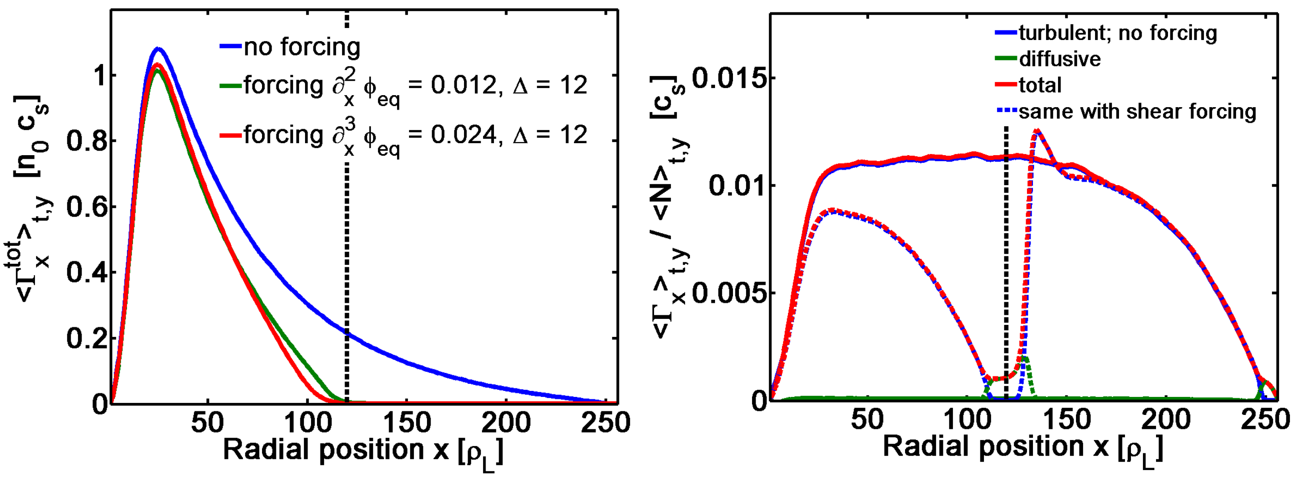

Figure 3.9: Radial profiles of:
- Left panel: Total radial particle flux without or with a forcing by the $\mathbf{E} \times \mathbf{B}$ shear or the $\mathbf{E} \times \mathbf{B}$ curvature mechanism.
- Right: Total, turbulent and diffusive effective radial velocities without forcing or with a forcing by the $\mathbf{E} \times \mathbf{B}$ shear mechanism with an amplitude of 1.2×10^{-2} and a width of $\Delta = 12\rho_L$.

In order to understand how the radial transport is modified, radial profiles of total, turbulent and diffusive fluxes are plotted in the right panel of Figure 3.9 in the case without forcing in solid lines and for the forcing with the $\mathbf{E} \times \mathbf{B}$ shear in dashed lines. These fluxes are normalized by the mean value of the density at the corresponding radial location. That is to say that these normalized fluxes correspond in fact to effective radial velocities. When no forcing is applied on the simulation, the total effective velocity is almost constant radially between $x = 30\rho_L$ and $x = 150\rho_L$ where it starts to decrease to reach zero and then match the outer boundary condition. This effective total velocity is nearly exclusively the result of turbulent transport since the diffusive contribution is almost zero. When the drive by the $\mathbf{E} \times \mathbf{B}$ shear is applied around $x = 120\rho_L$, a strong modification on the effective total velocity appears. In the area of the driven shear, from $x = 105\rho_L$ to $x = 135\rho_L$, it drops significantly to 2×10^{-3} which has to be compared to the 1.1×10^{-2} obtained in the case without forcing. This corresponds to a reduction by a factor 5 in the effective total velocity. But the effect of the shear is not limited to the forcing region: before this region, the total contribution is also found to be reduced by almost 20% on the outside of the source region ($x = 25\rho_L$) comparatively to the case without forcing. Conversely, no difference can be observed after the forcing area in which, after a strong increase of the total flux (at $x = 135\rho_L$), the effective total velocity with the drive of the shear matches perfectly the case without forcing. The forcing seems thus to have a strong impact on radial transport properties in the upstream region of the forcing area but not in the downstream one. This observation will be discussed and checked more precisely in a next paragraph. The global decrease of the total effective radial velocity when a forcing is imposed is in agreement with the increase of the density and the drop of total radial particle flux and results thus of the increase of the parallel losses. Finally, one can observe that the nature of the radial transport changes when a forcing is applied. As seen previously, the radial transport is fully turbulent in the case without forcing which is also true in the outside of the forcing region when the shear mechanism is applied. However, for $x \in [110; 130]\, \rho_L$ - in the area where the drive is applied - we can notice that the effective turbulent velocity drops almost to zero and that the radial transport crossing this area is only the result of diffusive effects. The results of radial effective velocities obtained with the $\mathbf{E} \times \mathbf{B}$ curvature forcing are qualitatively similar and are thus not been displayed here.

In order to understand how radial turbulent transport is stopped and what kind of turbulent events are stopped by the forcing mechanisms, a time- and radial- 2D plot of the poloidally averaged radial turbulent flux is presented in Figure 3.10. The vertical coordinate is the time normalized to invert ion cyclotron frequency and three different simulations - separated by horizontal white dashed lines - are gathered side by side. In the bottom one, no forcing had been used and we can see turbulent avalanches-like events propagating outward radially. These filaments are damped radially by particle losses in the parallel direction and larger events can cross the entire radial length of the simulated box. In the second simulation, from 1.25 to $2.5 \times 10^5 \omega_c^{-1}$, a small forcing by the $\mathbf{E} \times \mathbf{B}$ shear mechanism is imposed with an amplitude of 4×10^{-3} and a width of 12. One can observe that most of the avalanches are damped before crossing the forcing region around the vertical white dashed line at $x = 120\rho_L$. Only a few events are able to cross the barrier and to reach the outer boundary but with experiencing a strong reduction on their amplitudes comparatively with the case without forcing. When the amplitude of the forcing is increased - to 1.2×10^{-2} for the simulation in the top side of the Figure 3.10 - no significant event is able to cross the forcing region and the radial transport by turbulence is then nearly totally suppressed.

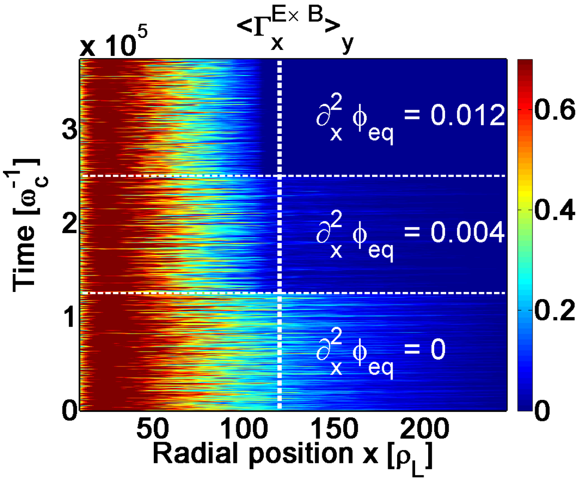

Figure 3.10: 2D - time and radial - map of mean radial turbulent flux $\langle\Gamma_x^{E\times B}\rangle_y$ for the drive by $\mathbf{E}\times\mathbf{B}$ shear mechanism with a width $\Delta = 12\rho_L$. White dashed lines represent a separation between simulations with different amplitudes of driven mechanism.

3.3.2 Transport barriers efficiency

3.3.2.1 Capability of a barrier to stop radial propagation of turbulence

In order to characterize the existence of barriers generated by these forced mechanisms, we define the efficiency of a transport barrier as its capability to reduce the radial transport of particles by turbulence. For that, a dimensionless criterion R_b, defined as the ratio of the poloidally averaged turbulent particle flux and the poloidally averaged total particle flux, has been identified in [Floriani 13]. In this study, we used a similar parameter, $\varepsilon_B(t,x) = 1 - R_b(t,x)$ called the barrier efficiency [Nace 16]. This efficiency ε_B is equal to 1 for a total transport barrier meaning all the radial transport in the barrier region is provided by non-turbulent processes: the barrier is then 100% efficient. It tends to 0 when there is no barrier such as radial transport is fully turbulent and the efficiency of the barrier is about 0%. In Tokam2D, in which radial transport is only the result of diffusive and $\mathbf{E}\times\mathbf{B}$ turbulent fluxes, this criterion ε_B writes:

$$\varepsilon_B(t,x) = \frac{\langle\Gamma_x^{\text{diff}}\rangle_y}{\langle\Gamma_x^{tot}\rangle_y} \tag{3.20}$$

where Γ_x^{diff} is the diffusive radial particle flux and $\Gamma_x^{tot} = \Gamma_x^{\text{diff}} + \Gamma_x^{E\times B}$ is the total radial particle flux. One can note that the barrier efficiency does not take into account the possible reduction of the total radial flux by the barrier as observed in Figure 3.9 but only the change of radial transport nature. Figure 3.11 presents the barrier efficiency - in a time and radial 2D plot - obtained with each driven mechanism: the $\mathbf{E}\times\mathbf{B}$ shear on the left panel and the $\mathbf{E}\times\mathbf{B}$ curvature on the right panel. In each case, three simulations are displayed in which different amplitudes of the driven mechanism have been applied. On the bottom simulation of each panel, no forcing has been used, the transport is thus fully turbulent and the barrier efficiency is equal to zero. When a drive is applied in the simulation, the barrier efficiency increases in the region in which the drive is imposed. For intermediate amplitudes, $\partial_x^2\phi_{\text{eq}} = 6\times10^{-3}$ for the $\mathbf{E}\times\mathbf{B}$ shear and $\partial_x^3\phi_{\text{eq}} = 1.4\times10^{-2}$ for the curvature drive, the barrier has an efficiency oscillating between 20% and 90% for the shear mechanism and between 40% and 70%

for the curvature one. When the amplitude of the drive is strongly increased the barrier becomes fully efficient: $\varepsilon_B > 95\%$ in the forcing region such that no turbulent transport can cross the barrier and no relaxation occurs. Such state can be visualized on the top simulation of the Figure 3.11 for an $\mathbf{E} \times \mathbf{B}$ shear amplitude of 1.2×10^{-2} and an amplitude of 2.4×10^{-2} for the curvature mechanism.

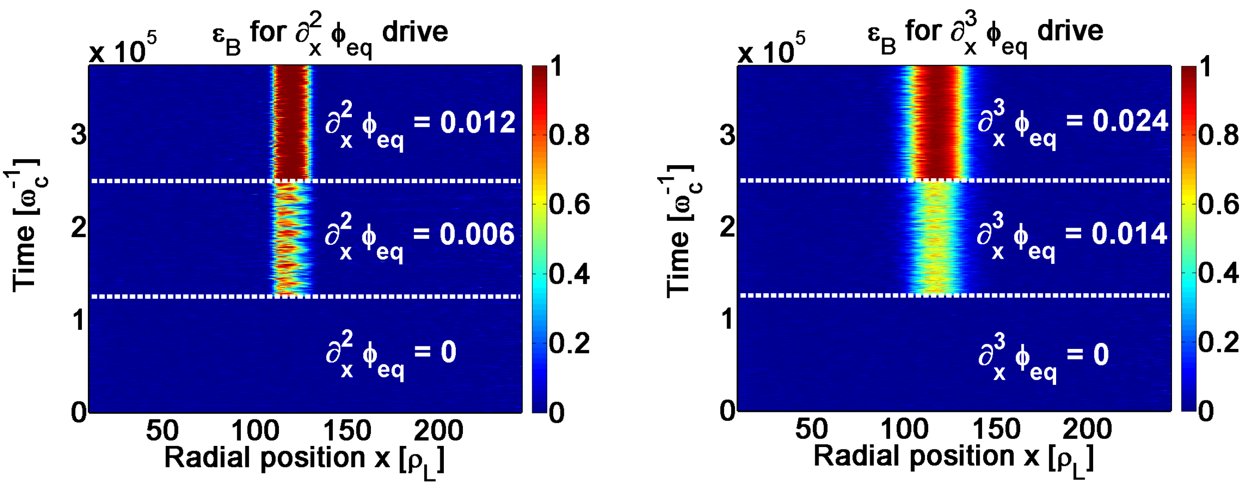

Figure 3.11: Barrier efficiency $\varepsilon_B(x,t)$ for the two driven mechanisms with a width $\Delta = 12\rho_L$. White dashed lines represent a separation between simulations with different amplitudes of the driven mechanism.
Left panel: $\mathbf{E} \times \mathbf{B}$ shear mechanism $\partial_x^2 \phi_{\text{eq}}$
Right panel: $\mathbf{E} \times \mathbf{B}$ curvature mechanism $\partial_x^3 \phi_{\text{eq}}$

One can observe that the spatial and time fluctuations of the two mechanisms differ significantly. For intermediate efficient barriers, the $\mathbf{E} \times \mathbf{B}$ curvature mechanism makes appear a more stable barrier in which only relaxations of small amplitude occur: the efficiency only varies from 40 to 70%. A radial variation of the barrier efficiency is also observed in this case: close to the center of the imposed drive, at $x = 120\rho_L$, the efficiency is maximal and decreases slowly down to the edge of the imposed region with an upstream-downstream symmetry. Note that for the strong amplitude drive, the barrier efficiency is non-zero in a region larger than the imposed one which can be probably explained by the Gaussian shape of the drive. Conversely, the $\mathbf{E} \times \mathbf{B}$ shear mechanism does not exhibit similar behaviour for intermediate efficient barriers: the maximal barrier efficiency can be almost anywhere within the upstream part of the imposed region and a strong asymmetry is observed between the two side of the gate shape. Indeed, the efficiency of the downstream side is almost twice smaller than the other half of the gate function. These barriers also exhibit strong relaxations in which the efficiency varies brutally from 90% to 25% before the barrier builds-up again. The spatial structure of the generated transport barrier is thus a useful criterion to discriminate the two mechanisms. Finally, we note that both mechanisms are able to generate fully efficient and stable barriers when the amplitude of the drive is high enough.

3.3.2.2 Influence of width and amplitude of the forced mechanism

As shown in Figure 3.11, a modification of the amplitude of the driven mechanism can lead to all kind of transport barriers: no barrier, intermediate efficient barriers which can exhibit strong relaxation and numerous fluctuations or fully stable barrier with no relaxation. This section focus on scanning the amplitude of the drive as well as the width of the barrier because the width will compete with turbulence spreading. Indeed, one can expect that larger the forcing regions are, the more efficient the barriers will be. The mean barrier efficiency is defined as the time averaged of the barrier efficiency and depends thus only on the radial direction. On Figure 3.12, we represent the maximal value of this mean barrier efficiency in the whole radial region of the imposed mechanism. On the left panel, this mean barrier efficiency is plotted as a function of the amplitude of the forced mechanism. Both mechanisms are forced in separate simulation and for two values of width: a thin barrier $\Delta = 4\rho_L$ and relatively large one $\Delta = 12\rho_L$. Each symbol represents thus a single simulation with a different couple amplitude/width for one of the two mechanisms. The qualitative behaviour is the same in each case: if the amplitude of the driven mechanism is too weak, there is no transport barriers and the efficiency is zero. When the drive amplitude is increased, the efficiency of the barrier rises until the barrier becomes fully efficient for large enough amplitudes. However, significant discrepancies can be found from a quantitative point of view. Within the same mechanism, barriers obtained with thinner drive ($\Delta = 4\rho_L$) are less efficient than for a larger imposed region ($\Delta = 12\rho_L$). For example, the maximal mean efficiency obtained with the $\mathbf{E} \times \mathbf{B}$ curvature drive and an amplitude of 10^{-2} is about 17% for an imposed width of $\Delta = 4\rho_L$ and is twice large: $\langle \varepsilon_B \rangle_t = 35\%$ for a width of $\Delta = 12\rho_L$. The effect is similar for barriers generated by the $\mathbf{E} \times \mathbf{B}$ shear mechanism.

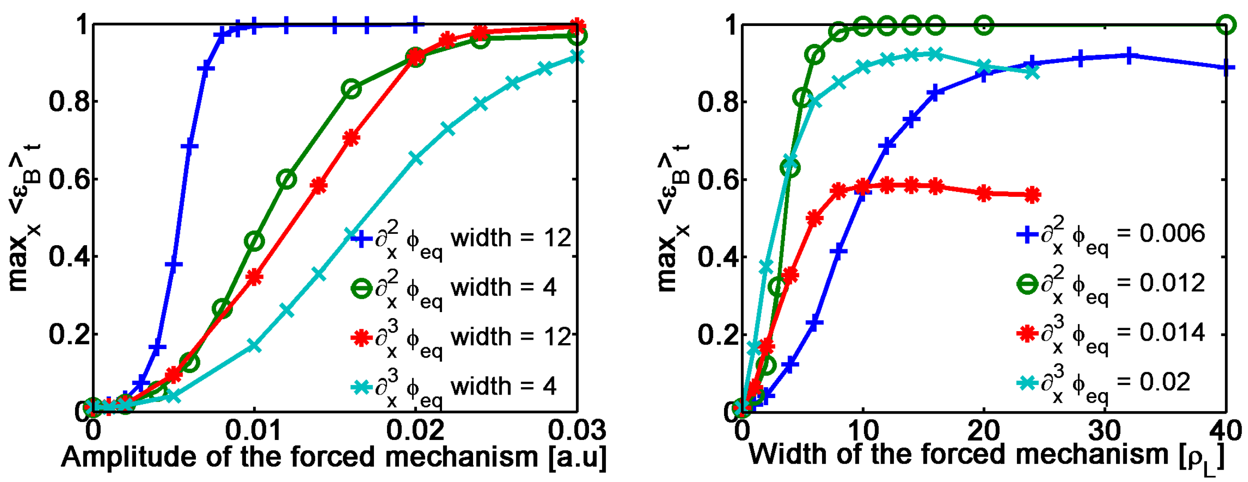

Figure 3.12: Maximal value of the time-averaged barrier efficiency for each mechanism as a function of:
Left panel: Amplitude of the forced mechanism.
Right panel: Width of the forced mechanism.

On the right side of Figure 3.12, a similar plot is displayed but this time as a function of the width of the forced mechanism for several amplitudes of the drive. Similar behaviour as previously mentioned is observed: for too thin drives, the barriers are not efficient. The efficiency increases with the width of the forced mechanism but a saturation of the barrier efficiency occurs such that increasing the width does not longer improve the capability of the barrier to stop radial propagation of turbulence. If the drive amplitude is strong enough - as for example in the case where the amplitude of the shear mechanism is 1.2×10^{-2} - this saturation does not appear while if the drive is too weak, as in the case where the curvature has an amplitude of 1.4×10^{-2}, the barrier efficiency saturates around 60%.

3.3.2.3 Consequences on turbulence properties

Until now, we have observed a reduction of total and turbulent radial particle fluxes and effective velocities associated with the formation of transport barriers. These barriers are reinforced by an increase of the amplitude or of the width of the driven mechanism and can lead to fully stable and efficient barrier or intermediate efficient barriers which exhibit large relaxations. In the following, we analyse how turbulent properties are modified within and outside the barrier. For that, the PDFs of density fluctuations are presented in Figure 3.13 at three radial locations: before the barrier region at $x = 50\rho_L$ (left panel), at the center of the forced region $x = 120\rho_L$ (central panel) and after the barrier at $x = 200\rho_L$ (right panel). These PDFs have been normalized to the time- and poloidal- averaged density in order to compare them easily. The PDFs are plotted for a drive by the $\mathbf{E} \times \mathbf{B}$ shear with $\Delta = 12\rho_L$ and in each panel for a case without forcing, with a forcing of 5×10^{-3} which corresponds to a mean barrier efficiency of about 40% and a fully efficient barrier with $\partial_x^2 \phi_{\rm eq} = 1.2 \times 10^{-2}$.

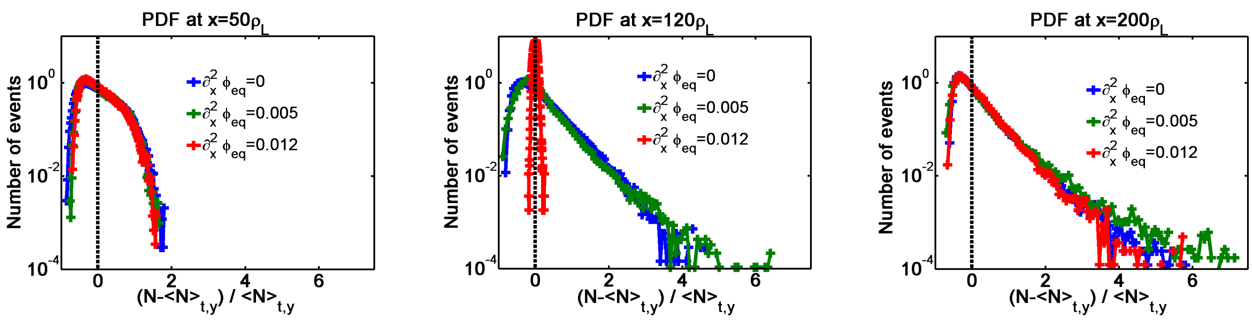

Figure 3.13: PDFs of normalized density fluctuations: $(N - \langle N\rangle_{t,y})/\langle N\rangle_{t,y}$ for the $\mathbf{E} \times \mathbf{B}$ shear drive with a width $\Delta = 12\rho_L$:
Left panel: before the forced barrier at $x = 50\rho_L$
Central panel: in the middle of the driven barrier $x = 120\rho_L$
Right panel: after the barrier at $x = 200\rho_L$

The central panel, at the center of the drive region, is first analysed. Without forcing and as we have seen in the beginning of this chapter, the normalized PDF has a Gaussian shape for small and medium events around zero and exhibits a large positive tail which represents large avalanche-like events. To compensate this large positive skewness, the most probable event is slightly negative. For the intermediate barrier with an efficiency of 40%, the shape of the PDF remains similar and no clear discrepancies can be identified in comparison to the case without forcing. Conversely, for a fully efficient transport barrier, the PDF of normalized density fluctuations is totally altered: the resulting PDF is close to a Dirac function centred in zero meaning that nearly all fluctuations inside the barrier have been damped by the $\mathbf{E} \times \mathbf{B}$ shear. The PDF is now close to a Gaussian with a vanishing skewness. On the upstream region of the barrier (left panel), one can see that the normalized density fluctuation is not impacted by the existence of a barrier downstream even if a small but non-significant reduction of large magnitude events is observe when the forcing increases. The radial position $x = 50\rho_L$ is slightly on the outside of the source region and the PDF begins to diverge from Gaussian shape with the apparition of a small positive tail and thus of first radial outward avalanches. The maximal amplitude of these over-densities is only half of the ones obtained at $x = 120\rho_L$ without or with a small forcing. On the right panel, the PDFs in a downstream region of the barrier are not strongly impacted by the existence or not of a barrier as the shape of the PDFs remains unchanged when scanning forcing amplitude. This means that interchange turbulence is able to develop from scratch after the barrier region such as its properties do not differ from turbulence coming from inner radial region as in the case without forcing. Only a small reduction of larger amplitude avalanches can be observed for the drive of $\mathbf{E} \times \mathbf{B}$ shear with an amplitude of 1.2×10^{-2}.

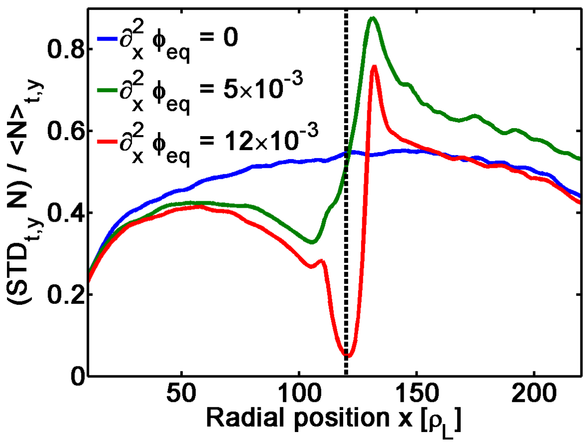

Figure 3.14: Radial profiles of relative density fluctuations $STD_{t,y}n/\langle n \rangle_{t,y}$ without forcing and with a forcing by two different amplitude of the $\mathbf{E} \times \mathbf{B}$ shear with a width $\Delta = 12\rho_L$.

Finally, the radial profiles of relative density fluctuations are displayed on Figure 3.14 for the same three different amplitudes of $\mathbf{E} \times \mathbf{B}$ shear drive. In the upstream region before the barrier, the relative density fluctuations are reduced by an increase of the drive amplitude, which is coherent with the observations made on PDFs plots. These relative fluctuations are strongly reduced inside the barrier and reach almost zero (5%) for the fully efficient barrier. One can notice a strong increase of the fluctuations level just after the forcing region. This fluctuations level raises up to 90% for fluctuating barriers and to 70% for stable ones. This corresponds to the area in which interchange turbulence develops again and can explain the unchanged shape of the PDFs at $x = 200\rho_L$. Finally, the fluctuations level decreases slightly in the radial direction for $x > 150$.

3.3.2.4 Relaxation frequency and amplitude

In the previous sections, we essentially focused on barriers generated by the $\mathbf{E} \times \mathbf{B}$ shear mechanism because all the results presented until now were qualitatively the same than the ones obtained with the $\mathbf{E} \times \mathbf{B}$ curvature mechanism. We now try to highlight which are the main discrepancies between the two mechanisms in order to be able to compare them and to understand which mechanism is the most likely to appear in a realistic situation with spontaneous transport barriers. The analysis of the time-radial 2D plot of barrier efficiency on Figure 3.11 seems to show that the relaxations of fluctuating barriers are quite different for the two mechanisms. In order to quantify these barrier fluctuations more rigorously, the radial profile of the time standard deviation of the barrier efficiency is presented on the left panel of Figure 3.15 for a forcing width of $\Delta = 12\rho_L$. For each mechanism, two amplitudes are displayed which correspond to a fluctuating barrier - *i.e* with a mean efficiency around 60% - and a fully stable barrier - *i.e* a mean efficiency above 95%. The two fluctuating barriers correspond to an amplitude of 5×10^{-3} for the $\mathbf{E} \times \mathbf{B}$ shear drive and 1.4×10^{-2} for the curvature one. The radial profiles obtained exhibit a strong increase of the standard deviation in the forcing region which signals strong fluctuations of the barrier efficiency in this area. These fluctuations are due to turbulent events which penetrate the forcing region and cross the barrier which loses thus its efficiency. One can also notice that in these cases, the standard deviation of the shear drive signal is nearly twice the one obtained with the curvature drive. For fully efficient barriers, with barrier efficiency close to 1, the radial profiles present a completely dissimilar shape. These barriers correspond to amplitudes of 2×10^{-2} and 3×10^{-2} respectively for $\mathbf{E} \times \mathbf{B}$ shear and $\mathbf{E} \times \mathbf{B}$ curvature drives. The standard deviation in the forcing region tends to zero while strong peaks of efficiency standard deviation appear at both extremities of this forcing region. For the shear mechanism, these peaks are localized at $x = 110\rho_L$ and $x = 129\rho_L$ with a characteristic width of $4\rho_L$ while in the curvature case, the peaks appear at $x = 103\rho_L$ and $x = 135\rho_L$ with a width around $10\rho_L$. The shapes of the forcing region can probably explain the difference of the peaks localisations and their widths give a valuable measure of the turbulence penetration lengths of the avalanches inside the barriers. Indeed, these peaks correspond to the radial length of strong fluctuations of the ratio of turbulent to total fluxes. Turbulent events coming from the inner region penetrate the barrier only on this penetration length as the standard deviation drops to zero just after - meaning that the barrier is no longer fluctuating. The turbulence penetration lengths inside the barriers explain why strongly efficient transport barriers cannot be obtained when the imposed region is too thin (for $\Delta \leq 2\rho_L$ on the right panel of Figure 3.12) even with a large amplitude forcing. On the outer side of the barrier, the width of the peak measures the radial position where interchange turbulence grows and develops again as well as the penetration length of inward turbulent events (as seen on right panel of Figure 3.4, a significant part of turbulent events are inwards with small amplitude).

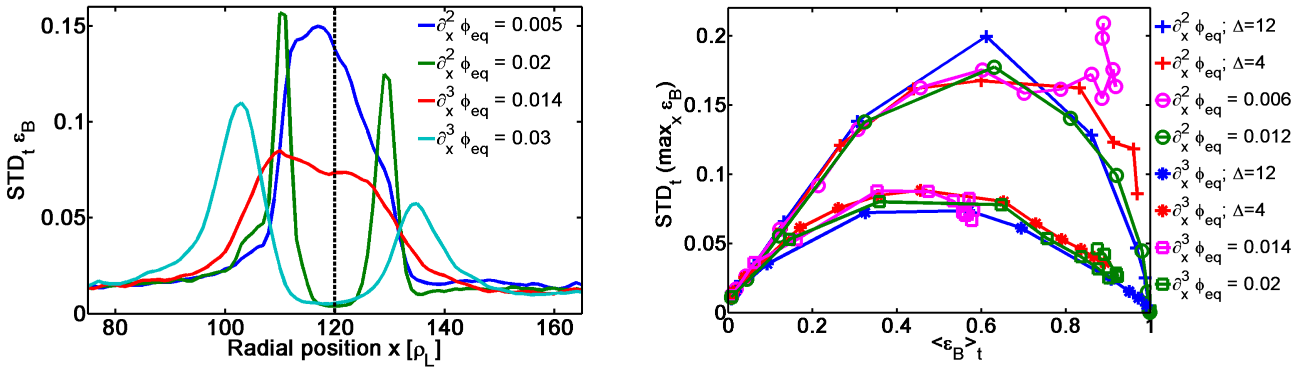

Figure 3.15:
Left panel: Radial profiles of standard deviation of the barrier efficiency ε_B for $\Delta = 12\rho_L$
Right panel: Time standard deviation of barrier efficiency as a function of mean barrier efficiency at $x = 120\rho_L$ from the total simulation database.

On the right panel of Figure 3.15, the standard deviation of the barrier efficiency at the position of its maximal amplitude within the forcing region is plotted as a function of the mean barrier efficiency at the same position. The full database of forcing simulations has been used which corresponds for each of the two mechanisms to scans of the amplitude for two given widths and to scans of the width for two given amplitudes. In total, around 50 simulations are used for each mechanism. First, we notice that the behaviour of the standard deviation as a function of the barrier efficiency is always the same: when the barrier is poorly efficient - i.e $\langle \varepsilon_B \rangle_t$ $\langle 0.1$ - the standard deviation is very low as well which means that the barrier does not fluctuate much. The same asymptotic behaviour is logically obtained for fully efficient barrier: if the barrier is fully stable with a mean efficiency close to 1 this means that the barrier presents very low relaxation frequency and/or relaxations of small amplitudes and thus the standard deviation is close to zero. When the mean efficiency of the barrier is between 10% and 90%, its standard deviation increases with a maximal value obtained in most case for a mean efficiency between 50 and 60%. Then, the more interesting fact of the right panel of Figure 3.15 is to remark that the standard deviation obtained with each mechanism for a given mean efficiency is almost always around the same value regardless the amplitude or the width of the forcing region. For example, all barriers obtained with the $\mathbf{E}\times\mathbf{B}$ curvature mechanism have a standard deviation around $(7 \pm 1) \times 10^{-2}$ for a mean efficiency between 40 and 60%. All the barriers obtained with the $\mathbf{E}\times\mathbf{B}$ shear drive have a standard deviation around twice those obtained with the curvature drive which is the proof of a deep difference between the two mechanisms. Barriers driven by the $\mathbf{E}\times\mathbf{B}$ shear exhibit stronger relaxation events in all cases which can be understood by the non-linear nature of this mechanism. Finally, an exotic behaviour is obtained in some simulations for barriers with a mean efficiency around 90%: the standard deviation does not tend to zero and seems to be saturating at a given fixed value. These cases correspond to thin forcing regions ($\Delta = 4\rho_L$, red curves with '+' and '$*$' symbols) or smallest amplitudes of the forcing (pink curves with circles and squares as well as green curve with square symbols). In these cases, even if the barriers are in average quite efficient, the forcing region exhibits brutal relaxations for which the barrier loses totally its efficiency and turbulent avalanches are able to cross the forcing region. That is to say that fully stable transport barriers cannot be obtained with too thin or too low $\mathbf{E} \times \mathbf{B}$ shear or curvature drives. This phenomenon can be easily discerned on Figure 3.16 in which the radial-time 2D barrier efficiency is presented for the $\mathbf{E} \times \mathbf{B}$ shear mechanism with an amplitude of 6×10^{-3} and a width of $\Delta = 32\rho_L$.

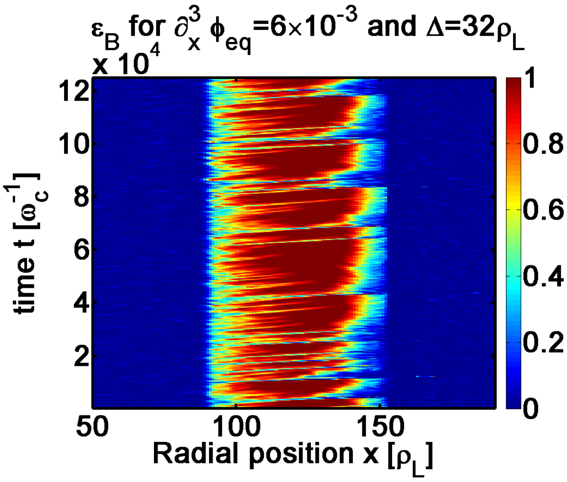

Figure 3.16: Barrier efficiency $\varepsilon_B(x,t)$ for a drive by the $\mathbf{E} \times \mathbf{B}$ shear with an amplitude of 6×10^{-3} and a width $\Delta = 32\rho_L$.

One can observe that the barrier is globally very efficient, above 90% but exhibits strong relaxation events coming from the inner region and propagating towards the barrier. Most of the events are able to cross the full width of the barrier while others are stopped in the middle. After the crossing of the avalanche and the collapse of the barrier, the barrier builds up again and the efficiency comes back close to 1.

3.4 Discussion, conclusion

In this chapter, two forcing mechanisms - induced by the shape of radial electric field profile - the $\mathbf{E} \times \mathbf{B}$ shear and the $\mathbf{E} \times \mathbf{B}$ curvature have been forced in our 2D slab simulations of Scrape-Off Layer. In our SOL simulations, most of the radial transport is usually carried by turbulence resulting from interchange instability. Such turbulence leads to avalanche-like events - called blobs - which propagate radially outward in ballistic motion. We drove the two mechanisms on a given radial extension and given amplitude and observed how radial transport is affected. We found that both $\mathbf{E} \times \mathbf{B}$ shear and $\mathbf{E} \times \mathbf{B}$ curvature are able to generate transport barriers as expected - respectively non-linearly and linearly - from theoretical point of view. The transport barriers lead to a drop of the total radial particle flux - due to the increase of the density which enhances particle parallel losses - and to a damping of turbulent events crossing the forcing area. In order to characterize these barriers, a criterion - called the barrier efficiency - measures the capability of a flux surface to reduce the radial transport by turbulence relatively of other transport mechanisms (here only the diffusive transport). It is found that both mechanisms can generate weakly, intermediate or strongly efficient transport barriers and that these barriers experienced relaxing events. Obviously, the barrier reinforces when the drive width or amplitude is increased. The standard deviation of the barrier efficiency measures the frequency and amplitude of relaxations without discerning the two quantities. For fully stable and efficient barriers, the standard deviation vanishes around the center of the imposed region and the peaks of the standard deviation at both extremities determine the turbulence penetration lengths inside the barrier. Barriers generated by $\mathbf{E}\times\mathbf{B}$ shear exhibit more frequent and brutal relaxations than by $\mathbf{E}\times\mathbf{B}$ curvature which permits to discriminate both effects.

The study of driven transport barriers in the Scrape-Off Layer is not directly relevant for the L-H transition. The first limit is that these transport barriers are forced in the Scrape-Off Layer while the edge transport barrier involved in the L-H transition is localized in the last closed field lines. The absence of feedback of turbulence on the mean $\mathbf{E}\times\mathbf{B}$ flows consists in the other main limit of the study as the interplay between turbulence and $\mathbf{E}\times\mathbf{B}$ shear is believed to be a key mechanism of this transition. Nevertheless, the study provides useful characteristics of the impact of $\mathbf{E}\times\mathbf{B}$ shear and $\mathbf{E}\times\mathbf{B}$ curvature on turbulence. In edge plasma, it is found that both mechanisms can impact on the shape and efficiency of edge transport barriers so that the two mechanisms are in competition in a real device. The calculation of first and second derivatives of the radial electric field from experimental measurements would permit to determine if the two mechanisms are involved in the L-H transition by comparison of the scan of width and amplitude of the forcing mechanism realized in this study. A comparison with experiments of biasing of the target plates would also be of great interest to have a better understanding of the interaction between turbulence and $\mathbf{E}\times\mathbf{B}$ flows in the Scrape-Off Layer.

Chapter 4

On the existence of spontaneous edge transport barriers in 2D and 3D slab simulations

- The amazing thing is that chaotic systems don't always stay chaotic. Sometimes they spontaneously reorganize themselves into an orderly structure.
- They suddenly become less chaotic?
- No, that's the thing. They become more and more chaotic until they reach some sort of chaotic critical mass. When that happens, they spontaneously reorganize themselves at a higher equilibrium level. It's called self-organized criticality.

Connie Willis, Bellwether

The L-H transition is characterized by the formation of an edge transport barrier in the pedestal. The key mechanisms and in particular the complex interplay between turbulence and $\mathbf{E} \times \mathbf{B}$ flows cannot be fully described using driven transport barriers. In this chapter, we focus on the existence and dynamics of spontaneous edge transport barriers in slab configuration using our 2D and 3D codes. Special attention is given to the role played by the ion energy channel and especially through the so-call generalized vorticity. The latter is indeed pointed out as a fundamental player of the spontaneous transport barriers obtained with the HESEL code [Rasmussen 16]. We first focus on spontaneous transport barriers obtained in Tokam2D in the full anisothermal model as an extension of the barriers obtained with the biperiodic isothermal version [Norscini 15]. The effect of electron and ion energy channels is investigated and a reduced isothermal model is developed in order to understand key players of barriers dynamics. In the second section, a discussion is started on the limits of bidimensional modelling as well as on the limits of slab configuration in the framework of the L-H transition. Finally, the parallel dynamic is added in our study by using Tokam3X in slab configuration in order to perceive the importance of 3D effects.

4.1 Spontaneous edge barriers in 2D slab geometry with Tokam2D

We first study the existence of edge transport barriers in our 2D slab code Tokam2D. Spontaneous edge transport barriers were found to appear in Tokam2D simplest isothermal and bi-periodic model [Norscini 15] when closed field lines are included in the model. We first try to recover these spontaneous barriers in the new full thermal version of Tokam2D presented at 2.6.2. The parameters used in this chapter are slightly different of those of the previous one: we use a curvature parameter $g = 10 \times 10^{-4}$, sheath conductivities $\sigma_N = \sigma_W = 10^{-4}$, diffusion coefficients $D_N = \nu = 10^{-2}$ and the sheath heat transfer coefficients $\gamma_{i/e}$ are calculated analytically in Appendix B. The simulated domain, when not explicitly detailed, is $L_x = L_y = 256\rho_L$ with a mesh grid $N_x = N_y = 256$ so that $dx = dy = \rho_L$. The LCFS is localized at the center of the radial domain at $x_{\text{sep}} = 128.5\rho_L$.

4.1.1 Full thermal version

4.1.1.1 Spontaneous transport barriers in closed field line region

The full thermal version is first used without putting energy on the ion channel using $T_i^{\text{inj}} = 0$ so that the model is close to the model with thermal electrons (with $T_e^{\text{inj}} = 1$) and cold ions. The system evolves until it reaches a quasi steady-state. The barrier efficiency obtained in this quasi steady-state is presented in Figure 4.1. On the left panel, for a long simulation of $10^6\omega_c^{-1}$, one can observe the existence of spontaneous transport barriers. The first observation that we can make is that barriers appear only in the closed field line region. Three barriers, oscillating in time, exist in this simulation: on the inner region of closed field lines, a large and efficient barrier develops between $x = 10$ and $x = 55\rho_L$. A low efficient barrier can also be notice around the LCFS with a thin radial extension of $8\rho_L$. The last one is located in the middle of the closed field line domain and extends from $x = 70$ to $x = 110\rho_L$. Fluctuations of these barriers are nearly periodic with large amplitude relaxations in which the barriers lose totally their ability to stop radial propagation of turbulence (i.e $\varepsilon_B \to 0$). A succession of quasi-periodic cycles of formations and relaxations of the barrier can be observed, especially for the left and the central barriers while the fluctuations of the barrier at the LCFS seem to be more random.

34 of these cycles can be counted in this simulation of $10^6\omega_c^{-1}$ which gives an average cycle for the build and the relaxation of the barrier around $3\times10^4\omega_c^{-1}$. In order to better characterize these barrier cycles, the barrier efficiency obtained from a more discretized simulation in time of $10^5\omega_c^{-1}$ is presented on the right panel of Figure 4.1 with a succession of nearly 4 barrier cycles. At the beginning of the simulation, between $t = 0$ and $t = 1.8\times10^4\omega_c^{-1}$, the barrier is already built with an efficiency close to 100%. The outer part of the central barrier, around $x = 100\rho_L$, fluctuates radially in time. One can notice that these fluctuations start from the barrier and propagate radially outward in the direction of the LCFS. It corresponds thus to turbulent events appearing on the outer extremity of the barrier and propagating radially to open field line region with a ballistic motion. Conversely, the inner extremity of the central barrier as well as the outer one of the left barrier - respectively at $x = 75\rho_L$ and $x = 55\rho_L$ - do not undergo radial fluctuations of such amplitudes. The first relaxation of the barriers occurs just before $t = 2\times10^4\omega_c^{-1}$. The radial origin of the breaking down of the barriers cannot be easily measured from Figure 4.1 but appears to be located inside the central barrier, i.e between $x = 80$ and $x = 128\rho_L$. However, we can clearly observe that the barrier relaxation propagates inwardly from these last closed field lines into the inner radial part of the domain through a ballistic event. This is why the relaxations of both left and central barriers are always correlated in time. The average speed of barrier relaxations is measured and corresponds to a radial propagation of about 1% of the acoustic velocity c_s. The average lifetime of the barriers is slightly inferior to $2\times10^4\omega_c^{-1}$ which corresponds to almost two thirds of the cycle duration. When the barrier is down, one can observe especially around $t = 5.5\times10^4$ and $t = 8\times10^4\omega_c^{-1}$ that turbulent events - propagating radially inward and coming from the LCFS region - prevent the barrier to build up again. Finally, the left barrier is the first to form again from the outer to the inner region while the central barrier develops on the opposite side, from the inner region in direction of the LCFS.

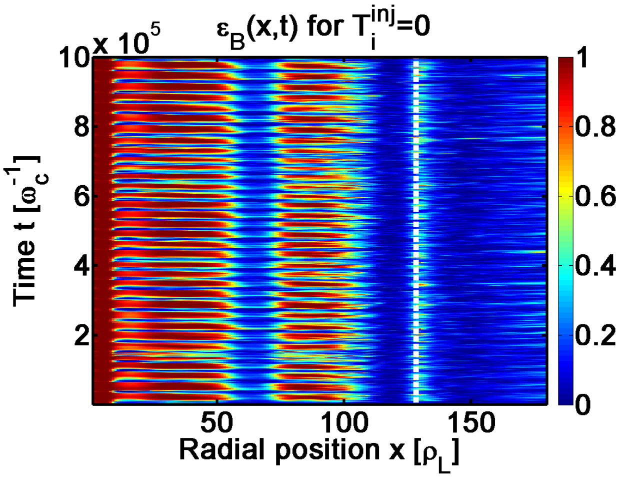

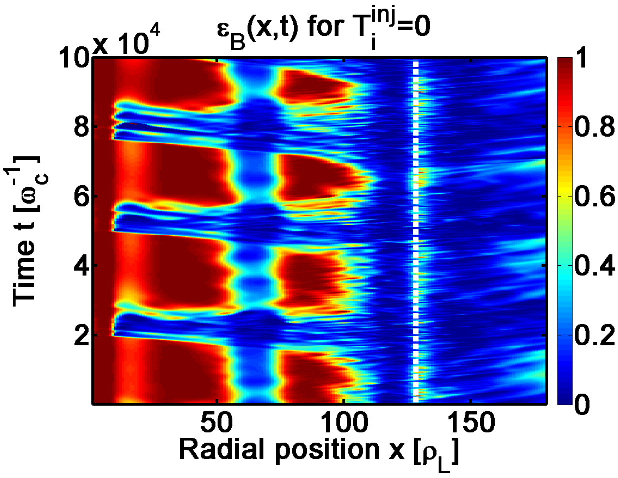

Figure 4.1: 2D - radial and time - maps of barrier efficiency $\varepsilon_B(x,t)$ for $T_i^{\text{inj}} = 0$ and $T_e^{\text{inj}} = 1$:
Left panel: for a long simulation of $10^6\omega_c^{-1}$.
Right panel: for a short simulation of $10^5\omega_c^{-1}$.

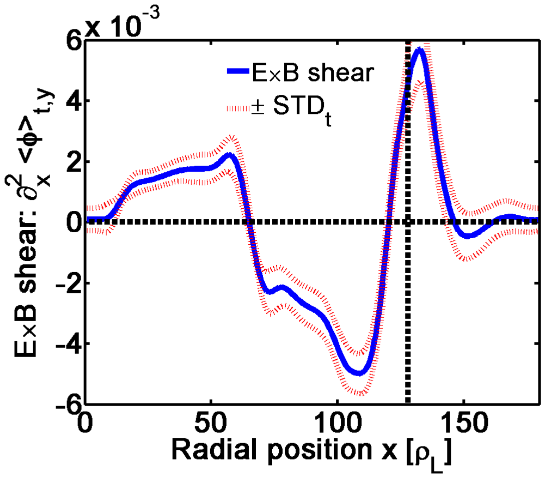

Figure 4.2: Radial profile of mean $\mathbf{E} \times \mathbf{B}$ shear $\partial_x^2 \langle \phi \rangle_{t,y}$ with time standard deviation for the long simulation of $10^6 \omega_c^{-1}$.

At this point, one can wonder what determines the number of transport barriers as well as the radial extension of each barrier. To answer this question, the radial profile of the time and poloidally averaged $\mathbf{E} \times \mathbf{B}$ shear is presented on Figure 4.2. The plot is horizontally aligned with the left panel of Figure 4.1, so that a vertical line between the two plots corresponds to the same radial position of simulated plasma. It shows that the radial regions without transport barriers - around $x = 60\rho_L$ and $x = 115\rho_L$ correspond to radial positions where the mean $\mathbf{E} \times \mathbf{B}$ shear is close to zero. Barriers are thus extending radially between two zeros value of the $\mathbf{E} \times \mathbf{B}$ shear. This seems in qualitative agreement with forcing barriers of Chapter 3: a sufficiently large $\mathbf{E} \times \mathbf{B}$ shear prevents the formation and the radial propagation of turbulence. The sign of the $\mathbf{E} \times \mathbf{B}$ shear does not change the existence of transport barrier: the left barrier is obtained with a positive shear while the central one undergoes a negative shear. Finally, the maximal shear magnitude is localized just after the LCFS and the weakly efficient barrier at the LCFS is not able to propagate into the Scrape-Off layer in which the radial transport is fully dominated by turbulence. That is to say that the parallel dynamic play an important role on the existence of edge transport barriers.

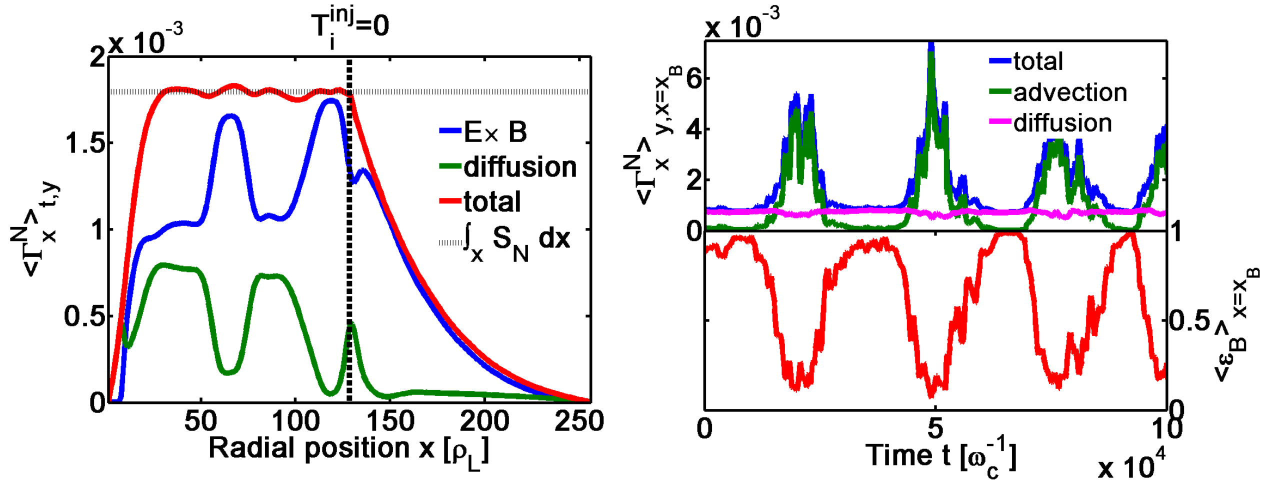

Figure 4.3:
Left panel: radial profiles of mean turbulent, diffusive and total radial fluxes for the long simulation of $10^6\omega_c^{-1}$.
Right panel: time evolution inside the central barrier ($x_B = [80;100]$) of mean total, $\mathbf{E}\times\mathbf{B}$ and diffusive fluxes $\langle\Gamma_x^N\rangle_{y,x=x_B}$ (top panel) and mean barrier efficiency $\langle\varepsilon_B\rangle_{x=x_B}$ (bottom panel) for the short simulation of $10^5\omega_c^{-1}$.

The global change in the nature of radial transport inside the barriers can be observed on the left panel of Figure 4.3. It exhibits the radial profiles of mean $\mathbf{E}\times\mathbf{B}$, diffusive and total radial fluxes inside the central barrier: $x = x_B = [80, 100]$. It is essential to point out that the total radial flux is constant in closed field lines and equal to the forcing flow. This latter corresponds to the integral of the particle source $\int_x S_N dx = 1.79\times10^{-3}n_0c_s$ since no particle are lost at the inner radial boundary. The two regions of closed field lines without transport barriers around $x = 60\rho_L$ and $x = 115\rho_L$ are fully dominated by turbulence while the diffusive contribution is almost negligible. Conversely, the diffusive flux is strongly enhanced inside the two barriers and contributes in average at around 40% of the total radial transport while the turbulent flux has been significantly reduced by a factor of 1.5. In open field lines, the total flux is decreasing exponentially due to particle losses at the limiter targets in the parallel direction and the radial transport is found to be fully turbulent with an almost vanishing diffusive contribution. These mean radial profiles specify the spatial change of the transport nature but do not provide any informations on the barrier dynamics and especially during barrier relaxations. To analyse the cycles of the barrier, the time evolution of total, $\mathbf{E}\times\mathbf{B}$ and diffusive radial fluxes - averaged poloidally and inside the central barrier ($x_B = [80, 100]$) - and the time evolution of the barrier efficiency for the same central barrier are respectively presented on top and bottom parts of the right panel of Figure 4.3. It is found that when the efficiency of the barrier is minimal - around $t = 5\times10^4\omega_c^{-1}$ for example - the total radial flux is mostly the consequence of turbulent transport and exhibits strong amplitude variations up to $7\times10^{-3}n_0c_s$. On the other hand, the diffusive flux only exhibits small amplitude fluctuations around a constant value of $8\times10^{-4}n_0c_s$. When the barrier builds up, the $\mathbf{E}\times\mathbf{B}$ turbulent flux strongly drops down to a quasi zero magnitude which leads the total flux to be equal to the diffusive one. The latter is not strongly impacted by the relaxation or the formation of the barrier which means that the barrier cycle is too fast in comparison with the characteristic time of density rise. Indeed, when the barrier appears, the upstream density grows slowly but the barrier undergoes a relaxation before the density gradient is large enough to enhance significantly the diffusive flux.

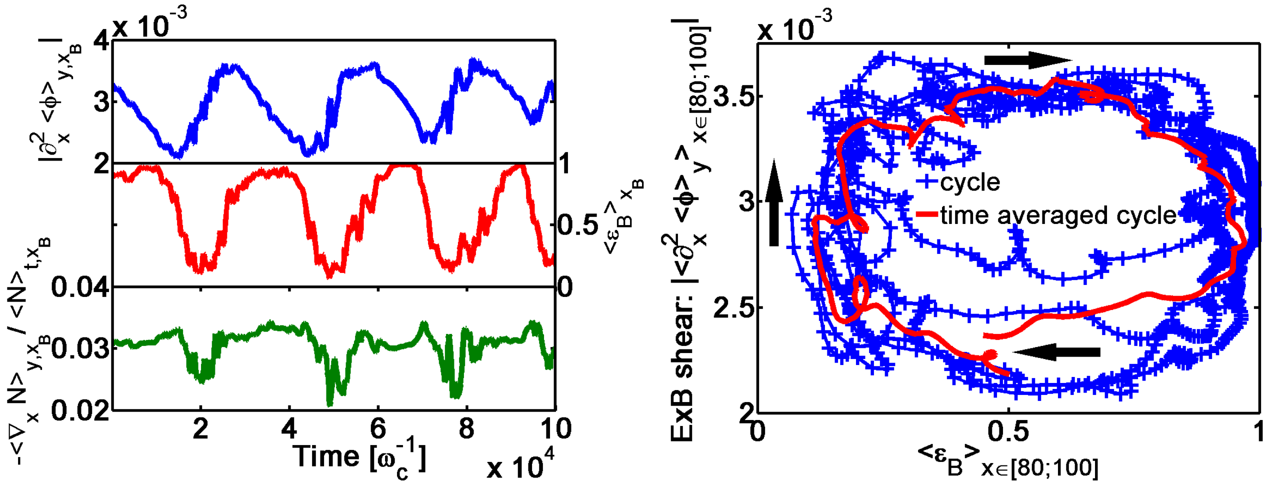

Figure 4.4:
Left panel: Time evolution of $\mathbf{E}\times\mathbf{B}$ shear (top panel, in blue), barrier efficiency (central panel, in red) and normalized density gradient (bottom panel, in green) for $x \in x_B = [80; 100]$ corresponding to the radial position of the central barrier from the short simulation of $10^5\omega_c^{-1}$.
Right panel: Illustration of the quasi hysteresis cycle between the $\mathbf{E}\times\mathbf{B}$ shear magnitude and the barrier efficiency averaged inside the central barrier ($x_B = [80; 100]$). Each marker '+' corresponds to a time save of the Tokam2D code and consecutive time saves are connected by solid lines clockwise (black arrows).

At this point, we underline the fundamental role played by the $\mathbf{E}\times\mathbf{B}$ shear on the spatial development of edge spontaneous transport barriers as well as the dynamic of the change in the nature of radial transport. In order to understand the interplay between the spontaneous barriers and the $\mathbf{E}\times\mathbf{B}$ shear, the time evolution of $\mathbf{E}\times\mathbf{B}$ shear magnitude, barrier efficiency as well as normalized density gradient are respectively plotted - from top to bottom - on the left panel of Figure 4.4 for the central barrier so that $x_B = [80; 100]$. The time interval corresponds to the short simulation of $10^5\omega_c^{-1}$ (right panel of Figure 4.1) and the 4 barrier cycles are clearly visible. At $t = 0$, the central barrier is fully efficient ($\varepsilon_B\rangle 0.9$), the $\mathbf{E}\times\mathbf{B}$ shear magnitude is maximal ($|\partial_x^2\phi| \sim 3.2\times10^{-3}$) and the normalized density gradient is maximal too ($-\nabla_x\langle N\rangle_{y,x=x_B}/\langle N\rangle_{y,x=x_B} \sim 3\times10^{-2}\rho_L^{-1}$). Up to $t = 10^4\omega_c^{-1}$, the barrier efficiency and the normalized density gradient stay globally unchanged while the $\mathbf{E}\times\mathbf{B}$ shear magnitude decreased progressively down to 2.4×10^{-3}. At this point, the barrier efficiency starts to drop brutally to reach an efficiency of only 10% between $t = 2\times10^4\omega_c^{-1}$ to $t = 2.3\times10^4\omega_c^{-1}$, time at which the barrier builds up again. One can notice that the normalized density gradient is strongly decreasing by a factor 2 when the efficiency drops meaning that density profile is flattened due to radial turbulent transport. Meanwhile, the $\mathbf{E}\times\mathbf{B}$ shear magnitude keeps decreasing down to reach its minimum value at $t = 1.5\times10^4\omega_c^{-1}$; the shear magnitude is then increasing up to the end of the cycle around $t = 2.7\times10^4\omega_c^{-1}$ and a new similar cycle can then start. A strong time correlation is thus observed between the $\mathbf{E}\times\mathbf{B}$ shear, the barrier efficiency and the normalized density gradient in agreement with expected impact of $\mathbf{E}\times\mathbf{B}$ shear on turbulence. To better analyse the interplay between $\mathbf{E}\times\mathbf{B}$ shear and transport barrier dynamic, the magnitude of this shear is plotted as a function of the barrier efficiency on the right panel of Figure 4.4. Each '+' symbol corresponds to a time save of the Tokam2D code for the short simulation of $10^5\omega_c^{-1}$. Consecutive time saves are connected by a solid line and reveal a strong correlation between the two variables. This correlation takes the form of an hysteresis cycle which must be read clockwise. If we start arbitrarily at low $\mathbf{E}\times\mathbf{B}$ shear magnitude and low barrier efficiency - at the bottom left corner and corresponding for example to the time $1.7\times10^4\omega_c^{-1}$ on the left panel - the barrier efficiency remains weak while the $\mathbf{E}\times\mathbf{B}$ shear magnitude keeps increasing up to a threshold around $|\partial_x^2\phi| = 3.5\times10^{-3}$. At this point, the $\mathbf{E}\times\mathbf{B}$ shear seems to be high enough to damp turbulence and the barrier is building up. The magnitude of the shear is constant until the barrier becomes fully dominated by diffusive transport (top right corner of the plot). Without turbulence, we can assume that the main source of zonal flows disappears and thus the $\mathbf{E}\times\mathbf{B}$ shear magnitude begins to decrease down to its initial value at the beginning of the cycle. Since the shear is now weak, the turbulence is developing again and leads to the collapse of the barrier and a new cycle occurs. The 4 cycles of barrier formation and relaxation are plotted in blue and we observe a similar behaviour for each of them. An averaging of the 4 cycles has been realized and leads to the time averaged cycle in red which follows the scheme detailed above. In a nutshell, the interplay between turbulence and $\mathbf{E}\times\mathbf{B}$ shear is responsible of the barrier cycles observed in the simulation: the $\mathbf{E}\times\mathbf{B}$ shear generates the transport barrier while the turbulence is a source for the $\mathbf{E}\times\mathbf{B}$ shear generation in agreement with simple predator-prey model [Diamond 94].

4.1.1.2 Influence of electron energy channel

The previous section focuses on spontaneous edge transport barriers obtained without putting energy on the ion channel ($T_i^{\text{inj}} = 0$). However, as mentioned in section [Rasmussen 16], the ion heat channel is expected to be a key player on edge transport barrier formation and dynamics so that one can wonder what is the impact of ion energy channel on spontaneous transport barriers obtained in our simulations. The next section focuses on answering this question. But first, we focus on the impact of the electron energy channel which is also expected to play a role on mean fields especially in the open field line region.

A scan of the electron injection temperature is realized. Simulations with $T_e^{\text{inj}} = 0.5$ and $T_e^{\text{inj}} = 2$ are left evolving until a quasi steady-state is reached in addition to the previous reference simulation with $T_e^{\text{inj}} = 1$. Ion energy channel is still disabled in all these simulation by using $T_i^{\text{inj}} = 0$. 2D - radial and time - maps of the barrier efficiency ε_B for half and twice the reference electron injection temperature are respectively presented on the left and right panels of Figure 4.5 and have to be compared to the right panel of Figure 4.1. The time duration of all these simulations is $10^5\omega_c^{-1}$. One can observe a strong impact of the electron injection temperature on barrier dynamics. Barriers behaviour with $T_e^{\text{inj}} = 0.5$ is relatively close to the reference simulation with $T_e^{\text{inj}} = 1$. Indeed, three barriers are also obtained, located nearly at the same radial positions and exhibiting similar cycles of relaxation and formation. One can however notice that both left and central barriers are less efficient with the smaller injection temperature and these two barriers never become fully efficient in this case ($\max_{x\in[20;50]\cup[80:100]}\varepsilon_B \lesssim 0.9$). Barrier relaxations are also less frequent as we only count 3 cycles in this simulation against 4 in the reference one. Finally, the thin barrier located at the LCFS is stronger with $T_e^{\text{inj}} = 0.5$ than with $T_e^{\text{inj}} = 1$ and propagates sometimes towards open field lines in a ballistic motion. This barrier is also correlated in time with the central and the left ones. Concerning the simulation with $T_e^{\rm inj} = 2$, the dynamic and the localisation of the barriers are strongly different. First, only two barriers can be observed in the simulation: a very thick one starting at the inner radial boundary $x = 10$ and up to $x = 80\rho_L$ with a strong efficiency and large amplitude relaxations (from $\varepsilon_B = 1$ to 0) and a low efficient barrier - with a maximal efficiency around 60% at $t = 5 \times 10^4 \omega_c^{-1}$, which extends from $x = 100$ to the LCFS at $x = 128.5\rho_L$. The thick barrier allows us to observe an interesting barrier behaviour: around $t = 2 \times 10^4$ and around $t = 5 \times 10^4 \omega_c^{-1}$, inward turbulent events are propagating inside the barrier without succeeding to cross it completely. It results that the barrier does not exhibit a complete relaxation and takes back its original width rapidly.

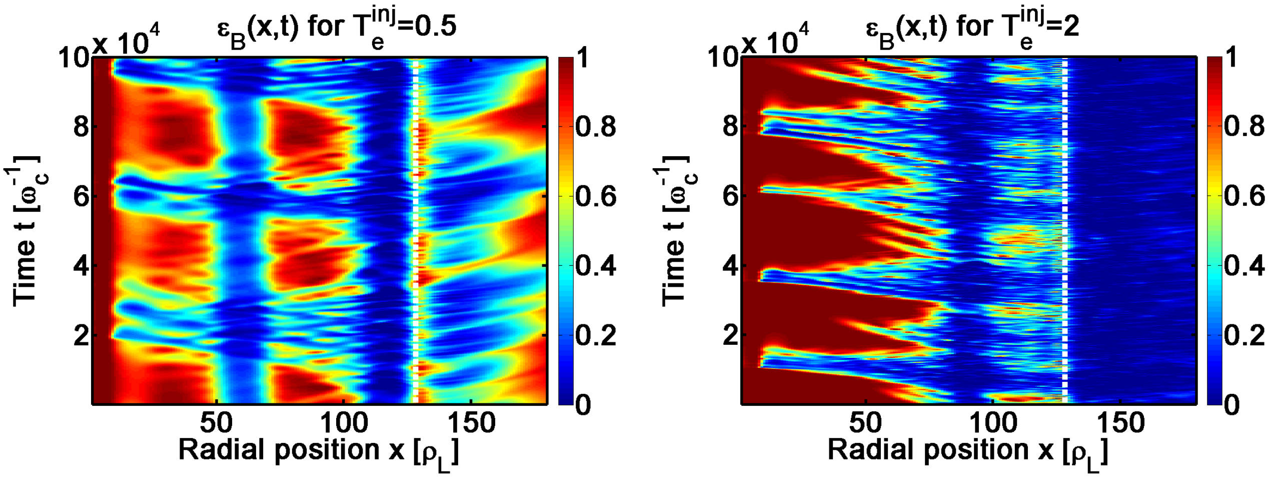

Figure 4.5: 2D - radial and time - maps of barrier efficiency $\varepsilon_B(x,t)$ for $T_i^{\rm inj} = 0$ and:
Left panel: $T_e^{\rm inj} = 0.5$.
Right panel: $T_e^{\rm inj} = 2$.

Such discrepancies on the number and strength of barriers between the simulation with $T_e^{\rm inj} = 2$ and the two other ones can be explained by the shape of the radial profile of $\mathbf{E} \times \mathbf{B}$ shear, displayed on the left panel of Figure 4.6. Similar radial profiles of $\mathbf{E} \times \mathbf{B}$ shear are obtained with $T_e^{\rm inj} = 0.5$ and $T_e^{\rm inj} = 1$ for which the zero values of the shear are located around the same radial locations in closed field lines ($x = 60\rho_L$ and $x = 120\rho_L$). Such shapes - really close one to each other - explain why the radial distribution of the barriers are quasi identical in the two simulations. The difference observed in the maximal efficiency of the barriers can also be clarified as the magnitude of the $\mathbf{E} \times \mathbf{B}$ shear is stronger in the reference case with $T_e^{\rm inj} = 1$ leading to a more efficient reduction of radial turbulent transport. Meanwhile, the $\mathbf{E} \times \mathbf{B}$ shear obtained with $T_e^{\rm inj} = 2$ cancels only once in closed field lines - at $x = 80\rho_L$ - which leads to the existence of only two barriers in this simulation. The strong efficiency of the left thick barrier results of the large magnitude of the $\mathbf{E} \times \mathbf{B}$ shear which is twice to three times larger compared to simulations with lower electron injection temperature. However, it does not explain why the barrier located at last closed field lines has a so low ability to stop radial propagation of turbulence whereas the $\mathbf{E} \times \mathbf{B}$ shear magnitude is maximal here.

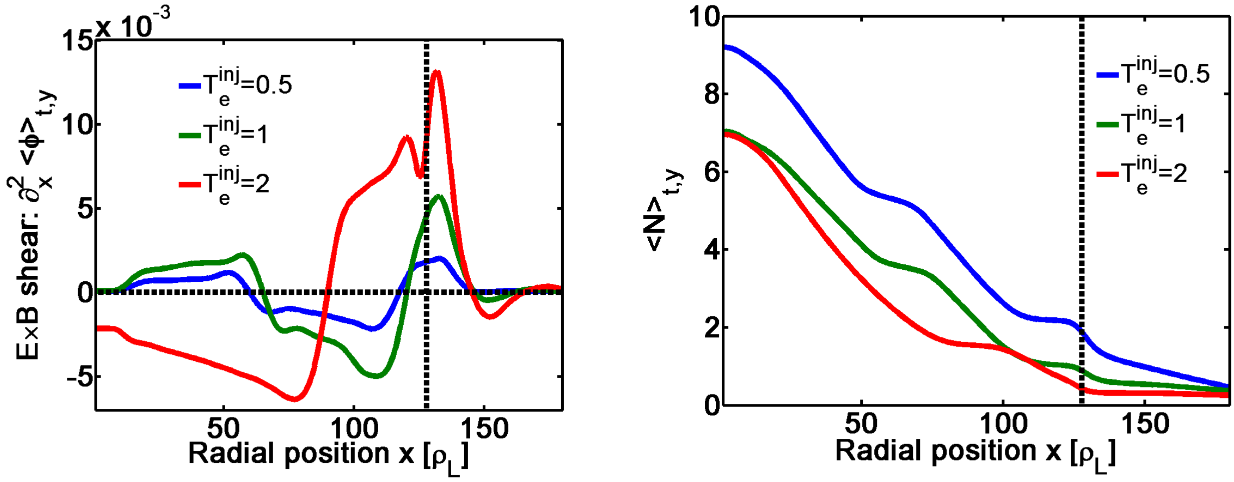

Figure 4.6: Scan of electron injection temperature, radial profiles of time and poloidally averaged:
Left panel: $\mathbf{E} \times \mathbf{B}$ shear: $\partial_x^2 \langle \phi \rangle_{t,y}$.
Right panel: density $\langle N \rangle_{t,y}$.

The consequences of electron injection temperature on particle confinement in closed field lines can be studied on the right panel of Figure 4.6 in which the radial density profiles are plotted for each simulation. The radial positions of the barriers can be recovered on density profiles as the profiles flatten at radial positions without barriers for example at $x = 60\rho_L$ for $T_e^{\text{inj}} = 0.5$ and $T_e^{\text{inj}} = 1$. The particle content in the whole simulated plasma decreases when the electron injection temperature is increased. The particle confinement time τ_N is defined - similarly to the energy confinement time - as the ratio between core particle content and the total radial flux at the LCFS:

$$\tau_N = \frac{\int_{x \in \text{CFL}} \langle N \rangle_{t,y}}{\langle \Gamma_x^{\text{tot}} \rangle_{t,y}(x_{\text{sep}})} \tag{4.1}$$

As seen previously, the total radial flux in the whole closed field line region - and thus also at the LCFS - is constant and depends only on the particle source which is the same in the three simulations. It follows that the particle confinement time only depends on the core particle confinement and thus decreases with an increase of electron injection temperature. One can however notice that the ratio between density at the inner boundary ($x = 0$) and at the LCFS ($x = 128.5\rho_L$) increases with the electron temperature: this ratio is equal to 5 for $T_e^{\text{inj}} = 0.5$, 8 for $T_e^{\text{inj}} = 1$ and reaches 17 for $T_e^{\text{inj}} = 2$. In order to explain this observation and to better understand why the $\mathbf{E} \times \mathbf{B}$ shear is so affected by the electron temperature, radial profiles of electrostatic potential are presented in Figure 4.7.

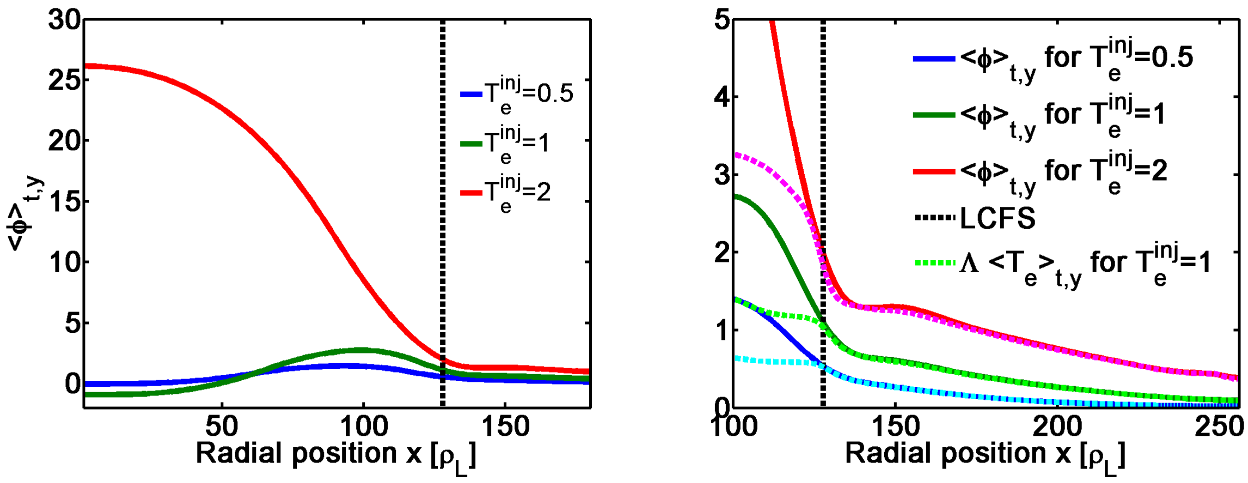

Figure 4.7: Radial profiles of time and poloidally averaged electrostatic potential $\langle\phi\rangle_{t,y}$:
Left panel: in the whole closed field line region and first open field lines.
Right panel: with a zoom in the Scrape-Off Layer region and last closed field lines.

On the left panel, potential profiles are displayed for the whole simulated closed field line region as well as the beginning of the Scrape-Off Layer region. In closed field lines, potential profile exhibits a large amplitude parabolic shape for $T_e^{\text{inj}} = 2$ while the profile are flatter for lower temperatures. Such discrepancy explains why the magnitude and shape of $\mathbf{E}\times\mathbf{B}$ shear profiles are so different. On the right panel, a zoom is made on the whole Scrape-Off Layer and the last closed field lines. Potential profiles are expected to be proportional to electron temperature profile due to Bohm's boundary conditions: $\langle\phi\rangle_{t,y} \sim \Lambda\langle T_e\rangle_{t,y}$. An excellent agreement is found with these theoretical profiles in our simulations for the whole open field line region. As the electrostatic potential follows the electron temperature - which is an exponential decay in the SOL due to parallel losses at the target plates - a larger electron injection temperature leads to a larger temperature gradient. Moreover, in closed field lines, the potential is unconstrained and is thus free to evolve regardless of electron temperature profiles. It follows that the electrostatic potential gradient is stronger when the electron injection temperature increases and so is the $\mathbf{E}\times\mathbf{B}$ shear close to the LCFS. Finally, another important effect of electron temperature has not been mentioned yet: its contribution on control parameter such as effective curvature and more especially on the acoustic velocity $c_s = \sqrt{\widehat{T_e}}$ which controls the level of particle and current parallel losses. Larger electron temperature leads to larger acoustic velocity, to larger parallel particle and current losses and thus to weaker SOL particle content.

In conclusion, electron temperature tends to enhance the $\mathbf{E}\times\mathbf{B}$ shear magnitude close to the LCFS due to sheath physics in the SOL but this effect is finally less significant on density profile than the impact of electron temperature on the acoustic velocity which controls particle damping in the parallel direction.

4.1.1.3 Influence of ion energy channel

As for the electron injection temperature, a scan of ion injection temperature is realized to understand the influence of the ion channel on transport barrier formation and dynamics. A constant electron injection temperature of $T_e^{\mathrm{inj}} = 1$ is used in each simulation. In addition to the reference case without ion energy ($T_i^{\mathrm{inj}} = 0$), two simulations with $T_i^{\mathrm{inj}} = 0.1$ and $T_i^{\mathrm{inj}} = 1$ are run up to quasi steady-state. The 2D - radial and time - maps of barrier efficiency are displayed in Figure 4.8 for simulations of $10^5\omega_c^{-1}$ duration. Only two barriers are developing on both panels - on the left for $T_i^{\mathrm{inj}} = 0.1$ and on the right for $T_i^{\mathrm{inj}} = 1$ - while three are developing in the reference case without the ion channel. The two barriers are very efficient: the left one extends from the inner radial boundary to $x = 75\rho_L$ and does not exhibit any complete relaxations. For $T_i^{\mathrm{inj}} = 0.1$, two turbulent events - one at $t = 10^4\omega_c^{-1}$ and one around $t = 6 \times 10^4\omega_c^{-1}$ - are close to crossing the entire barrier thickness from the edge towards the inner core region but these events are finally stopped and absorbed by the barrier. For $T_i^{\mathrm{inj}} = 1$, the penetration length of turbulent events inside the left barrier is even smaller: the largest turbulent event coming from outer plasma is not able to reach a radial position inner than $x = 45\rho_L$. An increase of ion temperature energy leads thus to fewer relaxations of the inner barrier which is thus more stable and efficient. The second barrier is located just before the LCFS, between $x = 90$ and $x = 125\rho_L$. For $T_i^{\mathrm{inj}} = 1$, one can notice that some fluctuations of the outer extremity of the barrier are penetrating into the open field line region. These barriers undergo relaxation events in which they lose their turbulence stopping capability. Barrier relaxations are less frequent for $T_i^{\mathrm{inj}} = 0.1$ than for $T_i^{\mathrm{inj}} = 1$, but the barrier takes longer to recover its original efficiency.

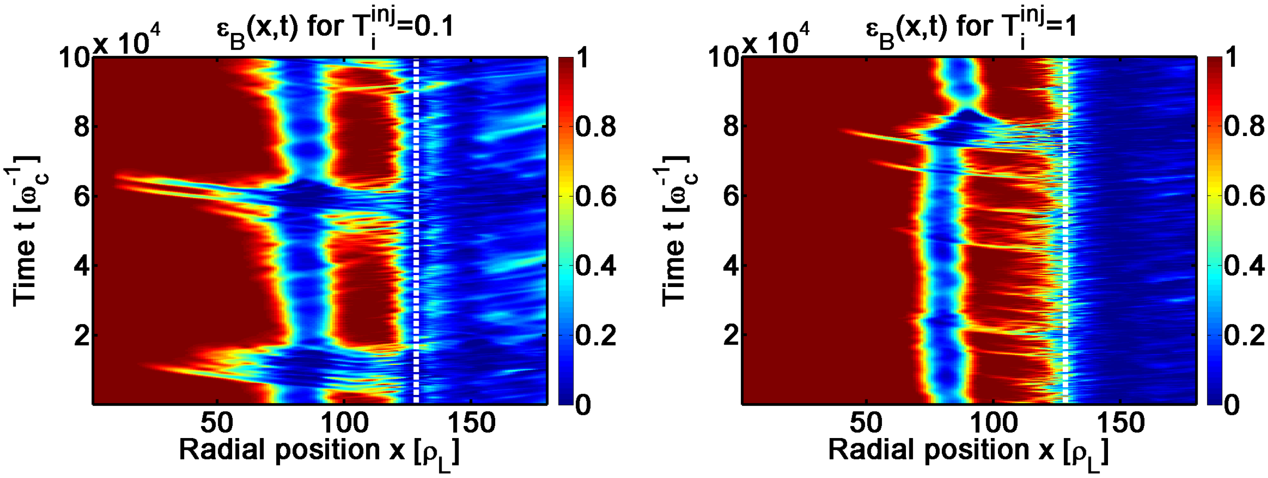

Figure 4.8: 2D - radial and time - maps of barrier efficiency $\varepsilon_B(x, t)$ for $T_e^{\mathrm{inj}} = 1$ and:
Left panel: $T_i^{\mathrm{inj}} = 0.1$.
Right panel: $T_i^{\mathrm{inj}} = 1$.

In contrast with the scan of electron temperature injection, an increase of the input ion temperature leads to an improvement of the particle confinement as it can be seen on density radial profiles on the left panel of Figure 4.9. Both particle content in closed field lines and the ratio between inner core density and the density at the LCFS attest of the strong improvement of the particle confinement. By activating the ion channel, the density at the inner radial boundary doubles with an input ion temperature of $T_i^{\mathrm{inj}} = 0.1$ which represents only 10% of the electron injection temperature. With a larger ion energy - $T_i^{\mathrm{inj}} = 1$ - the density keeps increasing but the growth is strongly reduced. In fact, only the barrier close to the LCFS leads to a further increase of the density profile because the inner barrier is already fully efficient with $T_i^{\mathrm{inj}} = 0.1$ so that the radial particle transport results only of diffusion.

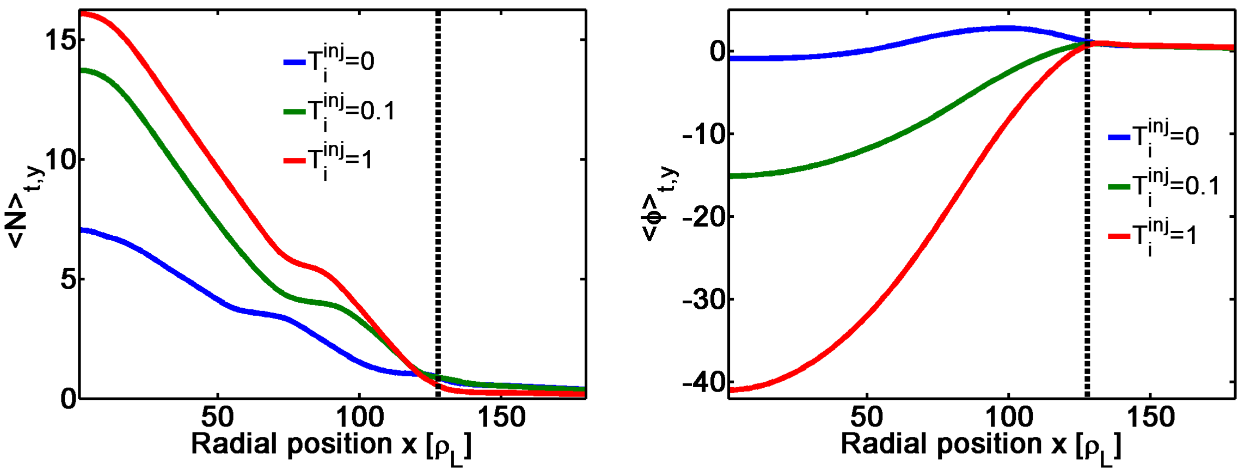

Figure 4.9: Radial profile of time and poloidally averaged:
Left panel: density $\langle N \rangle_{t,y}$
Right panel: electrostatic potential $\langle \phi \rangle_{t,y}$

Radial profiles of mean electrostatic potential $\langle \phi \rangle_{t,y}$ are presented on the right panel of Figure 4.9 for the three ion injection temperatures. Profiles are constrained in the SOL by the electron temperature profile so that $\langle \phi \rangle_{t,y} \sim \Lambda \langle T_e \rangle_{t,y}$. In closed field lines, there is no such direct constraint on potential profile. This latter is thus fixed at the LCFS by the value of electron temperature and have to fulfil Neumann's boundary condition in the inner boundary: $\partial_x \langle \phi \rangle_{t,y}(x=0) = 0$. The potential behaves in closed field lines like a string held by one end and relatively free to evolve somewhere else. The resulting shape is a parabolic branch which increases in magnitude with the ion injection temperature. The associated electric field and $\mathbf{E} \times \mathbf{B}$ shear, which are proportional to first and second radial derivatives of this electrostatic potential are presented respectively on the left and right panels of Figure 4.10. Without the ion channel, the radial electric field exhibits small negative and positive variations in closed field lines with a magnitude lower than 0.1. When a non zero ion injection temperature is used, the electric field well before the LCFS steepens in the whole closed field line region. As a consequence, the positive part of the radial electric field becomes smaller and is shifted into the SOL. Note that the Neumann boundary condition on electrostatic potential leads to a zero Dirichlet boundary condition on the electric field at this inner boundary. The impact of this inner radial boundary on the existence and dynamic of edge transport barriers will be discussed in a next section. Consequently, the $\mathbf{E} \times \mathbf{B}$ shear is strongly impacted by taking into account the ion energy channel. The shift of the extrema of the radial electric field from $x = 60\rho_L$ for $T_i^{\text{inj}} = 0$ to $x = 80\rho_L$ with $T_i^{\text{inj}} = 0.1$ and $T_i^{\text{inj}} = 1$ leads to a shift of the zero value of the $\mathbf{E} \times \mathbf{B}$ shear and thus to a shift of the barrier positions. The shear magnitude is strongly increased inside the barriers and especially for the inner barrier and at the LCFS. The resulting shear at the LCFS reaches a magnitude close to 3×10^{-2} which is twice the magnitude obtained in the previous section with $T_e^{\text{inj}} = 2$.

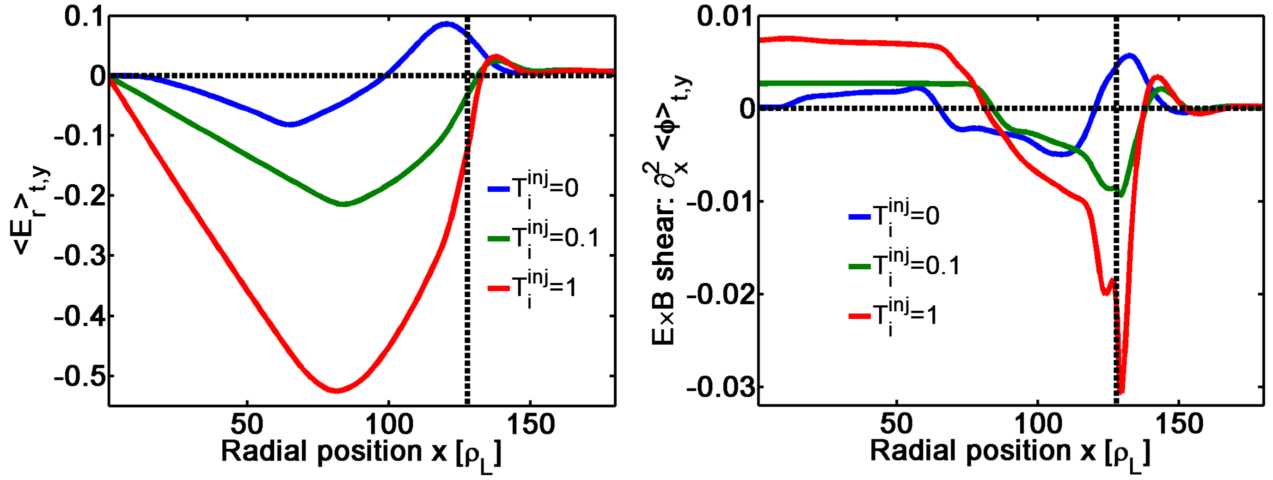

Figure 4.10: Radial profile of:
Left panel: mean radial electric field $\langle E_r \rangle_{t,y} = -\partial_x \langle \phi \rangle_{t,y}$
Right panel: mean $\mathbf{E} \times \mathbf{B}$ shear $\partial_x^2 \langle \phi \rangle_{t,y}$

Finally, we analyse the correlation between the $\mathbf{E} \times \mathbf{B}$ shear and the barrier efficiency for the simulation with $T_i^{\mathrm{inj}} = 1$. We focus on the central barrier between $x = 100\rho_L$ and $x = 110\rho_L$ which presents more barrier fluctuations. The result is presented in Figure 4.11. As the barrier does not exhibit strong relaxations, the previous hysteresis cycles cannot be recovered in this simulation. The connecting solid line between the markers '+' - which represents successive time saves - reveals nevertheless a similar trend between $\mathbf{E} \times \mathbf{B}$ shear magnitude and the rare relaxations of the barrier: the barrier experiences significant relaxations only when the $\mathbf{E} \times \mathbf{B}$ shear magnitude is under a certain threshold around 8.5×10^{-3}.

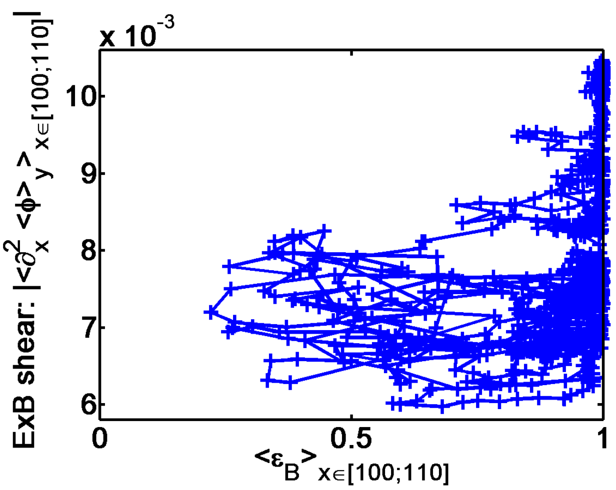

Figure 4.11: Correlation between $\mathbf{E} \times \mathbf{B}$ shear magnitude and barrier efficiency inside the right barrier for $x \in [100; 110]$ and for $T_i^{\mathrm{inj}} = 1$.

In summary, the ion energy channel strongly modifies the spatial distribution and dynamics of transport barriers by modifying the $\mathbf{E} \times \mathbf{B}$ shear profile. Its impact on edge particle confinement is prevailing over the electron energy channel. In both cases, an increase of injected energy is associated with an increase of the $\mathbf{E}\times\mathbf{B}$ shear magnitude, especially near the LCFS and in the inner part of closed field lines. We also notice less frequent barrier relaxations for larger ion injected energy. If the electron temperature impacts mainly on the parallel losses and the electrostatic profile in the Scrape-Off Layer, the effect of ion energy channel is less straightforward.

4.1.2 Reduced isothermal model

Ion and electron energy channels are at first sight very close to each other. Indeed, the two equations governing electron and ion energy evolution are quasi-identical. However - as seen previously - the impact of a non isothermal electron temperature leads to a modification of electrostatic potential in open fields lines due to Bohm sheath boundary conditions. Concerning the ion energy channel, the main hypothesis that we can postulate is that the contribution of ion pressure within the vorticity formulation - corresponding to the effect of the ion diamagnetic term in the polarization drift - is responsible for the improvement of particle confinement through the increase of $\mathbf{E}\times\mathbf{B}$ shear and thus for the reduction of turbulence. In order to validate this hypothesis, a reduced isothermal model is implemented in this section with a generalized vorticity which includes this contribution of diamagnetic effect on ion polarization drift.

4.1.2.1 Presentation of the model

A reduced isothermal model is set up to validate the impact of the so-call generalized vorticity on the dynamics of spontaneous edge transport barriers obtained with our 2D slab model Tokam2D. It corresponds to the isothermal version of Tokam2D with a generalized vorticity:

$$\partial_t \widehat{n} + \widehat{\boldsymbol{\nabla}} \cdot \left(\widehat{n}\widehat{\mathbf{u}}_{\perp}^{E\times B}\right) = D_N \nabla_{\perp}^2 \widehat{n} + S_N - \sigma \widehat{n} \exp\left(\Lambda - \widehat{\phi}\right) \tag{4.2}$$

$$\partial_t \widehat{W} + \widehat{\boldsymbol{\nabla}} \cdot \left(\widehat{W}\widehat{\mathbf{u}}_{\perp}^{E\times B}\right) = \nu \nabla_{\perp}^2 \widehat{W} + \frac{g}{\widehat{n}} \partial_y \widehat{n} + \sigma\left(1 - \exp\left(\Lambda - \widehat{\phi}\right)\right) \tag{4.3}$$

$$\widehat{W} = \nabla_{\perp}^2 \widehat{\phi} + \alpha_{Ti_0} \nabla_{\perp}^2 \ln \widehat{n} \tag{4.4}$$

The vorticity formulation (4.4) can be obtained by considering an isothermal version of the generalized vorticity with a constant hot ion temperature equal to α_{Ti_0}:

$$\begin{aligned} \widehat{W} &= \nabla_{\perp}^2 \widehat{\phi} + \boldsymbol{\nabla} \cdot \left(\frac{1}{\widehat{n}} \boldsymbol{\nabla}_{\perp} \widehat{P}_i\right) \\ &= \nabla_{\perp}^2 \widehat{\phi} + \nabla_{\perp}^2 \widehat{T}_i + \boldsymbol{\nabla} \cdot \left(\widehat{T}_i \boldsymbol{\nabla}_{\perp} \ln \widehat{n}\right) \end{aligned} \tag{4.5}$$

Which leads - with an isothermal hypothesis $\widehat{T}_i = \text{constant} = \alpha_{Ti_0}$ - to:

$$\boxed{\widehat{W} = \nabla_{\perp}^2 \widehat{\phi} + \alpha_{Ti_0} \nabla_{\perp}^2 \ln \widehat{n}} \tag{4.6}$$

Note that a modification of the value of α_{Ti_0} does not impact the other control parameters such as the effective curvature $g\left(Te_0 + Ti_0\right)$ or the acoustic velocity $c_{s_0} = \sqrt{Te_0 + Ti_0}$. A scan of control parameter α_{Ti_0} constitutes thus the perfect tool to validate or to refute our hypothesis on the impact of the generalized vorticity.

4.1.2.2 Comparison with full thermal version

Before evaluating the impact of the control parameter α_{Ti_0}, we verify that spontaneous edge transport barriers are still developing with the reduced isothermal model using a simple vorticity, i.e. with $\alpha_{Ti_0} = 0$. In such situation, the barrier efficiency - obtained in steady-state and with the same parameters used in the anisothermal simulations - is presented in the left panel of Figure 4.12. This is also a sanity check with respect to Norscini's results [Norscini 15].

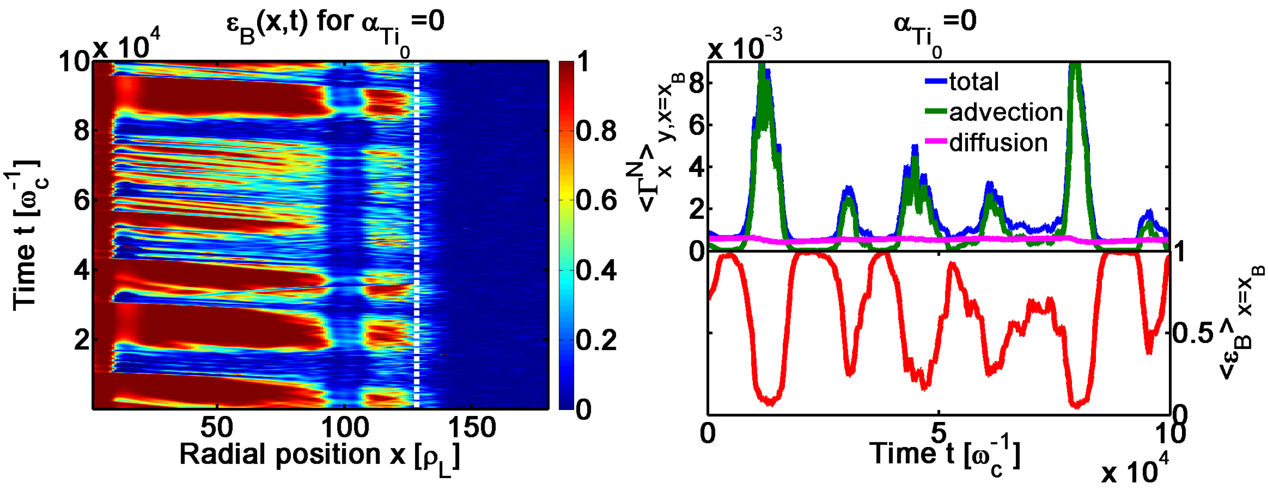

Figure 4.12:
Left panel: 2D - radial and time - map of barrier efficiency $\varepsilon_B(x, t)$ obtained with reduced isothermal model for $\alpha_{Ti_0} = 0$
Right panel: Time evolution of total, diffusive and turbulent radial particle fluxes (top panel) and barrier efficiency (bottom panel, in red) averaged poloidally and for $x \in x_B = [30; 90]$ corresponding to the radial extension of the left barrier.

Similarly to the thermal model, the simulation from reduced model exhibits spontaneous transport barriers in the whole closed field line region. Two barriers appear: a thick one between the inner radial boundary and up to $x = 90\rho_L$ and a thin barrier just before the LCFS for $x \in [105; 125]\,\rho_L$. As previously, these barriers relax simultaneously and 6 cycles of barrier formation and relaxation can be counted for a simulated time of $10^5\omega_c^{-1}$. The cycle duration has thus been reduced compared to the anisothermal simulation with $T_i^{\text{inj}} = 0$ and a typical cycle duration is now about $1.7 \times 10^4\omega_c^{-1}$ (versus $3 \times 10^4\omega_c^{-1}$ for the anisothermal simulation). The time evolutions of poloidally averaged total, advective and diffusive radial particle fluxes as well as mean barrier efficiency are respectively presented on top and bottom part of the right panel of Figure 4.12 for the inner barrier - i.e averaged for $x \in [30; 90]$. One can observe the same trend as for the anisothermal model: the formation of transport barriers is revealed by the vanishing of the turbulent radial flux while the diffusive flux remains mostly constant. For the third and forth cycles - i.e for t from 4.5×10^4 to $8 \times 10^4\omega_c^{-1}$, the barrier setting up is not complete and a succession of barrier formation is immediately interrupted by an inward relaxation. It results that the mean turbulent flux is reduced but not vanishing totally.

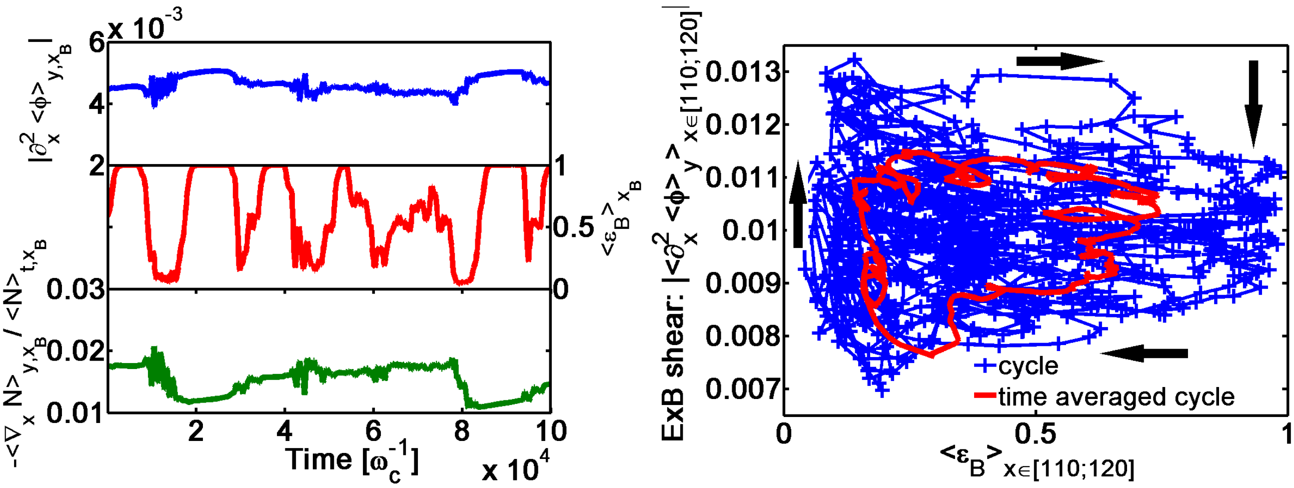

Figure 4.13:
Left panel: Time evolution of $\mathbf{E}\times\mathbf{B}$ shear (top panel, in blue), barrier efficiency (central panel, in red) and normalized density gradient (bottom panel, in green) for $x \in x_B = [30;90]$ corresponding to the radial extension of the left barrier.
Right panel: Correlation between the $\mathbf{E}\times\mathbf{B}$ shear magnitude and the barrier efficiency averaged inside the central barrier ($x_B = [110;120]$). Each marker '+' corresponds to a time save of the Tokam2D code and consecutive time saves are connected by solid lines clockwise (black arrows).

The interplay between mean $\mathbf{E}\times\mathbf{B}$ shear, barrier efficiency and normalized density gradient is less pronounced than in the anisothermal simulation. Indeed, for our reduced model with $\alpha_{Ti_0} = 0$, these three physical quantities are respectively plotted from top to bottom on the left panel of Figure 4.13. While the variation of the $\mathbf{E}\times\mathbf{B}$ shear magnitude with barrier dynamic is clear in the anisothermal model, we only observe fluctuations of shear magnitude and normalized density gradient when the barrier is down and the transport fully turbulent. Such complex interplay is also observed on the right panel of Figure 4.13 in which the correlation between $\mathbf{E}\times\mathbf{B}$ shear magnitude and barrier efficiency is displayed for the barrier close to the LCFS. The hysteresis cycle is not recovered except if we average over barrier cycles (red line).

In summarize, the reduced model reveals similar cycles of transport barrier formations and relaxations. If the typical duration of such cycle and the correlations between $\mathbf{E}\times\mathbf{B}$ shear, barrier efficiency and normalized density gradient are found to be slightly different in this isothermal simulation, the effect of $\mathbf{E}\times\mathbf{B}$ shear on turbulence - which explains the barrier dynamic - is recovered. Consequently, our reduced isothermal model can be used to study the impact of the ion energy channel - within the generalized vorticity - without modification of other physical quantities such as sound speed or effective curvature. In the following, the α_{Ti_0} parameter is scanned in order to change the weight of the diamagnetic term in the vorticity expression.

4.1.2.3 Scan of generalized vorticity

The barrier efficiency obtained for two simulations of the reduced anisothermal model with $\alpha_{Ti_0} = 0.1$ and $\alpha_{Ti_0} = 1$ are presented respectively on the left and right panels of Figure 4.14. Note that the values of α_{Ti_0} cannnot be directly compared to the ones of the scan of T_i^{inj} in the anisothermal model as the ion temperature is slightly weaker that the ion injected temperature in the simulation. That is to say that only a qualitative comparison between reduced isothermal and thermal models is realized.

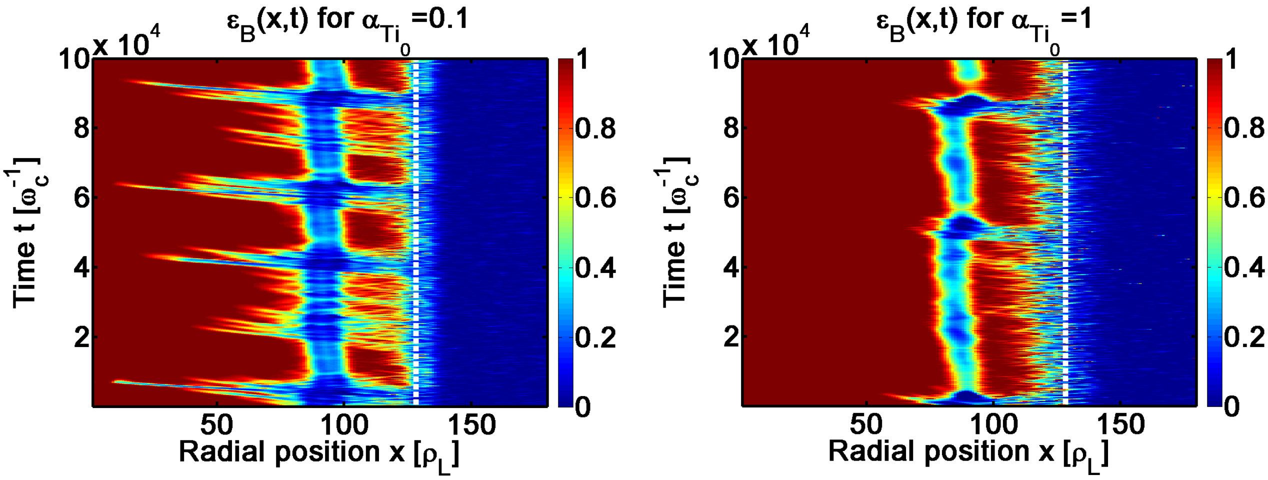

Figure 4.14: 2D - radial and time - maps of barrier efficiency $\varepsilon_B(x,t)$ with the reduced isothermal model:
Left panel: for $\alpha_{Ti_0} = 0.1$.
Right panel: for $\alpha_{Ti_0} = 1$.

The results with our reduced isothermal model are similar to anisothermal simulations: two barriers are developping in closed field lines, a thick one in the inner region up to $x = 80\rho_L$ and a thin one before the LCFS ($x \in [95; 120]$). For $\alpha_{Ti_0} = 0.1$, the inner barrier is found to be crossed by inward turbulent events but no complete relaxation of the barrier occurred. We note that the events which penetrate deeper into this inner barrier correspond to avalanches resulting from the relaxation of the other barrier before the LCFS. When the weight of ion pressure in the generalized vorticity increases, the left barrier becomes fully hermetic while only two relaxations of the right barrier occur during this simulation of $10^5\omega_c^{-1}$. The only discrepancy between the scan of ion injection temperature in the fully anisothermal model and of α_{Ti_0} in the reduced isothermal model is the characteristic time of the barrier cycle which is smaller with the reduced model as seen for $\alpha_{Ti_0} = 0$. Consequently, mean profiles of density (left panel of Figure 4.15), electrostatic potential (right panel of Figure 4.15), radial electric field (left panel of Figure 4.16) and $\mathbf{E} \times \mathbf{B}$ shear (right panel of Figure 4.16) present identical trends with our reduced model.

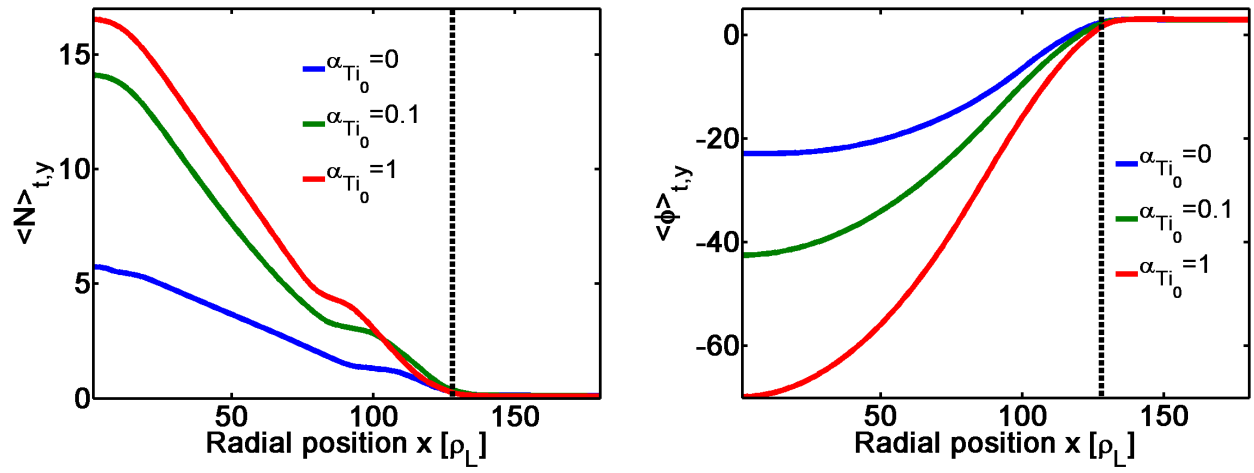

Figure 4.15: Radial profiles of time and poloidally averaged:
Left panel: density $\langle N \rangle_{t,y}$.
Right panel: electrostatic potential $\langle \phi \rangle_{t,y}$.

Concerning the electrostatic potential and its radial derivatives, we obtain an important well of radial electric field and thus a stronger $\mathbf{E} \times \mathbf{B}$ shear magnitude which is now localized at the LCFS for $\alpha_{Ti_0} = 0$ while simulation with $T_i^{\text{inj}} = 0$ reveals a maximal shear around $x = 110\rho_L$ and a lower magnitude.

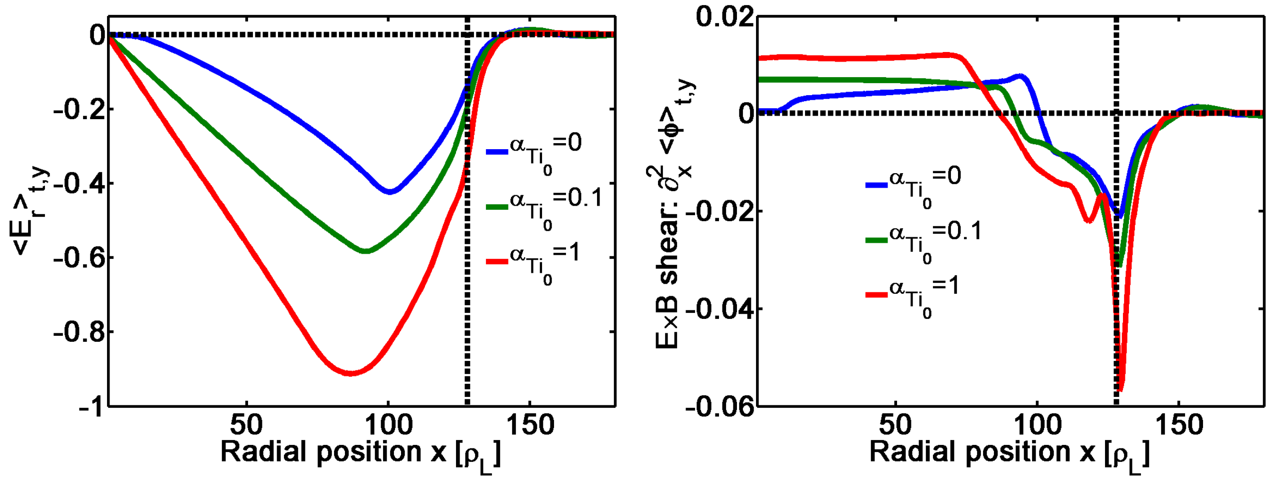

Figure 4.16: Radial profiles of time and poloidally averaged:
Left panel: radial electric field $\langle E_r \rangle_{t,y}$.
Right panel: $\mathbf{E} \times \mathbf{B}$ shear: $\partial_x^2 \langle \phi \rangle_{t,y}$.

To summarize, transport barriers are spontaneously obtained in our 2D slab code Tokam2D when closed field lines are added to the model. These barriers expand in the whole closed field line region - their number and radial extensions coinciding with the vanishing values of the mean $\mathbf{E} \times \mathbf{B}$ shear. Inside the barriers, turbulent transport drops while the diffusive radial flux remains quite constant. The cycles of transport barrier formation and relaxation can be explained using the time evolution of the $\mathbf{E} \times \mathbf{B}$ shear. When the shear exceeds a certain threshold, turbulence is damped so that the barrier begins to set up and keeps reinforcing until the barrier becomes fully efficient meaning that turbulence is not longer at play and cannot longer maintained the $\mathbf{E}\times\mathbf{B}$ shear. Consequently, the shear magnitude drops and becomes too weak to keep damping turbulence leading to the barrier relaxation and a new barrier cycle is occurring. These transport barriers are found to be reinforced by the ion energy channel while the electron energy channel only impacts the $\mathbf{E}\times\mathbf{B}$ shear at the LCFS and the parallel losses at target plates. The particularity of the ion energy channel is its impact on the vorticity formulation. In order to validate this hypothesis on the key role played by the generalized vorticity, a reduced isothermal model was tested with an explicit scanning parameter α_{Ti_0} which controls the weight of the ion diamagnetic term in the generalized vorticity. This reduced model exhibits similar behaviour as the full anisothermal one so that the fundamental role of the generalized vorticity on spontaneous edge transport barriers obtained within our 2D slab code Tokam2D is now established.

4.2 Discussion on the limits of 2D slab modelling

In this section, the consistency and the robustness of spontaneous edge transport barriers found in Tokam2D slab simulations are discussed. We first focus on the modelling of closed field line region and especially on its boundaries: the impact of the sharpness of the transition between closed and open field lines is investigated as well as the radial force balance and the impact of the inner radial boundary. Then, more general limits of Tokam2D are detailed. The absence of threshold on input energy for transport barrier formation in our simulations is discussed. A focus is made on sensitivity of transport barriers on dissipative processes such as diffusion and viscosity. Finally we point out the main differences between 2D slab models and more realistic configurations.

4.2.1 Modelling of closed field line region

4.2.1.1 Role of closed-open field lines transition

The analysis of spontaneous transport barriers obtained with Tokam2D reveals that these barriers develop in the whole closed field line region except at the radial locations for which the $\mathbf{E}\times\mathbf{B}$ shear is vanishing. One can legitimately wonder if these barriers are not fully artificial and not only due to the absence of appropriate parallel damping terms. Indeed, in experiments, transport barriers are found to have a limited radial extension and are found to develop mainly just before the LCFS in the so called pedestal region. That is to say that the sharp transition between closed and open field lines is expected to be a key player on edge transport barrier formation. In order to check if this transition between confined and unconfined domains is responsible for the barrier development in our 2D slab simulations with the reduced isothermal model and $\alpha_{Ti_0} = 1$, the sharpness of the transition between the two regions is modified. For that, a mask $\chi(x) = \frac{1}{2}\left(1 - \tanh\left[\left(x - x_{\text{sep}}\right)/\Delta x_{\text{sep}}\right]\right)$ is added in front of the term $\sigma\left(\widehat{\phi} - \langle\widehat{\phi}\rangle_{t,y}\right)$ in our simulations. Obviously, the opposite mask $(1-\chi(x))$ is also added in front of the parallel sinks. The variation of Δx_{sep} extends from 0.01 to 10 in our scanning which corresponds respectively to a width of core/SOL transition from zero to around $40\rho_L$. The masks χ resulting for these different values of Δx_{sep} are presented in Figure 4.17. Note that only a restricted radial extension of the simulated domain is plotted in this Figure.

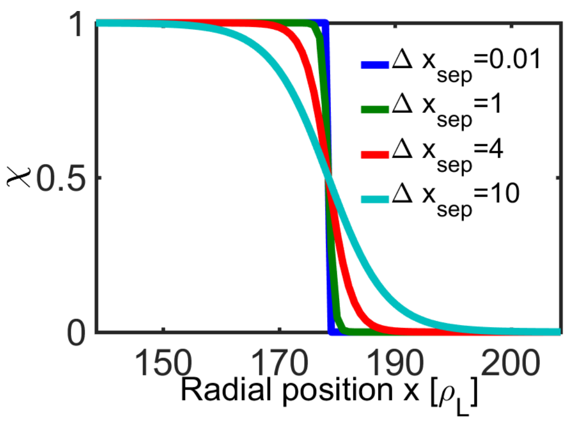

Figure 4.17: Radial profiles of the mask $\chi(x) = \frac{1}{2}\left(1 - \tanh\left[\left(x - x_{\mathrm{sep}}\right)/\Delta x_{\mathrm{sep}}\right]\right)$ used to model the transition between closed and open field lines in Tokam2D.

In steady-state, the radial profiles of barrier efficiency are presented on the left panel of Figure 4.18. It reveals that the width of the transition between closed and open field line regions strongly impacts the existence of spontaneous transport barriers. For transitions presenting a gate shape ($\Delta x_{\mathrm{sep}} = 0.01$) or very sharp ($\Delta x_{\mathrm{sep}} = 1$ which corresponds to a transition in $4\rho_L$), the radial profiles of barrier efficiency are not modified and two fully efficient and stable barriers appear in the confined region. When the transition becomes smoother - for $\Delta x_{\mathrm{sep}} = 4$, i.e a transition in around $20\rho_L$ - the barrier efficiency profile is shifted inwardly. More precisely, the width of the left barrier decreases while the right barrier experiences also a drop of its width as well as a lost of mean efficiency. For even smoother transition - $\Delta x_{\mathrm{sep}} = 10$ i.e a transition in around $40\rho_L$ - we observe that the two spontaneous transport barriers have disappeared except in the vicinity of the particle source. For this simulation, the radial transport in the confined region is fully turbulent and the particle confinement is thus drastically reduced as it can be seen on the radial profiles of mean density on the right panel of Figure 4.18. A smoothing of the transition from closed to open field lines leads to a degradation of core confinement and a reduction by a factor of 10 of the mean density at the inner boundary is obtained between the standard realistic sharp transition and the smoothest one ($\Delta x_{\mathrm{sep}} = 10$).

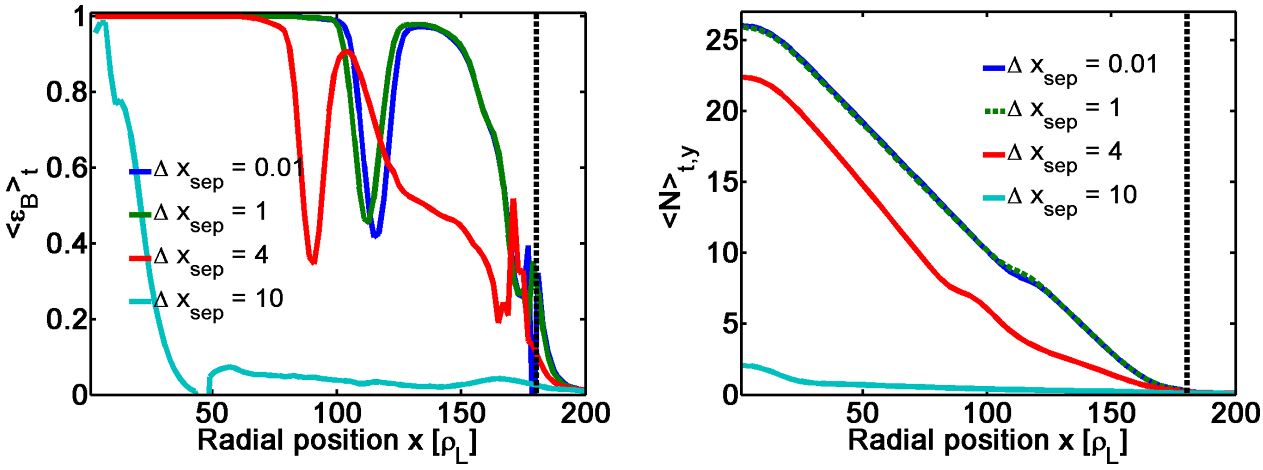

Figure 4.18: For several widths Δx_{sep} of transition between closed and open field line regions, radial profiles of:
Left panel: time averaged barrier efficiency $\langle \varepsilon_B \rangle_t$
Right panel: time and poloidally averaged density $\langle N \rangle_{t,y}$

The degradation of core particle content for the smoothest transition from closed to open field lines can be explained by the radial profile of mean $\mathbf{E} \times \mathbf{B}$ shear on Figure 4.19. It is found that the magnitude of the $\mathbf{E} \times \mathbf{B}$ shear is large and maximal at the LCFS for sharp transition. For the soft transition with $\Delta x_{\text{sep}} = 4$, the magnitude of the shear at the LCFS is half the one of sharp transition, resulting in a weaker density in the confined domain. For the smoothest transition, the shear is almost disappearing at the LCFS such as no spontaneous transport barrier develops.

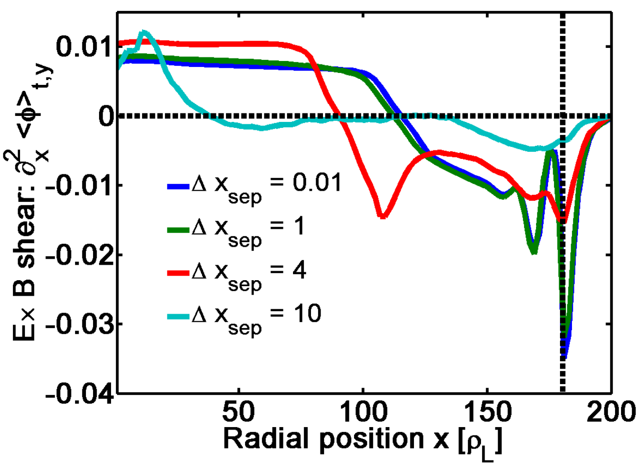

Figure 4.19: For several widths Δx_{sep} of transition between closed and open field line regions, radial profiles of $\mathbf{E} \times \mathbf{B}$ shear.

Even if a transition between closed and open field lines of $40\rho_L$ is absolutely not realistic, such numerical experiment permits to demonstrate the key role of the LCFS on the formation of spontaneous transport barriers in our simulations. That is to say that the spontaneous transport barriers obtained in closed field lines of Tokam2D slab simulations are induced by the presence of the sharp transition between confined and unconfined regions even if these barriers finally develop in the whole closed field line region.

4.2.1.2 Neoclassical physics

A radial force balance can be obtained by projection of the ion momentum equation on the radial direction. At largest order it writes:

$$\boxed{\widehat{E}_r - \widehat{B}_{\text{pol}}\widehat{u}_{i_\varphi} + \widehat{B}_{\text{tor}}\widehat{u}_{i_\theta} - \frac{\partial_r \widehat{p}_i}{\widehat{n}} = 0} \tag{4.7}$$

Equation 4.7 induced a coupling between the radial electric field - which controls zonal flows, the ion pressure gradient and with poloidal and toroidal components of the ion fluid velocity. In our 2D slab simulations, this toroidal contribution is neglected. In closed field lines, the poloidal ion velocity $\widehat{u}_{i_\theta}$ is expected to be mostly determined by neoclassical theory. This theory takes into account the effect of both passing and trapped particles. The latter consists of particles with low parallel velocity without enough energy to be able to overcome the high field side region. These particles become trapped on the low field side region into so-called banana orbits. The effect of the friction between trapped and passing particles has to be considered [Hinton 76] and leads to flux-averaged neoclassical ion poloidal flow:

$$\langle \widehat{u}_{i_\theta}^{\text{neo}} \rangle_{\text{F.S}} = \kappa_i \frac{\partial_r \langle \widehat{T}_i \rangle_{\text{F.S}}}{\widehat{B}} \tag{4.8}$$

where $\langle \cdot \rangle_{\text{F.S}}$ corresponds to an average on the flux-surface. κ_i depends on the collisionality $\nu_\star$, the aspect ratio $\mathcal{A}$ and the radial position. The exact expression can be found in [Hinton 76].
The collisional friction force is found to radically modify edge turbulence properties in the 3D fluid turbulence code Emedge3D in simulations where only closed field lines are simulated [Chôné 15]. In particular, a spontaneous generation of transport barriers is obtained with a threshold in input power. This friction force generated by collisions between passing and trapped particles can be taken into account in a fluid model by the addition of a right-hand side term in the vorticity equation [Chôné 14]. This term writes:

$$-\partial_x \left[\mu_i \left(\langle \widehat{u}_{i_\theta} \rangle_y - \langle \widehat{u}_{i_\theta}^{\text{neo}} \rangle_y \right) \right] \tag{4.9}$$

where $\widehat{u}_{i_\theta} = \widehat{u}_\theta^{E\times B} + \widehat{u}_{i_\theta}^\star$ is the first order poloidal ion drift velocity. μ_i is a poloidal flow damping defined in [Gianakon 02] which depends also on collisionality, aspect ratio, radial position as well as on the fraction of trapped particles. This friction term tends to set the ion poloidal flow equal to the neoclassical ion poloidal flow.
Such neoclassical contribution on radial force balance (4.7) is not taken into account in Tokam2D which means that the ion poloidal flow is at largest order only determined by first order ion drift velocities. In order to study if neglected neoclassical effects impacts on edge properties, a proof of concept is realized by adding the term (4.9) in the right hand side of vorticity equation but with a constant μ_i coefficient for simplicity. Within our isothermal reduced model and thus without ion temperature gradient, the neoclassical ion poloidal flow is null. Taking into account the friction force with a constant μ_i leads thus simply to a sink term driven by the gradient of mean ion poloidal flow: $-\mu_i \partial_x \langle \widehat{u}_{i_y} \rangle_y$. At equilibrium

we can expect to obtain: $\langle \widehat{u}_{i_y} \rangle_{t,y} = \langle \widehat{u}^{\mathrm{neo}}_{i_y} \rangle_{t,y} = 0$ and consequently:

$$\langle \widehat{u}_y^{E\times B} \rangle_{t,y} + \langle \widehat{u}^{\star}_{i_y} \rangle_{t,y} = 0 \tag{4.10}$$

Two simulations of Tokam2D are compared: a standard one obtained by setting $\mu_i = 0$ and a neoclassical one obtained with a constant $\mu_i = 0.2$. The poloidal flow balances are presented on left and right panels of Figure 4.20. In standard simulations without neoclassical friction force, the total ion poloidal flow is mainly detrmined by the $\mathbf{E} \times \mathbf{B}$ drift while the magnitude of the diamagnetic drift is about five times weaker in the whole closed field line region. When the friction force is turned on, we observe that the time and poloidally averaged total poloidal flow is close to zero in closed field lines as expected. That is to say that the $\mathbf{E} \times \mathbf{B}$ and the diamagnetic drifts are mainly compensating each other. The amplitude of the diamagnetic drift being mostly determined by density profile, it results that the $\mathbf{E} \times \mathbf{B}$ drift is the most impacted by this new neoclassical contribution. Indeed, one can observe the disappearance of the strong radial electric field well (as $\widehat{u}_y^{E\times B} = -E_r$ in Tokam2D) and a strong reduction of the maximal magnitude from 0.6 without the friction force to 0.15 before the LCFS with $\mu_i = 0.2$.

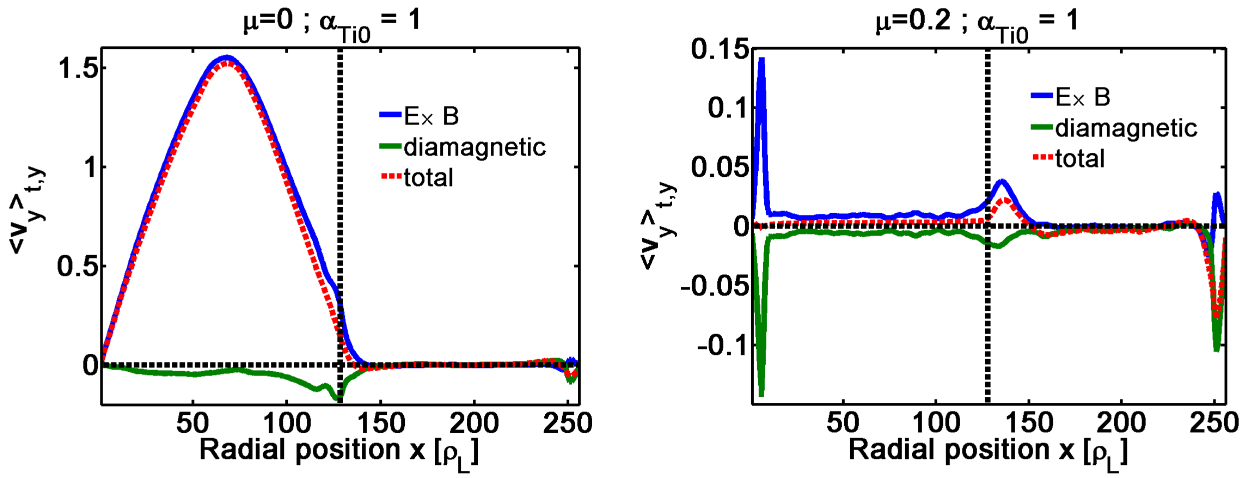

Figure 4.20: Proof of concept/sanity test: radial profiles of time and poloidally averaged $\mathbf{E} \times \mathbf{B}$, diamagnetic and total poloidal velocity without and with simplify neoclassical contribution:
Left panel: without neoclassical correction $\mu = 0$.
Right panel: with non self-consistent neoclassical correction $\mu = 0.2$.

The suppression of the strong radial electric well with $\mu = 0.2$ has a major consequence on core particle confinement as it can be seen on Figure 4.21: the density content in the confined domain falls by a factor of 10 and all the transport barriers have disappeared such as a fully turbulent radial transport is obtained.

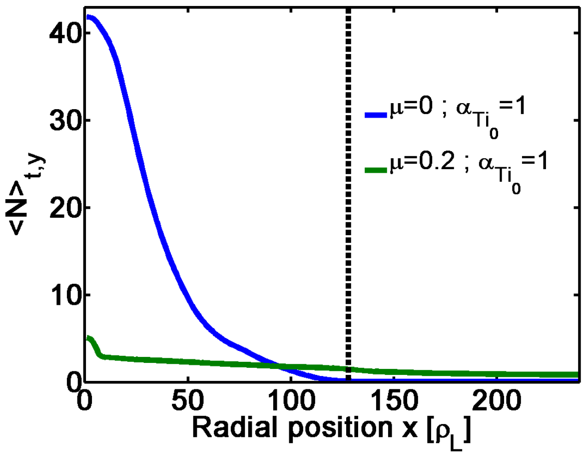

Figure 4.21: Radial profile of time and poloidally averaged density in a standard simulation or with a neoclassical friction force with a constant $\mu = 0.2$.

Taking into account a neoclassical friction force in our model seems to strongly impact equilibrium profiles in the closed field line region. Only a proof of concept has been realized with constant poloidal flow damping coefficient and the full consistent model has not been yet investigated. The neoclassical friction force seems to impact on edge turbulence in agreement with [Chôné 15]. In our isothermal simulation, taking into account such neoclassical term suppresses the transport barrier in the whole closed field line region. However, the neoclassical level of the ion poloidal velocity depends on ion temperature gradient such as this term may have a positive impact on the development of spontaneous transport barriers with anisothermal simulations.

4.2.1.3 Inner radial boundary

Boundary conditions are always a critical topic in numerics and this is also the case for edge turbulence codes. Here,we focus on the effect of our inner radial boundary conditions. For most of the fields involved in the model - the density $\widehat{n}$, the vorticity $\widehat{W}$ and the electrostatic potential $\widehat{\phi}$ - Neumann boundary conditions are used which means that the radial gradient of these fields is vanishing at the inner edge of the domain. Combined with the buffer zone, it prevents the existence of transverse currents and radial fluxes at the inner boundary and thus a good control of plasma polarisation as well as particle and energy contents. However, it generates a constraint on the radial electric field which vanishes at the inner boundary as it can be seen on the left panel of Figure 4.16. Such condition strongly impacts on the radial electric well which develops on the whole closed field line region. We observe that the radial electric field well is building close to the LCFS until reaching its maximal magnitude. At this point, it seems that the radial electric field is evolving quasi linearly up to the inner boundary in order to reach its imposed zero value.

At this point, we can legitimately wonder if spontaneous transport barriers are not strongly influenced by this inner radial boundary and consequently by the width of the simulated closed field line region. To analyse such influence, three simulations with varying confined region width are compared in the following. For that, the radial width of the whole simulated domain - including both open and closed field lines - are kept constant to $256\rho_L$. The position of the LCFS is adjusted at 140, 180 and $220\rho_L$ corresponding to the radial distance at the inner boundary. Note that the modification of the width of the simulated open field line region does not impact on the results presented here. The radial profiles of time averaged barrier efficiency obtained in these three simulations are presented on the left panel of Figure 4.22. The mean barriers obtained for simulations with LCFS at 140 and $180\rho_L$ are really similar: two transport barriers develop in the simulations. The outer one is obtained just before the LCFS and a small reduction of its width can be noticed for the case with $x_{\text{sep}} = 140\rho_L$. The width of the inner barrier is logically strongly reduced in the same case as the confined region has been shortened by $40\rho_L$ and a small reduction of the barrier efficiency also occurs. For the simulation with $x_{\text{sep}} = 220\rho_L$, three barriers appear. The width of the outer barrier is reduced by a factor around 2 compared to other simulations with an increase of efficiency up to $\varepsilon_B = 0.4$. The inner barrier obtained previously is split into 2 barriers quite efficient ($\langle\varepsilon_B\rangle_t \approx 50\%$). This is due to the $\mathbf{E} \times \mathbf{B}$ shear profile which exhibits a new zero value in closed field lines. Nevertheless, we see on the right panel of Figure 4.22, that the mean efficiency averaged in time and in the whole confined region is not significantly modified by the shift of the LCFS position as the mean barrier efficiency is still around 0.4 and 0.5 for the three simulations.

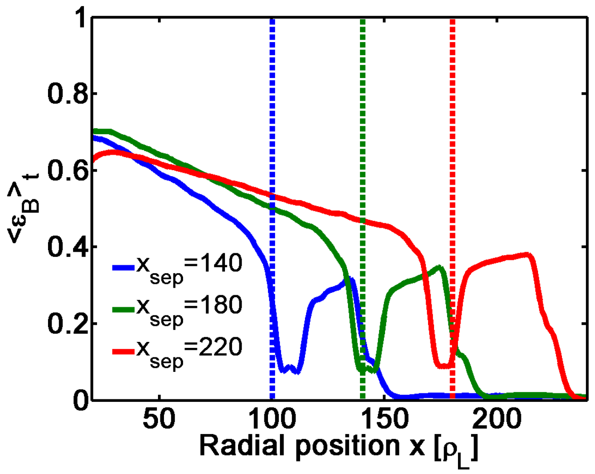

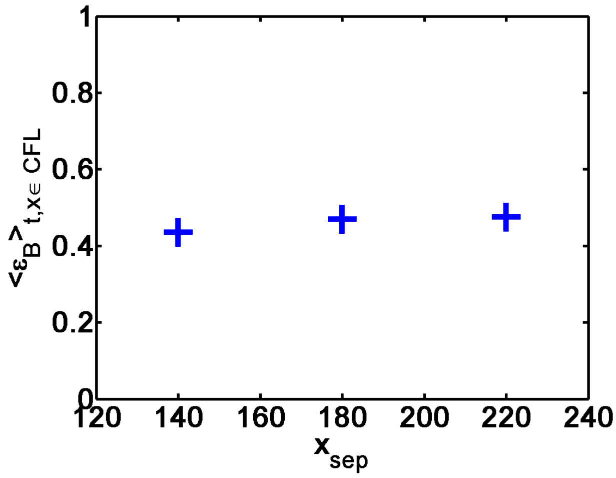

Figure 4.22: :
Left panel: Radial profiles of time averaged barrier efficiency for three different radial positions of the LCFS.
Right panel: Mean barrier efficiency inside the whole closed field line region as a function of the radial position of the LCFS in the simulated domain.

In summary, inner radial boundary conditions constrain equilibrium profiles and especially the radial electric field which has to vanish at the inner extremity. The radial electric well shape and amplitude is consequently impacted and can modified the number and widths of spontaneous transport barriers in the confined domain through the $\mathbf{E}\times\mathbf{B}$ shear. The scan of the radial position of LCFS shows however that it has little consequence on the mean value of barrier efficiency in the whole confined domain.

4.2.2 Limits of Tokam2D model

In the following, we raise and discuss the inherent limits of Tokam2D for modelling of edge transport barriersand especially concerning the relevancy with the L-H transition.

4.2.2.1 Absence of a threshold

The first limit of Tokam2D concerning the relevance - with respect to the L-H transition - of spontaneous edge barriers appearing in our simulations is the absence of threshold on input power. Indeed, these barriers develop even without ion input energy which is in contradiction with experimental observations. Such absence points out that a damping mechanism is probably missing in closed field lines of Tokam2D model. This missing term may be the parallel closure on vorticity equation which does not include any damping on mean flows or the contribution of the neoclassical friction in order to obtain a more realistic radial force balance as discussed previously. Nevertheless, the ion energy channel behaves as expected as it reinforces the efficiency of transport barriers to stop radial propagation by turbulence. One can expect that the add of a damping term will prevent the formation of spontaneous edge transport barrier when $T^{\mathrm{inj}_i} = 0$ (or $\alpha_{Ti_0} = 0$). It may lead to the existence of the threshold on ion input energy due to the key role of the generalized vorticity.

4.2.2.2 Sensitivity to dissipative processes

Another limit of Tokam2D - and of fluid models in general - can strongly impact on transport barriers existence and formation: the modelling of dissipative processes. Indeed, dissipative coefficients are assumed constant in space and time in Tokam2D. These processes result from collisions between particles, small scale dissipation of energy and depend thus on plasma background conditions especially in terms of density and temperature. More generally, there is no simple description of all the dissipative processes existing at small scale. In order to analyse the influence of dissipative coefficients in our model, a scan of the diffusion coefficient D_N is set up. Three simulations of reduced isothermal model with $\alpha_{Ti_0} = 0$ are compared, for diffusion coefficients D_N equal to 5×10^{-3} (left panel of Figure 4.23), 10^{-2} (reference simulation on left panel of Figure 4.12) and $D_N = 2 \times 10^{-2} \rho_L c_s$ (right panel of Figure 4.23). 2D maps of barrier efficiency reveal the key role of diffusion in the dynamics of edge transport barriers in our simulations. Indeed, if the radial position of transport barriers - and consequently the $\mathbf{E} \times \mathbf{B}$ shear profile - is not impacted by the diffusion coefficient, we observe a significant modification of transport barrier dynamics. For simulations of $10^5 \omega_c^{-1}$, the left barrier is fully efficient during only 25% for $D_N = 5 \times 10^{-3}$ while the barrier is up during more than 80% of the simulation for $D_N = 2 \times 10^{-2}$. The most interesting fact is that the characteristic duration of a barrier lifetime does not seem to be modified by diffusion and remains around $5 \times 10^3 \omega_c^{-1}$. But the barrier takes longer at small diffusion coefficients to recover and to build up again. At small diffusion, the presence of an efficient barrier is a quite rare event while this is the standard at large diffusion. This is also true for the thin barrier close to the LCFS. Such behaviour demonstrates that diffusive processes play a role in the formation of our spontaneous transport barriers but not on its relaxations.

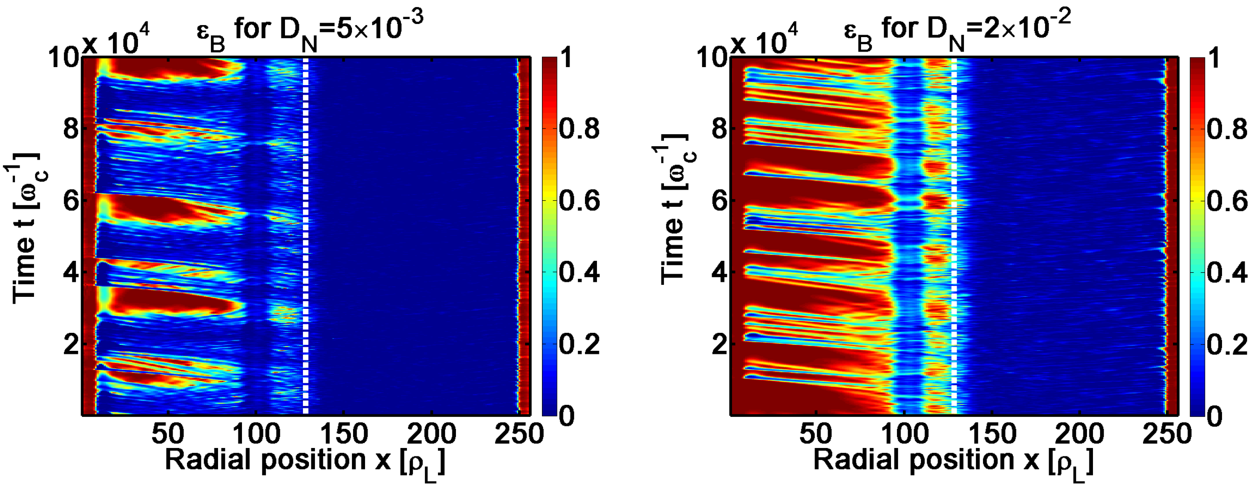

Figure 4.23: 2D - radial and time - maps of barrier efficiency obtained with reduced isothermal model and a diffusivity coefficient of:
Left panel: $D_N = 5 \times 10^{-3}$
Right panel: $D_N = 2 \times 10^{-2}$

Consequently of the modification of the barrier dynamic, the mean efficiency of the barrier depends on diffusive processes. Figure 4.24 presents the radial profile of time averaged barrier efficiency for the three simulations and the mean efficiency averaged in time and in the whole confined domain respectively on left and right panels. As said previously, the position of the barriers is mostly unchanged for the three diffusion coefficients even if a small outward shift of the LCFS barrier occurs when diffusion is increasing. The efficiency amplitude is strongly enhanced by diffusion. On the right panel, we observe that the confined region is in averaged 20% efficient to stop radial propagation of turbulence for $D_N = 5 \times 10^3$ and reaches around 80% for $D_N = 2 \times 10^2$. The dependency of the mean efficiency on the diffusion coefficient seems to increase linearly until a saturation is expected for fully efficient barriers or without barriers (thus for very small or very large D_N).

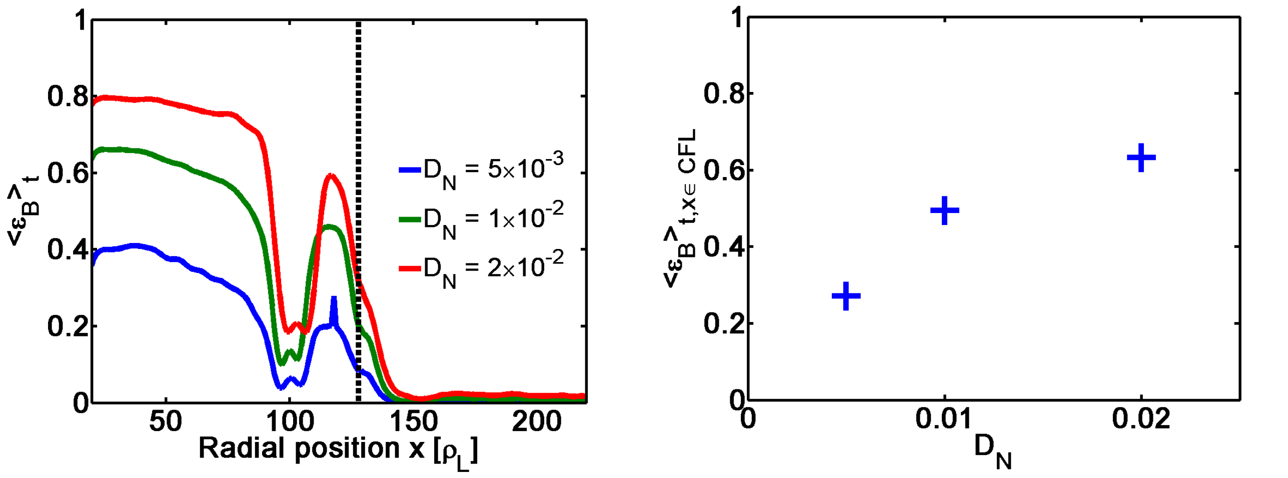

Figure 4.24: Scan of diffusion coefficient D_N:
Left panel: Radial profiles of time averaged barrier efficiency $\langle \varepsilon_B \rangle_t$.
Right panel: Barrier efficiency - averaged in time and in closed field line region - as a function of input diffusive coefficient D_N.

The diffusion - and similarly the viscosity - strongly impacts on the existence and dynamics of the spontaneous transport barriers obtained in Tokam2D. A more realistic model for dissipative processes is thus required in order to understand the interplay between turbulence, $\mathbf{E} \times \mathbf{B}$ shear and dissipative processes. At $D_N = 5 \times 10^{-3}$, there is almost no barrier developing on the confined region for $\alpha_{Ti_0} = 0$ which implies a relatively flat density profile. That is to say that a threshold is expected for low diffusion coefficient when the weight of ion energy channel - through generalized vorticity and α_{Ti_0} - is increased.

4.2.2.3 Fundamental differences with realistic geometry

Finally the strongest inherent limit of Tokam2D comes from its 2D slab nature. Indeed, the slab assumption and the flute hypothesis differ from realistic configuration as the parallel dynamic and the magnetic configuration are expected to play a significant role in the self-organisation of turbulence and in transport barrier development. The remaining of this manuscript focuses on the study of these two features by using the code Tokam3X. In the last section of this Chapter, we aim at understanding the role of parallel dynamics isolated from magnetic field effects by using a slab configuration similarly to Tokam2D. In the last Chapter, the influence of the magnetic equilibrium is analysed by simulating realistic tokamak geometries.

4.3 Inclusion of parallel dynamics using Tokam3X slab configuration

4.3.1 Existence of spontaneous transport barrier in 3D slab simulations

In this section, we focus on the existence of spontaneous transport barriers in the slab version of Tokam3X in order to understand if the barriers obtained in 2D still exist when parallel dynamics and 3D effects are considered. The parameters used in the following are: the aspect ratio $\mathcal{A} = 3.75$, $\rho_\star^{-1} = 256$, the diffusive coefficients $D_N = D_W = D_{\Gamma_i} = 5 \times 10^{-3} \rho_L c_s$ and the parallel resistivity

$\eta_{\|} = 10^{-5} B_0/(en_0)$. The grid resolution is $(N_r \times N_\theta \times N_\varphi) = (64 \times 128 \times 16)$.A simulation is run without generalized vorticity $\alpha_{Ti_0} = 0$ up to quasi steady-state and the 2D map of barrier efficiency obtained in this case is presented on the left panel of Figure 4.25. It is found that no transport barriers appear in this simulation in the whole confined or unconfined domain. Radial particle transport is thus fully dominated by turbulence as it can be seen on the right panel of Figure 4.25. Indeed, the total flux, almost constant as expected in closed field lines, is only induced by $\mathbf{E} \times \mathbf{B}$ transport while the diffusive contribution is quasi null except a small peak at the LCFS.

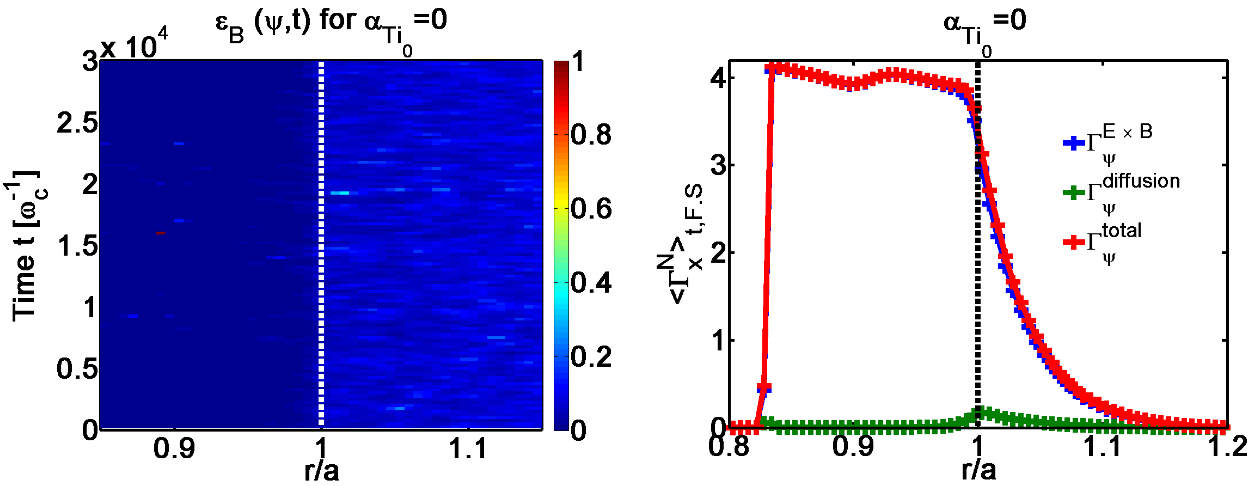

Figure 4.25:
Left panel: 2D - radial and time - map of barrier efficiency $\varepsilon_B(\psi, t)$ for $\alpha_{Ti_0} = 0$ in Tokam3X slab simulation.
Right panel: Radial profiles of total, turbulent and diffusive radial fluxes for $\alpha_{Ti_0} = 0$.

Transport barriers do not develop spontaneously in the closed field line region with the slab version of Tokam3X with a simple vorticity formulation - i.e $\alpha_{Ti_0} = 0$. One can wonder if taking into account ion energy effects - through the generalized vorticity - leads to the formation of such spontaneous barriers.

4.3.2 Impact of generalized vorticity

Two simulations with different weights of ion diamagnetic contribution in the generalized vorticity - $\alpha_{Ti_0} = 1$ and $\alpha_{Ti_0} = 2$ - are realized. The barrier efficiency obtained in the latter case is presented as a 2D - radial and time - map on the left panel of Figure 4.26. It is found than transport barriers do not develop in the confined region also in this case. However, one can observe some fluctuations of ε_B, especially around $r = 0.9a$ and at LCFS where the efficiency can punctually reaches 40%. The analysis of radial profiles of $\mathbf{E} \times \mathbf{B}$, diffusion and total radial fluxes - on the right panel of Figure 4.26 - rises two important points. First, the total flux is not constant in closed field lines and is smaller than the total flux obtained with $\alpha_{Ti_0} = 0$. That is to say that this simulation is not yet converged and is still evolving. In fact, Tokam3X simulations slab configuration are expensive numerically to reach a steady-state regime in comparison with Tokam2D but also surprisingly with Tokam3X simulations in circular limited geometry. The increase of α_{Ti_0} requires a smaller time step and takes thus even more time to converge. The second information given by this Figure is that, unlike the simulation without generalized vorticity, the diffusive contribution is not fully negligible. Two peaks of radial diffusive flux - around $r = 0.9a$ and $r = a$ - are responsible for the fluctuations noticed on the left panel plot.

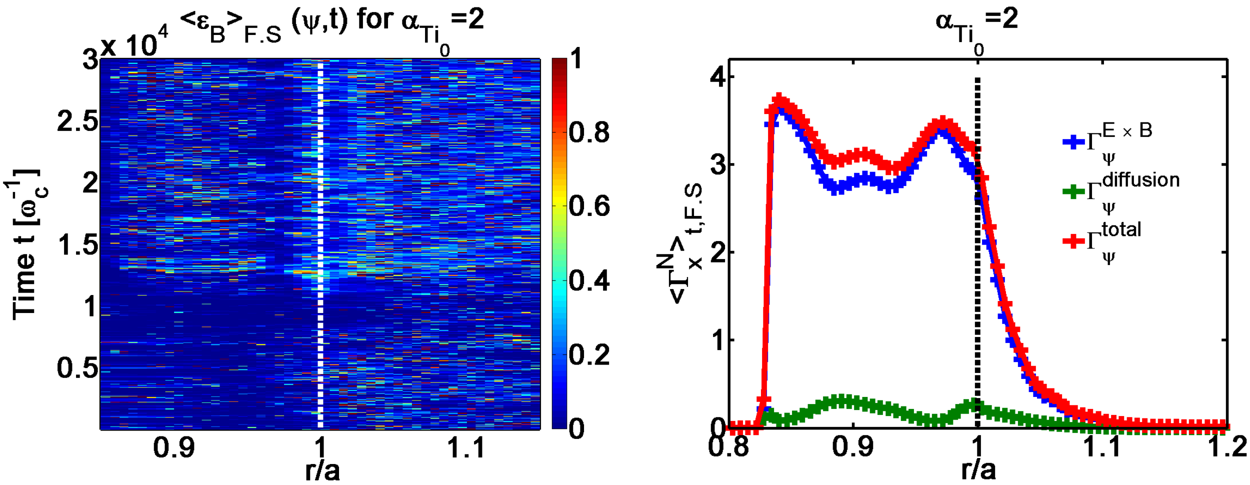

Figure 4.26:
Left panel: 2D - radial and time - map of barrier efficiency $\varepsilon_B(\psi, t)$ for $\alpha_{Ti_0} = 2$.
Right panel: Radial profiles of total, turbulent and diffusive radial fluxes for $\alpha_{Ti_0} = 2$.

The increase of α_{Ti_0} and thus of ion energy channel contribution does not appear to impact on the existence of spontaneous edge transport barriers even if small fluctuations of barrier efficiency appear locally. However, the simulation takes a very long time to reach a steady-state so that a bifurcation cannot be completely excluded.

4.3.3 On the existence of a threshold

Indeed, if small fluctuations of barrier efficiency and increase of radial diffusive flux do not lead to the reduction of the fraction of radial turbulent flux, it induces a significant change of the equilibrium state. Figure 4.27 presents respectively on the left and right panels the radial profiles of time and flux-surface averaged density and radial electric field for the three simulations with $\alpha_{Ti_0} = [0, 1, 2]$. The confinement is found to be significantly improved when the scanning parameter is increased. For simple vorticity formulation, the density profile is flat in closed field lines which means that the transport is fully turbulent. When α_{Ti_0} is increased an enhancement of density gradient is obtained at the LCFS and in last confined flux surfaces which induces a strong improvement of the core density from 3.5 for $\alpha_{Ti_0} = 0$ to 7.5 and 12 respectively for $\alpha_{Ti_0} = 1$ and $\alpha_{Ti_0} = 2$. Concerning the radial electric field, while a relatively flat profile is obtained without the generalized vorticity, the strong electric field well obtained with Tokam2D in the whole closed field line region is recovered. Note that the amplitude of the well is no longer modified between $\alpha_{Ti_0} = 1$ or 2 while the confinement still improves.

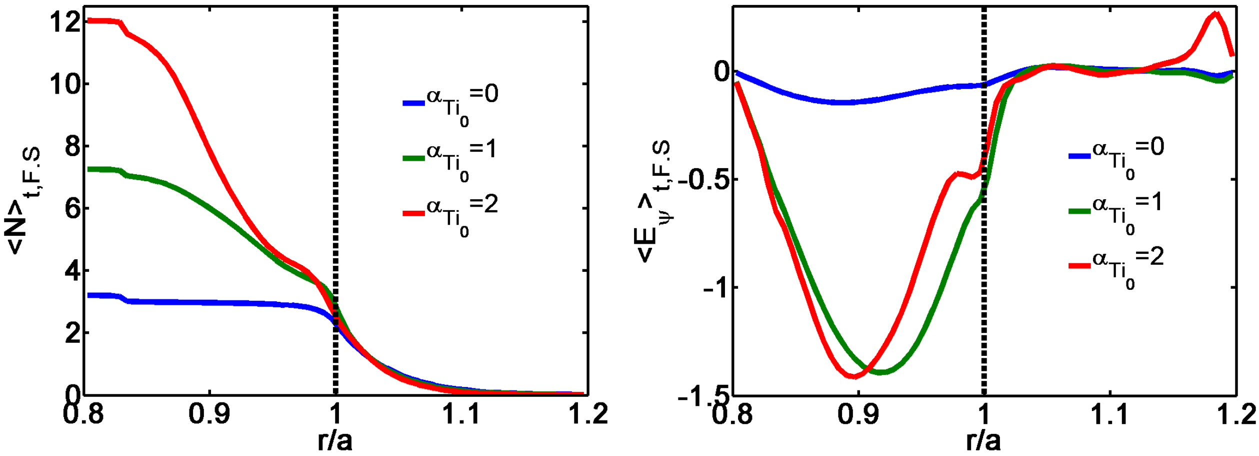

Figure 4.27: Radial profiles of time and flux-surface averaged:
Left panel: density $\langle N \rangle_{t,\mathrm{F.S}}$
Right panel: radial electric field $\langle E_\psi \rangle_{t,\mathrm{F.S}}$.

The enhancement of radial electric well in the closed field lines leads to an increase of the mean $\mathbf{E} \times \mathbf{B}$ shear, on the left panel of Figure 4.28 in particular on the vicinity of the LCFS. It explains the improvement of the core density content. Moreover, fluctuations of the $\mathbf{E} \times \mathbf{B}$ shear - so that zonal flows - are also found to strongly increase with the generalized vorticity, see the right panel of Figure 4.28. As these simulation are not converged, any further investigations appear to be overhasty. An interplay between turbulence, zonal and mean equilibrium $\mathbf{E} \times \mathbf{B}$ flows occur and will need to be characterized. The barrier efficiency criterion is inadequate to characterize the spontaneous transport barriers obtained in Tokam3X slab simulations. A possible explanation is that the diffusive radial flux is so negligible with respect to the turbulent one that even an increase by a factor of 10 does not lead to a notable barrier efficiency while the impact on density profile is significant.

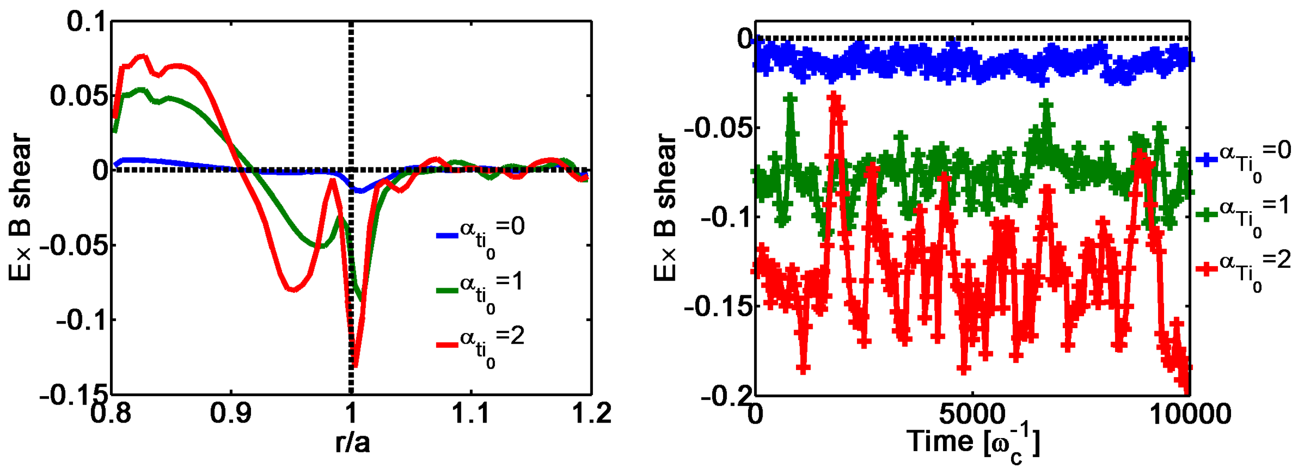

Figure 4.28: Radial profiles of time and flux-surface averaged:
Left panel: density $\langle N \rangle_{t,\mathrm{F.S}}$
Right panel: radial electric field $\langle E_\psi \rangle_{t,\mathrm{F.S}}$.

4.4 Conclusion

Taking into account parallel dynamic by moving from 2D to 3D slab simulations modifies our interpretation of analysis tools used in this Chapter. In 2D, spontaneous edge transport barriers are obtained systematically by taking into account closed field lines. These barriers are found in the whole confined domain with a radial extension and number fixed by the mean $\mathbf{E} \times \mathbf{B}$ shear profile. These barriers fluctuate in time in quasi-periodic barrier cycles of formation and relaxation. This cycle is correlated with the time evolution of the $\mathbf{E} \times \mathbf{B}$ shear inside the barrier and the interplay predicted by simple predator prey model is recovered. The electron energy channel is found to impact barrier dynamics especially due to the parallel dynamics in the SOL and by modifying the $\mathbf{E}\times\mathbf{B}$ shear at the LCFS. The ion energy channel has a significantly larger impact in particular in the closed field lines as it reinforces the efficiency of the barriers. Thanks to a reduced isothermal model, we show that this impact of the ion channel is mainly due to the diamagnetic contribution in the ion polarisation drift which takes the form of the so called generalized vorticity. The reduced model recovers qualitatively all the properties of the full anisothermal one.
The critical issues of modelling of confined domain have been raised. The LCFS is found to be the responsible of the formation of spontaneous transport barrier in the whole closed field lines while the inner radial boundary induces a constraint on the radial electric field which can modify spatial distribution and dynamics of these barriers. We point out that our model does not recovered an ion poloidal flow at neoclassical level. The addition of a neoclassical friction force permits to correct this issue, at least within a proof of concept leading to a significant change in the barrier phenomenology. The absence of threshold on (ion) input energy can rise the question of the relevance of these spontaneous barriers with respect to the H-mode physics even if the ion input energy behaves qualitatively as expected from experiments or other 2D modelling. A decrease of the particle diffusion coefficient may lead to the existence of a threshold as it modifies the time taken for a barrier to build up again after its relaxation. Finally, the effect of parallel dynamic has been investigated by moving from 2D to 3D slab simulations using the Tokam3X code. It is found that transport barriers are not spontaneously obtained in 3D without generalized vorticity. Simulations with generalized vorticity are slow to reach a quasi steady-state regime so that any definitive conclusion would be precipitated. The criterion ε_B - so called barrier efficiency - is not appropriate to study such simulations for a reason still unknown. Indeed, the barrier efficiency remains quite small while the particle core confinement is strongly improved with generalized vorticity. The radial electric field well developing in the whole confined domain in Tokam2D is recovered in 3D slab simulations with generalized vorticity. Similar trends to 2D slab simulations are obtained on the electric field and $\mathbf{E} \times \mathbf{B}$ shear profiles when the diamagnetic contribution on the vorticity is increased. We note also an increase of zonal flows which should be more investigated when a quasi steady-state will be reached.

Chapter 5

Impact of magnetic shear on turbulent transport and edge transport barriers in 3D circular geometry

Nature uses only the longest threads to weave her patterns, so that each small piece of her fabric reveals the organization of the entire tapestry.

Richard P. Feynman

In this chapter, we focus on the properties of edge turbulent transport and on the existence of spontaneous edge transport barriers in circular limited plasmas. We first study transport properties obtained with realistic magnetic configuration for such geometry and compare them with previous results obtained with slab geometry. Some discrepancies with recent Tokam3X divertor simulations are discussed and the roles of flux expansion and magnetic shear are investigated. For the latter, the magnetic configuration and especially the safety factor is modified in order to observe if magnetic shear can modify edge transport and can generate spontaneous edge transport barriers.

5.1 On the existence of spontaneous edge barriers in limited circular geometry

5.1.1 Magnetic configuration of realistic circular geometry

The magnetic configuration used in a standard Tokam3X simulation of realistic circular limited plasma is presented in Figure 5.1. On the left panel, the axisymmetric toroidal magnetic field B_{tor} is presented in a 2D-(R, Z) poloidal plane. This toroidal magnetic field decreases with major radius R from $1.4B_0$ at the far SOL of HFS midplane to $0.8B_0$ at the far SOL of LFS midplane. Note that this toroidal magnetic field is kept identical in all the simulations presented in this chapter. The magnetic configuration flexibility in Tokam3X is ensured by the poloidal magnetic field B_{pol} which is adapted in order to obtain the expected magnetic configuration especially in terms of safety factor and magnetic shear radial profiles. Our scanning parameter is the cylindrical safety factor $q^{\mathrm{cyl}} = \langle rB_{\mathrm{tor}}/(RB_{\mathrm{pol}})\rangle_\theta$ where the definition is abusively extended even in open field lines. From this definition, the cylindrical magnetic shear is defined as $s^{\mathrm{cyl}} = \langle r/q^{\mathrm{cyl}} dq^{\mathrm{cyl}}/dr\rangle_\theta$. Our reference magnetic configuration is realistic of medium size tokamaks in limiter configuration such as COMPASS-D and Tore Supra and corresponds to a parabolic q^{cyl}-profile [Bilyková 06]. The poloidal magnetic field which leads to such magnetic configuration is plotted on the right panel of Figure 5.1. The maximal magnitude is localised at the HFS midplane in the closed field line region and the minimal value - which is about half of the maximum one - in the far SOL of the LFS midplane. The parameters used in all simulations of this Chapter are identical of those in slab configuration: the aspect ratio $\mathcal{A} = 3.75$, $\rho_\star^{-1} = 256$, the diffusive coefficients $D_N = D_W = D_{\Gamma_i} = 5 \times 10^{-3}\rho_L c_s$ and the parallel resistivity $\eta_\parallel = 10^{-5}B_0/(en_0)$. The grid resolution is $(N_r \times N_\theta \times N_\varphi) = (64 \times 256 \times 32)$.

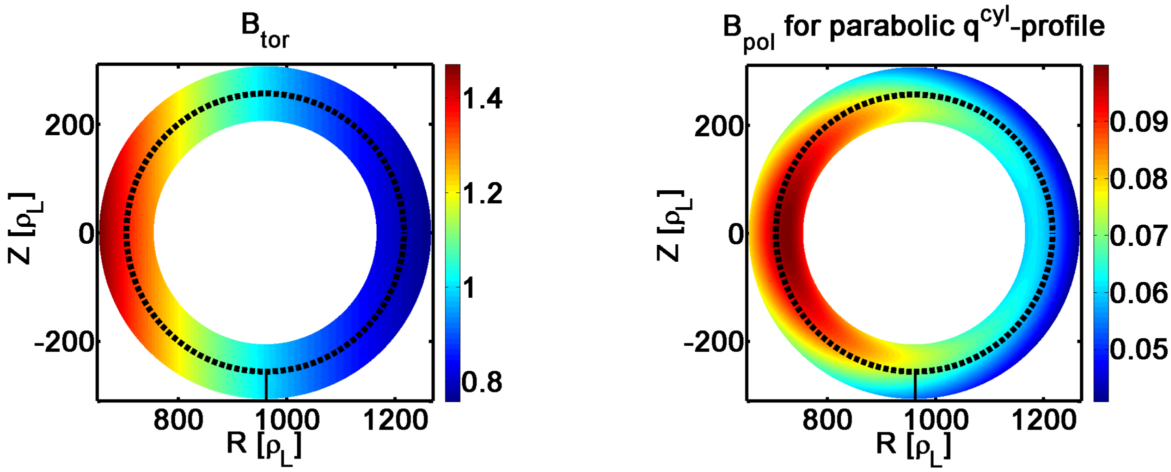

Figure 5.1: 2D-(R, Z) poloidal sections of:
Left panel: toroidal magnetic field B_{tor} used in all simulations.
Right panel: poloidal magnetic field B_{pol} used in the reference simulation with parabolic q^{cyl}-profile.

The radial profiles of the dimensionless cylindrical safety factor and magnetic shear obtained with such magnetic configuration are detailed on Figure 5.2. As said previously, the shape of q^{cyl} is a parabolic branch varying from 3 at $r = 0.8$a to 6.2 at $r = 1.2$a. The corresponding magnetic shear s^{cyl} increases radially from 0 at $r = 0.8$a to 3 at $r = 1.2$a.

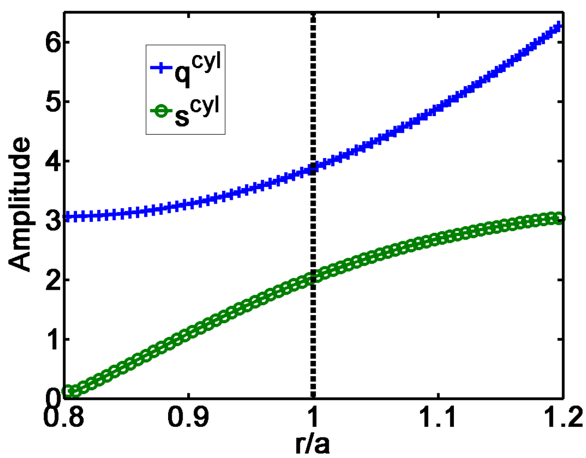

Figure 5.2: Radial profiles of cylindrical safety factor q^{cyl} and magnetic shear s^{cyl} for the reference simulation with parabolic q^{cyl}-profile.

One can notice however on Figure 5.3 that both the local cylindrical safety factor and magnetic shear exhibit poloidal asymmetries. The magnetic configuration reveals a strong HFS/LFS poloidal asymmetry for $q_{\text{loc}}^{\text{cyl}} = rB_{\text{tor}}/(RB_{\text{pol}})$ - on the left panel - with a local amplitude up to three times larger in the HFS compared to the LFS. The local magnetic shear $s_{\text{loc}}^{\text{cyl}} = r/q_{\text{loc}}^{\text{cyl}} dq_{\text{loc}}^{\text{cyl}}/dr$ exhibits a smaller poloidal asymmetry with amplitude variations around 10%.

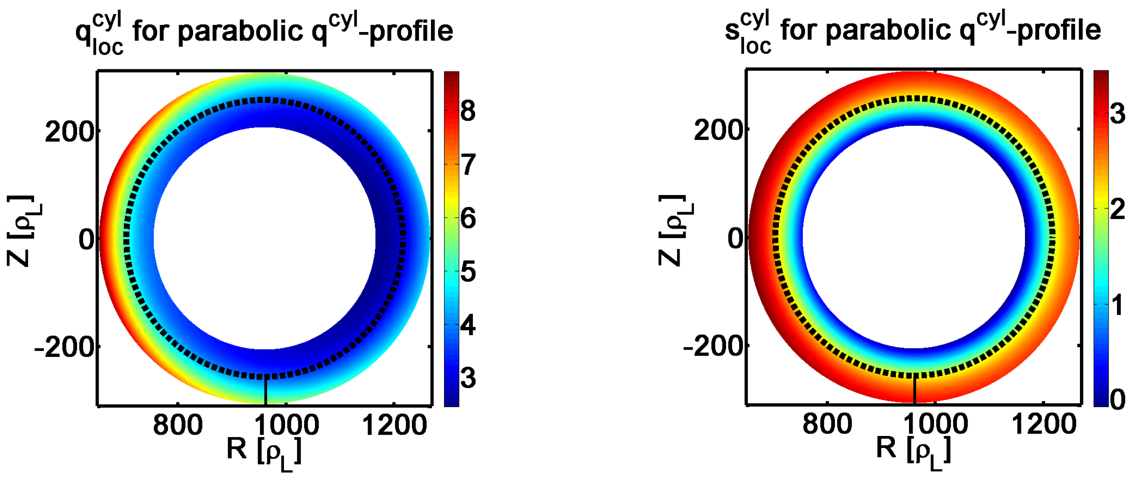

Figure 5.3: 2D-(R, Z) poloidal sections for the reference parabolic q^{cyl} simulation of:
Left panel: the local cylindrical safety factor $q_{\text{loc}}^{\text{cyl}} = \frac{rB_{\text{tor}}}{RB_{\text{pol}}}$
Right panel: the local cylindrical magnetic shear $s_{\text{loc}}^{\text{cyl}} = \frac{r}{q_{\text{loc}}^{\text{cyl}}} \frac{dq_{\text{loc}}^{\text{cyl}}}{dr}$

The magnetic configuration used for our reference simulation of realistic circular limited plasma is now fully described and we can focus on detailing transport properties obtained in this reference simulation at quasi steady state.

5.1.2 Fully turbulent radial transport: absence of edge barriers

The main turbulence characteristics of Tokam3X simulations have been extensively analysed in circular limiter geometry [Tamain 14], [Tamain 15] and first simulations in divertor configuration are presented in [Tamain 16]. We focus here on the physics of the L-H transition. First, we look at the global radial transport obtained in our reference case without a generalized vorticity - i.e $\alpha_{Ti_0} = 0$. For that, the 2D-(ψ, t) map of barrier efficiency and the radial profiles of time and flux-surface averaged $E \times B$, diffusive and total radial fluxes are presented respectively on the left and right panels of Figure 5.4. Both plots demonstrate a fully turbulent radial transport in the whole simulation domain such as the barrier efficiency never exceeds 5%. The cycles of formations and relaxations of transport barriers obtained in slab configuration are not recovered in this simulation of circular limited plasma. The level of radial transport by diffusion is fully negligible with respect to the turbulent one.

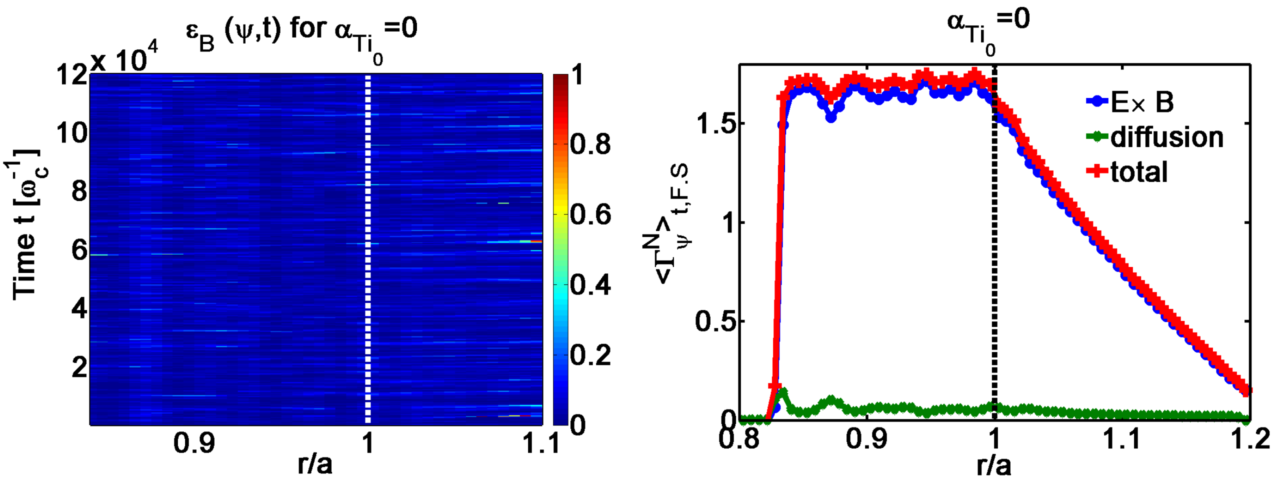

Figure 5.4:
Left panel: 2D - time and radial - map of barrier efficiency $\varepsilon_B(\psi, t)$ for a circular Tokam3X simulation with the reference magnetic configuration and a simple vorticity formulation: $\alpha_{Ti_0} = 0$.
Right panel: Radial profiles of time and flux-surface averaged turbulent, diffusive and total radial particle fluxes for a circular Tokam3X simulation with the reference magnetic configuration and a simple vorticity formulation: $\alpha_{Ti_0} = 0$.

The absence of transport barrier has a consequence on the mean profile of density $\langle N\rangle_{t,\mathrm{F.S}}$ and radial electric field $\langle E_\psi\rangle_{t,\mathrm{F.S}}$, as it can be seen on Figure 5.5. One can observe that the slope of density profile is almost unchanged between closed field lines and first open field lines such as the density profile only flattens from around $r = 1.06$a. The particle confinement is thus only slightly affected by crossing the LCFS. For the radial electric field, a positive amplitude is found in open field lines, in agreement with results from slab configuration. In closed field lines, we recover the negative trend of radial electric field found close to the LCFS in slab configuration and in experiments. However, two separate wells are obtained with magnitudes strongly reduced compare to the well found in slab configuration. Indeed, the ratio between negative and positive peak magnitudes is about 10 in slab configuration and only 1 in circular geometry. We precise that a strong buffer zone acts at $r \in [0.8; 0.83]$a: it results in a flat density profile and a linear radial electric field in order to satisfy the Neumann condition for the density and the zero Dirichlet boundary condition for the radial electric field at the inner boundary. As discussed with the slab configuration, such inner radial boundary conditions can impact on global transport properties and generation of zonal flows in the confined region.

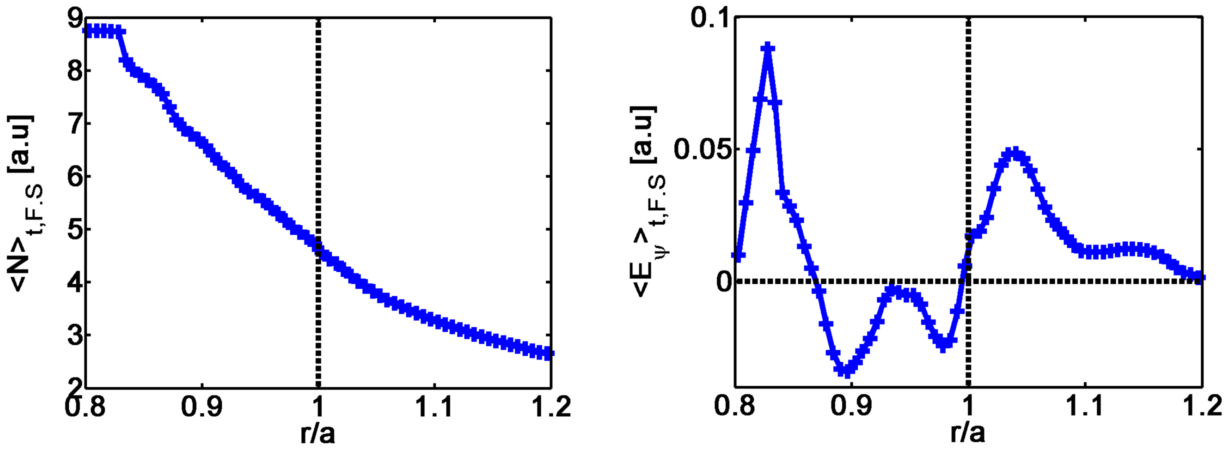

Figure 5.5: In circular limited geometry with parabolic $q^{\rm cyl}$ profile, radial profiles of time and flux-surface averaged:
Left panel: density $\langle N\rangle_{\rm t,F.S}$.
Right panel: radial electric field $\langle E_\psi\rangle_{\rm t,F.S}$.

5.1.3 Small impact of generalized vorticity

As seen in 2D and 3D slab geometry, particle confinement and the well of radial electric field can be increased by taking into account the diamagnetic contribution into the ion polarization drift through the so-called generalized vorticity and our scanning parameter α_{Ti_0}. Such scan in the isothermal version of Tokam3X is similar to the one realized with Tokam2D reduced isothermal model. The impact of this ion energy channel is now investigated in circular limited plasma with our reference and realistic magnetic configuration. For that, the 2D map of barrier efficiency $\varepsilon_B(\psi,t)$ and the radial profiles of $E\times B$, diffusive and total radial fluxes - as in Figure 5.4 - are presented in Figure 5.6 with the generalized vorticity and $\alpha_{Ti_0}=1$. It results that no quantitative or qualitative differences can be emphasis with generalized vorticity compared to the simulation with a simple vorticity formulation: the radial transport is fully ensured by $\mathbf{E}\times\mathbf{B}$ transport as the diffusive contribution is negligible.

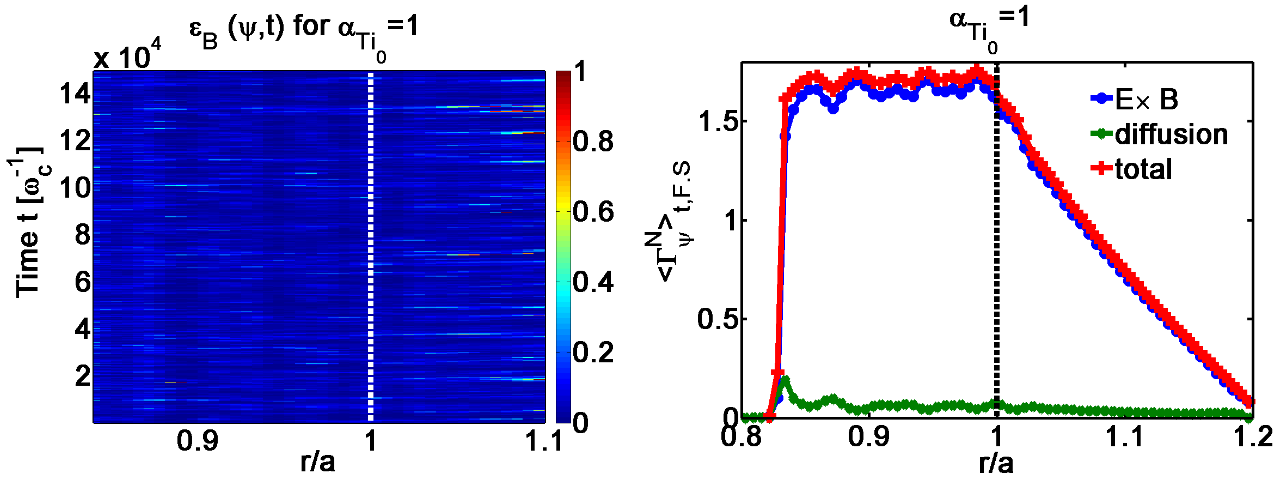

Figure 5.6:
Left panel: 2D - time and radial - map of barrier efficiency $\varepsilon_B(\psi, t)$ for a circular Tokam3X simulation with the reference magnetic configuration and a generalized vorticity formulation: $\alpha_{Ti_0} = 1$.
Right panel: Radial profiles of time and flux-surface averaged turbulent, diffusive and total radial particle fluxes for a circular Tokam3X simulation with the reference magnetic configuration and a generalized vorticity formulation: $\alpha_{Ti_0} = 1$.

In terms of mean fields, the effect of the generalized vorticity remains quite weak as it can be seen on Figure 5.7. On the left panel, one can observe that the normalized density gradient $-\nabla_\psi \langle N\rangle_{t,\mathrm{F.S}}/\langle N\rangle_{t,\mathrm{F.S}}$ is no altered by the modification of our scanning parameter α_{Ti_0}. We recovered the fact that the density gradient remains quite constant in closed and first open field lines before the density profile slightly flattens from $r = 1.06$a. The oscillations of the normalized density gradient in the closed field line region will be discussed in section 5.2.2. Concerning the radial electric field - on the right panel of Figure 5.7 - we note that the generalized vorticity steepens the negative wells localized between $r = 0.9$a and the LCFS. This increase remains however weak compared to the one obtained in slab configuration and is not strong enough to generate a transport barrier or to significantly impact the density profile - i.e the particle confinement.

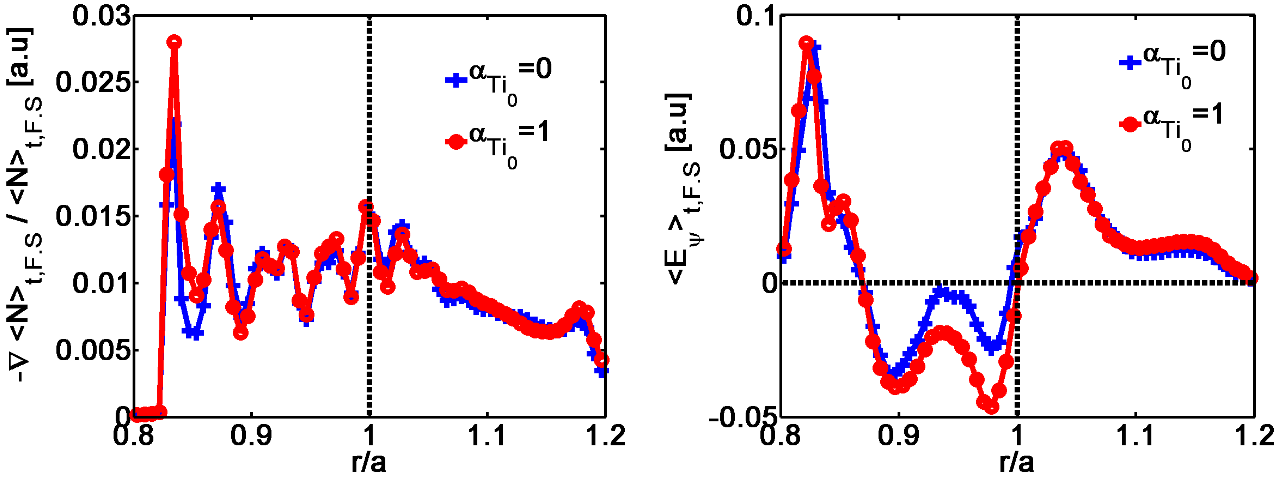

Figure 5.7: In a circular limited geometry with parabolic q^{cyl} profile, impact of generalized vorticity on radial profiles of time and flux-surface averaged:
Left panel: normalized density gradient $-\nabla_\psi \langle N \rangle_{\mathrm{t,F.S}} / \langle N \rangle_{\mathrm{t,F.S}}$.
Right panel: radial electric field $\langle E_\psi \rangle_{\mathrm{t,F.S}}$.

The impact of the generalized vorticity on global transport of circular limited plasma seems to be strongly reduced - at least in the parameter range used in our simulation - in comparison with slab limited plasmas. No substantial differences are obtained in terms of the particle confinement with a simple or a generalized vorticity formulation while a moderate steepening of radial electric field wells is observed. An increase of the scanning parameter α_{Ti_0} would provide a confirmation of the limited impact of the generalized vorticity on global transport of circular limited plasmas. In simulations up to $\alpha_{Ti_0} = 10$ - not presented here because not fully converged - no transport barriers develop in the simulated domain and the effect of α_{Ti_0} on the particle confinement and on the radial electric field remains marginal.

5.1.4 Differences with other geometries

At this point, the discrepancies observed in the existence and behaviour of edge transport barriers between slab and circular limited plasmas are not elucidated. In the following, we detail some dissimilarities between slab and circular geometry and then between circular and more complex realistic geometry i.e divertor configuration.

5.1.4.1 Differences with slab geometry

Vorticity balances obtained in slab and circular limited configuration are reported respectively on left and right panels of Figure 5.8 in which only closed field lines are considered. A vorticity balance corresponds to a radial profile of time and flux-surface averaging of vorticity equations terms. Each term of the vorticity equation (2.130) is averaged in time and in each flux-surface which leads to:

$$\int_{t_0}^{t_{\text{end}}} \oiint_{\text{F.S}} \partial_t \widehat{W} dSdt + \int_{t_0}^{t_{\text{end}}} \oiint_{\text{F.S}} \widehat{\nabla} \cdot \left(\widehat{W} \hat{\mathbf{u}}^{E\times B}\right) dSdt - \int_{t_0}^{t_{\text{end}}} \oiint_{\text{F.S}} \nabla \cdot \left(\widehat{n}\left(\hat{\mathbf{u}}_i^{\nabla B} - \hat{\mathbf{u}}_e^{\nabla B}\right)\right) dSdt$$
$$- \int_{t_0}^{t_{\text{end}}} \oiint_{\text{F.S}} \widehat{\boldsymbol{\nabla}} \cdot \left(D_W \widehat{\boldsymbol{\nabla}}_\perp \widehat{W}\right) dSdt = - \int_{t_0}^{t_{\text{end}}} \oiint_{\text{F.S}} \widehat{\nabla} \cdot \left(\widehat{W} \hat{u}_{i_\parallel} \mathbf{b}\right) dSdt + \int_{t_0}^{t_{\text{end}}} \oiint_{\text{F.S}} \widehat{\nabla} \cdot \left(\widehat{j}_\parallel \mathbf{b}\right) dSdt \tag{5.1}$$

In closed field lines, the two right hand side terms - which corresponds to the parallel dynamic - vanish. As the vorticity equation is a conservation equation, the sum of all these integrals must be equal to zero. During the transient regime, the temporal term is dominant which makes the vorticity evolves. When approaching a steady-state regime, the temporal term magnitude keeps decreasing until it becomes negligible. At this point, the equilibrium is reached and the dominant terms compensate each other in each flux surface. Such balance procedure allows us to understand which terms of the vorticity equation are the key players for each flux surface at the equilibrium. For the slab configuration, we can notify two regions in which the turbulent $\mathbf{E} \times \mathbf{B}$ term and the diffusive term compensate each other: for $r \in [0.85; 0.89]$a and for $r \in [0.96; 1]$a. In these regions, all the others terms are mostly negligible. For $r \in [0.89; 0.96]$a, the diffusive and the $E \times B$ contributions are compensated by the temporal terms which is the sign that the simulation is not fully converged so that any quantitative conclusion is avoided. In circular configuration on the right panel of Figure 5.8, the situation is completely different: the two dominant terms compensating each other are the $\mathbf{E} \times \mathbf{B}$ turbulent term and the curvature ∇B term. The latter corresponds to the divergence of the diamagnetic current. All the others terms are negligible in the whole closed field line region excepted the diffusive term which becomes significant close to the LCFS at $r =$a. In this circular simulation, one can see that the temporal term is quasi zero everywhere which means that the simulation is fully converged with enough statistics.

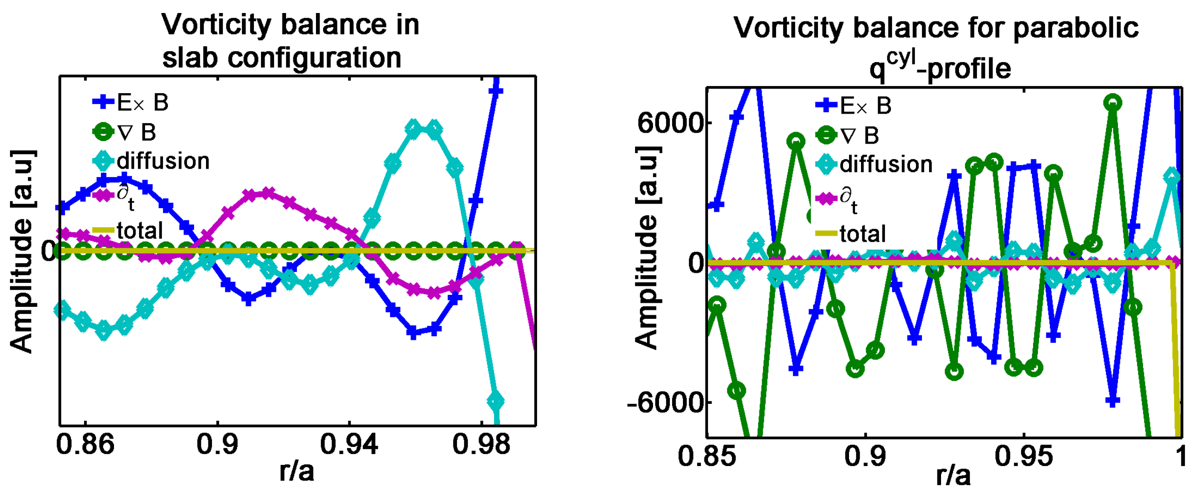

Figure 5.8: Vorticity balances - *i.e* time and flux-surface averaged of vorticity equation terms - for:
Left panel: a slab simulation with $\alpha_{Ti_0} = 1$
Right panel: a circular limited simulation with the reference magnetic configuration and $\alpha_{Ti_0} = 1$

In other words, in the slab case, the quasi-steady state is reached when the diffusion becomes large enough to compensate the $\mathbf{E} \times \mathbf{B}$ term. In fact, the curvature g-term used to model the diamagnetic current in slab configuration cannot contribute to the vorticity balance as its integration vanishes by construction. With a constant g, we have:

$$\oiint_{\mathrm{F.S}} g \partial_\theta N dS = 0 \tag{5.2}$$

It results that the vorticity and the vorticity gradient must grow until viscosity compensates the turbulent contribution. As the vorticity is strongly linked to the $\mathbf{E} \times \mathbf{B}$ shear, it leads to the generation of edge transport barriers and consequently to the enhancement of the particle confinement in the whole edge region. In limited circular configuration, the curvature ∇B term is no longer vanishing by construction and plays a key role on the vorticity balance by compensating the $\mathbf{E} \times \mathbf{B}$ contribution. The system can thus reach a steady-state without needing a strong increase of vorticity and thus of viscosity contribution. It is obvious that the situation is quite different in open field lines where the contribution of parallel terms adds a dominant player in the balance. It can explain why spontaneous barriers do not appear in the open fields lines in slab configuration both in Tokam2D and Tokam3X. Note that the parallel dynamic also impacts on turbulence properties and linear stability. The analysis of vorticity balances permits to understand why transport barriers - or at least improvement of the particle confinement - appear spontaneously in the whole closed field lines domain in slab configuration in comparison with realistic limited circular configurations. An improvement of the curvature g-term into a non-vanishing average form is thus required for 2D or 3D slab codes in order to reduce the gap with simulations of realistic circular geometry. For example, one can conceive a g coefficient which depends on the toroidal and/or poloidal direction - representing for example the HFS/LFS asymmetry of interchange instability - such the flux-surface average of ∇B-curvature would no longer be vanishing.

5.1.4.2 Differences with divertor configuration

Tokam3X simulations run in divertor configuration lead to the formation of a stable transport barrier [Galassi 17a]. This barrier is localised just before the separatrix with a radial extension of a few ion Larmor radii. The barrier efficiency remains constant around 20% and leads to a significant improvement of the particle confinement in closed field lines. Such barrier seems to be robust as it has been obtained both with COMPASS-like and JET-like divertor configurations. Two main discrepancies could potentially explain why spontaneous transport barriers are obtained in divertor X-point configuration and not on circular limiter: the existence of a substantial poloidal variation of the flux expansion in divertor configuration and the effect of the X-point itself.

Effect of flux expansion:
The impact of flux expansion - isolated from the presence of an X-point - has been investigated with Tokam3X in [Galassi 17b] by comparing three simulations in limiter configuration with different Shafranov shifts: one without Shafranov shift and two with a compression of circular flux surfaces at the LFS or at the HFS midplanes (obtained by a radial shift of the center position of flux surfaces). The definition of flux expansion used in this publication is:

$$f_x(\psi, \theta) = \frac{\langle \boldsymbol{\nabla} \psi(\psi, \theta) \rangle_\theta}{\boldsymbol{\nabla} \psi(\psi, \theta)} \tag{5.3}$$

It is found that the poloidal variation of turbulent particle fluxes - and in particular the turbulence ballooning - is very similar between the three simulations when these fluxes are normalized by the local value of the flux expansion f_x, i.e when fluxes are analysed in the magnetic space. Such normalization by flux expansion has also been used in divertor configuration in order to recover a turbulence ballooning at the LFS midplane while the analysis of turbulent particle flux in the real space exhibits a larger flux close to the top of the poloidal plane [Galassi 17a]. The Shafranov shift impacts also mean equilibrium properties. Indeed, when flux surfaces are more compressed at the LFS midplane, the density gradients are found to be steeper which is the sign of a better particle confinement and thus of an increase of turbulence stabilisation. Such stabilisation is believed to be the result of the modification of the magnetic geometry: the magnetic shear or the effective curvature - i.e the proportion of the field line on the LFS. However, no spontaneous edge transport barriers has been observed in circular geometry by modification of the Shafranov shift.

Effect of the presence of a X-point:
A particularity of the presence of the X-point is the formation of magnetic surfaces isolated from the main plasma and calls the Private Flux Region. This one is found to generate a complex circulation of particle and currents in the vicinity of the X-point. However, this private region is not expected to strongly impact on global equilibrium properties in Tokam3X simulations due to its very localized and isolated effect. Note that it will probably not longer be true if neutrals or impurities were taken into account in Tokam3X simulations but such influence is beyond the scope of this thesis. Another effect of the presence of the X-point is induced by the poloidal field singularity: a significantly large magnetic shear develops around the X-point. In the following, we focus on the impact of this magnetic shear on edge plasma properties to observe if magnetic shear can explained the formation of an edge transport barrier in divertor configuration. For that, the magnetic shear is decoupled from the effect of poloidally varying flux expansion.

5.2 Impact of safety factor and magnetic shear on edge transport properties

In order to focus only on the impact of pitch angle and thus of cylindrical safety factor and magnetic shear, we consider only cases with the minimum geometrical complexity: no poloidally varying flux expansion and no X-point. We opt consequently for limited plasmas in circular geometry and not on more complex geometry such as divertor X-point configuration. We first analyse the effect of safety factor profile by comparing our reference realistic magnetic configuration with a simulation with a flat q^{cyl}-profile. Then, we mimic the global effect of a X-point from a diverted plasma into our circular limiter magnetic configuration.

5.2.1 Modification of magnetic configuration

To understand the role played by the safety factor profile, a simulation with a flat q^{cyl}-profile is set up. For that, we modify the poloidal magnetic field B_{pol} as displayed in Figure 5.9. The maximum of B_{pol} is now localized at the far SOL of HFS region and its minimum in the inner closed field lines of LFS.

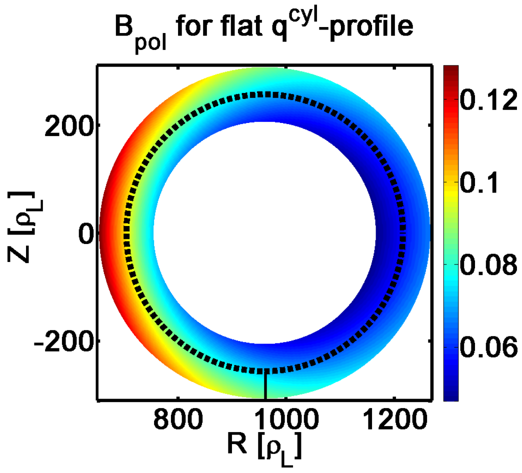

Figure 5.9: 2D-(R, Z) poloidal sections of poloidal magnetic field B_{pol} used in order to obtain a flat q^{cyl}-profile.

The resulting cylindrical safety factor q^{cyl} and magnetic shear s^{cyl} are represented in the form of radial profiles in Figure 5.10 and of 2D-(R, Z) maps on Figure 5.11. The q^{cyl}-profile obtained is effectively flat which leads to a zero s^{cyl}-profile. The amplitude of q^{cyl} in the flat profile is chosen in order to be equal to the one of the parabolic profile at the LCFS, i.e $q^{\text{cyl}}_{\text{flat}} \approx 3.85$. Nevertheless, poloidal asymmetries still exist with flat q^{cyl}-profile: the value of local cylindrical safety factor is as twice large in the HFS as in the LFS while the poloidal variation of local cylindrical magnetic shear is non zero but has a very weak magnitude compared to the magnetic shear of the parabolic q^{cyl} simulation and can thus be considered as quasi uniform in the poloidal plane.

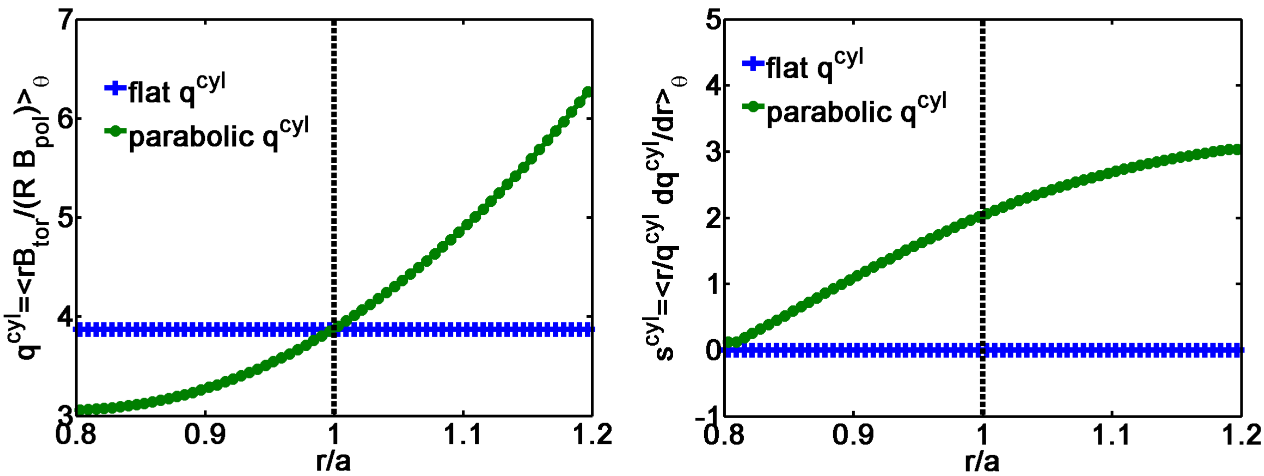

Figure 5.10: Radial profiles of flux-surface averaged
Left panel: cylindrical safety factor q^{cyl}
Right panel: cylindrical magnetic shear s^{cyl}

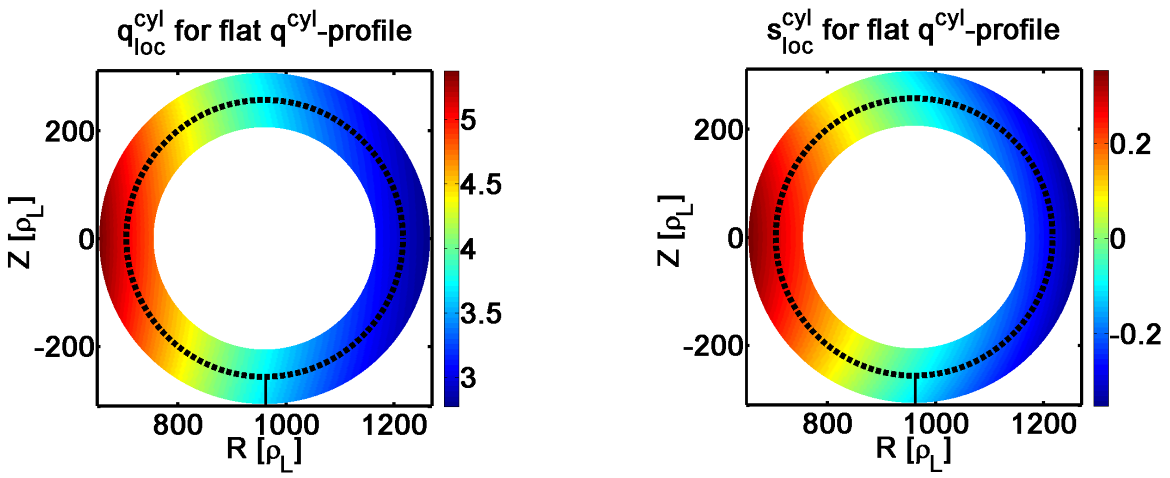

Figure 5.11: 2D-(R, Z) poloidal sections for flat $q^{\rm cyl}$-profile of:
Left panel: local cylindrical safety factor $q_{\rm loc}^{\rm cyl}$.
Right panel: local cylindrical magnetic shear $s_{\rm loc}^{\rm cyl}$.

5.2.2 Impact of safety factor: resonant magnetic surfaces

Before focusing on the impact of magnetic shear, we first come back to the fluctuations of normalized density gradient observed with the parabolic $q^{\rm cyl}$ magnetic configuration on the left panel of Figure 5.7. As one can see on both panel of Figure 5.12, these fluctuations disappear with a flat $q^{\rm cyl}$-profile. Left and right panels display the normalized gradient density $-\nabla_\psi \langle N \rangle_{t,\varphi} / \langle N \rangle_{t,\varphi}$ respectively on the HFS and LFS midplanes of the poloidal section. On both plots, the localization of cylindrical safety factor values multiple of quarters of integer are added in vertical red dashed lines. Theses $q^{\rm cyl}$-values corresponds to resonant modes for filaments as we only simulate a quart of the torus in the toroidal direction. A perfect correlation is found between these resonant magnetic surfaces and the sharp and very localized drop of normalized density gradients in the parabolic case. For the flat $q^{\rm cyl}$-profile case, we opted for a constant cylindrical safety factor which does not correspond to a rational value (at least from numerical point of view) and we thus do not observe such localized and brutal drop of density gradients. This phenomenon corresponds to a strong flattening of density within these resonant surfaces for which resonant modes ($k_\| = 0$) are strongly enhanced due to a better connexion between HFS and LFS: the filaments close on themselves and are thus more able to develop and to grow due to the change on parallel damping. The link between local density flattening and the HFS/LFS connexion is confirmed by the fact that the flattening is stronger in closed than in open field lines in which the flattening disappears from $r = 1.08$a for the HFS. Indeed, for open field lines, the filament ends up finally at the wall and can thus not fully develop: the limiter generates a symmetry breaking so that $k_\| \approx 0$ modes are able to develop even on non rational surfaces. Finally, the effect is found to be stronger in the HFS than in the LFS which may be due to the turbulence ballooning. Note that for the flat $q^{\rm cyl}$-profile on the LFS, similar drops of normalized density are obtained in the closed field lines and remain unexplained.

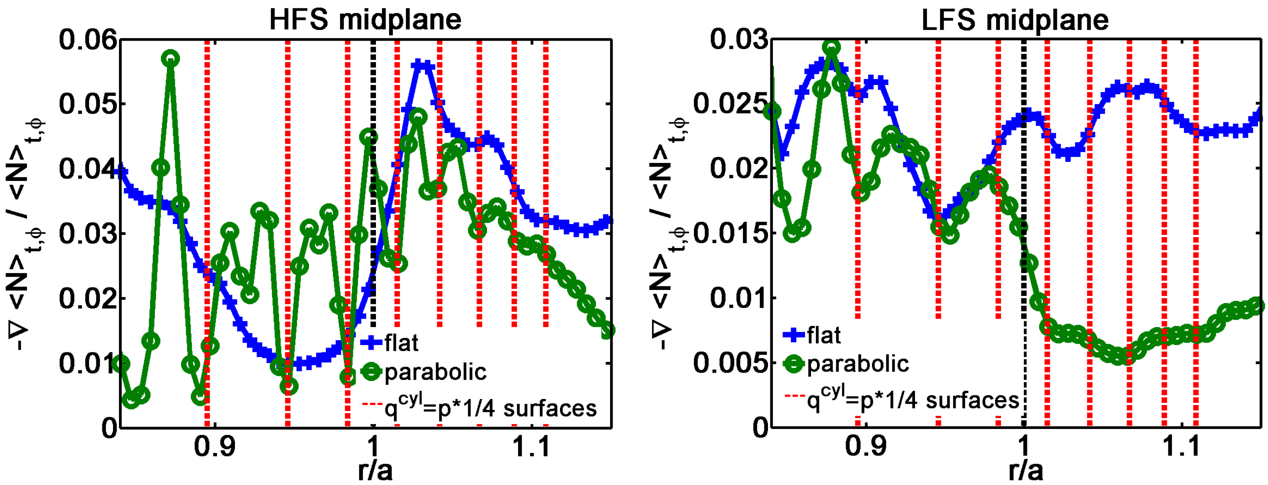

Figure 5.12: Time and toroidally averaged normalized density gradient profiles for flat and parabolic q^{cyl}-profiles at:
Left panel: HFS midplane
Right panel: LFS midplane
Vertical red dashed lines represent multiple of quarter of q^{cyl}-rational values corresponding for the code to resonant magnetic surfaces as only a quart of the torus is simulated in the toroidal direction.

5.2.3 Theoretical effect of magnetic shear: spatial tilting of fluctuations

The contribution of the magnetic shear on the generation of sheared flow by turbulence has been investigated in [Fedorczak 12]. First, the magnetic shear is found to generate a spatial tilting of ballooning modes in edge plasma. In the presence of a X-point, such tilting takes the form of poloidally up-down asymmetry with respect to LFS midplane as is can be seen on Figure 5.13. Structures on both sides of LFS midplane are tilted differentially in the poloidal direction.

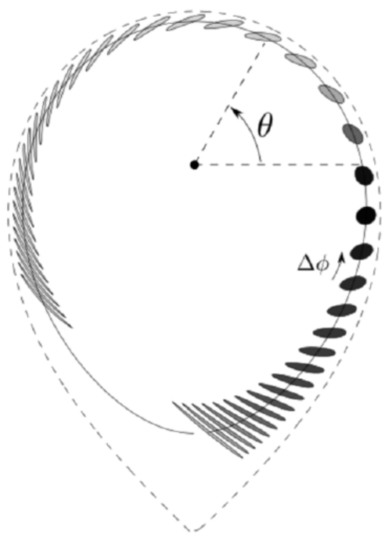

Figure 5.13: Poloidal cross section of the effect of magnetic shear on a circular flux tube along the field line [Courtesy N.Fedorczak].

Sheared flow generated by turbulence - or zonal flows - are usually considered as the result of Reynolds stress induced by $\mathbf{E} \times \mathbf{B}$ flow shear. In addition to this effect, the spatial tilting adds a contribution of the magnetic shear into the Reynolds Stress which can contribute to the generation of sheared flows and thus to an improvement of the particle confinement.

5.2.4 Impact of magnetic shear on transport properties

One can wonder if the theoretical impact of magnetic shear on turbulence structures is significant and is recovered in our fluid turbulence simulations with realistic circular geometry. To investigate the impact on density structures, we first look at density snapshots - in Figure 5.14 - in order to detect obvious discrepancies with and without magnetic shear. On the left panel, with a flat q^{cyl}-profile and thus no magnetic shear, the density structures have a quite small radial and poloidal extensions - between 5 and 10 ρ_L - compared to the ones resulting from a parabolic q^{cyl}-profile - see right panel - for which the size of the structures can reach several tens of ρ_L. A strong poloidal asymmetry exists in the parabolic case with more defined structures in LFS and more distorted structures in the HFS. Some large amplitude blobs penetrate in the LFS Scrape-Off Layer in the parabolic configuration while for the flat configuration we only distinguish a deeper penetration in the LFS compared to HFS but no large amplitude events.

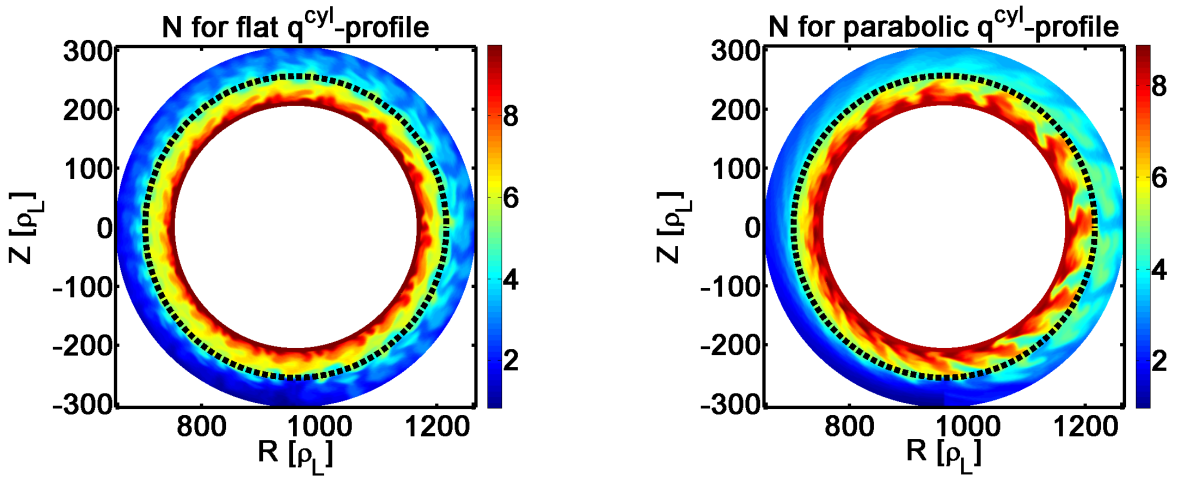

Figure 5.14: 2D-(R, Z) snapshots of density at a given toroidal position and time iteration for
Left panel: a flat q^{cyl}-profile
Right panel: the parabolic q^{cyl}-profile corresponding to the reference magnetic configuration.

Let us now analyse more quantitatively and precisely these differences.

5.2.4.1 Shape of fluctuations

Methodology of conditional averaging:

Patterns of density structures are investigated using a conditional averaging technique. The procedure is the following: first, the poloidal plane is split into 17 sectors: the closed field line region is divided into 8 sectors with the same poloidal extension of 45° while the Scrape-Off Layer is split into 7 sectors of 45° and two sectors of 22.5° on both sides of the limiter. In each sector, a conditional averaging on density is made on the center and only rare fluctuating events exceeding two standard deviations are considered. An example of the time evolution of density fluctuations can be found on Figure 5.15 for the center of the sector localized at the top of the poloidal plane and at the middle of closed field lines for an arbitrary toroidal position: $(r/a, \theta, i\varphi) = (0.9, 90°, 6)$. The horizontal red dashed line represents two standard deviations and maxima of density fluctuations which exceed this threshold are retained for the conditional averaging (blue circles).

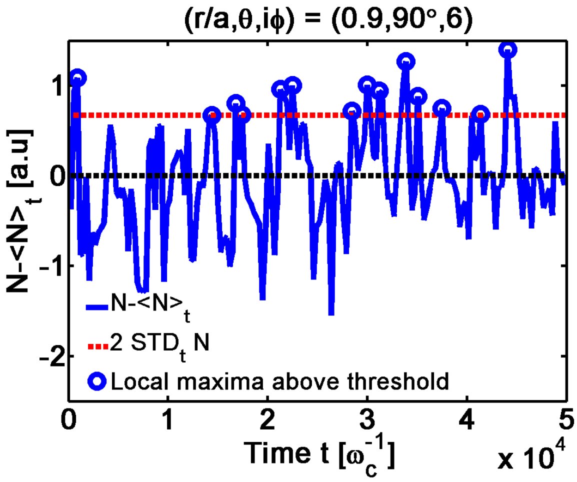

Figure 5.15: Extract of the time evolution of density fluctuations $N - \langle N \rangle_t$ at $(r/a, \theta, i\varphi) = (0.9, 90°, 6)$ - i.e at the top of the poloidal section and at the middle of closed field lines - for parabolic q^{cyl}-profiles.

Spatial tilting of structures by magnetic shear:

For these large amplitude events, we average the corresponding density fluctuations in the whole sector. Density patterns of large events resulting from this conditional averaging procedure can be observed on the left panel of Figure 5.16 for the simulation with a flat q^{cyl}-profile and on the right panel for the simulation with parabolic q^{cyl}-profile. Without magnetic shear, one can observe that the patterns of density fluctuations are quite circular and mostly isotropic on both open and closed field lines. No strong differences can be observed on the shape of fluctuations between high and low field sides even if density structures seem to be slightly more elongated in the poloidal direction in the HFS. Conversely, the patterns of density fluctuations are strongly impacted when the magnetic shear is included. First, in the LFS midplane, density fluctuations reveal a more elliptic shape and the size of the structures has strongly increased. On both sides of the LFS midplane, one can notice a spatial tilting of turbulent structures in opposite side: the expected theoretical poloidally up-down asymmetry in the presence of a symmetry breaking (for example a limiter at the bottom the chamber) of Figure 5.13 is recovered. When the poloidal distance with the LFS midplane increases, the spatial tilting keeps amplifying especially in the open field line region which can be explained as the connection between the LFS and the HFS is weaker in the SOL in comparison to closed field line region where a strong coupling exists between the HFS and the LFS. A zoom around the HFS midplane is presented on Figure 5.17 which confirms the discrepancy between confined and unconfined regions as well as the strong stretching of density structures induced by magnetic shear. The magnetic shear is thus found to have a strong impact on density patterns with a differential effect on the low and high field sides.

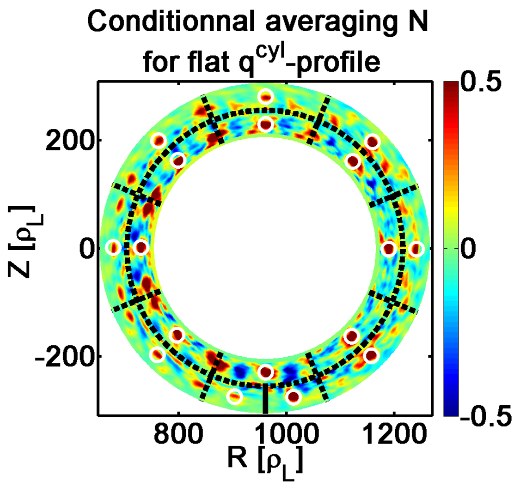

Figure 5.16: 2D-(R, Z) maps resulting of the conditional averaging procedure obtained with a simulation using:
Left panel: a flat $q^{\rm cyl}$-profile.
Right panel: the parabolic $q^{\rm cyl}$-profile which constitutes our reference case.
Sectors are delimited by black dashed lines and the white circles represent the centers of each sector where the conditional averaging is performed.

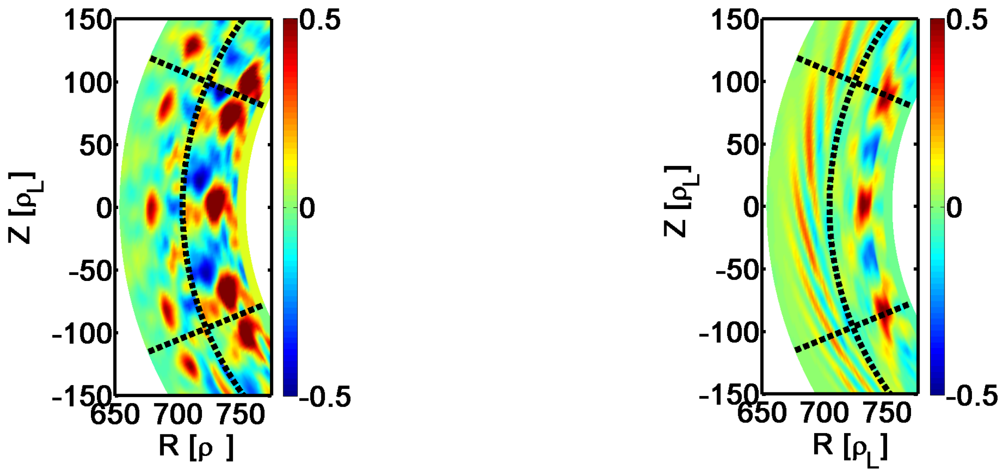

Figure 5.17: Same results of conditional averaging on density with a zoom around HFS midplane for:
Left panel: a flat $q^{\rm cyl}$-profile.
Right panel: the parabolic $q^{\rm cyl}$-profile which constitutes our reference case.

5.2.4.2 Radial transport - Poloidal asymmetries

In this section, we investigate the consequences of these differences of density fluctuation patterns on transport properties and especially on radial transport and poloidal asymmetries. In order to characterize turbulence properties in terms of radial penetration lengths and ballooning, Figure 5.18 displays 2D-(R, Z) maps of time and toroidally averaged radial $\mathbf{E} \times \mathbf{B}$ particle flux with identical color bar, on the left panel for the simulation with the flat $q^{\rm cyl}$-profile and on the right panel for the reference simulation with parabolic $q^{\rm cyl}$. In both simulations, one can notice a strong ballooning of turbulence in the LFS in agreement with our observations on normalized density gradient and with experiments.

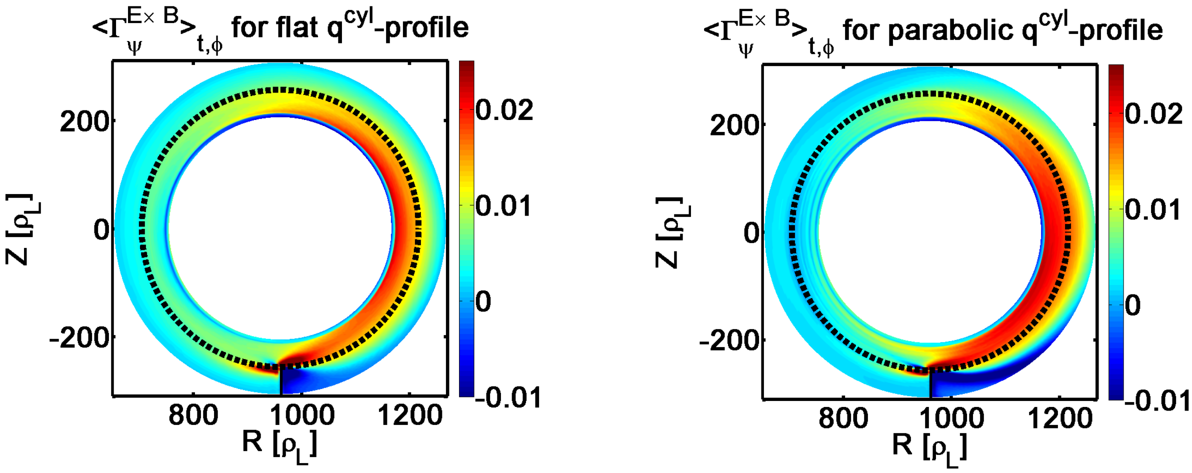

Figure 5.18: 2D-(R, Z) poloidal sections of time and toroidally averaged turbulent $\mathbf{E} \times \mathbf{B}$ radial flux $\langle \Gamma_{\psi}^{E\times B} \rangle_{t,\varphi}$ for a simulation with:
Left panel: a flat q^{cyl}-profile.
Right panel: the parabolic q^{cyl}-profile used in the reference case.

The poloidal profiles of this radial $\mathbf{E} \times \mathbf{B}$ particle fluxes are presented in Figure 5.19. For each magnetic configuration, the fluxes have been averaged in the whole closed field line region (solid lines) and in the whole SOL (dashed lines). It is found that the ballooning is stronger with parabolic q^{cyl}-profile compared to flat profile as the mean flux is both larger in LFS ($\theta = 0°$) and lower in HFS ($\theta = 180°$) with the first configuration. The radial penetration of turbulence in the Scrape-Off Layer on the LFS is also found to be larger with parabolic q^{cyl} as the $\mathbf{E} \times \mathbf{B}$ turbulent flux is still of the order of 10^{-2} at $r = 1.15$a while it almost vanishes at the same position without magnetic shear (Figure 5.18). Such increase of the radial penetration of turbulence in the Scrape-Off Layer with parabolic q^{cyl} is straightforward. Indeed, particle losses at target plates are proportional to invert of characteristic parallel length. The latter is proportional to q^{cyl} such as a larger safety factor magnitude with the parabolic profile leads to a decrease of the particle losses in the SOL and thus to a larger radial penetration of turbulence. There is thus no evidence that the magnetic shear - rather than the magnitude of the poloidal magnetic field - plays a role on the increase of turbulence ballooning.

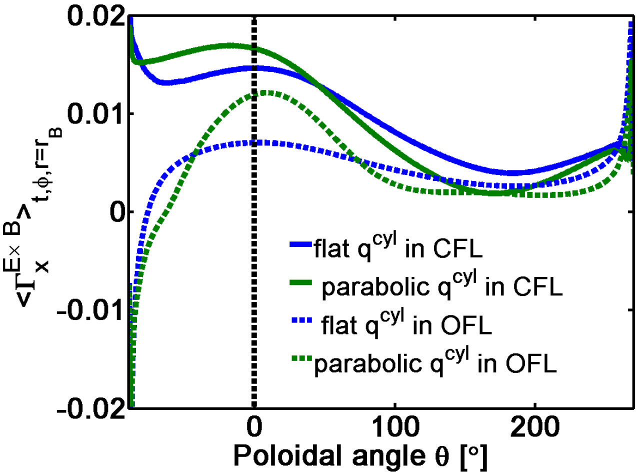

Figure 5.19: Poloidal profiles of turbulent $\mathbf{E}\times\mathbf{B}$ radial flux $\langle\Gamma_{\psi}^{E\times B}\rangle_{t,\varphi,r=r_B}$ averaged in time, toroidally and in open (OFL, $r_B = [0.8;1]$a) and in closed (CFL, $r_B = [1;1.2]$a) flux-surfaces for the simulations with a flat and a parabolic q^{cyl}-profiles.

5.2.4.3 Reynolds Stress:

The enhancement of turbulent flux with a parabolic q^{cyl} profile is susceptible to generate zonal flows able to strongly modify radial transport properties. The generation of zonal flows by turbulence is driven by the Reynolds stress which is suspected to play a key role in transport barrier formation and dynamics [Itoh 06]. The Reynolds stress (RS) corresponds to the radial transport of poloidal momentum: $RS = \langle\widetilde{u}_{\psi}\widetilde{u}_{\theta}\rangle_{t,\varphi}$. Poloidal sections of Reynolds stress are presented in Figure 5.20 respectively for flat and parabolic q^{cyl}-profiles on left and right panels. The same colorbar is applied on both plots. Without magnetic shear, the Reynolds stress magnitude does not exceed $5\times10^{-4}c_s^2$ with a maximal magnitude at the top of the device. The Reynolds stress does not present a significant poloidal asymmetry except close to the LCFS. Conversely, we note a strong enhancement of the Reynolds stress in the presence of magnetic shear with a magnitude larger than $10^{-3}c_s^2$ for most of the poloidal section. An up-down anti-symmetry is obtained in the closed field line region. Conversely, in the open field lines, a strong up-down asymmetry appears in the presence of magnetic shear. This asymmetry is due to the limiter which prevents the Reynolds Stress to extend on the HFS of the limiter. The enhancement of the Reynolds Stress magnitude as well as the up-down asymmetry are in agreement with the theoretical effect of magnetic shear in the presence of a limiter at the bottom (or top) of the chamber as mentioned previously.

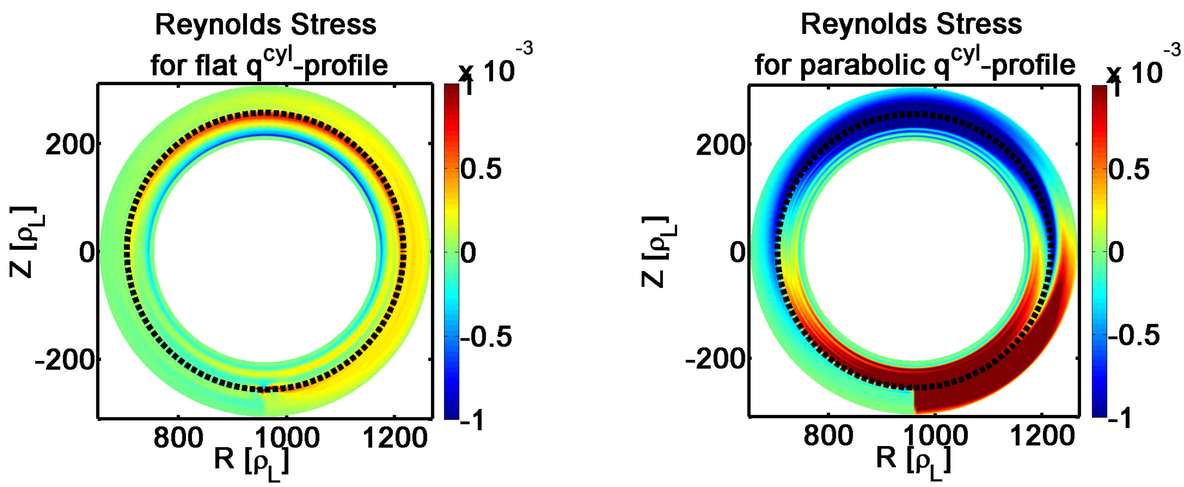

Figure 5.20: 2D-(R, Z) poloidal sections of Reynolds Stress (RS) for a simulation with:
Left panel: a flat q^{cyl}-profile.
Right panel: the parabolic q^{cyl}-profile used in our reference case.

One can obtain an equation for zonal flows by flux-surface averaging the ion poloidal momentum conservation equation. In the closed field lines, its simplest form writes:

$$\partial_t \langle n u_{i\theta}^{(1)} \rangle_{\mathrm{F.S}} + \partial_\psi \langle n u_{i\psi}^{(1)} u_{i\theta}^{(1)} \rangle_{\mathrm{F.S}} = D_W \partial_r^2 \langle u_{i\theta}^{(1)} \rangle_{\mathrm{F.S}} \tag{5.4}$$

From this equation, we note that the zonal flow is a sheared flow generated by turbulence via the Reynolds Stress gradient. The radial profile of the mean Reynolds Stress $\langle \tilde{u}_{i\psi}^{(1)} \tilde{u}_{i\theta}^{(1)} \rangle_{\mathrm{t,F.S}}$ is presented on Figure 5.21 for flat and parabolic q^{cyl}-profiles. In closed field lines, the same order of magnitude of the Reynolds Stress is found in both simulations. The local increase of the RS in the confined plasma due to the magnetic shear is compensated by the up-down anti-symmetry when a flux-surface averaging is applied. In the open field lines, this compensation is no longer occurring due to the symmetry breaking generated by the limiter and the associated up-down asymmetry. It results in a larger magnitude of the flux-surface average RS with the parabolic q^{cyl}-profile. We note that the mean Reynolds Stress exhibits also a stronger gradient with magnetic shear in the vicinity of the LCFS. The impact on equilibrium fields through the magnetic shear of such increase of Reynolds Stress magnitude in open field lines and of its gradient at the LCFS, is now investigated.

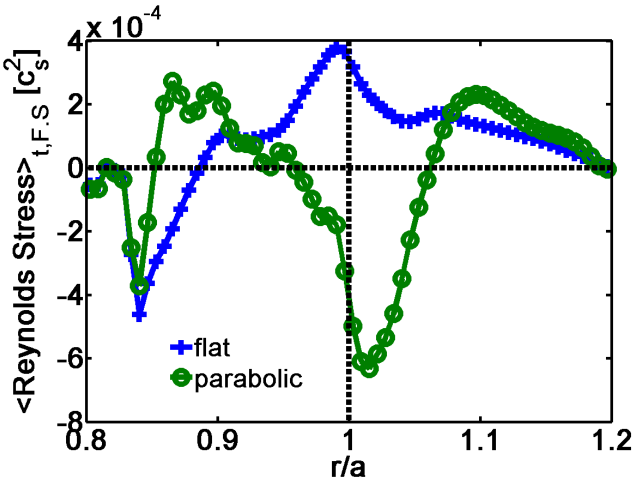

Figure 5.21: Radial profiles of time and flux-surface averaged Reynolds Stress with flat and parabolic $q^{\rm cyl}$-profiles.

5.2.4.4 Limited impact on mean profiles

We now look at the effect of the magnetic shear on mean field profiles. Concerning the particle confinement, we already describe how the normalized density gradient is impacted by resonant magnetic surfaces. On the left panel of Figure 5.22, the radial profiles of time and flux-surface averaged density are displayed for both magnetic configuration. A flattened density profile is obtained in the parabolic $q^{\rm cyl}$ simulation resulting in a slightly lower core particle confinement compared to the simulation without magnetic shear. Magnetic shear in a realistic circular limited plasma is not able to significantly modify the global particle confinement compared to a case without such shear. Concerning the radial electric field - which determines both zonal flows and $\mathbf{E}\times\mathbf{B}$ shear able to stabilize turbulence - the right panel of Figure 5.22 shows a weak impact of magnetic shear. Without it, we recover a single radial electric field well in closed field lines localized around $r = 0.94$a while two wells coexist with a realistic magnetic shear but the same order of magnitude is obtained. Note that the radial profile of electric field is no significantly modified by magnetic shear in the inner region of closed field lines - where the buffer zone applies - and in the Scrape-Off Layer from $r = 1.05$a to the outer boundary limit. The limited effect of magnetic shear on mean equilibrium properties is explained by its effect on the Reynolds Stress. In closed field lines, a same order of magnitude is found for the flux-surface averaged RS: a similar magnitude of zonal flows is obtained so that the impact of mean profiles is negligible. In open field lines, the radial electric field is mainly determined by the sheath boundary conditions in the parallel direction so that the impact of the increase of the flux-surface RS magnitude is very limited.

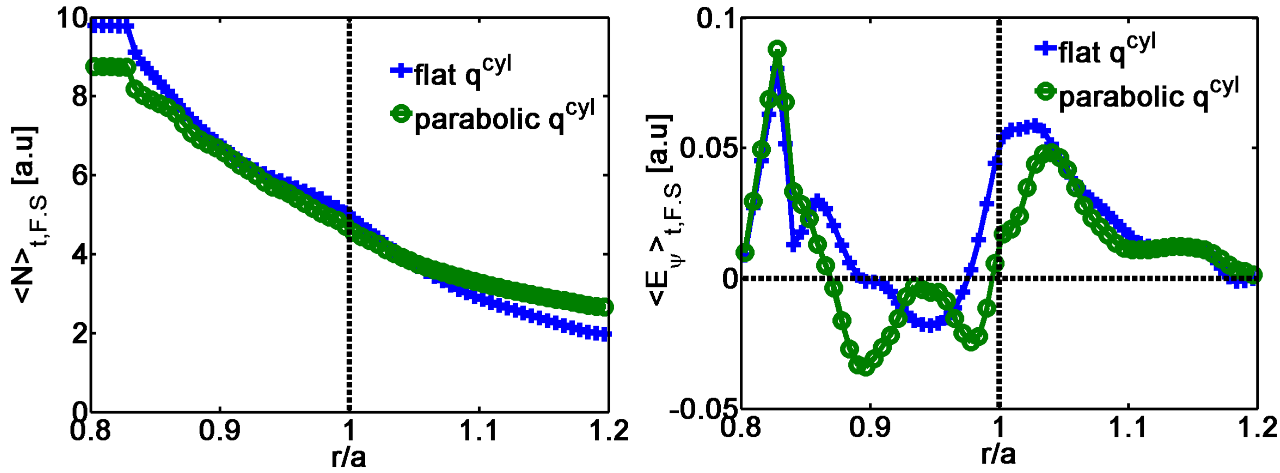

Figure 5.22: Radial profiles of time and flux-surface averaged:
Left panel: density $\langle N\rangle_{t,\mathrm{F.S}}$.
Right panel: radial electric field $\langle E_\psi\rangle_{t,\mathrm{F.S}}$.

One may wonder if this weak modification of the radial electric field profile around the LCFS affects notably the $\mathbf{E}\times\mathbf{B}$ shear. Figure 5.23 exhibits the radial profile of such $\mathbf{E}\times\mathbf{B}$ shear in both magnetic configurations. It is found that the magnitude of this shear is not strongly modified by the magnetic shear. In particular, exactly the same shear amplitude is obtained at the LCFS.

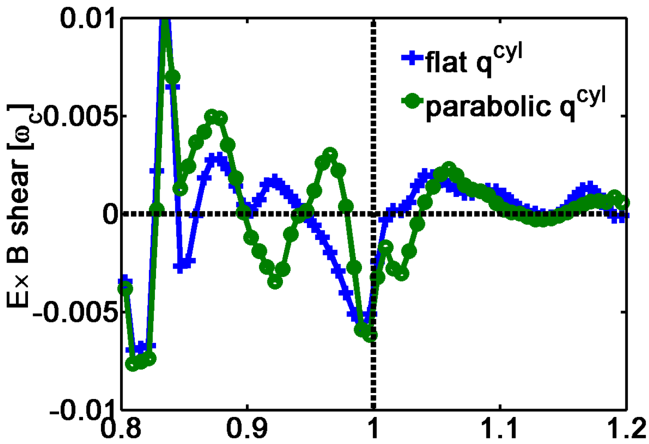

Figure 5.23: Radial profile of time and flux-surface averaged $\mathbf{E}\times\mathbf{B}$ shear for simulations with flat and parabolic q^{cyl}-profiles.

In summary, we point out the flattening of density profile by resonant magnetic surfaces, especially in the HFS region. The magnetic shear is found to modify patterns of density structures by inducing a spatial tilting of these filaments in conformity with its theoretical effect. This leads to an enhancement of poloidal asymmetries as well as a deeper penetration of turbulence in the Scrape-Off Layer in particular on the LFS region. The Reynolds Stress - which controls zonal flow - is locally enhanced by the magnetic shear. In the closed field lines region, an up/down antisymmetry compensates this local increase when a flux-surface averaging is applied so that no significant modifications of mean profiles and $\mathbf{E} \times \mathbf{B}$ flows are observed. In the open field lines, the limiter at the bottom of the chamber is a symmetry breaker so that the up/down asymmetry does not longer compensate the local enhancement of the Reynolds Stress. As the electric field of the unconfined plasma is mostly determined by the sheath physics, the consequences on mean profiles and $\mathbf{E} \times \mathbf{B}$ flows is reduced. Note that this is a potentially key difference between limiter and divertor configuration: in limiter configuration, it is the limiter that triggers the symmetry breaking so that the flux-surface averaged Reynolds Stress is impacted by the magnetic shear only in the SOL where the radial electric field is constrained and cannot respond significantly to this drive. In divertor configuration, the symmetry breaking is induced by the X-point and exists also in the outermost closed flux surfaces where the radial electric field is more sensitive - less constraint because no sheath in the parallel direction - to an enhancement of the Reynolds Stress.

5.3 Transport barriers generated by magnetic shear

5.3.1 X-point-like safety factor profile

In this last section, we try to reproduce the global effect of the magnetic shear induced by the presence of a X-point without taking into account its local effect or the impact of flux expansion. For that, a final simulation mimicking the flux-surface averaged magnetic shear generated by the presence of a X-point in a divertor geometry is made in our circular limited geometry. The shape of the magnetic equilibrium is inspired by a COMPASS experiment so that this simulation is referred as 'COMPASS-like q^{cyl}-profile' in all the Figures referring to this simulation and more generally as 'divertor-like q^{cyl}-profile' in the main text. The cylindrical safety factor and magnetic shear radial profiles are presented respectively in the left and right panels of Figure 5.24. Except in the LCFS area - for $r \in [0.95, 1.05]$a - the two profiles of q^{cyl} and s^{cyl} match exactly the parabolic case. In fact, we superimpose a Gaussian centred at the LCFS to the parabolic q^{cyl}-profile in order to reproduce the flux-surface averaged global effect of the X-point. It leads to a cylindrical magnetic shear profile exhibiting two large amplitude peaks: a positive one in the last closed flux-surfaces at the vicinity of the LCFS with a maximum at $r = 0.984$a and a negative one symmetric with respect to LCFS at $r = 1.016$a. Note that the magnitude of these two peaks has been increased by a factor of 2 compared to the value obtained from realistic divertor X-point geometry in order to increase the impact of the magnetic shear.

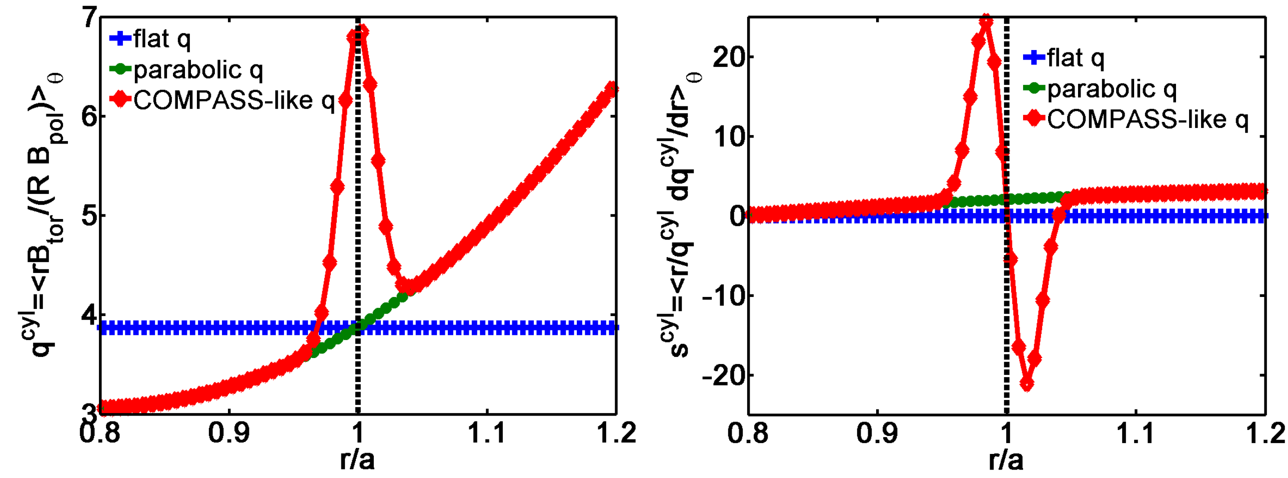

Figure 5.24: Radial profiles of flux-surface averaged:
Left panel: cylindrical safety factor q^{cyl}.
Right panel: cylindrical magnetic shear s^{cyl}.

Poloidal asymmetries induced by this new magnetic configuration can be examined on Figure 5.25. Both 2D-(R, Z) maps of local cylindrical parameters are similar to the parabolic reference simulation excepted in the vicinity of LCFS. It results in a very low level of poloidal asymmetries for s^{cyl} - considered thus as homogeneous poloidally - which makes a fundamental difference with a divertor configuration. In other words, the local effect of the X-point is not included in our circular limited simulation as the local magnetic shear is mostly homogeneous poloidally.

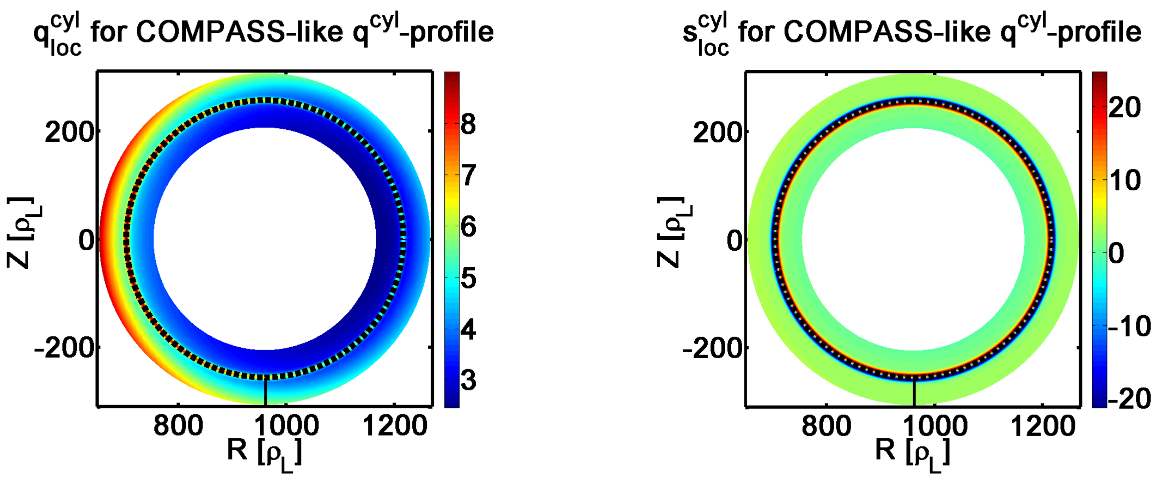

Figure 5.25: For the divertor-like simulation, 2D-(R, Z) poloidal sections of local:
Left panel: local cylindrical safety factor $q^{\mathrm{cyl}}_{\mathrm{loc}}$.
Right panel: local cylindrical magnetic shear $s^{\mathrm{cyl}}_{\mathrm{loc}}$.

5.3.2 Generation of localized stable transport barriers

The divertor-like magnetic configuration aims at reproducing the global effect of the strong magnetic shear existing close to the X-point. The question is to understand if the magnetic shear is responsible of the easier generation of transport barriers in divertor simulations without considering other geometrical effect such as the flux expansion. The barrier efficiency obtained with divertor-like magnetic configuration is displayed under a 2D-(R, Z) map on the left panel of Figure 5.26. It is found that two transport barriers appear spontaneously in our simulation. The first one is localized in the closed field lines, in the vicinity of the LCFS at $r \in [0.97; 0.99]$a with an efficiency of 25%. The second one - stronger and wider than the first one - is localized in the Scrape-Off Layer between 1.01 and 1.04a with a maximum efficiency of 40%. The two barriers can also be observed on radial profiles of $\mathbf{E} \times \mathbf{B}$, diffusive and total fluxes on the right panel of Figure 5.26. The total flux - nearly constant in closed field lines - is mostly turbulent up to $r = 0.94$a until the diffusive flux strongly raises up to 25% of the total flux. At the LCFS, the diffusive flux drops slightly before building up again to generate the second transport barrier at $r = 1.02$a.

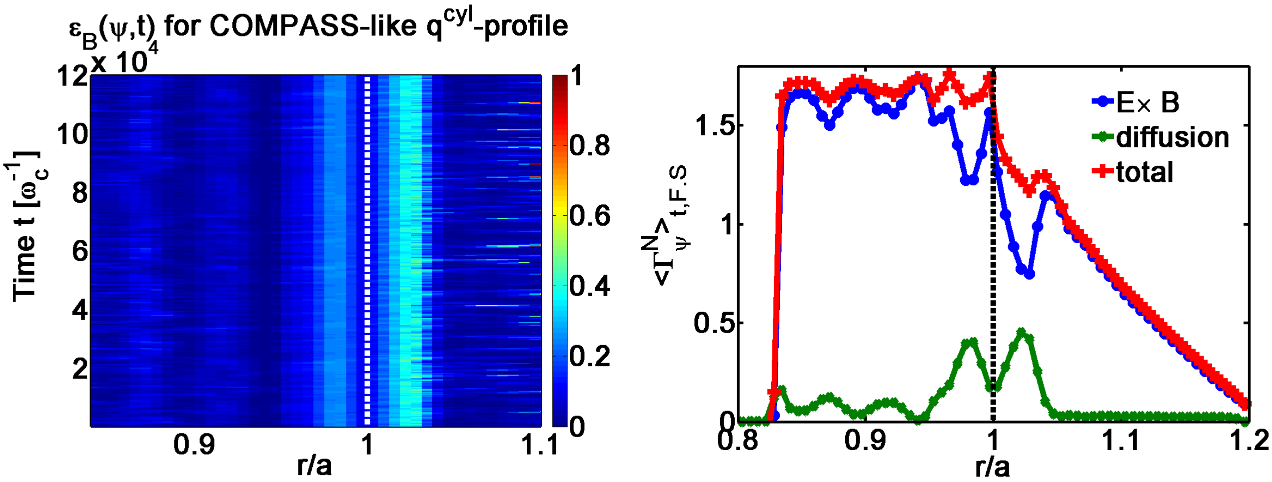

Figure 5.26: For the divertor-like magnetic configuration within our circular limited Tokam3X simulation:
Left panel: 2D - time and radial - map of barrier efficiency $\varepsilon_B(\psi, t)$.
Right panel: radial profiles of time and flux-surface averaged turbulent, diffusive and total radial particle fluxes.

The two spontaneous transport barriers found in our divertor-like configuration are particularly robust as no relaxations or significant barrier efficiency fluctuations occur in the simulation. For a more quantitative view, Figure 5.27 represents the profile of the time-averaged barrier efficiency. In contrast with simulations with flat or parabolic safety factor profiles, two barriers with significant efficiency to stop radial propagation of turbulence develop on both sides of the LCFS. The barrier in the confined domain around $r = 0.97$a is very stable with a quasi null standard deviation (black points). The barrier in the Scrape Off Layer experiences some fluctuations of its efficiency of several percent but not large enough to be considered as barrier relaxations.

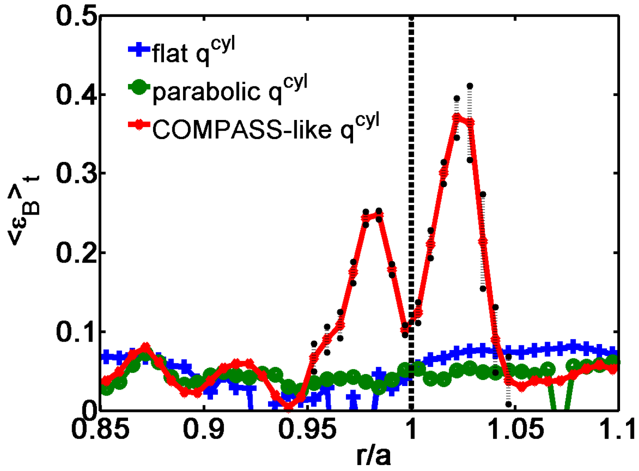

Figure 5.27: Radial profiles of time averaged barrier efficiency $\langle \varepsilon_B \rangle_t$ for simulations with flat, parabolic and COMPASS divertor-like q^{cyl}-profiles. For the latter, the vertical black dashed lines represent the standard deviation - i.e fluctuations - of the barrier efficiency.

One can wonder why the intermittency of turbulence does not induced time variation of the barrier efficiency. To answer this question, Figure 5.28 shows 2D - time and radial - maps of the flux-surface averaged $\mathbf{E} \times \mathbf{B}$ turbulent radial flux in the parabolic case (left panel) and the divertor-like simulation (right panel). With our reference parabolic simulation, turbulent avalanches propagate from the inner radial region to the SOL. A damping of turbulent events occurs in the open field line region due to the parallel losses at targets. Some avalanches can propagate up to the far SOL and even up to the outer boundary while weakest events are fully damped in the beginning of the SOL. With the divertor-like magnetic configuration, all turbulent avalanches coming from the inner region are strongly damped when crossing the strong magnetic shear region before the LCFS. The largest events which survive this region are reinforced at the LCFS before being damped again by the second large amplitude magnetic shear peak. At this point, a large part of turbulent events have been destroyed but the turbulence develops again after crossing this second magnetic shear area and propagates ballistically into the SOL as in the parabolic configuration.

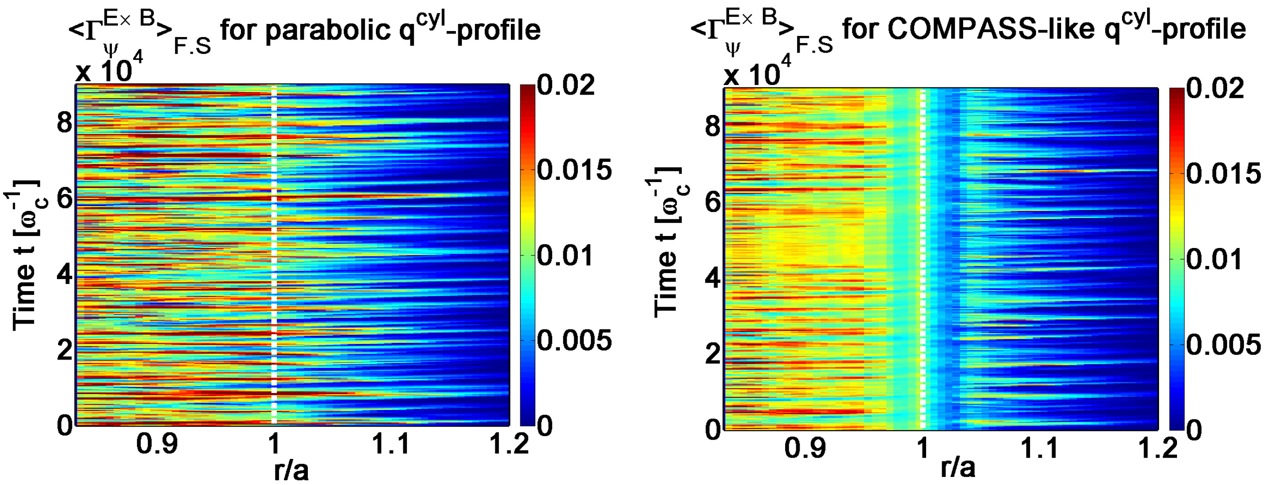

Figure 5.28: 2D-$(r/a, t)$ maps of flux-surface averaged radial $\mathbf{E} \times \mathbf{B}$ turbulent flux for simulation with:
Left panel: the parabolic q^{cyl}-profile.
Right panel: the COMPASS divertor-like q^{cyl}-profile.

The spontaneous generation of transport barriers in divertor-like configuration leads to a strong improvement of the particle confinement in comparison with flat and parabolic q^{cyl} simulations as it can be seen on the left panel of Figure 5.29. While the mean density amplitude for the three simulations is nearly the same in open field lines at $r = 1.05$a, the density in the core region is increased by a factor 1.5 and goes from approximatively 9 for the flat and parabolic simulations to 15 for the divertor-like magnetic shear simulation. One can remark that the rise of density occurs at the position of the peaks of the magnetic shear while the remaining of the density profile seems to evolve as in the parabolic case especially in the inner part of closed field lines. In order to corroborate this observation the normalized density gradients $-\nabla_\psi \langle N \rangle_{t,\mathrm{F.S}} / \langle N \rangle_{t,\mathrm{F.S}}$ are presented on the right panel of Figure 5.29. The plot confirms that the density profiles have the same behaviour in parabolic and divertor-like simulations prior to the first magnetic shear peaks around $r = 0.95$a even if the magnitude of the density gradient is slightly reduced in the divertor-like case. At this position, the normalized density gradient rises sharply by a factor 4 compared to the reference case. The sharpest part of density profile is reached at the second transport barrier position for which the normalized density gradient is 6 times larger than for the reference parabolic q^{cyl} simulation.

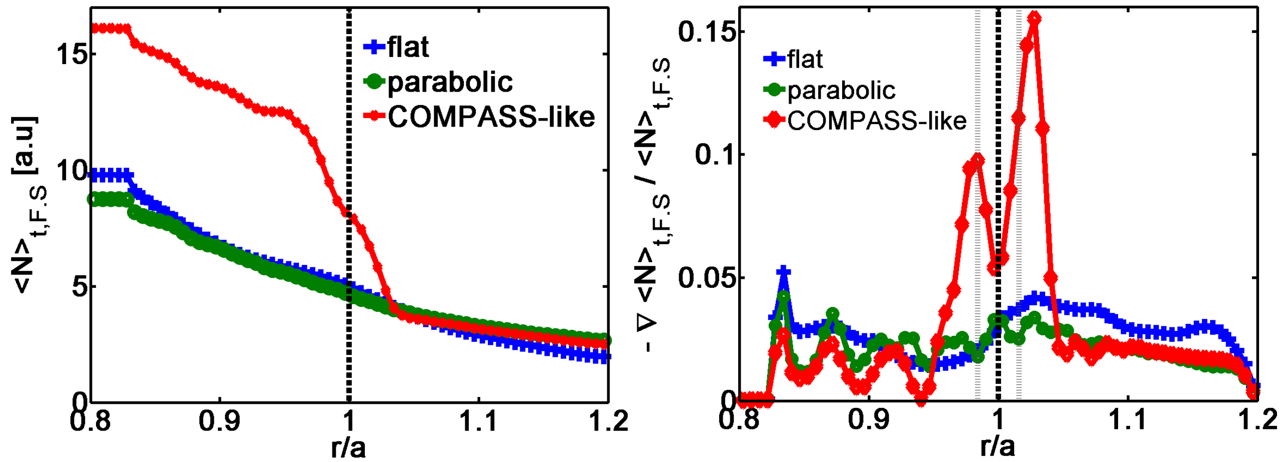

Figure 5.29: Radial profiles of time and flux-surface averaged:
Left panel: density $\langle N\rangle_{t,\mathrm{F.S}}$.
Right panel: normalized density gradient $-\nabla_\psi\langle N\rangle_{t,\mathrm{F.S}}/\langle N\rangle_{t,\mathrm{F.S}}$. The vertical black dashed lines represent the position of the maximum of the time-averaged efficiency of the two barriers in the simulation with the divertor-like q^{cyl}-profile.

Transport barriers are usually associated with zonal flows and thus linked to the radial electric field E_ψ and the $\mathbf{E}\times\mathbf{B}$ shear. One can wonder if the situation is similar for barriers generated by the magnetic shear. Both fields are presented on Figure 5.30 for the three different magnetic configurations. On the left panel, the radial electric field is found to be strongly enhanced on both sides of the LCFS compared to the reference or the flat q^{cyl}-profile configurations. The first well obtained around $r = 0.9$a in the reference case is recovered and slightly steepened while the second well becomes steeper and tighter at $r = 0.98$a. Such large variation of radial electric field leads to a huge $\mathbf{E}\times\mathbf{B}$ shear at the LCFS as it can be seen on the right panel of Figure 5.30. The magnitude of $\mathbf{E}\times\mathbf{B}$ shear is increased by a factor 5 very locally at the LCFS compared to flat or parabolic q^{cyl} simulations. The shear is negative at LCFS and becomes brutally positive in a few ρ_L. Far from LCFS, the $\mathbf{E}\times\mathbf{B}$ shear is unchanged compared to the reference configuration which means that the effect of magnetic shear on $\mathbf{E}\times\mathbf{B}$ shear is not significantly spreading upstream or downstream.

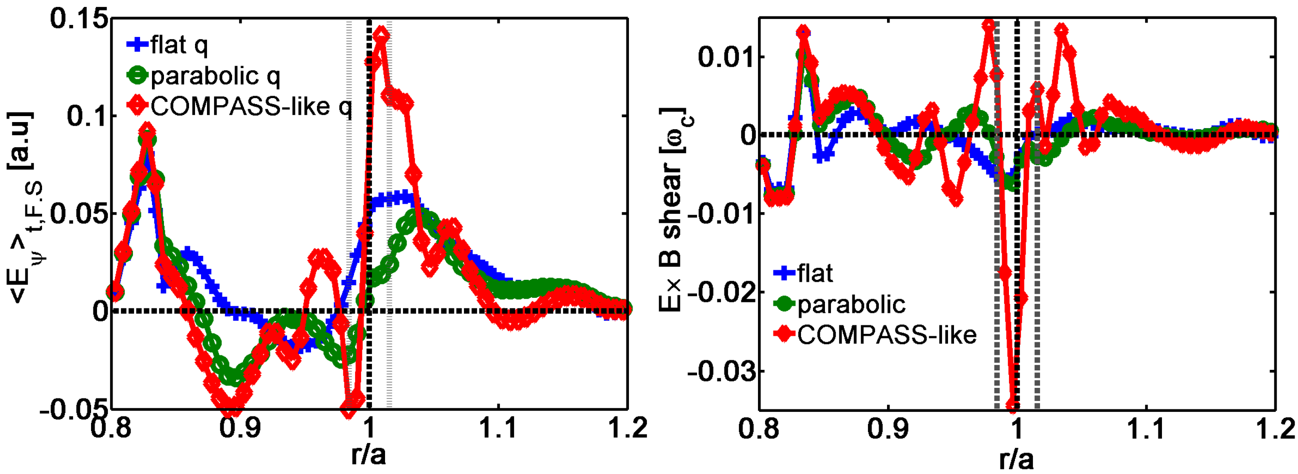

Figure 5.30: Radial profiles for the three simulations with flat, parabolic and COMPASS divertor-like q^{cyl}-profiles of time and flux-surface averaged:
Left panel: radial electric field $\langle E_\psi \rangle_{t,\text{F.S}}$.
Right panel: $\mathbf{E} \times \mathbf{B}$ shear.
The vertical black dashed lines represent the position of the maximum of the time-averaged efficiency of the two barriers in the simulation with the divertor-like q^{cyl}-profile.

5.3.3 Which shear generates the barrier?

The strong enhancement of the $\mathbf{E} \times \mathbf{B}$ shear by the magnetic shear raises a legitimate question: which of the $\mathbf{E} \times \mathbf{B}$ or magnetic shear is responsible of transport barrier formation. One would expect that the increase of the $\mathbf{E} \times \mathbf{B}$ shear - which is believed to be the key player in edge barrier formation - stabilizes turbulence which leads to the barrier establishment. If we focus on radial correlation between the barrier positions and the shapes of the two shears - as displayed on Figure 5.31 - this reasoning does not apply at our simulation. Indeed, the maxima of the barrier efficiency is found to be nearly perfectly aligned with the peaks of magnetic shear and not of those of $\mathbf{E} \times \mathbf{B}$ shear. For the latter, the maximal magnitude is reached near the LCFS where the barrier lost a part of its ability to stop radial propagation of turbulence.

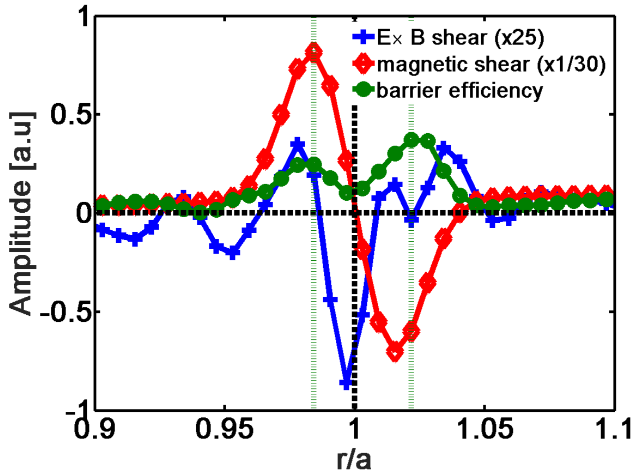

Figure 5.31: Radial profiles of mean $\mathbf{E}\times\mathbf{B}$ shear, cylindrical magnetic shear and mean barrier efficiency for the COMPASS divertor-like simulation. The vertical black dashed lines represent the position of the maximum of the time-averaged efficiency of the two barriers in the simulation with the divertor-like q^{cyl}-profile.

To validate this observation, the correlation between the barrier efficiency and the $\mathbf{E}\times\mathbf{B}$ shear is investigated on Figure 5.32. On the left panel, we observe that the $\mathbf{E}\times\mathbf{B}$ shear around the outer barrier ($r = 1.03$a) experiences some fluctuations around its mean quasi null value with insignificant amplitudes compared to the $\mathbf{E}\times\mathbf{B}$ shear magnitude obtained at the LCFS (see Figure 5.31). The barrier exhibits also fluctuations around its mean efficiency with a maximal magnitude close to 0.1. On the right panel, we found that these similar fluctuations of barrier efficiency and $\mathbf{E}\times\mathbf{B}$ shear are not correlated as no cycle or hysteresis occurred.

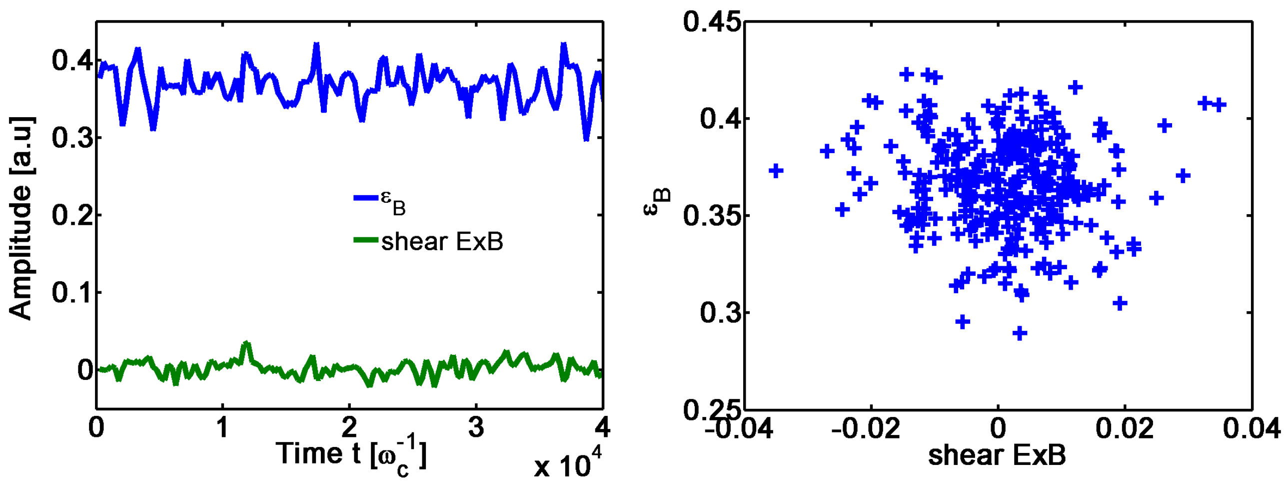

Figure 5.32: For the second transport barrier at $r = 1.03$a:
Left panel: time evolution of barrier efficiency and $\mathbf{E}\times\mathbf{B}$ shear.
Right panel: correlation between barrier efficiency fluctuations and $\mathbf{E}\times\mathbf{B}$ shear variations. Each symbol '+' represents their amplitudes at a time iteration of the simulation.

The analysis of the radial correlations between mean $\mathbf{E}\times\mathbf{B}$ and magnetic shear peaks combined with the absence of correlation between $\mathbf{E} \times \mathbf{B}$ shear and barrier fluctuations demonstrate that the two barriers obtained in COMPASS divertor-like within circular limiter configuration are directly generated by the magnetic shear. These barriers exhibit a identical behaviour - same width, localized in the vicinity of the LCFS and an absence of fluctuations in time - than the one obtained in divertor X-point geometry. The magnetic shear can thus be expected to be also an important player for the barrier generated in divertor configuration but a proper study on the effect of the $\mathbf{E} \times \mathbf{B}$ shear on X-point configuration would confirm it.

5.3.4 How this barrier impacts on transport properties and poloidal asymmetries?

The spontaneous formation of transport barriers generated by a strong magnetic shear as well as its impact on particle confinement and mean fields have been detailed previously. We now analyse the consequences of barrier formation on local transport properties and especially on poloidal asymmetries. For the configuration mimicking the global effect of a X-point, radial profiles of time and toroidally averaged density and $\mathbf{E}\times\mathbf{B}$ shear are detailed on both panels of Figure 5.33 for three poloidal positions: at the HFS midplane (or inboard midplane IMP), at the LFS midplane (outboard midplane OMP) and at the top of the poloidal plane. For the density plots, one can observe a more flattened profile in closed field lines at the outboard midplane as a consequence of the ballooned turbulence. In this case, turbulent events are able to penetrate closer to the LCFS such as the two barrier positions are clearly visible. For the top and IMP poloidal positions, turbulence seems to be damped at the beginning of the strong magnetic shear region near $r = 0.94$a such as the density profiles for $r \in [0.95; 1.03]$a are progressively but strongly affected by diffusive processes. Concerning the $\mathbf{E} \times \mathbf{B}$ shear, the magnitude in the vicinity of LCFS is found to be twice large at the top of the device compared to LFS and HFS midplanes. No strong discrepancies in $\mathbf{E} \times \mathbf{B}$ shear profiles and magnitudes are found between LFS and HFS midplanes in this simulation.

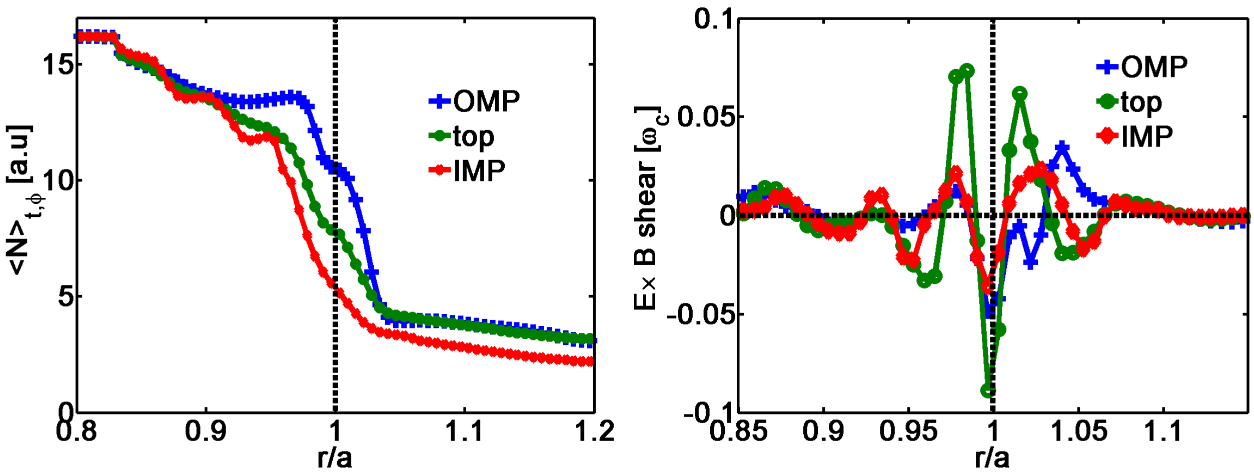

Figure 5.33: Radial profiles at three poloidal positions (top,LFS and HFS midplanes) for the simulation with COMPASS divertor-like magnetic configuration of time and toroidally averaged:
Left panel: density $\langle N\rangle_{t,\varphi}$.
Right panel: $\mathbf{E} \times \mathbf{B}$ shear.

In fact, the larger $\mathbf{E} \times \mathbf{B}$ shear obtained at the top of the device with the divertor-like magnetic configuration seems linked to a modification of the poloidal asymmetries of the turbulence as it can be noticed on the left panel of Figure 5.34. On this Figure, we plot the 2D poloidal section of time and toroidally averaged $\mathbf{E}\times\mathbf{B}$ radial particle flux. Note that the colorbar is similar to the one used in Figure 5.16 for flat and parabolic q^{cyl}-profiles. One can observe a complex organization of turbulence, see also poloidal profiles averaged on confined (solid lines) and unconfined (dashed lines) domains on the right panel. For the inner closed field lines, the turbulent flux is still localized around the LFS midplane and extends from the bottom to the top of the chamber in agreement with the reference simulation. Just before the LCFS, we note a strong reduction of turbulent flux at the LFS midplane, the maximum magnitude is now oriented around the top of the poloidal plane ($\theta = 75°$). The radial position where the modification of poloidal asymmetries occurred coincides with the position of the first transport barrier at $r = 0.98$a. After the LCFS, we recover the LFS ballooning of turbulence close to the reference parabolic simulation. It means that the negative peak of magnetic shear does not change the poloidal distribution of radial $\mathbf{E}\times\mathbf{B}$ particle flux in open field lines.

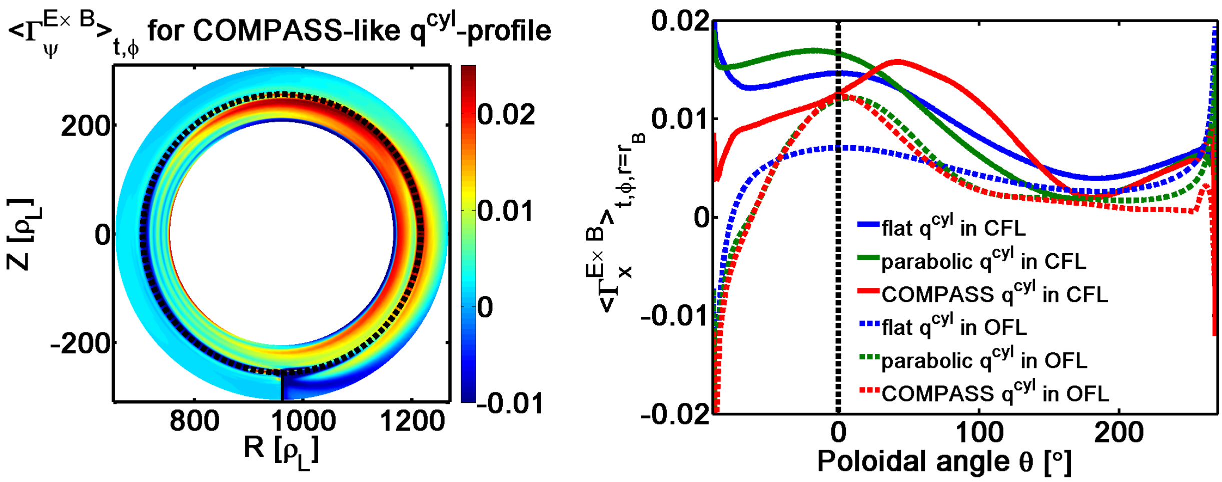

Figure 5.34: Radial $\mathbf{E}\times\mathbf{B}$ turbulent flux presented as:
Left panel: 2D-(R, Z) poloidal section and averaged in time and toroidally: $\langle\Gamma_\psi^{E\times B}\rangle_{t,\varphi}$ obtained with COMPASS divertor-like magnetic configuration.
Right panel: poloidal profiles $\langle\Gamma_\psi^{E\times B}\rangle_{t,\varphi,r=r_B}$ obtained with the 3 magnetic configurations and averaged for the whole open (OFL, $r_B = [0.8; 1]$a) and closed (CFL, $r_B = [1; 1.2]$a) flux surfaces.

On the left panel of Figure 5.35, the result of the conditional averaging procedure for the divertor-like magnetic configuration is presented. Far from the LCFS, the patterns of density fluctuations are close to the ones obtained in our reference parabolic configuration. This is no longer true in the vicinity of the LCFS: several strong and localized spatial tilting of density structures occur mostly in the high field side (see zoom on right panel) and the structures do not longer have a elliptic shape in the confined domain as a strong spatial tilting occurs with a characteristic length of largest structures of the order of $50\rho_L$ similar to the one existing in the Scrape-Off Layer. There is no evidence that these sheared flows are directly generated by the peaks of the magnetic shear rather than by the enhancement of the $\mathbf{E}\times\mathbf{B}$ shear.

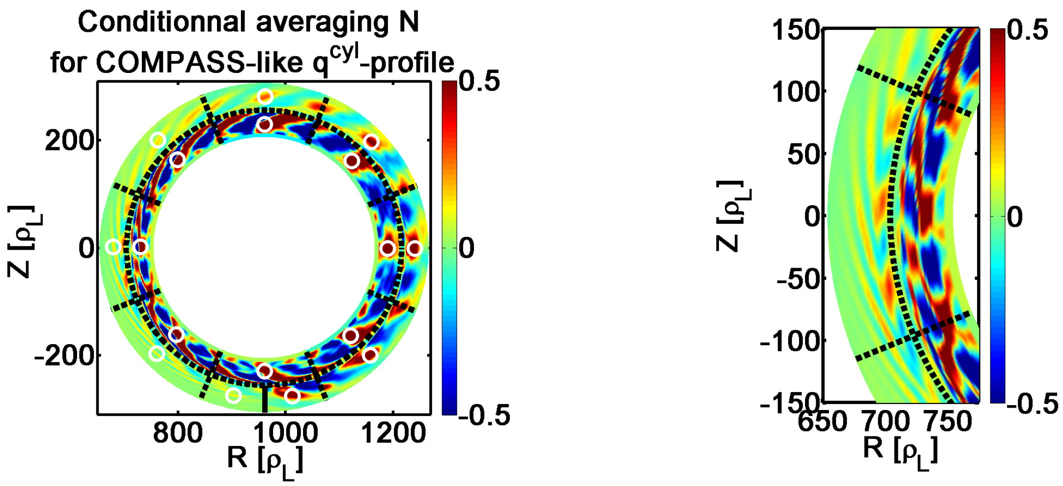

Figure 5.35: 2D-(R, Z) poloidal section obtained with COMPASS divertor-like simulation of density fluctuations resulting of the conditional averaging procedure.
Left panel: full poloidal section.
Right panel: zoom around HFS midplane.

The change of density patterns generated in divertor-like simulation leads also to a modification of Reynolds Stress poloidal distribution as it can be seen on the left panel of Figure 5.36. In closed field lines, the up/down anti-symmetry observed with parabolic safety factor is recovered but with some radial corrugations. The up/down asymmetry of the parabolic q^{cyl}-profile simulation in the open field lines is recovered too. The radial profile of time and flux-surface averaged Reynolds Stress - presented on the right panel of Figure 5.36 - confirms these observations. It shows also that more brutal sign inversions of Reynolds Stress occur in the divertor-like case at the vicinity of the LCFS. Even if the magnitude of the Reyolds Stress is reduced close to the LCFS, it results in larger Reynolds Stress gradients in a large part of the simulated domain i.e for $r \in [0.9; 1.05]a$. In particular, the Reynolds Stress gradient at the LCFS is maximal which can explained the enhancement of $\mathbf{E}\times\mathbf{B}$ shear magnitude close to the LCFS.

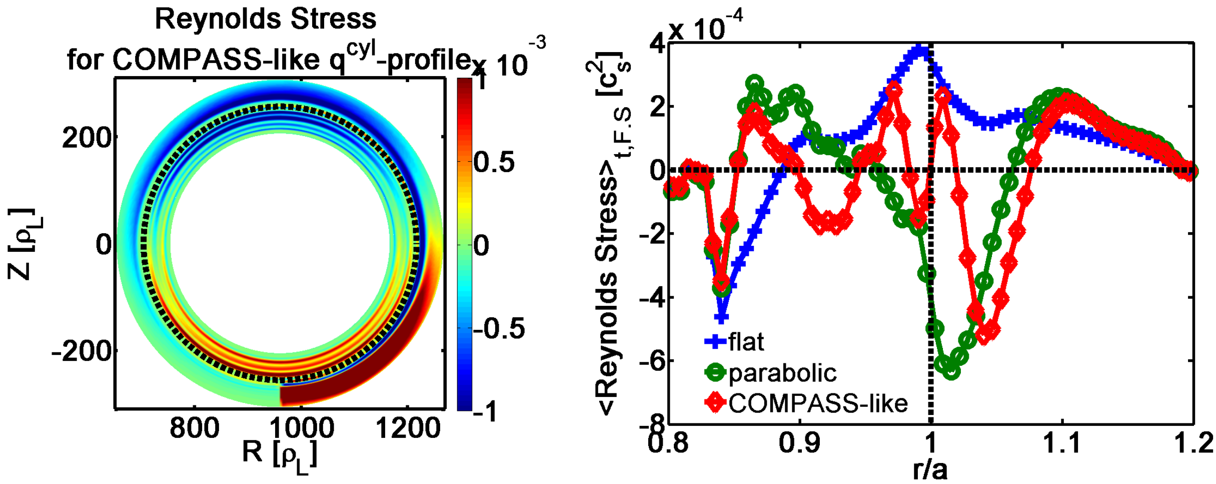

Figure 5.36: Reynolds stress presented as:
Left panel: 2D-(R, Z) poloidal section obtained with COMPASS divertor-like simulation and time and toroidally averaged.
Right panel: radial profiles for the 3 magnetic configurations and averaged in time and flux-surfaces.

5.4 Discussion, conclusion

The analysis of Tokam3X simulations using limiter configuration with circular flux-surfaces has permitted to close partially the gap between simulations in slab and divertor configurations.
First, the spontaneous edge transport barriers obtained in 2D and 3D slab simulations are not recovered in circular geometry for which the radial transport is fully dominated by turbulence. Moreover, the inclusion of the ion energy channel through the generalized vorticity in our isothermal model does not lead to the formation of such barriers or to a significant improvement of the particle confinement or of the radial electric field well. Such discrepancies have been explained by the analysis of the vorticity balance which points out the role of the ∇B curvature on the mean field equilibrium. Indeed, in circular configuration, the ∇B-curvature is found to compensate the $\mathbf{E} \times \mathbf{B}$ transport in most of the confined region. This is not the case in 2D and 3D slab configuration due to the modelling of such curvature term by a constant g parameter. This term has to be modified with a toroidal or poloidal dependency by for example considering the HFS/LFS asymmetry in order to obtain a non vanishing flux surface average. As a consequence of the vanishing of the curvature term in slab configuration, the density gradient raises until the diffusive contribution in the vorticity balance compensates the turbulent one. With such large gradient, turbulence is stabilized and spontaneous transport barriers develop in the whole closed field line domain.
Recent simulations of JET-like and COMPASS-like divertor X-point configuration with Tokam3X reveal the formation of a thin transport barrier before the LCFS. These barriers are stable and do not experience relaxations as it can be the case with Tokam2D. To explain the differences between circular and divertor geometry, the role of the flux expansion and of the strong magnetic shear in the vicinity of the X-point was pointed out. We focus in this thesis on the global effect of the magnetic shear without taking into account local effects or strongly poloidally varying flux expansion. We first compared realistic cylindrical safety factor with a constant one which does not induced mean magnetic

shear. We found that mean equilibrium properties are only slightly affected by a small or an absence of magnetic shear while over quantities such as the shape of density patterns,the poloidal distribution of Reynolds Stress are found to be in agreement with the theoretical impact of the magnetic shear, i.e a spatial tilting of density structures . In closed field lines, the magnetic shear induces an up/down antisymmetry of the RS which compensates the local increase of the RS magnitude with consequently no impact on the mean profiles. In the open field lines, the limiter is a symmetry breaker which leads to a up/down poloidal asymmetry of the RS. The effect on mean fields is nevertheless limited because the radial electric field - which controls the $\mathbf{E} \times \mathbf{B}$ shear and consequently the turbulence - is mainly determined by the sheath physics. This is a major difference with the divertor configuration for which the X-point also generates a symmetry breaking in the closed field lines region. The analysis of the poloidal asymmetry of the Reynolds Stress in a divertor simulation with a double-null X-point would be an interesting way to confirm our interpretation.

Finally, we mimic the large magnetic shear obtained in divertor configuration within our circular limited geometry by artificially modifying the cylindrical safety factor profile. Such configuration implies two strong peaks of magnetic shear on both sides of the LCFS and leads to the formation of two stable barriers with intermediate efficiency of 25 and 40%. These barriers stop the radial propagation of ballistic events and leads to a strong improvement - by a factor of 2 - of the particle confinement. Magnetic shear is also found to enhance the $\mathbf{E} \times \mathbf{B}$ shear at the LCFS probably due to the radial distribution of Reynolds Stress. Such $\mathbf{E} \times \mathbf{B}$ shear does not seem to be responsible for the barrier formation as the barrier efficiency is radially correlated with the peaks of the magnetic shear and not with the fluctuations of $\mathbf{E} \times \mathbf{B}$ one but non local effects cannot completely be excluded.

Chapter 6

Summary and perspectives

The radial outward transport alters the confinement of particles and energy in the plasmas of tokamaks and limits thus the performance of magnetically confined thermonuclear fusion reactors. This transport is mainly dominated by turbulence, the neoclassical and classical diffusions being usually marginal. In the edge plasmas of tokamaks, two instabilities - the interchange and the drift-waves mechanisms - are responsible of the turbulence development. An advanced confinement regime - so-called the H-mode - has been obtained in most of toroidal magnetic configurations including tokamaks and stellerators, as well as limiter and divertor X-point configurations [Wagner 07]. The H-mode has been intensively studied experimentally in the last decades, revealing its inherent characteristics: the improvement of the particle and energy content in the core plasma is due to the formation of a transport barrier in the closed field lines, at the vicinity of the Last Closed Flux Surface in the so-called pedestal region. It is associated with the suppression of turbulence, the formation and deepening of a well of the radial electric field and large gradients of pressure and density in the barrier region. The H-mode is also found to be a bifurcation mechanism which can be reached when the input power exceeds a certain threshold. The use and the improvement of simple predator-prey models reveal the key role and the complex interplay between the turbulence, the mean equilibrium $\mathbf{E} \times \mathbf{B}$ velocity shear and zonal flows (oscillating $\mathbf{E} \times \mathbf{B}$ flows) [Diamond 01]. The $\mathbf{E} \times \mathbf{B}$ shear is indeed found to be the main responsible of the suppression of turbulence by decorrelation of turbulent eddies.

Nevertheless, the physics associated with the H-mode and especially the dynamics leading to the L-H transition are still not fully understood. The development of advanced first-principle numerical tools is essential to answer these uncertainties and could even be used as predictive tools for future device such as the ITER tokamak. Recent 2D and 3D fluid simulations recovered some features of the L-H transition and point out the key role of the transition between confined and unconfined plasma [Norscini 15], the role of the ion energy channel [Nielsen 15] - especially through the generalized vorticity - and the importance of neoclassical considerations [Chôné 15]. In this thesis, the existence and dynamics of transport barriers have been investigated with numerical turbulence fluid models of increasing complexity from simple 2D slab geometry to realistic 3D circular limiter geometry. The Tokam2D and Tokam3D codes relied on the fluid approach and on the drift-reduced equations based on the Braginskii's closure. A new ordering procedure has been fully derived and applied on continuity, momentum and energy conservation equations as a starting point for future improvements of both 2D and 3D models (Chapter 2).

If the suppression of turbulence by the $\mathbf{E}\times\mathbf{B}$ shear is the main paradigm in the edge plasma community to explain the L-H transition, recent experimental results point out the role of the $\mathbf{E}\times\mathbf{B}$ curvature on the structure of spontaneous edge transport barriers [Kamiya 18]. These two mechanisms - corresponding to first and second derivatives of the electric field - are artificially driven in dedicated Tokam2D isothermal simulations in the Scrape-Off Layer (Chapter 3). It is found that both mechanisms can generate transport barriers. These barriers are reinforced by an increase of the amplitude and/or of the radial width of the drive. A criterion, the barrier efficiency, permits to measures the ability of a flux-surface to stop the radial propagation by turbulence relatively to other transport mechanisms such as diffusion. The analysis of this criterion reveals that several transport barrier regimes can be obtained according to the drive applied: weak barriers, intermittent (relaxing) barriers or fully stable barriers. The fluctuations of the barrier efficiency provide also information on barrier relaxations without discrimination between the frequency and the amplitude of these relaxations. It permits also to estimate the penetration length of turbulence on both sides of the stable barriers. The analysis of transport barriers artificially driven by the $\mathbf{E}\times\mathbf{B}$ shear and the $\mathbf{E}\times\mathbf{B}$ curvature mechanisms can contribute to the understanding of the L-H transition. Indeed, a comparison between first and second derivatives of the radial electric field profiles obtained in experiments and the scan in amplitude and width of the two driven mechanisms would demonstrate if both mechanisms are implied in the formation and dynamics of the edge transport barriers even if the measurement uncertainties on the electric field profile can lead to a large range of magnitude especially concerning the $\mathbf{E}\times\mathbf{B}$ curvature. This kind of analysis can also be useful to reproduce experiments involving biasing of the target plates and consequently improves our understanding of the turbulence behaviour in the Scrape-Off Layer. The two mechanisms are also found to act differently on turbulence, providing alternative ways to discriminate them. The spatial structure of the generated barriers differs in the two cases: for the $\mathbf{E}\times\mathbf{B}$ shear drive, the barrier is more efficient in the upstream part of the drive region while the $\mathbf{E}\times\mathbf{B}$ curvature acts similarly on upstream and downstream regions. It can be explained as the $\mathbf{E}\times\mathbf{B}$ curvature is a linear mechanism which has a damping effect in any finite size of turbulent structures. Conversely, the $\mathbf{E}\times\mathbf{B}$ shear is a complex non-linear mechanism in which a competition between shearing effects (filamentation), collisional processes and a linear destabilization acts differentially depending on the radial and poloidal extensions of filaments. Finally, the analysis of the full database of simulations of artificially driven transport barriers reveals that the fluctuations of barrier efficiency are typically twice larger with the $\mathbf{E}\times\mathbf{B}$ shear mechanism. A similar study with the full thermal model of Tokam2D would provide of more complete understanding of the role of the energy channels on the interaction between $\mathbf{E}\times\mathbf{B}$ flows and turbulence.

The main limit of artificially driven transport barriers is the absence of feedback on $\mathbf{E}\times\mathbf{B}$ flows by turbulence. The analysis of transport barriers developing spontaneously at the transition between closed and open field lines underlines the interplay between turbulence and the $\mathbf{E}\times\mathbf{B}$ shear (Chapter 4). Indeed, quasi-periodic relaxations of the barrier in the thermal version of Tokam2D reveal the existence of a hysteresis cycle between the $\mathbf{E}\times\mathbf{B}$ shear and turbulent transport. The suppression of turbulence by the $\mathbf{E}\times\mathbf{B}$ shear is recovered. When the turbulence is fully damped, the shear magnitude drops which demonstrates that the turbulence is an important source for the $\mathbf{E}\times\mathbf{B}$ shear. The latter

becomes to weak to stabilize turbulence which develops again , leading to a new enhancement of the $\mathbf{E} \times \mathbf{B}$ shear and to a new hysteresis cycle. A similar trend is observed with an isothermal reduced version of Tokam2D and also for barriers strongly efficient which experienced fewer and smaller relaxations even if no clear hysteresis cycle are recovered in these cases. This interplay, obtained in 2D slab simulations is not recovered in 3D simulations whether in slab or in circular limiter geometry. To explain such discrepancies, the limits of 2D slab models and the relevancy of the generated spontaneous transport barriers for L-H transition are discussed. First, the existence of spontaneous transport barriers in closed field line region is due to the sharp transition between confined and unconfined plasma which is in agreement with experiments and with our understanding of the transition. The absence of neoclassical considerations leads to a radial force balance different from recent observations on ASDEX Upgrade tokamak [Viezzer 14], [Ryter 14] in which the ion poloidal velocity is found to be at neoclassical levels. A proof of concept has been realized to include a non self-consistent neoclassical friction force and confirms the importance of neoclassical considerations. The development of a self-consistent neoclassical friction force in the Tokam2D model will permit to include a new player - important according to experiments - in the radial force balance and obtained consequently a more realistic equilibrium.
Finally, the absence of threshold on the input power in our simulations is deeply in contradiction with experiments of the L-H transition. However, a proper modelling of dissipative processes may lead to the existence of a threshold. Indeed, barrier efficiency are strongly dependent on diffusive coefficients and the qualitative impact of the ion energy channel is recovered in our simulations. We point out the key role of the ion diamagnetic contribution in the generalized vorticity for the reinforcement of the barrier efficiency associated with an increase of density gradients and a deepening of the well of radial electric field as observed in experiments. In 3D slab simulations the impact of generalized vorticity on all these characteristics is recovered apart from the barrier efficiency which remains close to zero. These simulations seem to underline a limit of this criterion which is not fully able to describe transport barriers dynamics. It seems that the diffusive contribution in these simulations remains too weak relatively to the turbulent transport even when the density gradient strongly increases. Furthermore, the scan of ion diamagnetic contribution in the generalized vorticity does not impact significantly on more complex and realistic geometry such as circular limiter configuration (Chapter 5). Such discrepancy between slab and more complex configurations is explained by using vorticity balances which disclose that the modelling of the curvature term in our slab model is inadequate. Indeed, a quasi-equilibrium state is reached on the closed flux-surfaces of circular geometry when the $\mathbf{E} \times \mathbf{B}$ contribution - linked to the Reynolds Stress - is compensated by the divergence of the diamagnetic current which is a curvature term. In our slab models, such compensation is impossible as this curvature term is vanishing by construction. Consequently, the density gradient grows until the diffusion contribution compensates the $\mathbf{E} \times \mathbf{B}$ one leading to the development of the spontaneous edge transport barriers. An improvement of the modelling of the curvature term is thus required to increase the relevancy of slab simulations.

Transport barriers are not obtained spontaneously in circular limiter geometry with Tokam3X as the radial transport remains fully turbulent in the simulations. Conversely, simulations of diverted X-point plasma lead to the formation of a spontaneous edge transport barrier in the last closed flux-surfaces [Galassi 17a]. This barrier is characterized by a small radial extension of a few Larmor radius and the absence of significant fluctuations of its efficiency. Two processes are suspected to generate this barrier: the magnetic shear and the effective curvature - i.e proportion of field line on the LFS. In order to discriminate the mechanism at the origin of the spontaneous transport barrier, simulations with varying safety factor profile - and thus of magnetic shear have been set up in our circular limiter geometry. The magnetic shear is found to increase poloidal asymmetries due to a spatial tilting of turbulent structures in a up-down asymmetry and linked to the position of the limiter. When the safety factor profile of a divertor X-point simulation is reproduced in our circular limiter configuration - without including the effects of poloidally varying flux expansion and magnetic shear - a spontaneous transport barrier is appearing with characteristic similar to the one obtained in divertor geometry. This study demonstrates that this spontaneous edge transport barrier obtained in divertor X-point simulations is generated directly by the magnetic shear and not by the $\mathbf{E} \times \mathbf{B}$ shear. A proper description of magnetic configuration - including magnetic shear - is thus required in the modelling of edge plasma.

The relevance of Tokam3X simulations in circular and divertor geometry for the modelling of the L-H transition is limited by the isothermal assumption. On-going work with the new thermal version of Tokam3X, including both electron and ion energy evolutions, would close the gap between experiments and numerical simulations. Up to now, no spontaneous edge transport barriers are obtained with this thermal model in circular geometry. No significant changes - at least for what concerns the L-H transition - have been observed in terms of mean field or turbulence properties. A significant increase of the $\mathbf{E} \times \mathbf{B}$ shear is however notice in the vicinity of the LCFS probably due to the increase of the electron temperature gradient in the Scrape-Off Layer due to the Bohm conditions at the limiter plates. An on-going scan of the injected ion temperature leads to an increase of the electric field well magnitude with ion input power. Consequently, the $\mathbf{E} \times \mathbf{B}$ shear is enhanced in the vicinity of the LCFS which could possibly lead to the development of a spontaneous edge transport barrier.

Appendix A

Details for the derivation of fluid equations

This appendix aims at detailing some of the calculations used in Chapter 2.2 to move from the kinetic description of the plasma to the fluid description.

A.1 Derivation of momentum equation

We first focus on the calculations of the 2 underlined terms involved in the derivation of the momentum balance equation (2.27). Note that an integration by parts is used for the calculation of the second term.

$$\begin{aligned}
\boxed{(2.27)\mathrm{i}} : \ & \boldsymbol{\nabla}_{\mathbf{x}} \cdot \left(\int_{\mathbf{v}} (\mathbf{u}_s + \mathbf{w}_s) \otimes (\mathbf{u}_s + \mathbf{w}_s) f_s d^3\mathbf{v} \right) \\
&= \boldsymbol{\nabla}_{\mathbf{x}} \cdot \left(\int_{\mathbf{v}} \mathbf{u}_s \otimes \mathbf{u}_s f_s d^3\mathbf{v} + \int_{\mathbf{v}} \mathbf{u}_s \otimes \mathbf{w}_s f_s d^3\mathbf{v} + \int_{\mathbf{v}} \mathbf{w}_s \otimes \mathbf{u}_s f_s d^3\mathbf{v} + \int_{\mathbf{v}} \mathbf{w}_s \otimes \mathbf{w}_s f_s d^3\mathbf{v} \right) \\
&= \boldsymbol{\nabla}_{\mathbf{x}} \cdot \left(\mathbf{u}_s \otimes \mathbf{u}_s \int_{\mathbf{v}} f_s d^3\mathbf{v} + \mathbf{u}_s \otimes \cancel{\int_{\mathbf{v}} \mathbf{w}_s f_s d^3\mathbf{v}} + \cancel{\int_{\mathbf{v}} \mathbf{w}_s f_s d^3\mathbf{v}} \otimes \mathbf{u}_s + \frac{1}{m_s} \bar{\bar{\Pi}}_s^{tot} \right) \\
&= \boldsymbol{\nabla}_{\mathbf{x}} \cdot \left(n_s \mathbf{u}_s \otimes \mathbf{u}_s + \frac{1}{m_s} \bar{\bar{\Pi}}_s^{tot} \right)
\end{aligned} \tag{A.1}$$

$$\begin{aligned}
\boxed{(2.27)\mathrm{ii}} : \ & \int_{\mathbf{v}} \mathbf{v} \boldsymbol{\nabla}_{\mathbf{v}} \cdot \left(\frac{\mathbf{F}_s}{m_s} f_s \right) d^3\mathbf{v} \\
&= \cancel{\left[\mathbf{v} \cdot \frac{\mathbf{F}_s}{m_s} f_s \right]_{-\infty}^{+\infty}} - \int_{\mathbf{v}} \frac{\mathbf{F}_s}{m_s} f_s d^3\mathbf{v} \\
&= -\frac{q_s}{m_s} \left(\int_{\mathbf{v}} \mathbf{E} f_s d^3\mathbf{v} + \int_{\mathbf{v}} (\mathbf{v} \times \mathbf{B}) f_s d^3\mathbf{v} \right) \\
&= -\frac{q_s}{m_s} \left(\mathbf{E} \int_{\mathbf{v}} f_s d^3\mathbf{v} + \int_{\mathbf{v}} \mathbf{v} f_s d^3\mathbf{v} \times \mathbf{B} \right) \\
&= -\frac{q_s}{m_s} n_s (\mathbf{E} + \mathbf{u}_s \times \mathbf{B})
\end{aligned} \tag{A.2}$$

A.2 Derivation of energy equation

We now focus on the calculations of the 3 terms involved in the derivation of the energy equation (2.31).

$$\begin{aligned}
\boxed{(2.31)\mathrm{i}} &= \partial_t\left(\int_{\mathbf{v}} \mathbf{v}\otimes\mathbf{v} f_s d^3\mathbf{v}\right) \\
&= \partial_t\left(\int_{\mathbf{v}} (\mathbf{u}_s+\mathbf{w}_s)\otimes(\mathbf{u}_s+\mathbf{w}_s) f_s d^3\mathbf{v}\right) \\
&= \partial_t\left(\int_{\mathbf{v}} \mathbf{u}_s\otimes\mathbf{u}_s f_s d^3\mathbf{v} + \cancel{\int_{\mathbf{v}} \mathbf{u}_s\otimes\mathbf{w}_s f_s d^3\mathbf{v}} + \cancel{\int_{\mathbf{v}} \mathbf{w}_s\otimes\mathbf{u}_s f_s d^3\mathbf{v}} + \int_{\mathbf{v}} \mathbf{w}_s\otimes\mathbf{w}_s f_s d^3\mathbf{v}\right) \\
&= \partial_t\left(n_s\mathbf{u}_s\otimes\mathbf{u}_s + \frac{1}{m_s}\bar{\bar{\Pi}}_s^{tot}\right)
\end{aligned} \tag{A.3}$$

$$\begin{aligned}
\boxed{(2.31)\mathrm{ii}} &= \boldsymbol{\nabla}_{\mathbf{x}}\cdot\left(\int_{\mathbf{v}} \mathbf{v}\otimes\mathbf{v}\otimes\mathbf{v} f_s d^3\mathbf{v}\right) \\
&= \boldsymbol{\nabla}_{\mathbf{x}}\cdot\left(\int_{\mathbf{v}} (\mathbf{u}_s+\mathbf{w}_s)\otimes(\mathbf{u}_s+\mathbf{w}_s)\otimes(\mathbf{u}_s+\mathbf{w}_s) f_s d^3\mathbf{v}\right) \\
&= \boldsymbol{\nabla}_{\mathbf{x}}\cdot\left(\int_{\mathbf{v}} \mathbf{u}_s\otimes\mathbf{u}_s\otimes\mathbf{u}_s f_s d^3\mathbf{v} + \int_{\mathbf{v}} \mathbf{u}_s\otimes\mathbf{u}_s\otimes\mathbf{w}_s f_s d^3\mathbf{v} + \int_{\mathbf{v}} \mathbf{w}_s\otimes\mathbf{u}_s\otimes\mathbf{u}_s f_s d^3\mathbf{v}\right. \\
&\quad + \int_{\mathbf{v}} \mathbf{u}_s\otimes\mathbf{w}_s\otimes\mathbf{u}_s f_s d^3\mathbf{v} + \int_{\mathbf{v}} \mathbf{w}_s\otimes\mathbf{w}_s\otimes\mathbf{u}_s f_s d^3\mathbf{v} + \int_{\mathbf{v}} \mathbf{w}_s\otimes\mathbf{u}_s\otimes\mathbf{w}_s f_s d^3\mathbf{v} \\
&\quad \left.+ \int_{\mathbf{v}} \mathbf{u}_s\otimes\mathbf{w}_s\otimes\mathbf{w}_s f_s d^3\mathbf{v} \int_{\mathbf{v}} \mathbf{w}_s\otimes\mathbf{w}_s\otimes\mathbf{w}_s f_s d^3\mathbf{v}\right) \\
&= \boldsymbol{\nabla}_{\mathbf{x}}\cdot\left((\mathbf{u}_s\otimes\mathbf{u}_s\otimes\mathbf{u}_s)\int_{\mathbf{v}} f_s d^3\mathbf{v} + \mathbf{u}_s\otimes\mathbf{u}_s\otimes\cancel{\int_{\mathbf{v}} \mathbf{w}_s f_s d^3\mathbf{v}} + \cancel{\int_{\mathbf{v}} \mathbf{w}_s f_s d^3\mathbf{v}}\otimes\mathbf{u}_s\otimes\mathbf{u}_s\right. \\
&\quad + \mathbf{u}_s\otimes\cancel{\int_{\mathbf{v}} \mathbf{w}_s f_s d^3\mathbf{v}}\otimes\mathbf{u}_s + \left(\int_{\mathbf{v}} \mathbf{w}_s\otimes\mathbf{w}_s f_s d^3\mathbf{v}\right)\otimes\mathbf{u}_s + \int_{\mathbf{v}} \mathbf{w}_s\otimes\mathbf{u}_s\otimes\mathbf{w}_s f_s d^3\mathbf{v} \\
&\quad \left.+ \mathbf{u}_s\otimes\left(\int_{\mathbf{v}} \mathbf{w}_s\otimes\mathbf{w}_s f_s d^3\mathbf{v}\right) + \frac{2}{m_s}\bar{\bar{\bar{Q}}}_s\right) \\
&= \boldsymbol{\nabla}_{\mathbf{x}}\cdot\left(n_s\mathbf{u}_s\otimes\mathbf{u}_s\otimes\mathbf{u}_s + \frac{1}{m_s}\left(\bar{\bar{\Pi}}_s^{tot}\otimes\mathbf{u}_s + \mathbf{u}_s\otimes\bar{\bar{\Pi}}_s^{tot}\right) + \int_{\mathbf{v}} \mathbf{w}_s\otimes\mathbf{u}_s\otimes\mathbf{w}_s f_s d^3\mathbf{v} + \frac{2}{m_s}\bar{\bar{\bar{Q}}}_s\right)
\end{aligned} \tag{A.4}$$

$$\begin{aligned}
\boxed{(2.31)\mathrm{iii}} &= \int_{\mathbf{v}} \mathbf{v}\otimes\mathbf{v}\boldsymbol{\nabla}_{\mathbf{v}}\cdot\left(\frac{\mathbf{F}_s}{m_s}f_s\right)d^3\mathbf{v} \\
&= -\left(\int_{\mathbf{v}} \frac{\mathbf{F}_s}{m_s}\otimes\mathbf{v} f_s d^3\mathbf{v} + \int_{\mathbf{v}} \mathbf{v}\otimes\frac{\mathbf{F}_s}{m_s} f_s d^3\mathbf{v}\right) \\
&= -\frac{q_s}{m_s}\left(\int_{\mathbf{v}} \mathbf{E}\otimes\mathbf{v} f_s d^3\mathbf{v} + \int_{\mathbf{v}} (\mathbf{v}\times\mathbf{B})\otimes\mathbf{v} f_s d^3\mathbf{v} + \int_{\mathbf{v}} \mathbf{v}\otimes\mathbf{E} f_s d^3\mathbf{v} + \int_{\mathbf{v}} \mathbf{v}\otimes(\mathbf{v}\times\mathbf{B}) f_s d^3\mathbf{v}\right) \\
&= -\frac{q_s}{m_s}\left(\mathbf{E}\otimes\int_{\mathbf{v}} \mathbf{v} f_s d^3\mathbf{v} + \int_{\mathbf{v}} \mathbf{v} f_s d^3\mathbf{v}\otimes\mathbf{E} + \frac{2}{q_s}\bar{\bar{W}}_s^{\mathbf{v}\times\mathbf{B}}\right) \\
&= -\frac{q_s}{m_s}n_s(\mathbf{E}\otimes\mathbf{u}_s + \mathbf{u}_s\otimes\mathbf{E}) - \frac{2}{m_s}\bar{\bar{W}}_s^{\mathbf{v}\times\mathbf{B}}
\end{aligned} \tag{A.5}$$

Appendix B

Analytical calculation of the sheath heat transfer coefficients γ_s

In this Appendix, we detail the derivation of the sheath heat transfer coefficients - calculated analytically from kinetic considerations in the sheath physics. The first section focuses on the distribution functions for a normal distribution. The electron and ion sheath heat transfer coefficients are then calculated in dedicated sections. In each case, the derivation is made for 1D and 3D cases.

B.1 Distribution functions

The distribution function $f_s(v_s)$ corresponds to the probability that a particle s is at the velocity v_s. For identical but distinguishable particles like electrons or ions in a high collisionality regime, the distribution function f_s follows a Boltzmann distribution which corresponds to a specific normal distribution (*i.e.* a Gaussian):

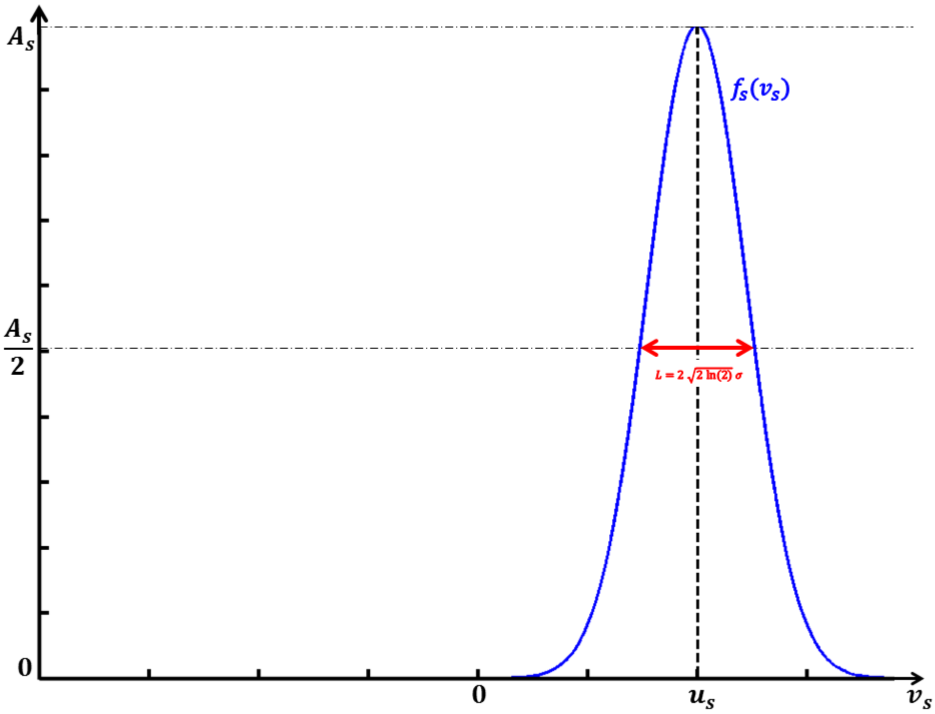

Figure B.1: Gaussian distribution $f_s(v_s) = A_s \exp\left(-\frac{1}{2}(\frac{v_s - u_s}{\sigma})^2\right)$ with a mean value u_s and a standard deviation σ.

The full width at half maximum (FWHM) of this distribution is $L = 2\sqrt{2\ln 2}\sigma \approx 2.355\sigma$.

B.1.1 1D case

In one dimensional case, the distribution function writes:

$$f_s^{1D} = A^{1D} \exp\left(-\frac{m_s(v_s - u_s)^2}{2k_B T_s}\right) \tag{B.1}$$

where u_s is the mean and most probable velocity of the population and corresponds to the fluid velocity of the specie s.
Here, the standard deviation is equal to the thermal velocity of the specie s: $\sigma = v_{th} = \sqrt{\frac{k_B T_s}{m_s}}$.

A^{1D} is a constant such as:

$$\int_{-\infty}^{+\infty} f_s^{1D} dv_s = n_s$$
$$\Leftrightarrow \int_{-\infty}^{+\infty} A^{1D} \exp\left(-\frac{m_s(v_s-u_s)^2}{2k_BT_s}\right) dv_s = n_s$$
$$\Downarrow \textit{ here, we used the substitution } v_s^* = \sqrt{\frac{m_s}{2k_BT_s}}(v_s-u_s);\ v_s = \sqrt{\frac{2k_BT_s}{m_s}}v_s^* + u_s;\ dv_s = \sqrt{\frac{2k_BT_s}{m_s}}dv_s^*.$$
$$\Leftrightarrow \int_{-\infty}^{+\infty} A^{1D} \exp\left(-v_s^*\right) \sqrt{\frac{2k_BT_s}{m_s}} dv_s^* = n_s$$
$$\Leftrightarrow A^{1D}\sqrt{\frac{2k_BT_s}{m_s}} \underbrace{\int_{-\infty}^{+\infty} \exp\left(-v_s^*\right) dv_s^*}_{=\sqrt{\pi}} = n_s$$
$$\Leftrightarrow A^{1D} = \frac{n_s}{\sqrt{2\pi}}\sqrt{\frac{m_s}{k_BT_s}} \tag{B.2}$$

Finally:

$$\boxed{f_s^{1D} = \frac{n_s}{\sqrt{2\pi}}\sqrt{\frac{m_s}{k_BT_s}} \exp\left(-\frac{m_s(v_s-u_s)^2}{2k_BT_s}\right)} \tag{B.3}$$

B.1.2 3D case

We consider now the three dimensional case with a privileged direction corresponding to the flow direction. The velocity in this direction is noted v_1 and had an associated fluid velocity u_1. The two velocities in the perpendicular plan of the flow are noted v_2 and v_3. Their distributions in these directions result from random collision processes such as their fluid velocities are assumed to be zero.

$$f_s^{3D} = A^{3D} \exp\left(-\frac{m_s((v_1-u_1)^2 + v_2^2 + v_3^2)}{2k_BT_s}\right) \tag{B.4}$$

where A^{3D} is a constant such as:

$$
\begin{aligned}
&\int_{-\infty}^{+\infty}\int_{-\infty}^{+\infty}\int_{-\infty}^{+\infty} f_s^{3D} dv_1 dv_2 dv_3 = n_s \\
\Leftrightarrow &\int_{-\infty}^{+\infty}\int_{-\infty}^{+\infty}\int_{-\infty}^{+\infty} A^{3D} \exp\left(-\frac{m_s((v_1-u_1)^2+v_2^2+v_3^2)}{2k_B T_s}\right) dv_1 dv_2 dv_3 = n_s \\
&\Downarrow \textit{ here, we used the substitutions } v_1^* = \sqrt{\frac{m_s}{2k_B T_s}}(v_1-u_1);\ v_2^* = \sqrt{\frac{m_s}{2k_B T_s}}v_2;\ v_3^* = \sqrt{\frac{m_s}{2k_B T_s}}v_3. \\
\Leftrightarrow & A^{3D}\left(\frac{2k_B T_s}{m_s}\right)^{3/2}\int_{-\infty}^{+\infty}\int_{-\infty}^{+\infty}\int_{-\infty}^{+\infty}\exp\left(-v_1^{*2}\right)\exp\left(-v_2^{*2}\right)\exp\left(-v_3^{*2}\right) dv_1^* dv_2^* dv_3^* = n_s \\
\Leftrightarrow & A^{3D}\left(\frac{2k_B T_s}{m_s}\right)^{3/2}\underbrace{\int_{-\infty}^{+\infty}\exp\left(-v_1^{*2}\right) dv_1^*}_{=\sqrt{\pi}}\underbrace{\int_{-\infty}^{+\infty}\exp\left(-v_2^{*2}\right) dv_2^*}_{=\sqrt{\pi}}\underbrace{\int_{-\infty}^{+\infty}\exp\left(-v_3^{*2}\right) dv_3^*}_{=\sqrt{\pi}} = n_s \\
\Leftrightarrow & A^{3D} = \frac{n_s}{(2\pi)^{3/2}}\left(\frac{m_s}{k_B T_s}\right)^{3/2}
\end{aligned}
\tag{B.5}
$$

Finally:

$$
\boxed{f_s^{3D} = \frac{n_s}{(2\pi)^{3/2}}\left(\frac{m_s}{k_B T_s}\right)^{3/2}\exp\left(-\frac{m_s((v_1-u_1)^2+v_2^2+v_3^2)}{2k_B T_s}\right)}
\tag{B.6}
$$

B.2 Sheath electron heat transfer coefficient

The sheath heat transfer coefficient γ_s for a specie s is defined as:

$$
\boxed{\gamma_s = \frac{q_s}{k_B T_s \Gamma_s}}
\tag{B.7}
$$

where Γ_s and q_s are respectively the particle flux and the heat flux at the wall.

B.2.1 Electron distribution

Only electrons able to overcome the potential wall repulsion can reach the wall and transfer their heat and momentum to the wall. It corresponds to electrons with a kinetic energy larger than the electrostatic energy generated by the difference of potential between the sheath entrance (ϕ_{se}) and the wall (ϕ_w):

$$
\begin{aligned}
&\frac{1}{2}m_e {v_e}^2 \geq e(\phi_{se}-\phi_w) \\
\Leftrightarrow\ & v_{e\mathrm{min}} = \sqrt{\frac{2e(\phi_{se}-\phi_w)}{m_e}}
\end{aligned}
\tag{B.8}
$$

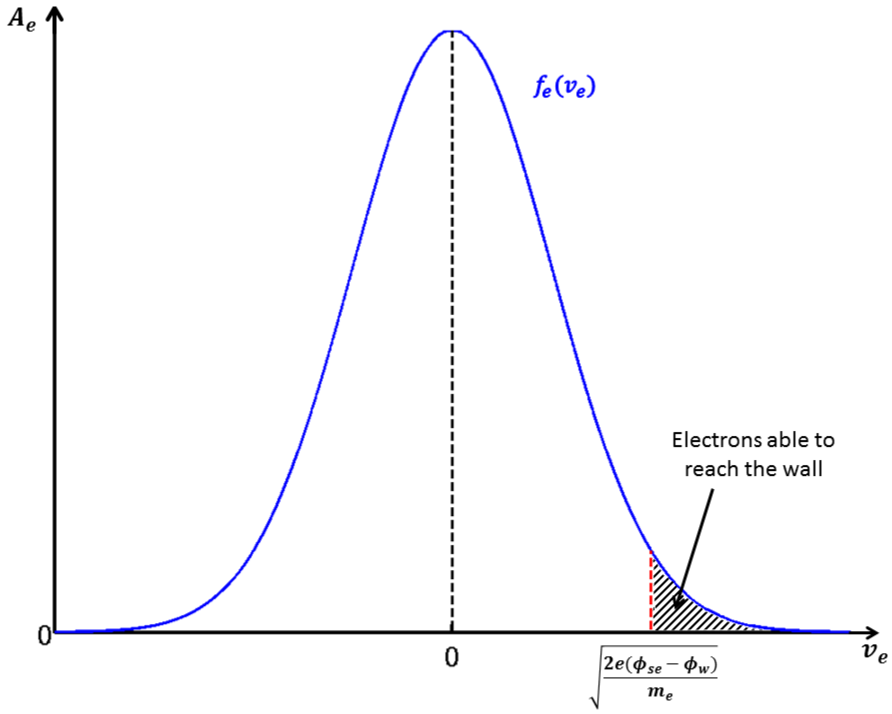

Figure B.2: Electron distribution $f_e(v_e)$

B.2.2 1D case

Calculation of the electron particle flux at the wall:

$$\begin{aligned}
\Gamma_e^{1D} &= \int_{v_{e\,\mathrm{min}}}^{+\infty} f_e^{1D} v_e dv_e \\
&= \int_{v_{e\,\mathrm{min}}}^{+\infty} \frac{n_e}{\sqrt{2\pi}}\sqrt{\frac{m_e}{k_B T_e}} \exp\left(-\frac{m_e v_e^2}{2k_B T_e}\right) v_e dv_e \\
&\Downarrow \; \textit{here, we used the substitutions } v_e^* = \sqrt{\frac{m_e}{2k_B T_e}} v_e . \\
&= \frac{n_e}{\sqrt{2\pi}}\sqrt{\frac{m_e}{k_B T_e}} \frac{2k_B T_e}{m_e} \int_{\sqrt{\frac{m_e}{2k_B T_e}} v_{e\,\mathrm{min}}}^{+\infty} v_e^* \exp\left(-v_e^{*2}\right) dv_e^* \\
&= \frac{2n_e}{\sqrt{2\pi}}\sqrt{\frac{k_B T_e}{m_e}} \left[-\frac{1}{2}\exp\left(-v_e^{*2}\right)\right]_{\sqrt{\frac{m_e}{2k_B T_e}} v_{e\,\mathrm{min}}}^{+\infty} \\
&= \frac{n_e}{\sqrt{2\pi}}\sqrt{\frac{k_B T_e}{m_e}} \exp\left(-\frac{m_e}{2k_B T_e} v_{e\,\mathrm{min}}^2\right) \qquad \text{(B.9)}
\end{aligned}$$

Finally:

$$\boxed{\Gamma_e^{1D} = \frac{n_e}{\sqrt{2\pi}}\sqrt{\frac{k_B T_e}{m_e}} \exp\left(-\frac{e(\phi_{se}-\phi_w)}{k_B T_e}\right)} \qquad \text{(B.10)}$$

Calculation of the electron heat flux at the wall:

$$
\begin{aligned}
q_e^{1D} &= \int_{v_{e\min}}^{+\infty} \frac{1}{2} m_e v_e^2 v_e f_e^{1D} dv_e \\
&= \int_{v_{e\min}}^{+\infty} \frac{1}{2} m_e v_e^3 \frac{n_e}{\sqrt{2\pi}} \sqrt{\frac{m_e}{k_B T_e}} \exp\left(-\frac{m_e v_e^2}{2k_B T_e}\right) dv_e \\
&\Downarrow \textit{ here, we used the substitutions } v_e^* = \sqrt{\frac{m_e}{2k_B T_e}} v_e. \\
&= \frac{m_e n_e}{2\sqrt{2\pi}} \sqrt{\frac{m_e}{k_B T_e}} \left(\frac{2k_B T_e}{m_e}\right)^{3/2} \sqrt{\frac{2k_B T_e}{m_e}} \int_{\sqrt{\frac{m_e}{2k_B T_e}} v_{e\min}}^{+\infty} v_e^{*3} \exp\left(-v_e^{*2}\right) dv_e^* \\
&= 2\frac{m_e n_e}{\sqrt{2\pi}} \left(\frac{k_B T_e}{m_e}\right)^{3/2} \int_{\sqrt{\frac{m_e}{2k_B T_e}} v_{e\min}}^{+\infty} v_e^{*3} \exp\left(-v_e^{*2}\right) dv_e^*
\end{aligned}
\tag{B.11}
$$

Let's calculate the previous integral separately:

$$
\begin{aligned}
\int_a^{+\infty} x^3 \exp\left(-x^2\right) dx &= \int_a^{+\infty} x^2 \quad x \exp\left(-x^2\right) dx \\
&= \left[-\frac{1}{2} x^2 \exp\left(-x^2\right)\right]_a^{+\infty} - \int_a^{+\infty} 2x(-\frac{1}{2}) \exp\left(-x^2\right) dx \\
&= \frac{1}{2} a^2 \exp\left(-a^2\right) + \left[-\frac{1}{2} \exp\left(-x^2\right)\right]_a^{+\infty} \\
&= \frac{1}{2}(1 + a^2) \exp\left(-a^2\right)
\end{aligned}
\tag{B.12}
$$

The electron heat flux at the wall becomes:

$$
q_e^{1D} = \frac{m_e n_e}{\sqrt{2\pi}} \left(\frac{k_B T_e}{m_e}\right)^{3/2} \left(1 + \frac{m_e}{2k_B T_e} v_{e\min}^2\right) \exp\left(-\frac{m_e}{2k_B T_e} v_{e\min}^2\right) \tag{B.13}
$$

And, finally:

$$
\boxed{q_e^{1D} = \frac{n_e}{\sqrt{2\pi}} \sqrt{\frac{k_B T_e}{m_e}} \left(k_B T_e + e(\phi_{se} - \phi_w)\right) \exp\left(-\frac{e(\phi_{se} - \phi_w)}{k_B T_e}\right)} \tag{B.14}
$$

We can now compute the sheath electron heat transfer coefficient:

$$
\begin{aligned}
\gamma_e^{1D} &= \frac{q_e^{1D}}{k_B T_e \Gamma_e^{1D}} \\
&= \frac{\cancel{\frac{n_e}{\sqrt{2\pi}}} \cancel{\sqrt{\frac{k_B T_e}{m_e}}} \left(k_B T_e + e(\phi_{se} - \phi_w)\right) \cancel{\exp\left(-\frac{e(\phi_{se} - \phi_w)}{k_B T_e}\right)}}{k_B T_e \cancel{\frac{n_e}{\sqrt{2\pi}}} \cancel{\sqrt{\frac{k_B T_e}{m_e}}} \cancel{\exp\left(-\frac{e(\phi_{se} - \phi_w)}{k_B T_e}\right)}}
\end{aligned}
\tag{B.15}
$$

We obtained:

$$
\boxed{\gamma_e^{1D} = 1 + \frac{e(\phi_{se} - \phi_w)}{k_B T_e}} \tag{B.16}
$$

B.2.3 3D case

Calculation of the electron particle flux at the wall:

$$
\begin{aligned}
\Gamma_e^{3D} &= \int_{-\infty}^{+\infty}\int_{-\infty}^{+\infty}\int_{v_{e\min}}^{+\infty} f_e^{3D} v_1 dv_1 dv_2 dv_3 \\
&= \int_{-\infty}^{+\infty}\int_{-\infty}^{+\infty}\int_{v_{e\min}}^{+\infty} \frac{n_e}{(2\pi)^{3/2}}\left(\frac{m_e}{k_B T_e}\right)^{3/2} \exp\left(-\frac{m_e(v_1^2+v_2^2+v_3^2)}{2k_B T_e}\right) v_1 dv_1 dv_2 dv_3 \\
&\Downarrow \textit{ here, we used the substitutions } v_1^* = \sqrt{\frac{m_e}{2k_BT_e}}v_1;\ v_2^* = \sqrt{\frac{m_e}{2k_BT_e}}v_2;\ v_3^* = \sqrt{\frac{m_e}{2k_BT_e}}v_3. \\
&= \frac{n_e}{(2\pi)^{3/2}}\left(\frac{m_e}{k_B T_e}\right)^{3/2}\int_{-\infty}^{+\infty}\int_{-\infty}^{+\infty}\int_{\sqrt{\frac{m_e}{2k_BT_e}}v_{e\min}}^{+\infty} \exp\left(-({v_1^*}^2+{v_2^*}^2+{v_3^*}^2)\right) v_1^*\left(\frac{2k_BT_e}{m_e}\right)^2 dv_1^* dv_2^* dv_3^* \\
&= \frac{2^{3/2}n_e}{(2\pi)^{3/2}}\sqrt{\frac{2k_BT_e}{m_e}}\underbrace{\int_{-\infty}^{+\infty}\exp\left(-{v_2^*}^2\right)dv_2^*}_{=\sqrt{\pi}}\underbrace{\int_{-\infty}^{+\infty}\exp\left(-{v_3^*}^2\right)dv_3^*}_{=\sqrt{\pi}}\int_{\sqrt{\frac{m_e}{2k_BT_e}}v_{e\min}}^{+\infty} v_1^*\exp\left(-{v_1^*}^2\right)dv_1^* \\
&= \frac{2n_e}{\sqrt{2\pi}}\sqrt{\frac{k_BT_e}{m_e}}\left[-\frac{1}{2}\exp\left(-{v_1^*}^2\right)\right]_{\sqrt{\frac{m_e}{2k_BT_e}}v_{e\min}}^{+\infty} \\
&= \frac{n_e}{\sqrt{2\pi}}\sqrt{\frac{k_BT_e}{m_e}}\exp\left(-\frac{m_e}{2k_BT_e}v_{e_{\min}}^2\right) \qquad \text{(B.17)}
\end{aligned}
$$

Finally:

$$
\boxed{\Gamma_e^{3D} = \frac{n_e}{\sqrt{2\pi}}\sqrt{\frac{k_BT_e}{m_e}}\exp\left(-\frac{e(\phi_{se}-\phi_w)}{k_BT_e}\right)} \qquad \text{(B.18)}
$$

Calculation of the electron heat flux at the wall:

$$
\begin{aligned}
q_e^{3D} &= \int_{-\infty}^{+\infty}\int_{-\infty}^{+\infty}\int_{v_{e\min}}^{+\infty} \frac{1}{2} m_e (v_1^2+v_2^2+v_3^3) v_1 f_e^{3D} dv_1 dv_2 dv_3 \\
&= \int_{-\infty}^{+\infty}\int_{-\infty}^{+\infty}\int_{v_{e\min}}^{+\infty} \frac{1}{2} m_e (v_1^2+v_2^2+v_3^3) v_1 \frac{n_e}{(2\pi)^{3/2}} \left(\frac{m_e}{k_B T_e}\right)^{3/2} \exp\left(-\frac{m_e(v_1^2+v_2^2+v_3^2)}{2k_B T_e}\right) dv_1 dv_2 dv_3 \\
&\Downarrow \textit{ here, we used the substitutions } v_1^* = \sqrt{\frac{m_e}{2k_B T_e}} v_1;\ v_2^* = \sqrt{\frac{m_e}{2k_B T_e}} v_2;\ v_3^* = \sqrt{\frac{m_e}{2k_B T_e}} v_3. \\
&= \frac{m_e n_e}{2\,(2\pi)^{3/2}} \left(\frac{m_e}{k_B T_e}\right)^{3/2} \int_{-\infty}^{+\infty}\int_{-\infty}^{+\infty}\int_{\sqrt{\frac{m_e}{2k_B T_e}} v_{e\min}}^{+\infty} \left(\frac{2k_B T_e}{m_e}\right)^3 ({v_1^*}^2+{v_2^*}^2+{v_3^*}^2) v_1^* \\
&\qquad \exp\left(-({v_1^*}^2+{v_2^*}^2+{v_3^*}^2)\right) dv_1^* dv_2^* dv_3^* \\
&= \frac{4 m_e n_e}{(2\pi)^{3/2}} \left(\frac{k_B T_e}{m_e}\right)^{3/2} \int_{-\infty}^{+\infty}\int_{-\infty}^{+\infty}\int_{\sqrt{\frac{m_e}{2k_B T_e}} v_{e\min}}^{+\infty} ({v_1^*}^3 + v_1^* {v_2^*}^2 + v_1^* {v_3^*}^2) \\
&\qquad \exp\left(-({v_1^*}^2+{v_2^*}^2+{v_3^*}^2)\right) dv_1^* dv_2^* dv_3^* \\
&= \frac{4 m_e n_e}{(2\pi)^{3/2}} \left(\frac{k_B T_e}{m_e}\right)^{3/2} \left[\int_{-\infty}^{+\infty}\int_{-\infty}^{+\infty}\int_{\sqrt{\frac{m_e}{2k_B T_e}} v_{e\min}}^{+\infty} {v_1^*}^3 \exp\left(-({v_1^*}^2+{v_2^*}^2+{v_3^*}^2)\right) dv_1^* dv_2^* dv_3^* \right. \\
&\qquad + \int_{-\infty}^{+\infty}\int_{-\infty}^{+\infty}\int_{\sqrt{\frac{m_e}{2k_B T_e}} v_{e\min}}^{+\infty} v_1^* {v_2^*}^2 \exp\left(-({v_1^*}^2+{v_2^*}^2+{v_3^*}^2)\right) dv_1^* dv_2^* dv_3^* \\
&\qquad \left. + \int_{-\infty}^{+\infty}\int_{-\infty}^{+\infty}\int_{\sqrt{\frac{m_e}{2k_B T_e}} v_{e\min}}^{+\infty} v_1^* {v_3^*}^2 \exp\left(-({v_1^*}^2+{v_2^*}^2+{v_3^*}^2)\right) dv_1^* dv_2^* dv_3^* \right]
\end{aligned}
\tag{B.19}
$$

Let's treat these three integrals separately:

- $$\int_{-\infty}^{+\infty}\int_{-\infty}^{+\infty}\int_{\sqrt{\frac{m_e}{2k_BT_e}}v_{e\min}}^{+\infty} v_1^{*3}\exp\left(-(v_1^{*2}+v_2^{*2}+v_3^{*2})\right)dv_1^*dv_2^*dv_3^*$$

$$= \int_{-\infty}^{+\infty}\int_{-\infty}^{+\infty}\int_{\sqrt{\frac{m_e}{2k_BT_e}}v_{e\min}}^{+\infty} v_1^{*3}\exp\left(-v_1^{*2}\right)\exp\left(-v_2^{*2}\right)\exp\left(-v_3^{*2}\right)dv_1^*dv_2^*dv_3^*$$

$$= \underbrace{\int_{-\infty}^{+\infty}\exp\left(-v_2^{*2}\right)dv_2^*}_{=\sqrt{\pi}}\underbrace{\int_{-\infty}^{+\infty}\exp\left(-v_3^{*2}\right)dv_3^*}_{=\sqrt{\pi}}\int_{\sqrt{\frac{m_e}{2k_BT_e}}v_{e\min}}^{+\infty} v_1^{*3}\exp\left(-v_1^{*2}\right)dv_1^*$$

$\Downarrow$ *here, we used the result obtained in equation (B.12).*

$$= \frac{\pi}{2}\left(1+\frac{m_e}{2k_BT_e}v_{e_{\min}}^2\right)\exp\left(-\frac{m_e}{2k_BT_e}v_{e_{\min}}^2\right) \tag{B.20}$$

- $$\int_{-\infty}^{+\infty}\int_{-\infty}^{+\infty}\int_{\sqrt{\frac{m_e}{2k_BT_e}}v_{e\min}}^{+\infty} v_1^{*}v_2^{*2}\exp\left(-(v_1^{*2}+v_2^{*2}+v_3^{*2})\right)dv_1^*dv_2^*dv_3^*$$

$$= \underbrace{\int_{-\infty}^{+\infty}v_2^{*2}\exp\left(-v_2^{*2}\right)dv_2^*}_{=\frac{\sqrt{\pi}}{2}}\underbrace{\int_{-\infty}^{+\infty}\exp\left(-v_3^{*2}\right)dv_3^*}_{=\sqrt{\pi}}\int_{\sqrt{\frac{m_e}{2k_BT_e}}v_{e\min}}^{+\infty} v_1^{*}\exp\left(-v_1^{*2}\right)dv_1^*$$

$$= \frac{\pi}{2}\left[-\frac{1}{2}\exp\left(-v_1^{*2}\right)\right]_{\sqrt{\frac{m_e}{2k_BT_e}}v_{e\min}}^{+\infty}$$

$$= \frac{\pi}{4}\exp\left(-\frac{m_e}{2k_BT_e}v_{e_{\min}}^2\right) \tag{B.21}$$

- $$\int_{-\infty}^{+\infty}\int_{-\infty}^{+\infty}\int_{\sqrt{\frac{m_e}{2k_BT_e}}v_{e\min}}^{+\infty} v_1^{*}v_3^{*2}\exp\left(-(v_1^{*2}+v_2^{*2}+v_3^{*2})\right)dv_1^*dv_2^*dv_3^*$$

$$= \frac{\pi}{4}\exp\left(-\frac{m_e}{2k_BT_e}v_{e_{\min}}^2\right) \tag{B.22}$$

This leads to:

$$q_e^{3D} = \frac{4m_en_e}{(2\pi)^{3/2}}\left(\frac{k_BT_e}{m_e}\right)^{3/2}\frac{\pi}{2}\left(2+\frac{m_e}{2k_BT_e}v_{e_{\min}}^2\right)\exp\left(-\frac{m_e}{2k_BT_e}v_{e_{\min}}^2\right)$$

$$= \frac{m_en_e}{\sqrt{2\pi}}\left(\frac{k_BT_e}{m_e}\right)^{3/2}\left(2+\frac{m_e}{2k_BT_e}v_{e_{\min}}^2\right)\exp\left(-\frac{m_e}{2k_BT_e}v_{e_{\min}}^2\right) \tag{B.23}$$

And, finally:

$$\boxed{q_e^{3D} = \frac{m_en_e}{\sqrt{2\pi}}\left(\frac{k_BT_e}{m_e}\right)^{3/2}\left(2+\frac{e(\phi_{se}-\phi_w)}{k_BT_e}\right)\exp\left(-\frac{e(\phi_{se}-\phi_w)}{k_BT_e}\right)} \tag{B.24}$$

We can now compute the sheath electron heat transfer coefficient:

$$\gamma_e^{3D} = \frac{q_e^{3D}}{k_B T_e \Gamma_e^{3D}}$$
$$= \frac{\cancel{\frac{m_e n_e}{\sqrt{2\pi}}} \cancel{\left(\frac{k_B T_e}{m_e}\right)^{3/2}} \left(2 + \frac{e(\phi_{se}-\phi_w)}{k_B T_e}\right) \cancel{\exp\left(-\frac{e(\phi_{se}-\phi_w)}{k_B T_e}\right)}}{\cancel{k_B T_e} \cancel{\frac{n_e}{\sqrt{2\pi}}} \cancel{\sqrt{\frac{k_B T_e}{m_e}}} \cancel{\exp\left(-\frac{e(\phi_{se}-\phi_w)}{k_B T_e}\right)}} \tag{B.25}$$

We obtained:

$$\boxed{\gamma_e^{3D} = 2 + \frac{e(\phi_{se}-\phi_w)}{k_B T_e}} \tag{B.26}$$

B.3 Sheath ion heat transfer coefficient

B.3.1 Ion distribution

Ions are not repulsed but attracted by the wall meaning all ions at the sheath entrance will transfer heat and momentum to the wall. However, unlike electrons, the mean velocity of the ion population is not negligible. Indeed, the fluid velocity for ions at the sheath entrance is equal to the sound speed $c_s = \sqrt{\frac{k_B(T_e+T_i)}{m_i}}$.

B.3.2 1D case

Calculation of the ion particle flux at the wall:

$$\Gamma_i^{1D} = \int_{-\infty}^{+\infty} f_i^{1D} v_i dv_i$$
$$= \int_{-\infty}^{+\infty} \frac{n_i}{\sqrt{2\pi}} \sqrt{\frac{m_i}{k_B T_i}} \exp\left(-\frac{m_i(v_i - c_s)^2}{2k_B T_i}\right) v_i dv_i$$
$$\Downarrow \textit{ using the substitutions } v_i^* = \sqrt{\frac{m_i}{2k_B T_i}}(v_i - c_s) \Leftrightarrow v_i = c_s + \sqrt{\frac{2k_B T_i}{m_i}} v_i^*;\ dv_i = \sqrt{\frac{2k_B T_i}{m_i}} dv_i^*.$$
$$= \frac{n_i}{\sqrt{2\pi}} \sqrt{\frac{m_i}{k_B T_i}} \left(\frac{2k_B T_i}{m_i} \underbrace{\int_{-\infty}^{+\infty} v_i^* \exp\left(-v_i^{*2}\right) dv_i^*}_{=0,\text{ odd function}} + c_s \underbrace{\int_{-\infty}^{+\infty} \exp\left(-v_i^{*2}\right) dv_i^*}_{=\sqrt{\pi}}\right)$$
$$= n_i c_s \tag{B.27}$$

Finally,

$$\boxed{\Gamma_i^{1D} = n_i c_s = n_i \sqrt{\frac{k_B(T_e + T_i)}{m_i}}} \tag{B.28}$$

This result was predictable as the fluid velocity u_s is defined as:

$$\Gamma_s = n_s u_s = \int_{-\infty}^{+\infty} v_s f_s dv_s$$

Calculation of the ion heat flux at the wall:

$$
\begin{aligned}
q_i^{1D} &= \int_{-\infty}^{+\infty} \frac{1}{2} m_i v_i^2 v_i f_i^{1D} dv_i \\
&= \int_{-\infty}^{+\infty} \frac{1}{2} m_i v_i^3 \frac{n_i}{\sqrt{2\pi}} \sqrt{\frac{m_i}{k_B T_i}} \exp\left(-\frac{m_i (v_i - c_s)^2}{2 k_B T_i}\right) dv_i \\
&\Downarrow \textit{ using the substitutions } v_i^* = \sqrt{\frac{m_i}{2 k_B T_i}} (v_i - c_s) \Leftrightarrow v_i = c_s + \sqrt{\frac{2 k_B T_i}{m_i}} v_i^*;\ dv_i = \sqrt{\frac{2 k_B T_i}{m_i}} dv_i^*. \\
&= \frac{m_i n_i}{2\sqrt{2\pi}} \sqrt{\frac{m_i}{k_B T_i}} \sqrt{\frac{2 k_B T_i}{m_i}} \int_{-\infty}^{+\infty} \left(\sqrt{\frac{2 k_B T_i}{m_i}} v_i^* + c_s\right)^3 \exp\left(-v_i^{*2}\right) dv_i^* \\
&= \frac{m_i n_i}{2\sqrt{\pi}} \Bigg[\underbrace{\int_{-\infty}^{+\infty} \left(\frac{2 k_B T_i}{m_i}\right)^{3/2} v_i^{*3} \exp\left(-v_i^{*2}\right) dv_i^*}_{=0,\ \text{odd function}} \\
&\qquad + 3 \underbrace{\int_{-\infty}^{+\infty} \frac{2 k_B T_i}{m_i} v_i^{*2} c_s \exp\left(-v_i^{*2}\right) dv_i^*}_{= \frac{2 k_B T_i}{m_i} c_s \frac{\sqrt{\pi}}{2}} \\
&\qquad + 3 \underbrace{\int_{-\infty}^{+\infty} \sqrt{\frac{2 k_B T_i}{m_i}} v_i^* c_s^2 \exp\left(-v_i^{*2}\right) dv_i^*}_{=0,\ \text{odd function}} \\
&\qquad + \underbrace{\int_{-\infty}^{+\infty} c_s^3 \exp\left(-v_i^{*2}\right) dv_i^*}_{= c_s^3 \sqrt{\pi}} \Bigg] \\
&= \frac{m_i n_i c_s}{2} \left(c_s^2 + 3 \frac{k_B T_i}{m_i}\right)
\end{aligned}
\tag{B.29}
$$

And, finally:

$$
\boxed{q_i^{1D} = \frac{m_i n_i c_s}{2} \left(c_s^2 + 3 \frac{k_B T_i}{m_i}\right) = \frac{n_i}{2} \sqrt{\frac{k_B (T_e + T_i)}{m_i}} \left(k_B T_e + 4 k_B T_i\right)}
\tag{B.30}
$$

We can now compute the sheath ion heath transfer coefficient :

$$
\begin{aligned}
\gamma_i^{1D} &= \frac{q_i^{1D}}{k_B T_i \Gamma_i^{1D}} \\
&= \frac{\frac{\cancel{n_i}}{2} \cancel{\sqrt{\frac{k_B (T_e + T_i)}{m_i}}} \left(k_B T_e + 4 k_B T_i\right)}{k_B T_i \cancel{n_i} \cancel{\sqrt{\frac{k_B (T_e + T_i)}{m_i}}}}
\end{aligned}
\tag{B.31}
$$

We obtained:

$$
\boxed{\gamma_i^{1D} = 2 + \frac{1}{2} \frac{T_e}{T_i}}
\tag{B.32}
$$

B.3.3 3D case

Calculation of the ion particle flux at the wall:

$$
\begin{aligned}
\Gamma_i^{3D} &= \int_{-\infty}^{+\infty}\int_{-\infty}^{+\infty}\int_{-\infty}^{+\infty} f_i^{3D} v_1 dv_1 dv_2 dv_3 \\
&= \int_{-\infty}^{+\infty}\int_{-\infty}^{+\infty}\int_{-\infty}^{+\infty} v_1 \frac{n_i}{(2\pi)^{3/2}} \left(\frac{m_i}{k_B T_i}\right)^{3/2} \exp\left(-\frac{m_i((v_1-c_s)^2+v_2^2+v_3^2)}{2k_B T_i}\right) dv_1 dv_2 dv_3 \\
&\Downarrow \textit{ here, we used the substitutions } v_1^* = \sqrt{\frac{m_i}{2k_B T_i}}(v_1-c_s);\ v_2^* = \sqrt{\frac{m_i}{2k_B T_i}}v_2;\ v_3^* = \sqrt{\frac{m_i}{2k_B T_i}}v_3. \\
&= \frac{n_i}{(2\pi)^{3/2}} \left(\frac{m_i}{k_B T_i}\right)^{3/2} \left(\frac{2k_B T_i}{m_i}\right)^{3/2} \underbrace{\int_{-\infty}^{+\infty} \exp\left(-v_2^{2*}\right) dv_2^*}_{=\sqrt{\pi}} \underbrace{\int_{-\infty}^{+\infty} \exp\left(-v_3^{2*}\right) dv_3^*}_{=\sqrt{\pi}} \\
&\qquad * \left(\underbrace{\int_{-\infty}^{+\infty} \sqrt{\frac{2k_B T_i}{m_i}} v_1^* \exp\left(-v_1^{2*}\right) dv_1^*}_{=0,\text{ odd function}} + c_s \underbrace{\int_{-\infty}^{+\infty} \exp\left(-v_1^{2*}\right) dv_1^*}_{=\sqrt{\pi}}\right) \\
&= n_i c_s
\end{aligned} \tag{B.33}
$$

Finally,

$$
\boxed{\Gamma_i^{3D} = n_i c_s = n_i \sqrt{\frac{k_B(T_e+T_i)}{m_i}}} \tag{B.34}
$$

Calculation of the ion heat flux at the wall:

$$
\begin{aligned}
q_i^{3D} &= \int_{-\infty}^{+\infty}\int_{-\infty}^{+\infty}\int_{-\infty}^{+\infty} \frac{1}{2} m_i (v_1^2+v_2^2+v_3^2) v_1 f_i^{3D} dv_1 dv_2 dv_3 \\
&= \int_{-\infty}^{+\infty}\int_{-\infty}^{+\infty}\int_{-\infty}^{+\infty} \frac{1}{2} m_i (v_1^2+v_2^2+v_3^2) v_1 \frac{n_i}{(2\pi)^{3/2}} \left(\frac{m_i}{k_B T_i}\right)^{3/2} \\
&\qquad\qquad \exp\left(-\frac{m_i((v_1-c_s)^2+v_2^2+v_3^2)}{2k_B T_i}\right) dv_1 dv_2 dv_3 \\
&\Downarrow \textit{ using the substitutions } v_1^* = \sqrt{\frac{m_i}{2k_B T_i}}(v_1-c_s);\ v_2^* = \sqrt{\frac{m_i}{2k_B T_i}} v_2;\ v_3^* = \sqrt{\frac{m_i}{2k_B T_i}} v_3. \\
&= \frac{m_i n_i}{2(2\pi)^{3/2}} \left(\frac{m_i}{k_B T_i}\right)^{3/2} \left(\frac{2k_B T_i}{m_i}\right)^{3/2} \iiint_{-\infty}^{+\infty} \left(\left(\sqrt{\frac{2k_B T_i}{m_i}} v_1^* + c_s\right)^2 + v_2^{*2} + v_3^{*2} \right) \left(\sqrt{\frac{2k_B T_i}{m_i}} v_1^* + c_s\right) \\
&\qquad\qquad \exp\left(-\left(v_1^{*2}+v_2^{*2}+v_3^{*2}\right)\right) dv_1^* dv_2^* dv_3^* \\
&= \frac{m_i n_i}{2\pi^{3/2}} \Bigg[\underbrace{\int_{-\infty}^{+\infty} \left(\sqrt{\frac{2k_B T_i}{m_i}} v_1^* + c_s\right)^3 \exp\left(-v_1^{*2}\right) dv_1^*}_{=\sqrt{\pi} c_s (c_s^2 + 3\frac{k_B T_i}{m_i}),\ \text{see (B.29)}} \underbrace{\int_{-\infty}^{+\infty} \exp\left(-v_2^{*2}\right) dv_2^*}_{=\sqrt{\pi}} \underbrace{\int_{-\infty}^{+\infty} \exp\left(-v_3^{*2}\right) dv_3^*}_{=\sqrt{\pi}} \\
&\quad + \left(\frac{2k_B T_i}{m_i}\right)^{3/2} \underbrace{\int_{-\infty}^{+\infty} v_1^* \exp\left(-v_1^{*2}\right) dv_1^*}_{=0,\ \text{odd function}} \underbrace{\int_{-\infty}^{+\infty} v_2^{*2} \exp\left(-v_2^{*2}\right) dv_2^*}_{=\frac{\sqrt{\pi}}{2}} \underbrace{\int_{-\infty}^{+\infty} \exp\left(-v_3^{*2}\right) dv_3^*}_{=\sqrt{\pi}} \\
&\quad + c_s \frac{2k_B T_i}{m_i} \underbrace{\int_{-\infty}^{+\infty} \exp\left(-v_1^{*2}\right) dv_1^*}_{=\sqrt{\pi}} \underbrace{\int_{-\infty}^{+\infty} v_2^{*2} \exp\left(-v_2^{*2}\right) dv_2^*}_{=\frac{\sqrt{\pi}}{2}} \underbrace{\int_{-\infty}^{+\infty} \exp\left(-v_3^{*2}\right) dv_3^*}_{=\sqrt{\pi}} \\
&\quad + \left(\frac{2k_B T_i}{m_i}\right)^{3/2} \underbrace{\int_{-\infty}^{+\infty} v_1^* \exp\left(-v_1^{*2}\right) dv_1^*}_{=0,\ \text{odd function}} \underbrace{\int_{-\infty}^{+\infty} \exp\left(-v_2^{*2}\right) dv_2^*}_{=\sqrt{\pi}} \underbrace{\int_{-\infty}^{+\infty} v_3^{*2} \exp\left(-v_3^{*2}\right) dv_3^*}_{=\frac{\sqrt{\pi}}{2}} \\
&\quad + c_s \frac{2k_B T_i}{m_i} \underbrace{\int_{-\infty}^{+\infty} \exp\left(-v_1^{*2}\right) dv_1^*}_{=\sqrt{\pi}} \underbrace{\int_{-\infty}^{+\infty} \exp\left(-v_2^{*2}\right) dv_2^*}_{=\sqrt{\pi}} \underbrace{\int_{-\infty}^{+\infty} v_3^{*2} \exp\left(-v_3^{*2}\right) dv_3^*}_{=\frac{\sqrt{\pi}}{2}} \Bigg]
\end{aligned}
\tag{B.35}
$$

It leads to:

$$
\begin{aligned}
q_i^{3D} &= \frac{m_i n_i}{2\pi^{3/2}} \left(\pi^{3/2} c_s (c_s^2 + 3\frac{k_B T_i}{m_i}) + \pi^{3/2} c_s \frac{k_B T_i}{m_i} + \pi^{3/2} c_s \frac{k_B T_i}{m_i} \right) \\
&= \frac{m_i n_i c_s}{2} (c_s^2 + 5\frac{k_B T_i}{m_i})
\end{aligned}
\tag{B.36}
$$

Finally:

$$
\boxed{q_i^{3D} = \frac{m_i n_i c_s}{2} \left(c_s^2 + 5\frac{k_B T_i}{m_i}\right) = \frac{n_i}{2} \sqrt{\frac{k_B(T_e+T_i)}{m_i}} \left(k_B T_e + 6k_B T_i\right)}
\tag{B.37}
$$

We can now compute the sheath ion heath transfer coefficient :

$$\begin{aligned}
\gamma_i^{3D} &= \frac{q_i^{3D}}{k_B T_i \Gamma_i^{3D}} \\
&= \frac{\frac{\cancel{n_i}}{2}\cancel{\sqrt{\frac{k_B(T_e+T_i)}{m_i}}}\left(k_B T_e + 6k_B T_i\right)}{k_B T_i \cancel{n_i}\cancel{\sqrt{\frac{k_B(T_e+T_i)}{m_i}}}}
\end{aligned} \tag{B.38}$$

We obtained:

$$\boxed{\gamma_i^{3D} = 3 + \frac{1}{2}\frac{T_e}{T_i}} \tag{B.39}$$

Bibliography

[Amponsah 14] N.Y. Amponsah, M. Troldborg, B. Kington, I. Aalders & R.L. Hough. *Greenhouse gas emissions from renewable energy sources: A review of lifecycle considerations.* Renewable and Sustainable Energy Reviews, vol. 39, pages 461 – 475, 2014.

[Baudoin 18] C. Baudoin, P. Tamain, H. Bufferand, G. Ciraolo, N. Fedorczak, D. Galassi, Ph. Ghendrih & N. Nace. *Turbulent heat transport in TOKAM3X edge plasma simulations (accepted).* Contributions to Plasma Physics, 2018.

[Benkadda 01] S. Benkadda, P. Beyer, N. Bian, C. Figarella, O. Garcia, X. Garbet, P. Ghendrih, Y. Sarazin & P.H. Diamond. *Bursty transport in tokamak turbulence: Role of zonal flows and internal transport barriers.* Nuclear Fusion, vol. 41, no. 8, page 995, 2001.

[Beyer 00] P. Beyer, S. Benkadda, X. Garbet & P.H. Diamond. *Nondiffusive Transport in Tokamaks: Three-Dimensional Structure of Bursts and the Role of Zonal Flows.* Phys. Rev. Lett., vol. 85, pages 4892–4895, Dec 2000.

[Beyer 05] P. Beyer, S. Benkadda, G. Fuhr-Chaudier, X. Garbet, Ph. Ghendrih & Y. Sarazin. *Nonlinear Dynamics of Transport Barrier Relaxations in Tokamak Edge Plasmas.* Phys. Rev. Lett., vol. 94, page 105001, Mar 2005.

[Beyer 07] P. Beyer, S. Benkadda, G. Fuhr-Chaudier, X. Garbet, Ph. Ghendrih & Y. Sarazin. *Turbulence simulations of transport barrier relaxations in tokamak edge plasmas.* Plasma Physics and Controlled Fusion, vol. 49, no. 4, page 507, 2007.

[Biglari 90] H. Biglari, P.H. Diamond & P.W. Terry. *Influence of sheared poloidal rotation on edge turbulence.* Physics of Fluids B: Plasma Physics, vol. 2, no. 1, pages 1–4, 1990.

[Bilyková 06] O. Bilyková, V. Fuchs, R. Pánek, J. Urban, F. Žáček, J. Stöckel, I. Voitsekhovitch, M. Valovič & M. Fitzgerald. *COMPASS-D magnetic equilibria with lh and NBI current drive.* Czechoslovak Journal of Physics, vol. 56, no. 2, pages B24–B30, Oct 2006.

[BP 17] BP. *BP Statistical Review of World Energy 2017. https://www.bp.com/en/global/corporate/energy-economics/statistical-review-of-world-energy.html.* 2017.

[Braginskii 65] S.I. Braginskii. *Reviews of plasma physics*, 1965.

[Brown 11] J.H. Brown, W.R. Burnside, A.D. Davidson, J.P. DeLong, W.C. Dunn, M.J. Hamilton, N. Mercado-Silva, J.C. Nekola, J.G. Okie, W.H. Woodruff & W. Zuo. *Energetic Limits to Economic Growth.* BioScience, vol. 61, no. 1, pages 19–26, 2011.

[Burrell 97] K.H. Burrell. *Effects of E×B velocity shear and magnetic shear on turbulence and transport in magnetic confinement devices.* Physics of Plasmas, vol. 4, no. 5, pages 1499–1518, 1997.

[Carreras 94] B.A. Carreras, D. Newman, P.H. Diamond & Y.M. Liang. *Dynamics of low to high ("L" to "H") confinement bifurcation: Poloidal flow and ion pressure gradient evolution.* Physics of Plasmas, vol. 1, no. 12, pages 4014–4021, 1994.

[Chôné 14] L. Chôné, P. Beyer, Y. Sarazin, G. Fuhr, C. Bourdelle & S. Benkadda. *L-H transition dynamics in fluid turbulence simulations with neoclassical force balance.* Physics of Plasmas, vol. 21, no. 7, page 070702, 2014.

[Chôné 15] L. Chôné, P. Beyer, Y. Sarazin, G. Fuhr, C. Bourdelle & S. Benkadda. *Mechanisms and dynamics of the external transport barrier formation in non-linear plasma edge simulations.* Nuclear Fusion, vol. 55, no. 7, page 073010, 2015.

[Connor 95] J.W. Connor. *Transport in tokamaks: Theoretical models and comparison with experimental results.* Plasma Physics and Controlled Fusion, vol. 37, no. 11A, page A119, 1995.

[Conway 08] G.D. Conway. *Turbulence measurements in fusion plasmas.* Plasma Physics and Controlled Fusion, vol. 50, no. 12, page 124026, 2008.

[Conway 11] G.D. Conway, C. Angioni, F. Ryter, P. Sauter & J. Vicente. *Mean and Oscillating Plasma Flows and Turbulence Interactions across the L−H Confinement Transition.* Phys. Rev. Lett., vol. 106, page 065001, Feb 2011.

[Diamond 94] P.H. Diamond, Y-M. Liang, B.A. Carreras & P.W. Terry. *Self-Regulating Shear Flow Turbulence: A Paradigm for the L to H Transition.* Phys. Rev. Lett., vol. 72, pages 2565–2568, Apr 1994.

[Diamond 01] P.H. Diamond, S. Champeaux, M. Malkov, A. Das, I. Gruzinov, M.N. Rosenbluth, C. Holland, B. Wecht, A.I. Smolyakov, F.L. Hinton, Z. Lin & T.S. Hahm. *Secondary instability in drift wave turbulence as a mechanism for zonal flow and avalanche formation.* Nuclear Fusion, vol. 41, no. 8, page 1067, 2001.

[Doyle 91] E.J. Doyle, R.J. Groebner, K.H. Burrell, P. Gohil, T. Lehecka, N.C. Luhmann Jr., H. Matsumoto, T.H. Osborne, W.A. Peebles & R. Philipona. *Modifications in turbulence and edge electric fields at the L–H transition in the DIII-D tokamak.* Physics of Fluids B: Plasma Physics, vol. 3, no. 8, pages 2300–2307, 1991.

[Dunne 17] M.G. Dunne. *Impact of impurity seeding and divertor conditions on transitions, pedestal structure and ELMs.* Nuclear Fusion, vol. 57, no. 2, page 025002, 2017.

[Eich 13] T. Eich, A.W. Leonard, R.A. Pitts, W. Fundamenski, R.J. Goldston, T.K. Gray, A. Herrmann, A. Kirk, A. Kallenbach, O. Kardaun, A.S. Kukushkin, B. LaBombard, R. Maingi, M.A. Makowski, A. Scarabosio, B. Sieglin, J. Terry, A. Thornton, ASDEX Upgrade Team & JET EFDA Contributors. *Scaling of the tokamak near the scrape-off layer H-mode power width and implications for ITER.* Nuclear Fusion, vol. 53, no. 9, page 093031, 2013.

[Fedorczak 12] N. Fedorczak, P.H. Diamond, G. Tynan & P. Manz. *Shear-induced Reynolds stress at the edge of L-mode tokamak plasmas.* Nuclear Fusion, vol. 52, no. 10, page 103013, 2012.

[Floriani 13] E. Floriani, G. Ciraolo, Ph. Ghendrih, R. Lima & Y. Sarazin. *Self-regulation of turbulence bursts and transport barriers.* Plasma Physics and Controlled Fusion, vol. 55, no. 9, page 095012, 2013.

[Fujisawa 06] A. Fujisawa, A. Shimizu, H. Nakano, S. Ohsima, K. Itoh, H. Iguchi, Y. Yoshimura, T. Minami, K. Nagaoka, C. Takahashi, M. Kojima, S. Nishimura, M. Isobe, C. Suzuki, T. Akiyama, Y. Nagashima, K. Ida, K. Toi, T. Ido, S-I. Itoh, K. Matsuoka, S. Okamura & P.H. Diamond. *Turbulence and transport characteristics of a barrier in a toroidal plasma.* Plasma Physics and Controlled Fusion, vol. 48, no. 4, page S205, 2006.

[Galassi 17a] D. Galassi. *Numerical modelling of transport and turbulence in the tokamak edge plasma with X-point magnetic geometry.* Theses, Université d'Aix Marseille, 2017.

[Galassi 17b] D. Galassi, P. Tamain, C. Baudoin, H. Bufferand, G. Ciraolo, N. Fedorczak, Ph. Ghendrih, N. Nace & E. Serre. *Flux expansion effect on turbulent transport in 3D global simulations.* Nuclear Materials and Energy, 2017.

[Garbet 91] X. Garbet, L. Laurent, J-P. Roubin & A. Samain. *A model for the turbulence in the scrape-off layer of tokamaks.* Nuclear Fusion, vol. 31, no. 5, page 967, 1991.

[Ghendrih 03] Ph. Ghendrih, Y. Sarazin, G. Attuel, S. Benkadda, P. Beyer, G. Falchetto, C. Figarella, X. Garbet, V. Grandgirard & M. Ottaviani. *Theoretical analysis of the influence of external biasing on long range turbulent transport in the scrape-off layer.* Nuclear Fusion, vol. 43, no. 10, page 1013, 2003.

[Ghendrih 07] Ph. Ghendrih, Y. Sarazin, G. Ciraolo, G. Darmet, X. Garbet, V. Grangirard, P. Tamain, S. Benkadda & P. Beyer. *Transport barrier fluctuations governed by SOL turbulence spreading.* Journal of Nuclear Materials, vol. 363-365, pages 581 – 585, 2007. Plasma-Surface Interactions-17.

[Ghendrih 09] Ph. Ghendrih, G. Ciraolo, Y. Larmande, Y. Sarazin, P. Tamain, P. Beyer, G. Chiavassa, G. Darmet, X. Garbet & V. Grandgirard. *Shearing effects on density burst propagation in SOL plasmas.* Journal of Nuclear Materials, vol. 390-391, pages 425 – 427, 2009. Proceedings of the 18th International Conference on Plasma-Surface Interactions in Controlled Fusion Device.

[Gianakon 02] T.A. Gianakon, S.E. Kruger & C.C. Hegna. *Heuristic closures for numerical simulations of neoclassical tearing modes.* Physics of Plasmas, vol. 9, no. 2, pages 536–547, 2002.

[Gohil 08] P. Gohil, G.R. McKee, D. Schlossberg, L. Schmitz & G. Wang. *Dependence of the H-mode power threshold on toroidal plasma rotation in the DIII-D tokamak*. Journal of Physics: Conference Series, vol. 123, no. 1, page 012017, 2008.

[Groebner 90] R.J. Groebner, K.H. Burrell & R.P. Seraydarian. *Role of edge electric field and poloidal rotation in the L-H transition*. Phys. Rev. Lett., vol. 64, pages 3015–3018, Jun 1990.

[Hidalgo 11] C. Hidalgo. *Multi-scale physics and transport barriers in fusion plasmas*. Plasma Physics and Controlled Fusion, vol. 53, no. 7, page 074003, 2011.

[Hinton 71] F.L. Hinton & C.W. Horton Jr. *Amplitude Limitation of a Collisional Drift Wave Instability*. The Physics of Fluids, vol. 14, no. 1, pages 116–123, 1971.

[Hinton 76] F. L. Hinton & R. D. Hazeltine. *Theory of plasma transport in toroidal confinement systems*. Rev. Mod. Phys., vol. 48, pages 239–308, Apr 1976.

[Horacek 10] J. Horacek, J. Adamek, H.W. Müller, J. Seidl, A.H. Nielsen, V. Rohde, F. Mehlmann, C. Ionita, E. Havlíčková & the ASDEX Upgrade Team. *Interpretation of fast measurements of plasma potential, temperature and density in SOL of ASDEX Upgrade*. Nuclear Fusion, vol. 50, no. 10, page 105001, 2010.

[Hornung 13] G. Hornung, F. Clairet, G.L. Falchetto, R. Sabot, H. Arnichand & L. Vermare. *Turbulence correlation properties measured with ultrafast sweeping reflectometry on Tore Supra*. Plasma Physics and Controlled Fusion, vol. 55, no. 12, page 125013, 2013.

[Hurricane 14] O.A. Hurricane, D.A. Callahan, D.T. Casey, P.M. Celliers, C. Cerjan, E.L. Dewald, T.R. Dittrich, T. Döppner, D.E. Hinkel, L.F.B. Hopkins, J.L. Kline, S. Le Pape, T. Ma, A.G. Macphee, J.L. Milovich, A. Pak, H.-S. Park, P.K. Patel, B.A. Remington, J.D. Salmonson, P.T. Springer & R. Tommasini. *Fuel gain exceeding unity in an inertially confined fusion implosion*. Nature, vol. 506, pages 343–348, 2014.

[Ida 90] K. Ida, S. Hidekuma, Y. Miura, T. Fujita, M. Mori, K. Hoshino, N. Suzuki & T. Yamauchi. *Edge electric-field profiles of H-mode plasmas in the JFT-2M tokamak*. Phys. Rev. Lett., vol. 65, pages 1364–1367, Sep 1990.

[International Energy Agency report 17] International Energy Agency report. *Key World Energy Statistics 2017. https://www.iea.org/publications/freepublications/publication/key-world-energy-statistics.html.* 2017.

[IPCC 14] IPCC. Climate change 2014–impacts, adaptation and vulnerability: Regional aspects. Cambridge University Press, 2014.

[ITER Physics 99] Basis Editors ITER Physics, ITER Physics Expert Group Chairs, Co-Chairs, ITER Joint Central Team & Physics Integration Unit. *Chapter 1: Overview and summary.* Nuclear Fusion, vol. 39, no. 12, page 2137, 1999.

[Itoh 88] S-I. Itoh & K. Itoh. *Model of L to H-Mode Transition in Tokamak.* Phys. Rev. Lett., vol. 60, pages 2276–2279, May 1988.

[Itoh 96] K. Itoh & S-I. Itoh. *The role of the electric field in confinement.* Plasma Physics and Controlled Fusion, vol. 38, no. 1, page 1, 1996.

[Itoh 06] K. Itoh, S.-I. Itoh, P.H. Diamond, T.S. Hahm, A. Fujisawa, G.R. Tynan, M. Yagi & Y. Nagashima. *Physics of zonal flows.* Physics of Plasmas, vol. 13, no. 5, page 055502, 2006.

[Itoh 14] S-I. Itoh & K. Itoh. *Zero-dimensional model for the critical condition for the L–H transition in the flux–gradient relation.* Nuclear Fusion, vol. 54, no. 11, page 114017, 2014.

[Itoh 15] K. Itoh, S-I. Itoh, K. Kamiya & N. Kasuya. *On the spatial structure of solitary radial electric field at the plasma edge in toroidal confinement devices.* Plasma Physics and Controlled Fusion, vol. 57, no. 7, page 075008, 2015.

[Itoh 16] K. Itoh, S-I. Itoh, T. Kobayashi, K. Kamiya, T. Ido, T. Tokuzawa, S. Inagaki & N. Kasuya. *On the Origin of Steep and Localized Radial Electric Field in the Transport Barrier at Plasma Edge.* Contributions to Plasma Physics, vol. 56, no. 6-8, pages 522–527, 2016.

[Kamiya 16] K. Kamiya, K. Itoh & S-I. Itoh. *Experimental validation of non-uniformity effect of the radial electric field on the edge transport barrier formation in JT-60U H-mode plasmas.* Scientific Reports, vol. 6, page 30585, August 2016.

[Kamiya 18] K. Kamiya, K. Itoh, S-I. Itoh, K. Ida & T. Kobayashi. *Role of electric field curvature in the formation of edge transport barrier in the JT-60U tokamak.* Plasma Physics and Controlled Fusion, vol. 60, no. 1, page 014023, 2018.

[Kim 03] E. Kim & P. H. Diamond. *Zonal Flows and Transient Dynamics of the $L-H$ Transition.* Phys. Rev. Lett., vol. 90, page 185006, May 2003.

[Kočan 10] M. Kočan & J.P. Gunn. *Comparison of scrape-off layer profiles in outboard-versus inboard-limited plasmas in Tore Supra.* Plasma Physics and Controlled Fusion, vol. 52, no. 4, page 045010, 2010.

[Lambert 14] J.G. Lambert, C.A.S. Hall, S. Balogh, A. Gupta & M. Arnold. *Energy, EROI and quality of life.* Energy Policy, vol. 64, pages 153 – 167, 2014.

[Liewer 85] P.C. Liewer. *Measurements of microturbulence in tokamaks and comparisons with theories of turbulence and anomalous transport.* Nuclear Fusion, vol. 25, no. 5, page 543, 1985.

[Miki 12] K. Miki, P.H. Diamond, Ö.D. Gürcan, G.R. Tynan, T. Estrada, L. Schmitz & G.S. Xu. *Spatio-temporal evolution of the $L \to I \to H$ transition.* Physics of Plasmas, vol. 19, no. 9, page 092306, 2012.

[Moulton 14] D. Moulton, Y. Marandet, P. Tamain, Ph. Ghendrih & R. Futtersack. *Density and Temperature Correlations in the SOL; Implications for Gas Puff Imaging of Turbulence.* Contributions to Plasma Physics, vol. 54, no. 4-6, pages 575–579, 2014.

[Myra 06] J.R. Myra, D.A. Russell & D.A. D'Ippolito. *Collisionality and magnetic geometry effects on tokamak edge turbulent transport. I. A two-region model with application to blobs.* Physics of Plasmas, vol. 13, no. 11, page 112502, 2006.

[Nace 16] N. Nace, M. Perin, P. Tamain, G. Ciraolo, C. Baudoin, R. Futtersack, Ph. Ghendrih & C. Norscini. *Turbulence Interaction with Driven Transport Barriers in the Scrape-Off Layer of Tokamaks.* Contributions to Plasma Physics, vol. 56, no. 6-8, pages 581–586, 2016.

[Nielsen 15] A.H. Nielsen, G.S. Xu, J. Madsen, V. Naulin, J. Juul Rasmussen & B.N. Wan. *Simulation of transition dynamics* *to high confinement in fusion plasmas.* Physics Letters A, vol. 379, no. 47, pages 3097 – 3101, 2015.

[Norscini 15] C. Norscini. *Self-organized turbulent transport in fusion plasmas.* Theses, Université d'Aix Marseille, November 2015.

[Oost 03] G. Van Oost, J. Adámek, V. Antoni, P. Balan, J.A. Boedo, P. Devynck, I. Ďuran, L. Eliseev, J.P. Gunn, M. Hron, C. Ionita, S. Jachmich, G.S. Kirnev, E. Martines, A. Melnikov, R. Schrittwieser, C. Silva, J. Stöckel, M. Tendler, C. Varandas, M. Van Schoor, V. Vershkov & R.R. Weynants. *Turbulent transport reduction by $E \times B$ velocity shear during edge plasma biasing: recent experimental results.* Plasma Physics and Controlled Fusion, vol. 45, no. 5, page 621, 2003.

[Park 15] G.Y. Park, S.S. Kim, H. Jhang, P.H. Diamond, T. Rhee & X.Q. Xu. *Flux-driven simulations of turbulence collapse.* Physics of Plasmas, vol. 22, no. 3, page 032505, 2015.

[Pasten 12] C. Pasten & J.C. Santamarina. *Energy and quality of life.* Energy Policy, vol. 49, pages 468 – 476, 2012. Special Section: Fuel Poverty Comes of Age: Commemorating 21 Years of Research and Policy.

[Rasmussen 16] J.J. Rasmussen, A.H. Nielsen, J. Madsen, V. Naulin & G.S. Xu. *Numerical modeling of the transition from low to high confinement in magnetically confined plasma.* Plasma Physics and Controlled Fusion, vol. 58, no. 1, page 014031, 2016.

[Ryter 14] F. Ryter, L. Barrera Orte, B. Kurzan, R.M. McDermott, G. Tardini, E. Viezzer, M. Bernert, R. Fischer & The ASDEX Upgrade Team. *Experimental evidence for the key role of the ion heat channel in the physics of the L–H transition.* Nuclear Fusion, vol. 54, no. 8, page 083003, 2014.

[Ryter 16] F. Ryter, M. Cavedon, T. Happel, R.M. McDermott, E. Viezzer, G.D. Conway, R. Fischer, B. Kurzan, T. Pütterich, G. Tardini, M. Willensdorfer & the ASDEX Upgrade Team. *L-H transition physics in hydrogen and deuterium: key role of the edge radial electric field and ion heat flux.* Plasma Physics and Controlled Fusion, vol. 58, no. 1, page 014007, 2016.

[Sakai 93] O. Sakai, Y. Yasaka & R. Itatani. *High radial confinement mode induced by dc limiter biasing in the HIEI tandem mirror.* Phys. Rev. Lett., vol. 70, pages 4071–4074, Jun 1993.

[Sarazin 98] Y. Sarazin & Ph. Ghendrih. *Intermittent particle transport in two-dimensional edge turbulence.* Physics of Plasmas, vol. 5, no. 12, pages 4214–4228, 1998.

[Sarazin 03] Y. Sarazin, Ph. Ghendrih, G. Attuel, C. Clément, X. Garbet, V. Grandgirard, M. Ottaviani, S. Benkadda, P. Beyer, N. Bian & C. Figarella. *Theoretical understanding of turbulent transport in the SOL.* Journal of Nuclear Materials, vol. 313-316, pages 796 – 803, 2003. Plasma-Surface Interactions in Controlled Fusion Devices 15.

[Schmitz 12] L. Schmitz, L. Zeng, T.L. Rhodes, J.C. Hillesheim, E.J. Doyle, R.J. Groebner, W.A. Peebles, K.H. Burrell & G. Wang. *Role of Zonal Flow Predator-Prey Oscillations in Triggering the Transition to H-Mode Confinement.* Phys. Rev. Lett., vol. 108, page 155002, Apr 2012.

[Scott 05] B.D. Scott. *Drift wave versus interchange turbulence in tokamak geometry: Linear versus nonlinear mode structure.* Physics of Plasmas, vol. 12, no. 6, page 062314, 2005.

[Shaing 89] K.C. Shaing & E.C. Crume. *Bifurcation theory of poloidal rotation in tokamaks: A model for L-H transition.* Phys. Rev. Lett., vol. 63, pages 2369–2372, Nov 1989.

[Shu 09] C-W. Shu. *High order weighted essentially nonoscillatory schemes for convection dominated problems.* SIAM review, vol. 51, no. 1, pages 82–126, 2009.

[Sidikman 94] K.L. Sidikman, B.A. Carreras, P.H. Diamond & L. Garcia. *Theory of electric-field curvature effects on long-wavelength drift wave turbulence.* Physics of plasmas, vol. 1, no. 5, pages 1142–1153, 1994.

[Staebler 91] G.M. Staebler & R.R. Dominguez. *Electric field effects on ion temperature gradient modes in a sheared slab.* Nuclear Fusion, vol. 31, no. 10, page 1891, 1991.

[Stangeby 95] P.C. Stangeby & A.V. Chankin. *The ion velocity (Bohm–Chodura) boundary condition at the entrance to the magnetic presheath in the presence of diamagnetic and E×B drifts in the scrape-off layer.* Physics of Plasmas, vol. 2, no. 3, pages 707–715, 1995.

[Stangeby 00] P.C. Stangeby. *Plasma Physics Series.* The Plasma Boundary of Magnetic Fusion Devices, Institute of Physics, Bristol and Philadelphia, page 97, 2000.

[Stocker 14] T. Stocker. Climate change 2013: the physical science basis: Working group i contribution to the fifth assessment report of the intergovernmental panel on climate change. Cambridge University Press, 2014.

[Stroth 11] U. Stroth, P. Manz & M. Ramisch. *On the interaction of turbulence and flows in toroidal plasmas.* Plasma Physics and Controlled Fusion, vol. 53, no. 2, page 024006, 2011.

[Tamain 14] P. Tamain, H. Bufferand, G. Ciraolo, C. Colin, Ph. Ghendrih, F. Schwander & E. Serre. *3D Properties of Edge Turbulent Transport in Full-Torus Simulations and their Impact on Poloidal Asymmetries.* Contributions to Plasma Physics, vol. 54, no. 4-6, pages 555–559, 2014.

[Tamain 15] P. Tamain, Ph. Ghendrih, H. Bufferand, G. Ciraolo, C. Colin, N. Fedorczak, N. Nace, F. Schwander & E. Serre. *Multi-scale self-organisation of edge plasma turbulent transport in 3D global simulations.* Plasma Physics and Controlled Fusion, vol. 57, no. 5, page 054014, 2015.

[Tamain 16] P. Tamain, H. Bufferand, G. Ciraolo, C. Colin, D. Galassi, Ph. Ghendrih, F. Schwander & E. Serre. *The TOKAM3X code for edge turbulence fluid simulations of tokamak plasmas in versatile magnetic geometries.* Journal of Computational Physics, vol. 321, pages 606 – 623, 2016.

[Taylor 89] R.J. Taylor, M.L. Brown, B.D. Fried, H. Grote, J.R. Liberati, G.J. Morales, P. Pribyl, D. Darrow & M. Ono. *H-mode behavior induced by cross-field currents in a tokamak.* Phys. Rev. Lett., vol. 63, pages 2365–2368, Nov 1989.

[Terry 00] P.W. Terry. *Suppression of turbulence and transport by sheared flow.* Rev. Mod. Phys., vol. 72, pages 109–165, Jan 2000.

[Tynan 13] G.R. Tynan, M. Xu, P.H. Diamond, J.A. Boedo, I. Cziegler, N. Fedorczak, P. Manz, K. Miki, S. Thakur, L. Schmitz, L. Zeng, E.J. Doyle, G.M. McKee, Z. Yan, G.S. Xu, B.N. Wan, H.Q. Wang, H.Y. Guo, J. Dong, K. Zhao, J. Cheng, W.Y. Hong & L.W. Yan. *Turbulent-driven low-frequency sheared $E \times B$ flows as the trigger for the H-mode transition.* Nuclear Fusion, vol. 53, no. 7, page 073053, 2013.

[United Nations report 17] United Nations report. *World Population Prospects: The 2017 Revision. https://esa.un.org/unpd/wpp/.* 2017.

[van Leer 79] B. van Leer. *Towards the ultimate conservative difference scheme. V - A second-order sequel to Godunov's method.* Journal of Computational Physics, vol. 32, pages 101–136, July 1979.

[Viezzer 14] E. Viezzer, T. Pütterich, C. Angioni, A. Bergmann, R. Dux, E. Fable, R.M. McDermott, U. Stroth, E. Wolfrum & the ASDEX Upgrade Team. *Evidence for the neoclassical nature of the radial electric field in the edge transport barrier of ASDEX Upgrade.* Nuclear Fusion, vol. 54, no. 1, page 012003, 2014.

[Wagner 82] F. Wagner, G. Becker, K. Behringer, D. Campbell, A. Eberhagen, W. Engelhardt, G. Fussmann, O. Gehre, J. Gernhardt, G.v. Gierke, G. Haas, M. Huang, F. Karger, M. Keilhacker, O. Klüber, M. Kornherr, K. Lackner, G. Lisitano, G G. Lister, H.M. Mayer, D. Meisel, E.R. Müller, H. Murmann, H. Niedermeyer, W. Poschenrieder, H. Rapp, H. Röhr, F. Schneider, G. Siller, E. Speth, A. Stäbler, K.H. Steuer, G. Venus, O. Vollmer & Z. Yü. *Regime of Improved Confinement and High Beta in Neutral-Beam-Heated Divertor Discharges of the ASDEX Tokamak.* Phys. Rev. Lett., vol. 49, pages 1408–1412, Nov 1982.

[Wagner 84] F. Wagner, G. Fussmann, T. Grave, M. Keilhacker, M. Kornherr, K. Lackner, K. McCormick, E.R. Müller, A. Stäbler, G. Becker, K. Bernhardi, U. Ditte, A. Eberhagen, O. Gehre, J. Gernhardt, G.v. Gierke, E. Glock, O. Gruber, G. Haas, M. Hesse, G. Janeschitz, F. Karger, S. Kissel, O. Klüber, G. Lisitano, H.M. Mayer, D. Meisel, V. Mertens, H. Murmann, W. Poschenrieder, H. Rapp, H. Röhr, F. Ryter, F. Schneider, G. Siller, P. Smeulders, F. Söldner, E. Speth, K-H. Steuer, Z. Szymanski & O. Vollmer. *Development of an Edge Transport Barrier at the H-Mode Transition of ASDEX.* Phys. Rev. Lett., vol. 53, pages 1453–1456, Oct 1984.

[Wagner 93] F. Wagner & U. Stroth. *Transport in toroidal devices-the experimentalist's view.* Plasma Physics and Controlled Fusion, vol. 35, no. 10, page 1321, 1993.

[Wagner 07] F. Wagner. *A quarter-century of H-mode studies.* Plasma Physics and Controlled Fusion, vol. 49, no. 12B, page B1, 2007.

[Wesson 11] J. Wesson. Tokamaks, volume 149. Oxford university press, 2011.

[Weynants 92] R.R. Weynants, G. Van Oost, G. Bertschinger, J. Boedo, P. Brys, T. Delvigne, K.H. Dippel, F. Durodie, H. Euringer, K.H. Finken*et al.* *Confinement and profile changes induced by the presence of positive or negative radial electric fields in the edge of the TEXTOR tokamak.* Nuclear Fusion, vol. 32, no. 5, page 837, 1992.

[Zimbardo 00] G. Zimbardo, P. Pommois & P. Veltri. *The Kubo number as a parameter governing the level of chaos in magnetic turbulence.* Physica A: Statistical Mechanics and its Applications, vol. 280, no. 1, pages 99–105, 2000.

[Zweben 09] S.J. Zweben, R.J. Maqueda, A.L. Roquemore, C.E. Bush, R. Kaita, R.J. Marsala, Y. Raitses, R.H. Cohen & D.D. Ryutov. *Local scrape-off layer control using biased electrodes in NSTX.* Plasma Physics and Controlled Fusion, vol. 51, no. 10, page 105012, 2009.

Summary

Performances of magnetic fusion devices are limited by radial outward transport which is mainly driven by turbulence. Experimentally, a high confinement regime, the H-mode, is obtained in most of magnetic devices when a threshold level on heating power is exceeded. The H-mode is characterized by the suppression of edge plasma turbulence, the apparition of a transport barrier and the increase of pressure gradient in the pedestal. While the $\mathbf{E} \times \mathbf{B}$ shear has been identified as a key mechanism of the transition from low to high confinement regimes, mainly through the generation of a sheared flow, the complete interplay between turbulence and sheared flows is still not fully understood. Recently, numerical simulations using fluid turbulence models of tokamak edge plasma recovered some features of the L-H transition. 2D slab simulations underlined the importance of the transition between closed and open field lines as well as the role played by the ion energy channel. Meanwhile, an improved confinement regime has been obtained in 3D simulations of closed field lines by taking into account a neoclassical friction force (collisional effects inherent in toroidal magnetized plasmas). In this thesis, the dynamics of driven and spontaneous edge transport barriers are investigated using 2D and 3D numerical simulations. In particular, we focus on the impact of magnetic geometry. It is shown that transport barriers can be generated by forcing an artificial $\mathbf{E} \times \mathbf{B}$ shear or $\mathbf{E} \times \mathbf{B}$ curvature in open field line region with a large variability of barriers behavior in terms of amplitude, frequency of barrier relaxations, and capability of transport barriers to stop radial transport by turbulence. Transport barriers develop spontaneously when closed field lines are included in thermal 2D slab simulations and the ion energy channel is found to reinforce the efficiency of the barriers thanks to the ion energy contribution in the so-called generalized vorticity. The interplay between sheared flow and turbulence - as predicted by simple predator-prey models - is recovered in hysteresis cycles. The relevance of 2D or 3D slab simulations to reproduce quantitatively a L-H transition is discussed in particular in light of the model approximations and inherent limits of slab geometry. Spontaneous edge transport barriers are not recovered on 3D isothermal simulations of realistic circular limiter geometry even with an increase of the contribution of ion energy channel on generalized vorticity. In this circular limited geometry, two thin spontaneous edge transport barrier - stable over time - are however observed on both sides of the Last Closed Flux Surface when mimicking the safety factor profile of divertor X-point configuration. It is found that these barriers are generated by the magnetic shear which modifies turbulence properties. It explains the discrepancies observed between circular limiter and divertor X-point configurations in 3D simulations but the relevance of these barriers for H-mode remains to be assessed for example by scanning ion input energy in 3D thermal simulations.

Résumé

Le transport radial, principalement turbulent, limite les performances des machines à fusion par confinement magnétique. Un mode de confinement avancé, le mode H, est obtenu avec la plupart des machines quand un seuil est franchi sur la puissance de chauffage. Il est caractérisé par la suppression de la turbulence dans le plasma de bord, par la formation d'une barrière de transport et un raidissement du profil de pression dans le piédestal. Si le cisaillement ExB est identifié comme un mécanisme clé de la transition vers le mode H, notamment via la génération d'un écoulement cisaillé, l'interaction entre cet écoulement et la turbulence reste en partie incompris. Récemment, des simulations numériques du plasma de bord utilisant des codes de turbulence fluide ont retrouvés plusieurs caractéristiques d'une telle transition. Des simulations 2D en géométrie slab ont montré l'importance de la transition entre les lignes de champ magnétique ouvertes et fermées ainsi que le rôle du canal d'énergie ionique. La prise en compte d'une force de friction néoclassique (effets collisionnels inhérents à la configuration magnétique toroïdale) dans des simulations 3D des lignes de champs fermées a conduit à l'obtention d'un régime de confinement amélioré. Dans cette thèse, la dynamique des barrières de transport forcées et spontanées du plasma de bord est étudiée par le biais de simulations numériques 2D et 3D et l'impact de la géométrie magnétique est en particulier analysé. Des barrières de transport peuvent être générées en forçant artificiellement le cisaillement ou la courbure ExB. Les barrières obtenues présentent une large variabilité en termes d'amplitude et de fréquence de relaxation ainsi que de capacité à stopper la propagation radiale par turbulence. Des barrières se développent spontanément quand les lignes de champs fermées sont ajoutées dans le modèle 2D anisotherme en géométrie slab. L'efficacité des barrières est renforcée par la contribution de l'énergie ionique dans la vorticité généralisée. L'interaction entre les écoulements cisaillés et la turbulence est retrouvé dans des cycles d'hystérésis similairement aux prédictions de modèles proie-prédateurs simples. La pertinence des simulations 2D ou 3D en géométrie slab pour reproduire une transition L-H est remise en question en raison des approximations des modèles et des limites inhérentes à cette géométrie. Ces barrières de transport spontanées ne sont pas retrouvées en simulations isotherme 3D en géométrie circulaire réaliste avec un limiteur même en augmentant l'énergie des ions dans la vorticité généralisée. Dans cette même géométrie, deux barrières de transport spontanées, avec une faible extension radiale et constantes en temps, sont néanmoins observées de part et d'autre de la dernière surface magnétique fermées quand le profil de facteur de sécurité d'une géométrie divertor à point-X est reproduit. Ces barrières sont générées par le cisaillement magnétique qui modifie les propriétés de la turbulence. Ceci explique les différences observées entre les géométries limiteur et divertor dans les simulations 3D mais la pertinence de ces barrières pour le mode H doit encore être déterminée par exemple en scannant l'énergie injectée des ions dans des simulations 3D anisothermes.